Title	Theoretical Design for Efficient Singlet Fission Systems based on Molecular Aggregate Structures: From Generation to Directional Migration of Correlated Triplet Exciton Pair
Author(s)	宮本, 孟
Citation	大阪大学, 2025, 博士論文
Version Type	VoR
URL	https://doi.org/10.18910/101726
rights	
Note	

Theoretical Design for Efficient Singlet Fission Systems based on Molecular Aggregate Structures: From Generation to Directional Migration of Correlated Triplet Exciton Pair

Hajime MIYAMOTO

MARCH 2025

Theoretical Design for Efficient Singlet Fission Systems based on Molecular Aggregate Structures: From Generation to Directional Migration of Correlated Triplet Exciton Pair

A dissertation submitted to
THE GRADUATE SCHOOL OF ENGINEERING SCIENCE
OSAKA UNIVERSITY
in partial fulfillment of the requirements for the degree of
DOCTOR OF PHILOSOPHY IN SCIENCE

BY

Hajime MIYAMOTO
MARCH 2025

ABSTRACT

This dissertation study is dedicated to constructing theoretical design guidelines for highly efficient singlet fission (SF) materials, focusing on the role of molecular aggregate structures in determining the yield of correlated triplet pair (TT) states and spatiotemporal distribution of triplet excitons following SF. The dissertation is divided into three parts. PART I introduces a fundamental theoretical framework for treating the excited electronic states in SF dye molecular aggregate systems and the computational and analytical methods for modeling the exciton dynamics, considering the vibronic coupling. Electronic couplings related to the triplet-triplet exciton transfer (TTET) coupling are also introduced. In PART II, we explore the structure–SF property relationships in ring-shaped pentacene molecular aggregates to establish design guidelines for efficient TT generation. This part is composed of two chapters. In Chapter II.1, we focus on J- and H-type ring aggregate models, where the transition dipole moments of constituent molecules align tangentially and perpendicularly to the ring, respectively. Quantum dynamics simulation revealed that the TT generation rate decreases while the TT yield increases with the number of molecules N. The dynamics in the H-type ring aggregates show an interesting odd-even behavior due to the symmetry of the excited states. This phenomenon is explained through a combination of the group theoretical and relative relaxation factor (RRF) analyses. In Chapter II.2, we attempted to construct symmetry-based design guidelines for efficient SF by rotating individual pentacene molecules along the long axis in the H-ring system to lower the structural symmetry from D_{Nh} to C_{Nh}. We examine the relationships between the rotation angle and TT pair generation rate and yield. Analysis based on the perturbation approach has revealed that lowering the structural symmetry contributes to stabilizing one of the two equivalent charge transfer states and enhancing the SF rate without reducing the TT yield. The findings in PART II provide a novel insight into the micro-to-mesoscale structural factors for designing highly efficient SF systems. PART III investigates the SF process in molecular aggregates consisting of two different molecular species, aiming to establish guidelines to control the spatial distribution of TT pairs. Symmetric heterotrimer models are constructed with unsubstituted or 6,13-substituted pentacenes and how the combination of molecular species affects the electronic states, electronic couplings, and SF dynamics. We identify conditions for balancing the high-TT yield and directional TT pair migration by optimizing molecular combination and intermolecular distances. This dissertation identifies key factors of aggregate structures that govern the SF process and are useful as novel descriptors for the efficient formation of TT pairs. These results not only deepen our understanding of SF phenomena but also pave the way for the development of quantum functional materials and their applications involving various exciton processes in condensed phases.

PREFACE

Over the past decades, researchers have experimentally and theoretically established fundamental principles and methodologies to analyze dynamic physical and chemical phenomena on various spatial and temporal scales of matter as a medium for energy and information. Specifically, microscopic quantum mechanical processes of molecular materials have gained significant attention for their potential to explore their unique and valuable functions, like conversion and storage of energy and information, quantum sensing, and computing operations. This motivation has driven recent studies on singlet fission (SF) dynamics since SF can be utilized for applications in organic solar cells and quintet spin generators for dynamic nuclear polarization. In pursuing theoretical studies on SF dynamics, I would like to contribute to establishing a needs-driven material design tailored to specific applications for the conversion and storage of energy and information. I became strongly aware of the importance of identifying the key factors governing the SF process in molecular aggregates: The yield and generation rate of correlated triplet pairs (TT; the energy and information carrier in SF), as well as their efficient spatiotemporal separation, should be maximized and optimized based on the key factors governing the SF process.

A key phrase, “the structure–SF property relationships,” appears repeatedly throughout the dissertation study. This theme presents a challenging problem, as it involves a complex entanglement of various factors, including the constituent molecular species, electronic states, several kinds of interactions, relative intermolecular configuration, and overall topology of the aggregate systems: These factors are linked with each other and influence the resulting dynamic physical phenomena. To address this issue, establishing an effective and practical theoretical model allows me to unentangle the complicated relations between them. I believe that this dissertation work will inspire many researchers by offering novel perspectives on the theoretical design of materials based on exciton dynamics, spanning from the microscopic to mesoscale levels.

This dissertation study was carried out under the supervision of Professor Dr. Masayoshi Nakano and Professor Dr. Yasutaka Kitagawa at the Division of Chemical Engineering, Department of Materials Engineering Science, Graduate School of Engineering Science, Osaka University, from April 2020 to March 2025. I dedicate this dissertation to the late Professor Dr. Masayoshi Nakano.

Hajime MIYAMOTO
Division of Chemical Engineering,
Department of Materials Engineering Science,
Graduate School of Engineering Science, Osaka University
March 2025

CONTENTS

GENERAL INTRODUCTION

1. Exciton Process and Application

Exploring new properties and functions of materials induced by light-matter interactions has become an important subject from the perspective of realizing sustainable development and advanced information society. Irradiation of molecular materials with light at wavelengths in the ultraviolet-visible (UV-vis) region usually causes electronic excitation, which consists of transitions from occupied orbital levels to virtual orbital levels, resulting in the generation of electron-hole pairs. The electron-hole pairs bound by Coulomb interaction behave like quantum mechanical particles and acts as energy carriers in the material. Such quasi-particles (elementary excitations) are called *excitons*. Excitons appear in various natural phenomena and plays important roles in condensed matter physics, photochemistry, biophysics, and information science. Understanding and controlling phenomena involving excitons is crucial for the development of various technologies: light absorption and emission processes, photoelectric conversion devices like organic solar cells (OSCs) and organic light emitting diodes (OLEDs), high efficiency photocatalysis, and modern *sensing* and *quantum information technologies* utilizing transient electronic and spin states.

These technologies utilize various exciton photophysical processes, such as *intersystem crossing* and *reverse intersystem crossing* (ISC and rISC in **Figure 1(a)**)[1], *singlet fission* and *triplet-triplet annihilation* (SF and TTA in **Figure 1(b)**)[2-6], and the formation of *excimers* or *exciplexes* (in **Figure 1(c)**)[7]. Spin conversion, multi-exciton-generation (MEG), and charge transfer between molecules are unique features of these processes and key factors for developing modern photochemical and photophysical devices.

Comprehensive understanding of the correlation between aggregate structures and exciton dynamics is indispensable for establishing these exciton-based technologies. Excitons appear in condensed phases, such as crystalline systems and biological systems. For example, the light-harvesting antenna complexes (LHCs) in plants and photosynthetic bacteria are known to consist of chromophores in a well-aligned cyclic aggregation structure surrounded by protein environment.[8-10] Such a structural feature is crucial in collecting and utilizing the absorbed photon energies efficiently. Directional exciton migration from the chromophores to the reactive center is highly controlled even in such complex systems. The spatio-temporal evolution of excitons, i.e., the exciton dynamics are greatly influenced by the molecular species, intermolecular interactions, aggregate structures, and nuclear motions including atomic/molecular vibrations. Unraveling the correlations among these key factors in the exciton processes will lead to the discovery of new functional materials, the establishment of rational design principles, and exploration of new frontiers in science and engineering.

Here, we focus on the singlet fission (SF) process, where one singlet exciton splits into two triplet excitons in molecular aggregate systems. As will be discussed later, the transient exciton states produced by the SF process, called correlated triplet exciton pair (TT), have attractive properties for constructing novel device materials. Recent progress in theory and experiment for SF has revealed the effects of molecular species, intermolecular interactions, and nuclear motions on the efficiency of SF (rates and yields of triplet exciton generation) at the monomer and dimer levels. It is necessary to obtain design guidelines for aggregate structures that consider not only the efficient exciton generations but also the controlled directional triplet exciton migrations.

This dissertation work aims to:

1. Clarify the effects of the molecular aggregate topology (the presence/absence of edge, the structural symmetry) on the exciton dynamics.
2. Construct the novel design guidelines for efficient SF systems based on the molecular aggregate structure considering the generation and spatial separation processes of TT.

The outcome of this work will contribute to bridging the gap between the bottom-up and top-down approaches for materials design of SF systems and help establish rational design strategies that satisfy the required conditions for efficient generation and directional migrations of TT.

The following sections introduce the background of research on SF and the position of this dissertation within that context.

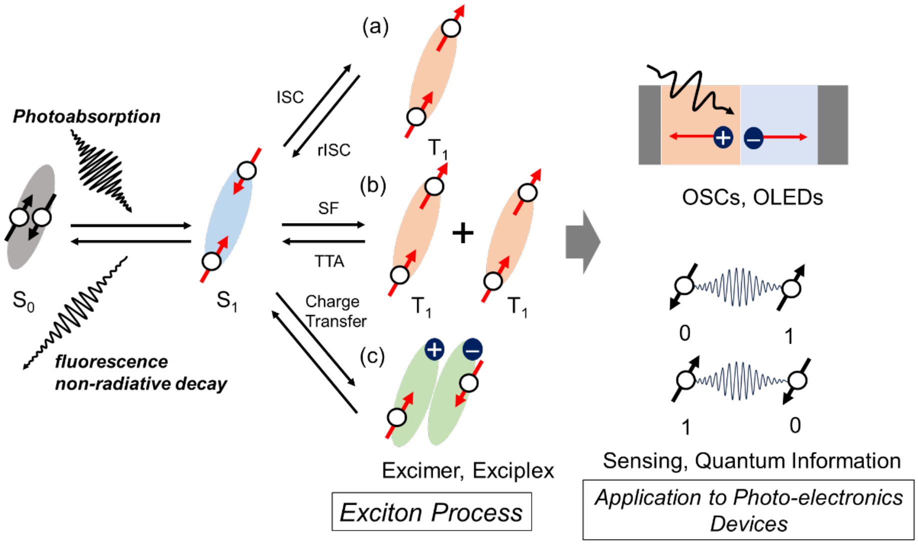

Figure 1 Schematic illustration of exciton processes and their application to photo-electronics.

2. Singlet Fission

Singlet fission (SF) is a MEG process converting a singlet exciton (S_1) into two triplet excitons ($2T_1$). In this process the energy of S_1 state is shared with the neighboring ground state molecule (S_0) resulting in two T_1 excitons with half the energy of S_1 exciton as shown in **Figure 2**. SF is described by the forward process in the following most simplified kinetic equation[2,3]:

$$S_1 \rightleftarrows {}^1(TT) \rightleftarrows {}^1(T \cdots T) \rightleftarrows T_1 + T_1 \tag{1.1}$$

The initial process in eq. (1.1) includes the generation of the correlated triplet pair states [^{1}(TT) denoted as TT]. Since the ^{1}(TT) state is overall singlet excited state in dimer system with spin-correlation between two triplets, the initial process in eq. (1.1) is the spin-allowed process and is known to occur within fs – ps timescales. The second process in eq. (1.1) is called the TT dissociation process, where the correlated triplet pair is spatially separated by the triplet-triplet exciton transfer (TTET) between neighboring molecules. Electronic coupling between the triplets is lost by the separation except for the exchange coupling which preserves the spin-entanglement and the singlet TT state $^1(T \cdots T)$ is maintained during the separation. The last process is the spin decoherence of TT states, leading to the individual triplets ($T_1 + T_1$). Because various spin states, including totally triplet and quintet TT pairs denoted as ^{3}(TT) and ^{5}(TT), are involved in the spin-decoherence process, this process is much slower than TT generation and the spatial separation process (ns – μs) [11].

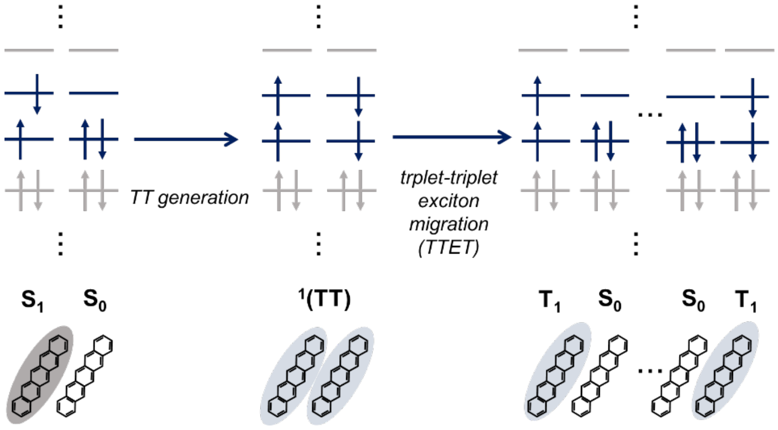

Figure 2. Concepts of SF

The interesting features of SF, such as the generation of two excitons from a single photon and the spin-entanglement of the transient TT state, have attracted many researchers' attention from the viewpoint of creating photo-functional materials that are necessary to realize sustainable development and advanced information society. A brief history of SF in this perspective is explained in the next section. Generally, a T_1 state has a longer lifetime than a S_1 state due to the spin-forbidden process of nonradiative decay. In 2006, Hanna and Nozik proposed a potential application of the SF to the exciton carrier multiplication and improvement in photoelectronic conversion efficiency in OSCs.[12] In 2023, Kawashima et al. pointed out that the high-spin states generated during the SF process, such as the ^{5}(TT), can be utilized to enhance the sensitivity of nuclear magnetic resonance (NMR) spectroscopy in combination with the dynamic nuclear polarization (DNP) technique.[13] We here should note that the SF is defined as the overall three processes given in eq. (1.1), including the spin decoherence process. However, the spin decoherence process is usually much slower than the spatial separation in molecular aggregate systems. Therefore, in this dissertation, we focus on the first two processes, the generation of ^{1}(TT) and their spatial separation, unless otherwise noted.

3. History and Observation of SF Process

In this section, we briefly review the history and experimental observation of SF. SF has a long history of over 60 years. The first discovery of SF was in 1963 when Singh et al. observed a dark state quantum yield in anthracene crystals which did not appear in free anthracene molecules (n = 1 of compound **1** in **Table 1.**).[14] The fundamental mechanism of SF was proposed in 1960s to explain the low fluorescence quantum yields observed in tetracene crystals (n = 2 of compound **1** in **Table 1.**).[15] In 1970s, several theoretical models were constructed to explain the fluorescence changes under an external magnetic field.[16-19] Kinetic models were constructed by Johnson and Merrifield and improved by Suna to include the triplet diffusion process.[16,20,21] These simple models achieved success at the initial stage of theoretical studies. Further progress in more detailed theoretical analysis had to await the development of modern quantum chemical calculation programs. After that, research on SF becomes inactive until 2000s. Progress during the period is observation of SF in carotenoid system (Rademaker et al.),[22] conjugated polymer (Austin et al.),[23] and pentacene (n = 3 of compound **1** in **Figure 3.** Jundt et al.).[24] Today, pentacene is widely recognized as the most typical SF chromophore.

SF regained attention after 2006 when Hanna and Nozik pointed out in their theoretical model study that MEG processes like SF could be applied to improve the photoelectronic conversion efficiency of OSCs.[12] They showed that energy losses due to the absorption with excess energy over the band gap in conventional OSCs are improved by using SF materials. In 2010, Rao et al. experimentally examined triplet generation and photo-currency of the pentacene/C_{60} interface.[25] They revealed that SF occurs in the timescale of approximately sub-200 fs on the p-type donor layer, followed by the separation and charge formation occurring over about 2-10 ns. Additionally, theoretical simulation studies on the improvement of interface structures have begun.[26]

The progress on SF research in the direction of molecular design owes to the pioneering theoretical work of Smith and Michl. They summarized this topic in review papers published in 2010 and 2013.[2,3] After the pioneering work by Michl et al., a lot of theoretical and experimental investigation have been conducted to propose candidate molecules exhibiting SF efficiently (hereafter, we call them SF molecules): Polyaromatic hydrocarbons (PAH) and related compounds, such as rylenes (**2**)[27] and their diimide derivatives (**3**),[28,29] and diradical molecules, such as zethrenes (**4**),[30] 1,3-diphenylisobenzofurane (**5**),[31] diketopyrrolopyrroles (**6**),[32] and 9,9'-bifluorenylidene (BFN) (**7**).[33] In addition, theoretical studies simulating the quantum dynamics of SF process (SF dynamics) have also been conducted.[4,6,34–40] These advanced computational simulations have contributed to establishing design guidelines for SF molecules and clarifying the several key factors of controlling the SF dynamics: Electronic coupling[2,3,6] and vibronic coupling[34–40] originating from π-orbital overlap and electron-nuclear motion interaction, respectively.

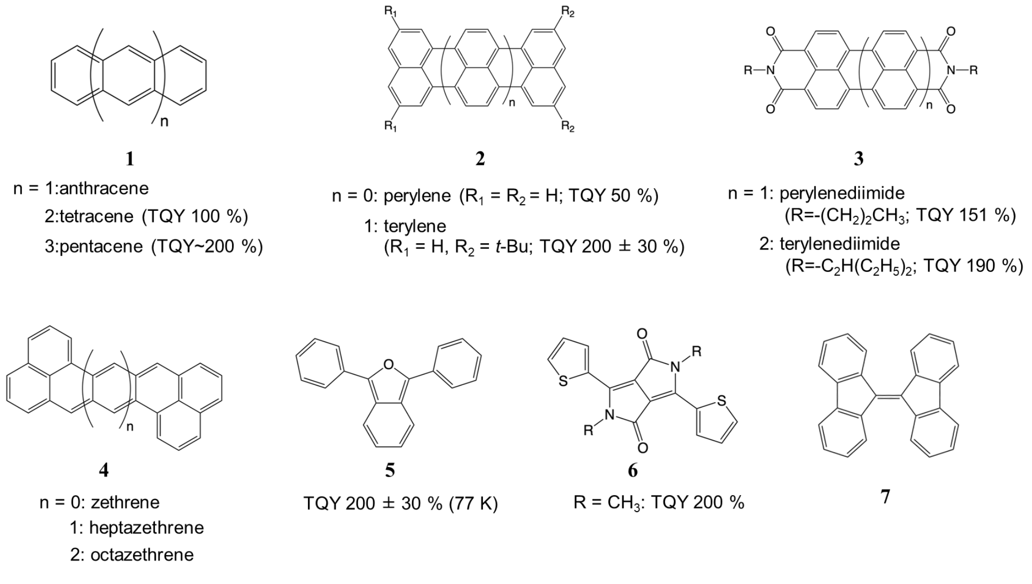

1

n = 1:anthracene
2:tetracene (TQY 100 %)
3:pentacene (TQY~200 %)

2

n = 0: perylene (R_1 = R_2 = H; TQY 50 %)
1: terylene
(R_1 = H, R_2 = *t*-Bu; TQY 200 ± 30 %)

3

n = 1: perylenediimide
(R=$-(CH_2)_2CH_3$; TQY 151 %)
2: terylenediimide
(R=$-C_2H(C_2H_5)_2$; TQY 190 %)

4

n = 0: zethrene
1: heptazethrene
2: octazethrene

5

TQY 200 ± 30 % (77 K)

6

R = CH_3: TQY 200 %

7

Figure 3. Candidates of SF molecules

In the community of SF research, the ultrafast time-resolved transient absorption (TR-TA) spectroscopy including femtosecond TA (fsTA)[41.42] and the time-resolved electron spin resonance (TR-ESR)[43–45] are powerful experimental techniques to directly observe the individual elementary steps of SF process including TT formation. **Figure 4** schematically illustrates the concept of TR-TA spectroscopy. First, a pump laser is irradiated on a sample to create $S_0 \rightarrow S_1$ excitations. Then, the formation and decay processes of bright and dark excited state populations as transient species are monitored by irradiating a time-delayed probe pulse and analyzing the transient absorption (or transmission) spectra with different delay times. In general, the TR-TA line-shapes consist of the signals from many transient species. The time evolutions of peak positions and intensities are analyzed, and important species are assumed to construct the kinetic models. Recently, the timescales of TT generation and spatial TT dissociation in SF crystals are estimated as a few hundred femtoseconds and few picoseconds by analyzing the peaks corresponding to ^{1}(TT) and ^{1}(T...T).[25]

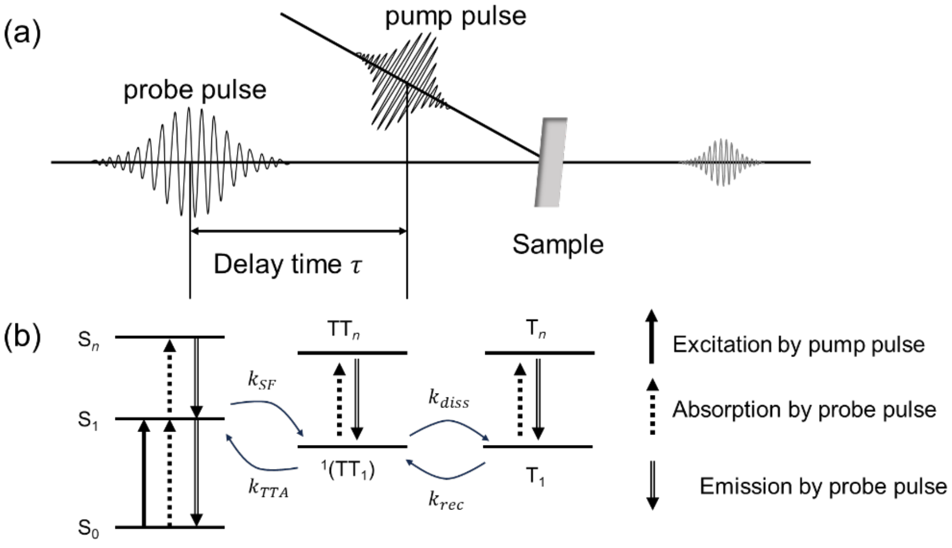

Figure 4. (a) Concepts of TR-TA and (b) kinetic model during TR-TA measurements of SF.

Over the past decade, significant progress has been made in research on the formation mechanisms and control of correlated triplet pair states in SF. This is mainly due to the recent rapid progress in quantum information science and technology, which has attracted attention and broad interest in phenomena related to quantum entanglement in material systems. During the SF process, spin-entangled states in organic molecular aggregate systems, such as the totally singlet ^{1}(TT) and quintet states ^{5}(TT), are transiently formed. Although the possibility of generating ^{5}(TT) states in the SF process was suggested by Merrifield et al. in 1971,[46] their direct observation was first reported in 2017 by Tayebjee et al. using TR-ESR spectroscopy.[44] Subsequently, Nagashima et al. proposed a widely accepted mechanism: the spatial separation of ^{1}(TT) leading to the populations of ^{5}(T...T) states followed by the formation of completely independent triplets.[45] Furthermore, a study on intramolecular SF systems (covalently linked systems of SF molecules) has demonstrated that the frequency of bond rotation after TT formation affects the spin decoherence process.[47] These observations have clarified that the timescale of spin-decoherence (about ns–μs) is much slower than the formation of ^{1}(T...T) process (about ps). Still, our current understanding of the SF dynamics remains insufficient from the viewpoint of controlling the spatio-temporal evolution of triplet excitons and spin decoherence process, which are essential for the further development of SF applications in the direction of quantum information science and technology.

4. Application of SF

4.1. Organic Solar Cells (OSCs) and SF

Let us explain the mechanism of producing current in organic solar cells (OSCs) and why the SF-based OSCs have a potential to convert photoexcitation energy more efficiently than single p–n junction solar cells. **Figure 5** illustrates the device structure of single p–n junction OSCs. In general, OSC devices consist of a donor layer (p-type semiconductors), an acceptor layer (n-type semiconductors), and electrodes (anodes and cathodes). As shown in **Figure 5**, the generation of photo-current is divided into the following four steps:

(i) Photo-absorption: Single exciton is generated from single photon.
(ii) Exciton migration: The excitons migrate in the donor layer to reach the donor/acceptor interface.
(iii) Charge separation: At the donor/acceptor interface, an electron in the conduction band or LUMO of dye molecule is transferred from the donor to the acceptor layer, resulting in the spatial separation of a hole and an electron.
(iv) Charge migration: The holes and electrons migrate from the interface to reach the electrodes.

The power conversion efficiency (PCE) of OSCs is defined as the product of the energy efficiency at each step (i)–(iv). The theoretical limit of PCE of single junction OSCs is estimated as 31 %, known as Shockley–Queisser limit (SQ-limit).[48]

According to the pioneering work by Hanna and Nozik in 2006, there are the following four factors contributing to the energy loss in conventional OSCs[12]:

(1) Incomplete photo-absorption: Photons with energy below the band gap energy E_{gap} are not absorbed.
(2) Thermalization (carrier cooling): The excess energy of photons with energy above E_{gap} is typically lost as heat.
(3) Thermodynamic loss: The available energy (Gibbs free energy or chemical potential) of the thermalized excited states is always less than their initial energy.
(4) Radiative recombination: The electron and hole of an exciton recombine radiatively with a certain probability, returning to the ground state.

OSCs utilizing MEG process, including SF, are expected to overcome the SQ-limit by doubling the number of carrier excitons. This is considered as a key concept for the third-generation solar cell. The MEG process in SF mitigates the energy losses due to carrier cooling process by utilizing the excess photon energy, which is greater than twice the bandgap energy, $2E_{\mathrm{gap}}$, to generate another triplet exciton. Moreover, since the recombination process of triplet excitons is spin-forbidden, their lifetimes are significantly extended, increasing the probability of excitons reaching the p-n interface. Although the MEG process is also observed in inorganic materials, such as quantum dots (QDs), SF-based OSCs have an advantage due to the significantly longer lifetimes of carrier excitons (on the order of μs). In contrast, excitons in inorganic materials typically decay within ~10 ps by Auger recombination.[49] This longer exciton lifetime in SF-based systems enhances the probability of efficient charge separation and migration. It has been estimated that the theoretical limit of PCE in SF-based OSCs could exceed 40 % by surpassing the SQ-limit.[12]

After the pioneering remarks by Hanna and Nozik, the first SF-based solar cell was reported by Yoo and coworkers. They found that a device consisting of pentacene (donor) and fullerenes (acceptor) exhibited external quantum efficiency (EQE) up to 69 % and PCE up to 1.8±0.2 %.[50] The SF-based OSCs with EQEs over 100 % have been achieved by Baldo et al. They could increase the EQEs in pentacene/C_{60} OSCs up to 145±7 %.[51] Moreover, Kawata et al. reported a SF-based OSC device with 4.9 % PCE, which is constructed by a 9,9'-bifluorenylidene (BFN) derivative as a SF material.[33] Still, the PCE values in SF-based OSCs are much lower than the conventional champion data (19.47 % PCE with devices based on PM6/BTP-eC9).[52] Thus, further improvement in the PCE of SF-based OSCs is required by optimization of the entire process, including TT generation, TT migration, and current generation process.

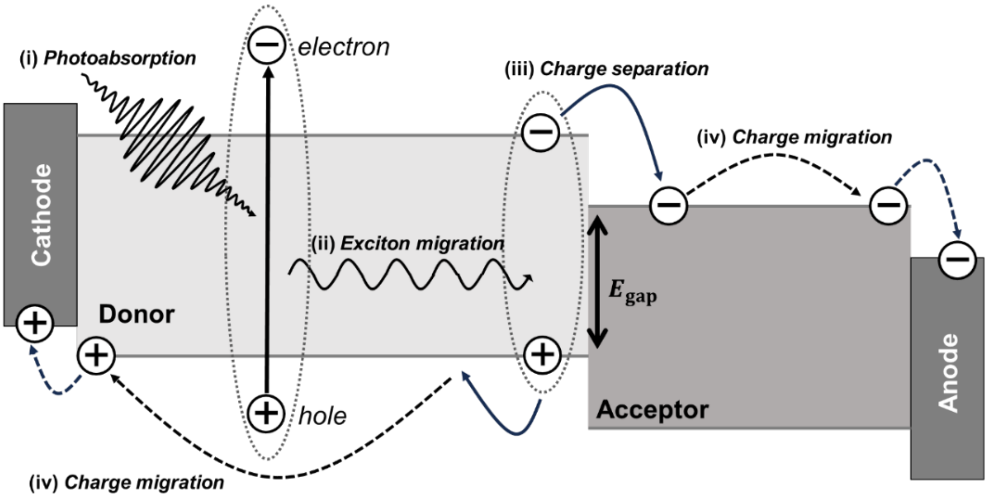

Figure 5. Device structure of (single-junction) organic solar cells

4.2. Quantum Spin Information Technologies

Recently, quantum information technology has gained much interest from the viewpoint of its application to various fields, such as physics, chemistry, and biology. In this dissertation, quantum information technology is defined as logical operations or measurement techniques with unconventional mechanisms utilizing phenomena unique to quantum systems, such as coherence or entanglement. Since these properties of quantum systems are easily disturbed and collapsed by thermal fluctuations, their experimental realization is challenging. As we mentioned before, the correlated triplet pair states are regarded as spin-entangled states generated in organic materials even at the room temperature. Therefore, its application to the quantum spin technology is one of the central topics in the research community of SF.

As shown in **Figure 6**, the TT states are described as state vectors in the direct product space consisting of three states, T_+, T_0, and T_- states, for each triplet exciton. There are totally nine eigenstates satisfying spin symmetry for singlet ^{1}(TT), triplet ^{3}(TT), and quintet ^{5}(TT) states. As Merrifield has proposed, fine-structure interactions combine the ^{1}(TT) with the $^5(TT)_0$, and the TT states with quintet characters are initially generated during the dephasing of ^{1}(TT). It is expected that, owing to the entangled nature of such triplet pairs, the ideal observation of spin state of one triplet can determine the spin state of the other triplet. These intermediate spin-entangled states of SF are potentially utilized for applications to the quantum spin information technology, such as quantum computing. However, the logical operations with quantum gate on the TT states have still been limited because of the technical bottleneck in tracking the spatial distribution and operating the spin states of individual triplet excitons independently.

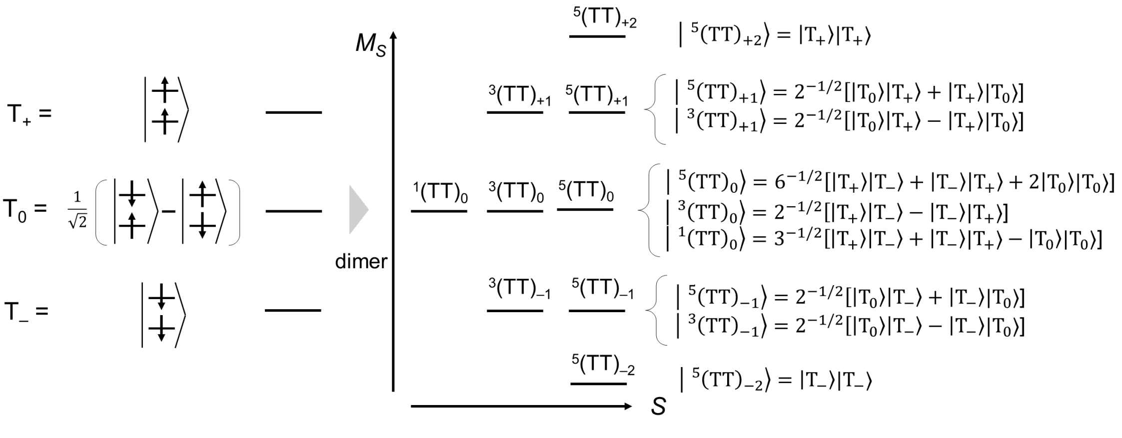

Figure 6. Spin structures of triplet (left) and correlated triplet pair (TT) states (right).

In the following part of this section, we explain the mechanism of dynamics nuclear polarization (DNP) induced by SF, as an example of application of SF to quantum information technology. DNP is a phenomenon firstly suggested by Overhauser[53] and was experimentally demonstrated by Carver and Slichter[54] in the 1950s. DNP transfers the spin polarization of unpaired electron to nuclear spins under electron spins interacting with external microwaves. Since the gyromagnetic ratios between electron spins (γ_e) and nuclear spins (γ_{H} for ^{1}H and γ_{C} for ^{13}C) are $\gamma_e/\gamma_{\mathrm{H}} \sim 660$ and $\gamma_e/\gamma_{\mathrm{C}} \sim 2640$, DNP can potentially improve the sensitivities of NMR and MRI signals.[55]

In early studies on DNP, the cryogenic temperature condition (~1 K) and high magnetic field (~7 T) were used to achieve nuclear polarization ranging from a few percent to about 40 %. This is because these techniques used electron spin polarization at thermal equilibrium and Larmor frequency was lower than $k_B T$ (k_B is Boltzmann constant and T is temperature). Therefore, such conditions limit applications to the measurements in living organisms. On the other hand, triplet DNP and SF-based DNP employ non-equilibrium polarization which allows electrons to polarize nuclear spin even at room temperature and low magnetic fields.[55] This is because their spin polarization processes are independent of the external magnetic field and temperature. The triplet DNP was first reported by Deimling et al. in 1980.[56] The operations in the triplet and SF-based DNP are summarized in **Figure 7 (a)** and **(b)**;

(i) Laser irradiation: Pulse laser is irradiated on a sample to generate excited states of chromophore. Then, triplet excitons (or a quintet TT pair) are formed by spin conversion process via ISC or SF.

(ii) Microwave irradiation: Microwave is irradiated to form a dressed state between the spin-sublevel transition ($T_0 \rightarrow T_\pm$ for triplets or $^5(TT)_0 \rightarrow {}^5(TT)_{\pm1}$ for quintet TT pair) and a microwave photon.

(iii) External magnetic field sweep: The spin polarization is transferred from electrons to nuclear spins for the resonance between electronic spin-microwave dressed state and nuclear magnetic spin.

(iv) NMR measurement: After repeating the operation (i)-(iii), NMR measurement is conducted.

For example, Tateishi et al. reported a ^{1}H polarization of 34 % at 0.4 T under room temperature using deuterated p-terphenyl single crystals doped with deuterated pentacene.[57] For the SF-based DNP, Kawashima et al. recently achieved DNP of water glycerol mixtures using spin-polarized quintet states derived from SF. They examined DNP in sodium 4,4'-(pentacene-6,13-diyl) dibenzoate (NaPDBA), which is pentacene derivative soluble in water, and their 2:2 inclusion supramolecular complex with γ-cyclodextrin (γCD) as spin-polarizer.[13] They clarified that hyperpolarization of water using the spin-polarized quintet TT pair enhance ^{1}H NMR signal by 20 times in NaPDBA and 6.5 times in γCD-NaPDBA at 100 K and 0.6 T. As we mentioned before, in the SF-based DNP, the quintet state $^5(TT)_0$ is generated at first during spin-decoherence process after TT generation (**Figure 7 (b)**). Rabi frequency in the transition between spin sublevel

$m_S \rightarrow m_S'$ is proportional to $\langle S, m_S'|S_+|S, m_S\rangle = \sqrt{S(S+1) - m_S' m_S}$. Therefore, Rabi frequency of the ^{5}(TT)$_0$ → ^{5}(TT)$_{\pm1}$ transitions is $\sqrt{3}$ times larger than that of the T$_0$ → T$_\pm$ transitions. This feature can have the beneficial result of reducing the optimal microwave power by $1/\sqrt{3}$ compared to T$_0$ → T$_\pm$ transitions. It is important to prevent spin relaxation of ^{5}(TT) state to design the SF systems applicable to the SF-based DNP.

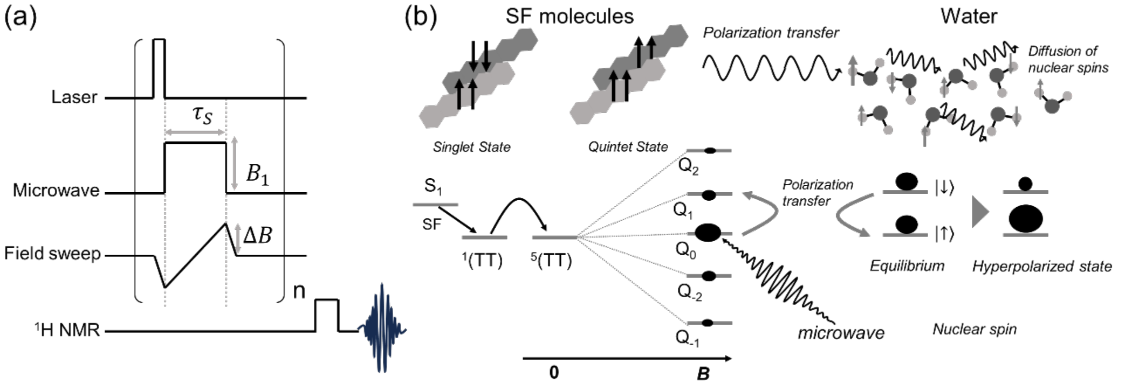

Figure 7. (a) Operation applied to the SF-based DNP systems and (b) mechanism of hyperpolarization induced by SF.

5. Key Factors Governing Singlet Fission Process

Recent development in theoretical and experimental investigation on SF enabled us to extract the relationships between the microscopic structures and SF dynamics. There are three key factors governing the SF process in aggregate systems[58]: (i) *energy matching condition*, (ii) *electronic coupling*, and (iii) *exciton dynamics* at the level ranging from monomer to multimer structures. Exploration of highly efficient SF materials typically proceeds by considering the hierarchy of these three steps (a bottom-up approach shown in **Figure 8**). In this bottom-up approach, the S$_1$ and T$_1$ excitation energies at the monomer level are firstly examined to narrow down a list of SF candidate molecules. Then, effects of several important interactions, i.e., intermolecular electronic interactions (called electronic coupling) and vibronic coupling on the SF dynamics must be considered as the system size increase from dimers to multimers, and as the properties be examined expand from static to dynamic. We have to obtain the comprehensive design guidelines for efficient SF systems by evaluating the TT generation rate (called SF rate), TT yield, and triplet spatial migration dynamics and then combing the knowledge obtained at each step.

On the other hand, establishing a top-down or needs-driven approach shown in **Figure 8** is also necessary if one attempts to design an entire SF system suitable for a target application. The yield and spetio-temporal dynamics of TT pair depend on the energy matching conditions of adiabatic states (the eigenstates of exciton model Hamiltonian). At the molecular aggregate level, the energy matching conditions should be determined by the intermolecular π-orbital overlaps and aggregation topology, as well as the relative energy levels of the S$_0$ and T$_1$ states of monomers. We here introduce these important key factors in details.

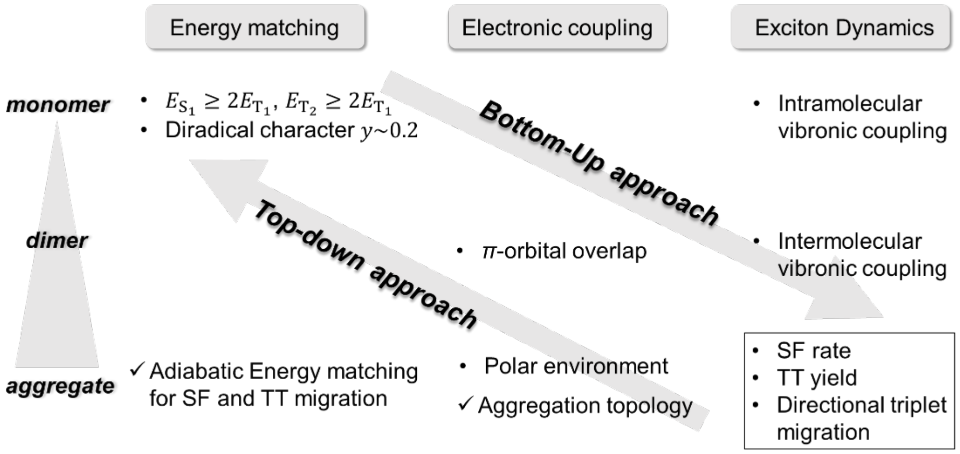

Figure 8. Key factors and bottom-up/top-down approaches for efficent SF material design.

5.1 Energy-Level Matching Conditions

Not all molecules exhibit efficient SF. The fundamental requirement for efficient SF chromophore proposed by Michl et al. indicates that the excitation energy of S$_1$ should be higher than or equal to twice that of T$_1$:

$$\Delta E_{\mathrm{SF}} = E_{S_1} - 2E_{T_1} \geq 0 \qquad (1.2)$$

where E_{S_1} and E_{T_1} is excitation energies of singlet and triplet excitons. This equation represents the iso- and exothermal energetical condition for SF, assuming that the final double triplets are sufficiently separated so that the interaction between them can be neglected. As the ΔE_{SF} indicates the energy loss during the SF, systems with a small ΔE_{SF} and high E_{T_1} are favorable for the application to the OSC devices.[2,3] It is important to keep in mind that another energy matching condition ($\Delta E_{\mathrm{rec}} = E_{\mathrm{T}_{n\geq 2}} - 2E_{\mathrm{T}_1}$) should also be satisfied to prevent a competing decay path: the triplet recombination resulting in monomeric triplet states with higher energies $\mathrm{T}_{n\geq 2}$. However, the first condition (1.2) is more fundamental because the second condition is usually satisfied for typical SF molecules.

Typical organic molecules have a negative ΔE_{SF} because of a relatively small S$_1$-T$_1$ energy splitting compared to the average of S$_1$ and T$_1$ excitation energies. Increasing the exchange integral between the HOMO and LUMO (denoted as K_{HL}) and decreasing the HOMO-LUMO energy gap are strategies to satisfy the condition (1.2). A pioneering research by computational screening was conducted by Michl et al. They evaluated the condition for 69 SF candidate molecules and concluded that (i) alternant hydrocarbons and (ii) diradicaloids are suitable for SF molecules.[59] For alternant hydrocarbon, the S_1-T_1 energy splitting is approximately described as twice the exchange integral ($= 2K_{\mathrm{HL}}$). K_{HL} is defined as follows:

$$K_{\mathrm{HL}} = \int \mathrm{d}\boldsymbol{r}_1 \mathrm{d}\boldsymbol{r}_2 \phi_{\mathrm{H}}(\boldsymbol{r}_1)\phi_{\mathrm{L}}(\boldsymbol{r}_1) r_{12}^{-1} \phi_{\mathrm{H}}(\boldsymbol{r}_2)\phi_{\mathrm{L}}(\boldsymbol{r}_2) \tag{1.3}$$

where $\phi_{\mathrm{H}}(\boldsymbol{r})$ and $\phi_{\mathrm{L}}(\boldsymbol{r})$ are the HOMO and LUMO of a SF candidate molecule and $r_{12} = |\boldsymbol{r}_1 - \boldsymbol{r}_2|$ is the distance between the positions of electrons 1 and 2. From this definition, K_{HL} becomes large when the spatial distributions of HOMO and LUMO are similar, i.e., the spatial overlap between the HOMO and LUMO is large. Alternant hydrocarbons usually satisfy this requirement.

Diradicaloids are diradical-like species. In disjoint diradicals, two unpaired electrons are localized on two radical sites in a chromophore, and two singly occupied molecular orbitals (SOMOs) are degenerated. In diradicaloids, two radical electrons interact with each other, and the HOMO-LUMO energy gap becomes large. To meet the condition (1.2), tuning the balance between the magnitude of S_1 and T_1 energies and their splitting is necessary. This corresponds to optimizing the HOMO-LUMO energy gap by tuning the interactions between radicals[2,3,59].

The relationships between the molecular structure and excitation energies can be understood in terms of the degree of open-shell (open-shell character). Open-shell character of a molecule can be evaluated by a theoretical index, diradical character (y) defined for the S_0 ground state. After the remark on diradicaloid by Michl, Minami and Nakano proposed a y-based interpretation for the energy matching conditions.[60,61] The value of y corresponds to half the (effective) number of unpaired electrons and it describes the weakness of a chemical bonding. In the valence bond (VB) theory, the degree of a chemical bond is determined by the interactions between the radical sites (described by the transfer integral and effective Coulomb repulsion). The correlation among y, interaction between the radical sites, HOMO-LUMO energy gap and occupation numbers of these MOs is simply explained in H_2 model as shown in **Figure 9**. At the equilibrium geometry, H_2 molecule is in the closed-shell state ($y = 0$) as two electrons occupy the HOMO. At the dissociation limit, the HOMO-LUMO energy gap becomes zero and the occupation numbers of bonding (HOMO) and antibonding (LUMO) orbitals become 1, resulting in two electrons are localized on each atom ($y = 1$). In between the limits, the open-shell character is in the intermediate regime ($0 < y < 1$). Based on the energy matching conditions, it has been clarified that typical SF molecules tend to have an intermediate y value ranging from $0.1 < y < 0.5$.

Based on these strategy, various SF candidate molecules have been proposed by evaluating y and excitation energies theoretically, followed by experimental examinations. In alternant hydrocarbon, acene derivatives,[61] terylene derivatives,[62] and carotenoid.[63] In diradical molecules, 1,3-diphenylisobenzofuran,[59] zethrene,[30] and tetracyanoquinodimethane bithiophene[64], BFN derivatives[33] have been examined from the viewpoint of the energy matching conditions.

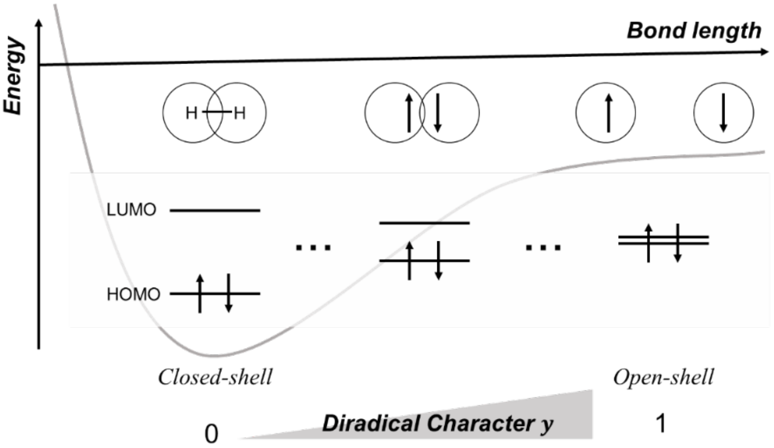

Figure 9. Concept of diradical character.

5.2 Electronic Coupling

Since SF occurs in molecular aggregates consisting of two or more chromophores, the effect of intermolecular interactions must be considered for optimizing SF rate and TT yield. The electronic coupling, which is electronic interaction between the chromophores originating from the intermolecular π-orbital overlap, is evaluated as the exciton or electron transfer integral in the research community of SF. The main electronic states in the initial process of SF are the lowest singlet state (S_1S_0 and S_0S_1), totally singlet correlated triplet pair states (^{1}TT), and charge transfer states (CT).[65] **Figure 10** shows electron configurations for a neighboring dimer system considering the HOMO and LUMO of each chromophore. The CT states are considered as intermediate states of SF, which include the cation-anion (CA) and anion-cation (AC) pairs. Since the magnitude of direct coupling connecting the initial and final states (S_1-TT coupling) represented by two-electron integrals is small, it is important to consider the stepwise interaction paths via the CT states. This type of coupling is represented by one-electron transfer integrals, V_{ij}, where i and j denotes the HOMO(H) and/or the LUMO(L) of each monomer. The larger value of V_{ij} indicates the larger degree of mixing between the S_1–CT and CT–TT states, which also modulates the energies of adiabatic states (the eigenenergies of exciton model Hamiltonian for multimers). Such modulations of excitation energies in aggregates influence the energy matching conditions. Therefore, it is important to examine the SF rate and TT yield considering the electronic couplings in molecular aggregates. Here, we explain the electronic structure of aggregate systems by focusing on the characteristics of S_1, CT, and TT states. Hereafter, we denote the adiabatic states, primarily described by the FE, CT, TT, and (T...T) diabatic state bases, with prime (‘) symbol, like FE’, CT’, TT’ and (T...T)’.

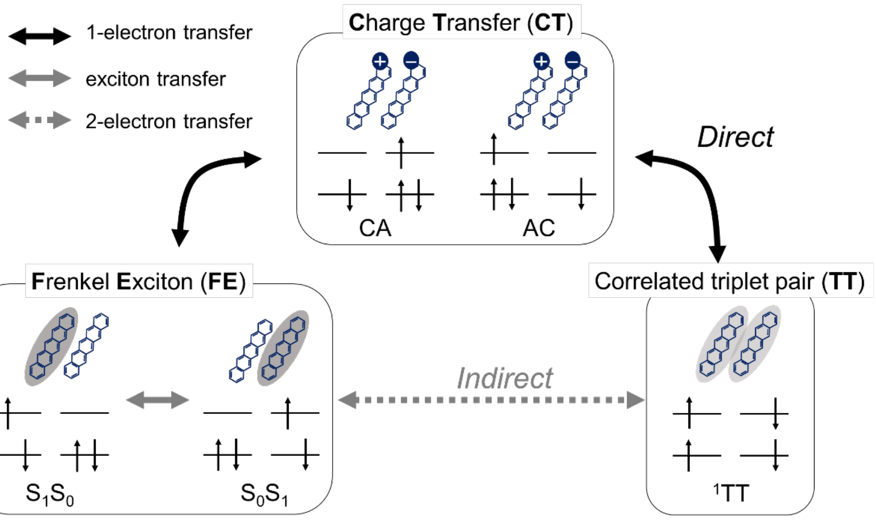

Figure 10. Direct/indirect mechanism of SF.

5.2.1. S_1 State (Frenkel Exciton; FE)

The lowest singlet state (S_1) is called a Frenkel exciton (FE) state which is generated by the initial photo-excitation. Optical excitations tend to delocalize over the aggregate systems owing to the interaction between the transition dipoles of monomers, which is called FE coupling (denoted as V_{ex}). This kind of interaction results in the band-like exciton level structures called Davydov splitting.[66] If molecules form a so-called J-aggregate, where the transition dipoles are aligned in the head-to-tail configuration, the photo-absorption band is red-shifted compared to that of the monomer. Conversely, in the case of an H-aggregate where the transition dipoles are aligned in the head-to-head configuration, the opposite trend of spectrum is observed (**Figure 11**). Since the Davydov splitting stabilize the energy of the lowest S_1-like adiabatic state in molecular aggregates, a larger Davydov splitting tends to reduce the TT yield.

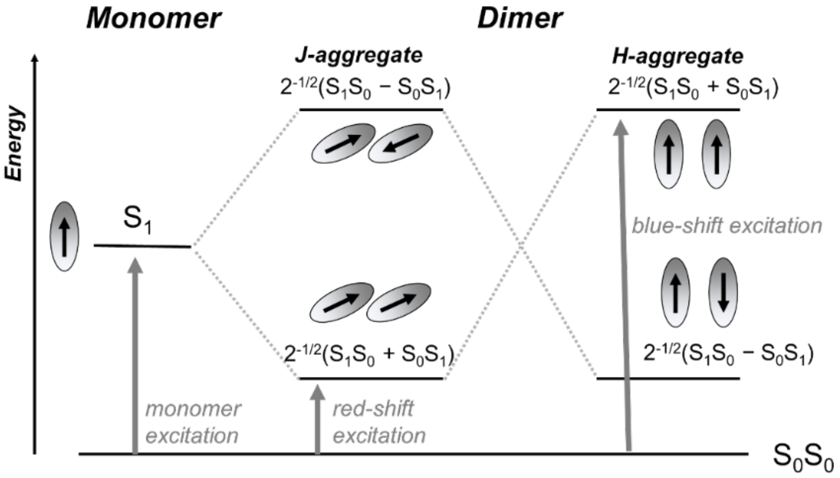

Figure 11. Davydov splitting of S_1 exciton and schematic illustration of and J-/H- aggregates.

5.2.2. Charge Transfer State (CT)

CT states are the excited states where an electron is transferred from one molecule to its neighboring molecule. The role of the CT states in SF is a key to distinguish the CT-mediate SF from the two-step SF mechanism (**Figure 12**).[4,6,65] To explain the difference between them, it should be noted that the *adiabatic states* are described as superpositions of the S_1, CT, and TT states. The S_1 and TT states can mix with the CT states. The the CT-mediate and two-step SF mechanisms are roughly classified by the energy ordering of S_1- and TT-like adiabatic states (denoted as S_1', TT') and CT-like adiabatic states (CT').

When the CT' energy is higher than the S_1' and TT' energies, a transition path between the adiabatic S_1' and TT' states via the one-step transition mainly contributes to SF. In this case, the CT states mix with the S_1' and TT' states, which assists the formation of TT in a super-exchange mechanism. This type of transition is known as a CT-mediate path, where "virtual" CT states contribute to the transition between the adiabatic states. When the CT states combined with a non-vanishing intermolecular coupling are energetically close to the S_1 and TT states, the CT states mix with the S_1 and TT states. This induces a Davidov splitting for the S_1 state, extending the exciton delocalization and lowering the energies of both the lowest S_1' and TT' states. Thus, it is important to balance these stabilization energies of the S_1' and TT' for achieving a higher TT yield in the aggregate systems.

(a) CT-mediate mechanism

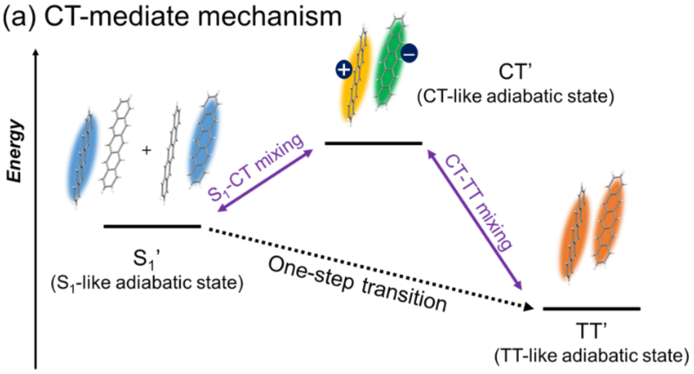

(b) Two-step mechanism

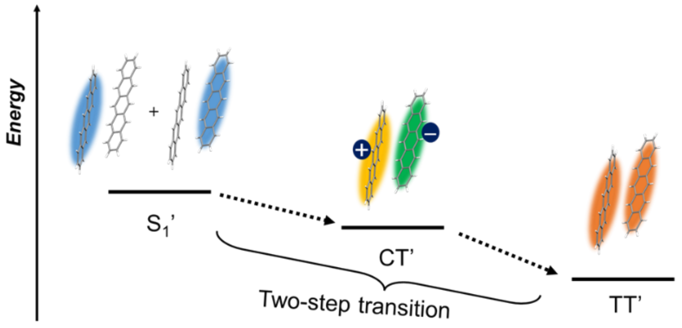

Figure 12. Schematic illustration of CT mediate path and Two-step transition path.

On the other hand, when the energies of CT' adiabatic states are close to or lower than the S_1' state, a sequential population transition from S_1' to TT' via CT' occurs. This mechanism is referred to as the two-step mechanism, where the exciton population migrates transiently to "real" CT states, and then it reaches the TT states. In the dimer systems and molecular crystals consisting of identical SF dye molecules, such as pentacenes, the CT state is higher than the S_1 and TT states, and SF is expected to proceed by the CT-mediate mechanism.

5.2.3. Correlated Triplet Pair State (TT)

As we mentioned before, the TT state corresponds to a correlated pair of triplet excitons forming an overall singlet state. We stress that the TT state couples to other electronic states, such as the CT states. In the CT-mediate SF mechanism, a larger CT–TT coupling leads to a lower nearest-neighboring TT-like adiabatic state and results in a higher TT yield. Moreover, a larger CT–TT coupling enhances the mixing of CT and TT states, which increases the SF rate. Michl et al. have clarified that this CT–TT coupling becomes larger in slip-stacked dimer structures than face-to-face dimers for molecules with the D_{2h} symmetry like pentacene.[67] This is because the CT–TT coupling depends on the transfer integrals between the HOMO and LUMO (V_{LH} and V_{HL}) of each molecule, which vanish in the latter structure (**Figure 13**) due to the symmetry reason.

Moreover, to discuss the spatial dissociation process of triplets after the TT formation, it is necessary to consider the triplet-triplet exciton transfer (TTET) coupling. This also leads to the delocalization of triplet excitons and Davydov splitting of the adiabatic TT' states, in addition to those in the FE states. From the viewpoint of TT separation or spatial control of TT distribution, a larger CT–TT coupling stabilizes the nearest-neighboring TT-like adiabatic state and localizes the TT exciton pair. On the contrary, a larger TTET coupling delocalizes or separates the triplet exciton pairs. Since the energy gap, CT–TT coupling, and TTET coupling depend on the relative intermolecular configurations in aggregates, it is important to balance or optimize their packing structures.

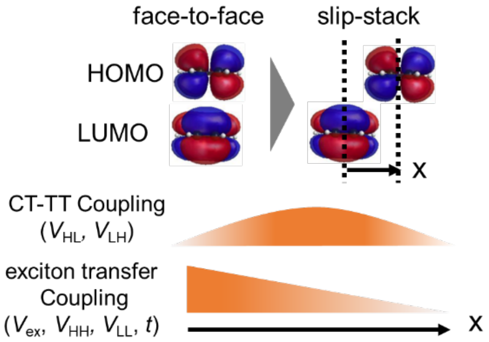

Figure 13. Correlation between dimer configuration and electronic coupling

5.3 Exciton Dynamics

In previous subsections, we have discussed the electronic states concerning the SF process. However, when discussing the time evolution of exciton states (*exciton dynamics*), it is necessary to consider the effect of interaction between the electronic states and nuclear motions, which is called *vibronic coupling* (VC). The VC plays an important role not only in SF but also in various non-equillibrium phenomena, such as exciton migration in photosynthetic systems and spin relaxation dynamics.

In aggregate systems, vibrational modes contributing to the VC can be treated as a phonon heat bath. When the electronic states were decoupled from the phonon bath, the (average) energy of the system (electronic state) is conserved after the Franck-Condon excitation. Following the principles of quantum mechanics, this results in a coherent time-evolution where the populations of electronic states oscillate periodically with time (time-reversible dynamics). On the other hand, in a more realistic situation, the electronic states and phonon bath are coupled. The energy and (quasi-)particle exchanges between these subsystems lead to the time-irreversible dynamics that will converge to a quasi-equilibrium state within a timescale of exciton relaxation dynamics (typically, it is significantly faster than the non-radiative relaxation toward the grand state). In this sense, the VC is considered as a driving force of the irreversible transitions between the excited state.

For the theoretical simulation of SF dynamics considering the VC, we must go beyond the Born–Oppenheimer approximation. Zimmermann first presented a quantum master equation (QME) approach to obtain the time-evolution of S_1, CT, and TT populations.[34-37,68–73] Berkelbach [34,35] and Tempelaar et al.[37,72,73] overviewed the fundamental theory for treating the SF dynamics. On the other hand, non-adiabatic molecular dynamics (NAMD) approaches have also been developed based on the nuclear wave-packet dynamics considering the hopping between the potential energy surfaces (PESs), such as the trajectory surface hopping (TSH),[74] or the multi-configurational time-dependent Hartree (MCTDH) method.[39, 40]

VC sometimes opens new relaxation pathways that were closed in view of the electronic coupling. For example, Miyata et al. demonstrated that the VC originating from intermolecular symmetry-breaking vibrational modes causes the main-contributing pathways between the S_1 and TT states in the face-to-face stacked rubrene crystal although the CT-TT electronic coupling was estimated to be zero from the transient absorption spectrum and quantum chemical calculation.[75]

6. Theoretical Design Based on Aggregate Structure

In previous sections, we briefly summarized backgrounds of SF, explaining research history, related technologies for potential applications, and fundamental factors governing SF. Many theoretical studies on SF have focused on the bottom-up approach based on the monomeric energy matching condition, intermolecular relative configurations, and quantum dynamics considering nuclear motions. These conventional theoretical works mainly deal with the neighboring dimer structures embedded in crystal models or aggregate systems. However, because discussion on SF must consider electron and exciton transfer couplings, the effect of exciton delocalization over the aggregate system should be important. The degree of delocalization is also affected by the number of constituent molecules (called aggregate size N) and the topology of aggregate systems. Theoretical clarification of how these factors influence the SF dynamics, i.e., the SF rate, TT yield, and TT spatial separation process, is necessary.

Moreover, recent progress in the synthetic chemistry has realized several supramolecular aggregate structures with various topologies, such as finite-sized linear oligomers[76,77], ring-shaped aggregates,[78] and branched structure,[79] as well as the positional control of SF dye molecules by covalent bonds (called intramolecular SF systems). For example, Kuroda et al. have synthesized a ring-shaped acene trimer system connected by covalent linkers that exhibited a high triplet quantum yield (ca. 180 %).[78] Furthermore, several architectures embedding SF dye molecules in covalent organic frameworks (COFs)[80] and metal organic frameworks (MOFs)[81] have been proposed. These unique structural topologies of molecular aggregates would contribute to pioneering novel functionalities of SF materials and enhancing the efficiency of existing SF-based technologies.

Theoretical research on the SF dynamics in aggregate systems with such unique geometric features has often been conducted after the experimental discovery, limiting the efficient exploration and design of new SF systems. It is efficient to establish a deductive approach that reveals the influence of topological characteristics (e.g. symmetry) in some ideal aggregate model systems on the SF dynamics by assuming the minimum necessary conditions. However, theoretical work based on such a deductive approach remains limited despite its importance in view of engineering and optimizing molecular aggregate structure for highly efficient SF. Next, we introduce several ideal model systems considered in this dissertation.

Ring-shaped aggregate systems

Ring-shaped molecular aggregates possess a periodic (rotational) symmetry. Excitons in a ring-shaped aggregate with no "edges" tend to delocalize over the entire aggregate system compared to a finite linear aggregate system with edges. Ring-shaped aggregates of chromophores can be found in photosynthetic light-harvesting antenna complexes that exhibit notable optical responses[8–10]. Due to the exciton delocalization, the magnitude of transition dipole moments of a ring-shaped aggregate system become larger than those of isolated molecules. Minami et al. demonstrated that, when the transition dipole moments are oriented parallel to the ring, the rotational symmetry of ring-shaped aggregates allow them to couple to a circularly polarized light[82]. Moreover, efficient separation of the TT exciton pair and suppression of the recombination is expected in ring-shaped aggregates.[83] Such features are expected to highlight the unique optical response properties in ring-shaped aggregates compared with linear aggregate systems, in combination with the SF.

Nakano et al. constructed models employing parametrically fixed intermolecular electronic couplings (obtained from dimer structure shown in **Figure 14 (b)**) and compared how the number of molecules (aggregate size *N*) and the FE coupling affect the SF rates and TT yields in both the linear and ring-shaped aggregate systems.[70] They revealed that each aggregate structure exhibits a peak of the SF rate at different *N* as shown in **Figure 14 (c)**. The intermolecular relative configuration depending on *N* also influenced the SF dynamics. In two types of aggregate structures shown in **Figure 15 (a)** and **(b)**, the relative orientation of adjacent molecules become J- or H-aggregates as the *N* increases, which potentially changed the SF dynamics behavior of these systems. This motivated us to discuss the size dependence of SF dynamics for J- and H-type rings (described in Chapter II.1), and their intermediate structures (**Figure 15 (c)**) (in Chapter II.2). Through these simulations, we elucidate how the aggregation topology, intermolecular interactions, and excited electronic states of ring-shaped aggregates influence the TT yield and SF rate, which is crucial for a comprehensive understanding of the structure–SF dynamics relationships.

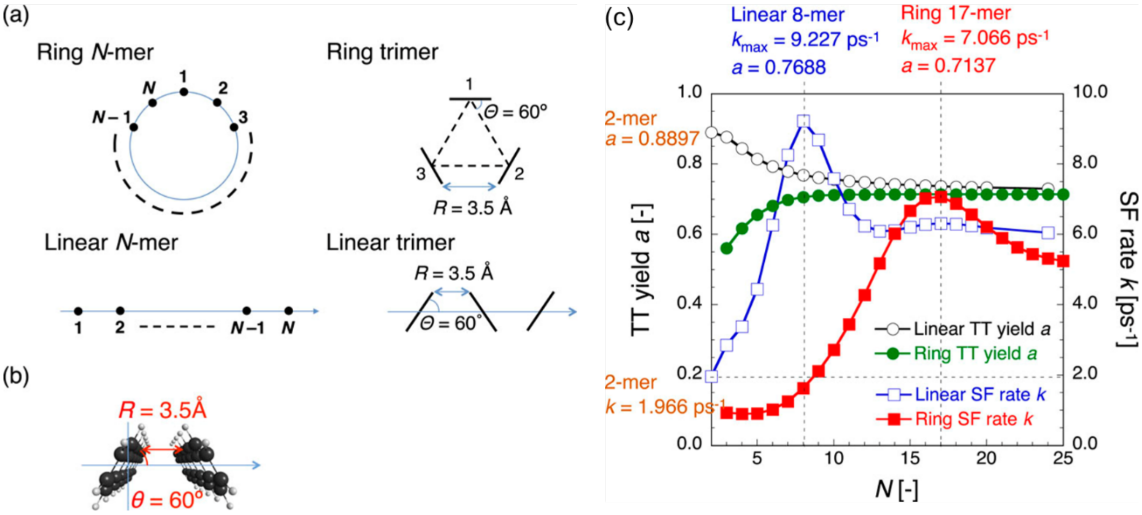

Figure 14. (a) Model structures in pentacene linear/ring shaped aggregate systems, (b) pentacene dimer structure to obtain intermolecular electronic coupling, and (c) TT yield (left vertical axis) and SF rate (right vertical axis) of SF rate in linear and ring-shaped aggregate system as functions of size *N* of aggregate systems.

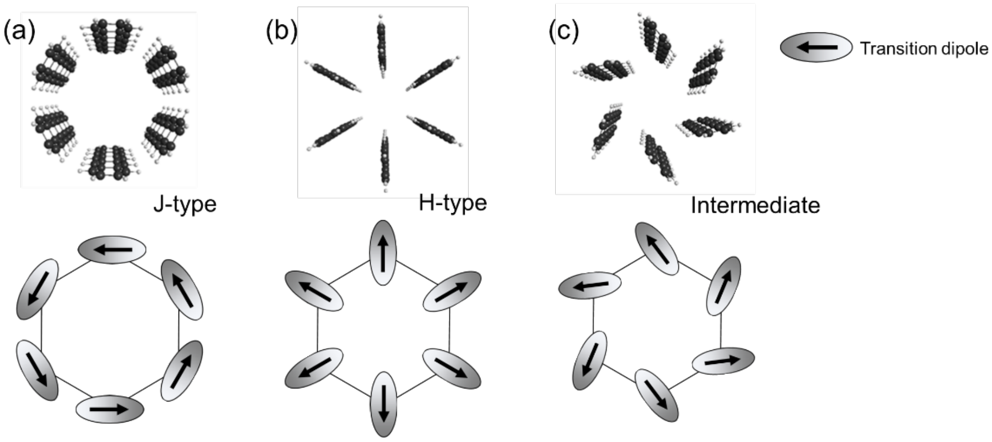

Figure 15. Various pentacene ring-shaped aggregate models and directions of transition dipole moments of consisting molecules.

Effective Adiabatic Energy Matching Condition for Various Aggregate System

As we mentioned in Section 5.1, electronic couplings modulate the energies of initial and final states. In some interacting aggregates, the TT generation process from the S_1 may become endothermic even if the monomeric energy matching condition (1.2) is satisfied. It is important to consider not only $\Delta E_{\mathrm{SF}} = E_{\mathrm{S}_1} - 2E_{\mathrm{T}_1}$, but also the influence of intermolecular interactions and aggregate structures.

Furthermore, in molecular aggregate systems, such as crystals and covalently linked oligomers, all the molecules are not arranged in a uniform manner. Instead, a non-uniform arrangement may be preferred, incorporating various relative intermolecular configurations, such as an alternating structure. However, it is difficult to discuss how such an inhomogeneous structures influences the SF process even qualitatively. This difficulty arises because there are various factors, including molecular aggregate topologies and intermolecular interaction the excited electronic states in molecular aggregates, such as the extent of exciton localization/delocalization and ordering of energy levels.

Therefore, it is both challenging and desirable to propose model equations that describe the energy matching conditions for aggregate systems. We denote a condition corresponding to (1.2) as $\Delta E'_{\mathrm{SF}}$, which can be expressed as a function of ΔE_{SF}, coupling parameters and topology of aggregate structure. Such a model would help easily identify the main contributors determining the adiabatic state energies. Developing these model equations could provide valuable insights for constructing a top-down design guideline (**Figure 8**), starting from the requirements imposed by the SF process and guiding the selection of optimal molecular and molecular aggregate structures.

7. Theoretical Design of SF Materials showing Directional TT Migration

It is also important to control the spatial distribution of TT pair. From the viewpoints of preventing the triplet annihilations due to recombination, the fast dissociation of TT pair is considered preferable. However, the key factors and design guidelines for SF dynamics including TT dissociation process have not been proposed yet. In this dissertation, we examined how to control such directional triplet migrations by optimizing molecular aggregate structures.

To control the TT distribution after the SF, it is necessary to design aggregate structures that contain substructures serving as triplet acceptors. In other words, energy gradients corresponding to changes in spatial distribution of triplets should be prepared as shown in **Figure 16** to ensure the TT pair migration to the acceptor sites. Two approaches can be considered: Introducing a heterofission system and position dependent-intermolecular interactions. We here focus on finite aggregate systems, since it would be difficult to control and detect the spatial position of triplet excitons in the crystal phases where triplet excitons diffuse over by the hopping TTET mechanism.

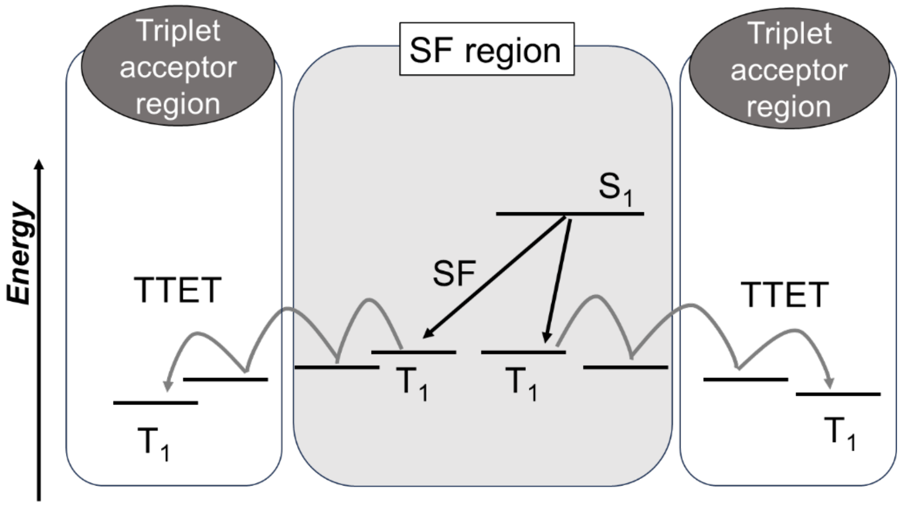

Figure 16. Concept of SF materials with directional triplet migration.

The SF process which occurs between different molecular species is called heterofission. Utilizing the heterofission is expected to broaden the optical absorption band and generate triplet excitons on molecules that do not satisfy the energy matching condition for the homofission (SF between the same molecular species) process. For example, Zeiser and coworkers have reported that a covalently-linked heterofission systems consisting of tetracene and pentacene yields more efficient TT generation than tetracene dimer systems.[84] This is because energetic disadvantage of

SF in the tetracene dimer ($\Delta E_{\mathrm{SF}} = -180$ meV) is relaxed to $\Delta E_{\mathrm{SF}} = -90$ meV in the tetracene-pentacene pair. This is interpreted that the exothermic SF energy matching condition of pentacene drives the formation of triplet exciton on tetracene with higher energy. However, there has been no systematic investigation of the possibility of using heterofission for controlling the spatial distribution of triplet excitons.

We here consider symmetric homotrimer (**Figure 17 (a)**) and heterotrimer systems (**Figure 17 (b)**). The former consists of identical three molecules Y and the latter consists of two different molecular species, X and Y. In the homotrimer system, the triplet excitons are expected to delocalize over the three molecules. In the heterotrimer system, when the exothermic condition of both SF ($\Delta E_{\mathrm{SF}} > 0$) and triplet migration from X to Y ($\Delta E_{\mathrm{TTET}} = E(\mathrm{T}_1^Y) - E(\mathrm{T}_1^X) > 0$, where $E(\mathrm{T}_1^X)$ and $E(\mathrm{T}_1^Y)$ denote the triplet excitation energy of molecules X and Y) is satisfied, two triplets are expected to localize on X at the edge of trimer. Since different molecular species have different frontier MO energies, the SF rate and TT yields are modulated due to the lower energies of CT states. We must find an optimal combination of X and Y for which the large SF rate, high TT yield, and efficient directional migration of triplet excitons can be obtained.

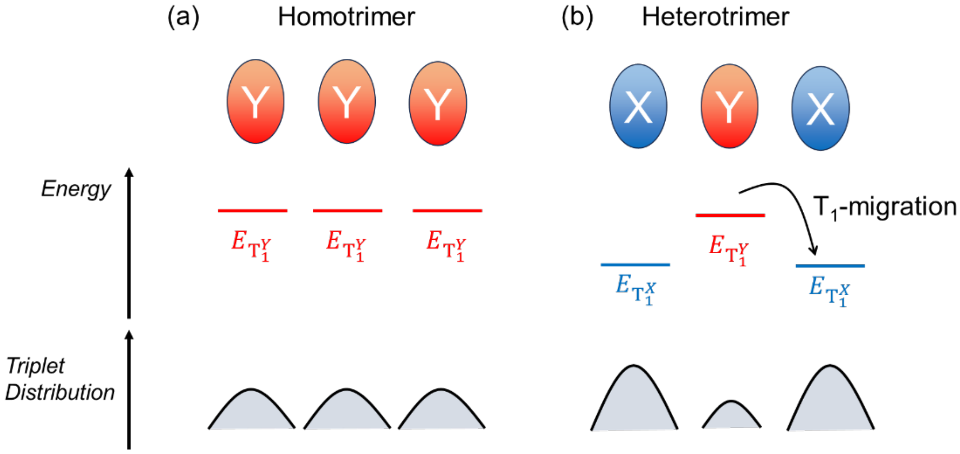

Figure 17. Concepts of directional control of triplet exciton migration in heterotrimer systems.

The second strategy, introducing positionally dependent-intermolecular interactions, can help localize excitons on a certain region of aggregate systems consisting of identical molecules. As we mentioned in Section 5.2.3, a larger intermolecular exciton transfer coupling leads to a larger Davydov splitting. **Figure 18** illustrates the mechanism of localization of a triplet exciton pair in the molecular aggregates where different types of molecular orientations are introduced. **Figure 18 (a)** illustrates the situation where the exciton transfer coupling for the left dimer part (V_{strong}) is much larger than that for the right dimer part (V_{weak}). We can discuss the energy levels and spatial distributions of exciton states by considering the electronic couplings step by step: (1) At first, the three energy levels of localized triplet exciton are degenerated before considering the electronic couplings. (2) Then, the degeneracy is partly solved by considering only V_{strong} for the left dimer part. (3) After that, considering the V_{weak} further modulates the energy levels and wavefunctions. Consequently, the lowest exciton state in the final step (3) is mainly contributed from the lowest states in the step (2) whose exciton wavefunction is localized primarily on the left two molecules.

By utilizing this strategy, two triplet excitons of a linear aggregate system shown in **Figure 18 (b)** in the lowest exciton state will localize at the edge of the aggregate systems. Namely, the TT pair generated in the center region is expected to migrate and separate into the edge of aggregate system. To date, no systematic investigation has been conducted to clarify the condition for both efficient SF and TT dissociation in such a complex aggregate structure. The effective model equations to estimate adiabatic energy matching condition discussed in Section 6 is expected to be a powerful tool to obtain this condition.

(a) Single T_1 exciton

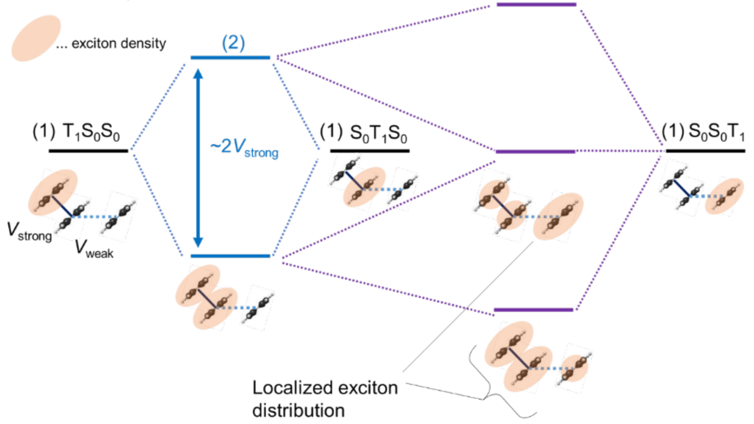

(b) TT exciton pair

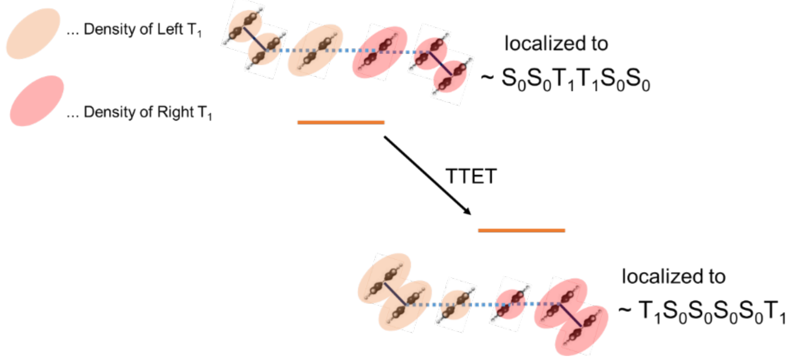

Figure 18. Exciton localization in linear aggregates with position-dependent intermolecular couplings.

8. Outline of this Dissertation

The objective of this dissertation is to clarify the relationships between the aggregation structure and SF properties by examining the static properties (energy levels and electron couplings) and dynamic behaviors (spatio-temporal evolution of excitons) in several aggregate models having unique geometric features. We aim to develop theory and models for a *top-down approach* for exploration of novel SF systems showing fast and high-yield SF, and well-controlled spatial distributions of TT. Because the exciton dynamics of the SF process depends on the molecular species, intermolecular configurations, and aggregation topologies, it is necessary to establish a model-based approach to grasp the general trends of electronic structure and SF dynamics as a function of these factors.

This dissertation consists of three parts: PART I – III. PART I describes the general theory related to the SF dynamics. In Chapter I-1, we explain theoretical modeling of the main electronic states concerning the SF in general aggregate systems and the vibronic coupling. Chapter I-2 introduces the quantum master equation (QME) approach to simulate the SF dynamics considering the vibronic coupling.

PART II describes the structure – SF dynamics relationships in several types of ring-shaped aggregate systems, focusing on the TT yield and SF rate. In Chapter II-1, we focus on the difference in the dynamics results between the J-type and H-type ring-shaped aggregate models consisting of pentacene molecules. We have examined the SF rate and nearest-neighboring TT yield as a function of the number of molecules, based on a group theoretical approach for treating the symmetry of exciton states. In Chapter II-2, we demonstrate the effects of introducing a symmetry-breaking in the ring-shaped aggregate systems on the SF rate and TT yield. We examine how the structural symmetry-breaking affects the dynamics through the symmetry-breaking of the CT states from the viewpoint of quantum interference effect. We conclude that the SF rate becomes significantly fast up to tens of ps^{-1}, which is comparable to the SF rate in pentacene herringbone crystal structure (ca. 13 ps^{-1}).

PART III describes the theoretical design for efficient TT generation and spatial TT separation in linear aggregate systems. We propose optimal conditions for achieving such SF properties in symmetric linear heterotrimer models composed of unsubstituted or 6,13-disubstituted pentacene derivatives by focusing on the roles of asymmetric CT states for an efficient heterofission process.

Throughout this dissertation, we clarify the structure–SF relationships in several aggregate systems for further theoretical understanding of SF dynamics including TTET dynamics, which help open novel quantum functionalities of SF materials.

References

(1) H. Nakanotani, Y. Tsuchiya, C. Adachi *Chem. Lett.* **2021**, *50*, 938-948.

(2) M. B. Smith, J. Michl *Chem. Rev*. **2010**, *110*, 6891-6936.

(3) M. B. Smith, J. Michl *Annu. Rev. Phys. Chem.* **2013**, *64*, 361-386.

(4) D. Casanova *Chem. Rev.* **2018**, *118*, 7164-7207.

(5) K. Miyata, F. S. Conrad-Burton, F. L. Geyer, X.-Y. Zhu *Chem. Rev.* **2019**, *119*, 4261-4292.

(6) F. Mirjani, N. Renaud, N. Gorczak, F. C. Grozema *J. Phys. Chem. C* **2014**, *118*, 14192-14199.

(7) W. T. Yip, D. H. Levy *J. Phys. Chem.* **1996**, *100*, 11539-11545.

(8) R. van Grondelle, J. P. Dekker, T. Gillbro, V. Sundström, *Biochim. Biophys. Acta.* **1994**, *1187*, 1-65.

(9) G. McDermott, S. M. Prince, A. A. Freer, A. M. Hawthornthwaite-Lawless, M. Z. Papiz, R. J. Cogdell, N. W. Isaacs, *Nature.* **1995**, *374*, 517-521.

(10) T. Pullerits, V. Sundström, *Acc. Chem. Res.* **1996**, *29*, 381-389.

(11) S. Matsuda, S. Oyama, Y. Kobori *Chem. Sci.* **2020**, *11*, 2934.

(12) M. C. Hanna, A. J. Nozik *J. Appl. Phys.* **2006**, *100*, 074510.

(13) Y. Kawashima, T. Hamachi, A. Yamauchi, et al. *Nat. Commun.* **2023**, *14*, 1056.

(14) S. Singh, B. P. Stoicheff *J. Chem. Phys.* **1963**, *38*, 2032−2033.

(15) C. E. Swenberg, W. T. Stacy *Chem. Phys. Lett.* **1968**, *2*, 327−328.

(16) R. C. Johnson, R. E. Merrifield *Phys. Rev. B* **1970**, *1*, 896−902.

(17) C. E. Swenberg, M. A. Ratner, N. E. Geacintov *J. Chem. Phys.* **1974**, *60*, 2152−2157.

(18) G. Klein, R. Voltz *Int. J. Radiat. Phys. Chem.* **1975**, *7*, 155−174.

(19) M. Chabr, D. F. Williams *Phys. Rev. B* **1977**, *16*, 1685−1693.

(20) R. E. Merrifield *J. Chem. Phys.* **1968**, *48*, 4318−4319.

(21) A. Suna *Phys. Rev. B* **1970**, *1*, 1716−1739.

(22) H. Rademaker, A. J. Hoff, R. Van Grondelle, L. N. M. Duysens *Biochim. Biophys. Acta, Bioenerg.* **1980**, *592*, 240−257.

(23) R. H. Austin, G. L. Baker, S. Etemad, R. Thompson *J. Chem. Phys.* **1989**, *90*, 6642−6646.

(24) C. Jundt, G. Klein, B. Sipp, J. Le Moigne, M. Joucla, A. A. Villaeys *Chem. Phys. Lett.* **1995**, *241*, 84−88.

(25) A. Rao, M. W. B. Wilson, J. M. Hodgkiss, S. Albert-Seifried, H. Bässler, R. H. Friend*, J. Am. Chem. Soc.* **2010**, *132*, 12698–12703.

(26) K. Aryanpour, J. A. Muñoz, S. Mazumdar *J. Phys. Chem. C* **2013**, *117*, 4971－4979.

(27) S. W. Eaton, S. A. Miller, E. A. Margulies, L. E. Shoer, R. D. Schaller, M. R. Wasielewski, *J. Phys. Chem. A*, **2015**, *119*, 4151–4161.

(28) A. K. Le, J. A. Bender, D. H. Arias, D. E. Cotton, J. C. Johnson, S. T. Roberts, *J. Am. Chem. Soc.*, **2018**, *140*, 814–826.

(29) E. A. Margulies, J. L. Logsdon, C. E. Miller, L. Ma, E. Simonoff, R. M. Young, G. C. Schatz, M. R. Wasielewski *J. Am. Chem. Soc.*, **2017**, *139*, 663–671.

(30) S. Lukman, J. M. Richter, L. Yang, P. Hu, J. Wu, N. C. Greenham, A. J. Musser, *J. Am. Chem. Soc*. **2017**, *139*, 18376－18385.

(31) J. C. Johnson, A. J. Nozik and J. Michl, J. Am. Chem. Soc., 2010, 132, 16302–16303.

(32) C. M. Mauck, P. E. Hartnett, E. A. Margulies, L. Ma, C. E. Miller, G. C. Schatz, T. J. Marks and M. R. Wasielewski *J. Am. Chem. Soc.*, **2016**, *138*, 11749−11761.

(33) S. Kawata, J. Furudate, T. Kimura, H. Minaki, A. Saito, H. Katagiria Y.-J. Pu *J. Mater. Chem. C*, **2017**, *5*, 4909–4914.

(34) T. C. Berkelbach, M. C. Hybertsen, D. R. Reichman *J. Chem. Phys.* **2013**, *138*, 114102.

(35) T. C. Berkelbach, M. C. Hybertsen, D. R. Reichman *J. Chem. Phys.* **2013**, *138*, 114103.

(36) G. Tao *J. Phys. Chem. C* **2014**, *118*, 27258−27264.

(37) R. Tempelaar, D. R. Reichman *J. Chem. Phys.* **2018**, *148*, 244701.

(38) S. Ito, T. Nagami, M. Nakano *J. Phys. Chem. Lett.* **2015**, *6*, 4972−4977.

(39) J. Zheng, Y. Xie, S. Jiang, Z. Lan *J. Phys. Chem. C* **2016**, *120*, 1375−1389.

(40) S. R. Reddy, P. B. Coto, M. Thoss *J. Chem. Phys.* **2019**, *151*, 044307.

(41) R. D. Pensack, E. E. Ostroumov, A. J. Tilley, S. Mazza, C. Grieco, K. J. Thorley, J. B. Asbury, D. S. Seferos, J. E. Anthony and G. D. Scholes, *J. Phys. Chem. Lett.*, **2016**, *7*, 2370–2375.

(42) K. Miyata, F. S. Conrad-Burton, F. L. Geyer and X. Y. Zhu, *Chem. Rev.*, **2019**, *119*, 4261–4292.

(43) S. Matsuda, S. Oyama and Y. Kobori, *Chem. Sci.*, **2020**, *11*, 2934–2942.

(44) M. J. Y. Tayebjee, S. N. Sanders, E. Kumarasamy, L. M. Campos, M. Y. Sfeir and D. R. McCamey, *Nat. Phys.*, **2017**, *13*, 182–188.

(45) H. Nagashima, S. Kawaoka, S. Akimoto, T. Tachikawa, Y. Matsui, H. Ikeda and Y. Kobori, *J. Phys. Chem. Lett.*, **2018**, *9*, 5855–5861.

(46) R. E. Merrifield *Pure Appl. Chem.* **1971**, *27*, 481– 498.

(47) T. Hasobe, S. Nakamura, N. V. Tkachenko, Y. Kobori *ACS Energy Lett.* **2022**, *7*, 390−400.

(48) W. Shockley, H. J. Queisser *J. Appl. Phys.* **1961**, *32*, 510−519.

(49) V. I. Klimov *J. Phys. Chem. B* **2006**, *110*, 16827−16845.

(50) S. Yoo, W. J. Potscavage Jr., B. Domercq, S.-H. Han, T.-D. Li, S. C. Jones, R. Szoszkiewicz, D. Levi, E. Riedo, S. R. Marder, B. Kippelen *Solid-State Electron.* **2007**, *51*, 1367−1375.

(51) J. Lee, P. Jadhav and M. A. Baldo, *Appl. Phys. Lett.*, **2009**, *95*, 10–13.

(52) J. Huang, J. Fu, B. Yuan, et al. *Nat. Commun.* **2024**, *15*, 10565.

(53) A. W. Overhauser *Phys. Rev.* **1953**, *92*, 411−415.

(54) T. R. Carver, C. P. Slichter *Phys. Rev.* **1956**, *102*, 975−980.

(55) T. Hamachi, N. Yanai *Prog. Nucl. Magn. Reson. Spectrosc.* **2024**, *142−143*, 55−68.

(56) M. Deimling, H. Brunner, K. P. Dinse, K. H. Hauser *J. Magn. Reson.* **1980**, *39*, 185−202.

(57) K. Tateishi, M. Negoro, S. Nishida, A. Kagawa, Y. Morita, M. Kitagawa *Proc. Natl. Acad. Sci. U. S. A.* **2014**, *111*, 7527−7530.

(58) S. Ito, T. Nagami, M. Nakano *J. Photochem. Photobiol. C* **2018**, *34*, 85−120.

(59) I. Paci, J. C. Johnson, X. Chen, G. Rana, D. Popović, D. E. David, A. J. Nozik, M. A. Ratner, J. Michl, *J. Am. Chem. Soc.* **2006**, *128*, 16546-16553.

(60) T. Minami, M. Nakano, *J. Phys. Chem. Lett.* **2012**, *3*, 145－150.

(61) T, Minami, S. Ito, M. Nakano *J. Phys. Chem. Lett.* **2013**, *4*, 2133−2137.

(62) T, Minami, S. Ito, M. Nakano *J. Phys. Chem. Lett*. **2012**, *3*, 2719－2723.

(63) J. Alster, T. Polívka, J. B. Arellano, P. Chábera, F. Vácha, J. Pšenčík *Chem. Phys.* **2010**, *373*, 90−97.

(64) O. Varnavski, N. Abeyasinghe, J. Aragó, J. J. Serrano-Pérez, E. Ortí, J. T. López Navarrete, K. Takimiya, D. Casanova, J. Casado, T. Goodson *J. Phys. Chem. Lett.* **2015**, *6*, 1375−1384.

(65) E. A. Margulies, J. L. Logsdon, C. E. Miller, L. Ma, E. Simonoff, R. M. Young, G. C. Schatz, M. R. Wasielewski *J. Am. Chem. Soc.* **2017**, *139*, 663−671.

(66) A. S. Davydov, *Sov. Phys. Uspekhi* **1964**, *7*, 145−178.

(67) E. A. Buchanan, Z. Havlas, J. Michl *Adv. Quantum Chem.* **2017**, *75*, 175−227.

(68) M. Nakano, S. Ito, T. Nagami, Y. Kitagawa, T. Kubo, *J. Phys. Chem. C.* **2016**, *120*, 22803-22816.

(69) M. Nakano, T. Nagami, T. Tonami, K. Okada, S. Ito, R. Kishi, Y. Kitagawa, T. Kubo, *J. Comput. Chem.* **2019**, *40*, 89-104.

(70) M. Nakano, *J. Chem. Phys*. **2019**, *150*, 234305.

(71) M. Nakano, K. Okada, T. Nagami, T. Tonami, R. Kishi, and Y. Kitagawa, Molecules. **2019**, *24*, 541.

(72) R. Tempelaar, D. R. Reichman, *J. Chem. Phys.* **2017**, *146*, 174703.

(73) R. Tempelaar, D. R. Reichman, *J. Chem. Phys.* **2017**, *146*, 174704.

(74) G. Tao, *J. Phys. Chem. C* **2014**, *118*, 17299−17305.

(75) K. Miyata, Y. Kurashige, K. Watanabe, et al. *Nature Chem.* **2017**, *9*, 983−989.

(76) A. B. Pun, A. Asadpoordarvish, E. Kumarasamy, M. J. Y. Tayebjee, D. Niesner, D. R. McCamey, S. N. Sanders, L. M. Campos, M. Y. Sfeir *Nat. Chem.* **2019**, *11*, 821−828.

(77) S. Nakamura, H. Sakai, M. Fuki, R. Ooie, F. Ishiwari, A. Saeki, N. V. Tkachenko, Y. Kobori, T. Hasobe *Angew. Chem.* **2023**, *135*, e202217704.

(78) K. Kuroda, K. Yazaki, Y. Tanaka, M. Akita, H. Sakai, T. Hasobe, N. V. Tkachenko, M. Yoshizawa, *Angew. Chem. Int. Ed.* **2019**, *58*, 1115-1119.

(79) J. Kim, H. T. Teo, Y. Hong, Y. C. Liau, D. Yim, Y. Han, J. Oh, H. Kim, C. Chi, D. Kim *J. Am. Chem. Soc.* **2023**, *145*, 19812−19823.

(80) V. Laszlo, T. Kowalczyk *J. Mater. Chem. A* **2016**, *4*, 10500−10507.

(81) A. Yamauchi, K. Tanaka, M. Fuki, S. Fujiwara, N. Kimizuka, T. Ryu, M. Saigo, K. Onda, R.

Kusumoto, N. Ueno *Sci. Adv.* **2024**, *10*, eadi3147.

(82) T. Minami, H. Fukui, H. Nagai, K. Yoneda, R. Kishi, H. Takahashi, M. Nakano *J. Phys. Chem. C* **2009**, *113*, 3332−3338.

(83) F. Campaioli, A. Pagano, D. Jaschke, S. Montangero PRX Energy **2024**, *3*, 043003.

(84) C. Zeiser, L. Moretti, D. Lepple, G. Cerullo, M. Maiuri, K. Broch *Angew. Chem. Int. Ed.* **2020**, *59*, 19966–19973.

PART I

GENERAL THEORY

Chapter 1

Theoretical Approach to Singlet Fission Dynamics

From three key factors described in General Introduction, we introduce theoretical method to conduct SF dynamics simulation in molecular aggregate systems. In this Chapter, we give brief explanations of *adiabatic states*, *diabatic exciton basis*, and *vibronic coupling*. Section 1.1 explain adiabatic and diabatic representation starting from the time-independent Schrödinger equation in molecular aggregate systems. In the next Section 1.2, we obtain more detail formalisms of diabatic exciton basis and electronic coupling in dimer substructure, which is proposed by Michl and coworkers. In Section 1.3, we give the definition and calculation method of vibronic coupling constant, which is required to model exciton–phonon coupling described in the following Chapter 2.

1.1 Beyond Born-Oppenheimer Approximation

1.1.1 Adiabatic representation

In photophysical process with transition between different electronic excited state including SF, it is necessary to discuss the non-equilibrium process. In this process, the time-evolution of electronic state is affected by nuclear vibrational motion, which is called vibronic coupling. The non-relativistic Hamiltonian of molecule or molecular aggregate in atomic unit ($\hbar = m_e = e = 1$) is written as[1,2]

$$\begin{aligned}\hat{H}(\boldsymbol{r},\boldsymbol{R}) &= \hat{T}_{\mathrm{e}}(\boldsymbol{r}) + \hat{U}_{\mathrm{ee}}(\boldsymbol{r}) + \hat{T}_{\mathrm{N}}(\boldsymbol{R}) + \hat{U}_{\mathrm{NN}}(\boldsymbol{R}) + \hat{U}_{\mathrm{e}\mathbf{N}}(\boldsymbol{r};\boldsymbol{R}) \\ &= -\sum_{i}^{N_e}\frac{1}{2}\nabla_i^2 + \sum_{ij}^{N_e}\frac{1}{|\boldsymbol{r}_i-\boldsymbol{r}_j|} - \sum_{A}^{N_A}\frac{1}{2M_A}\nabla_A^2 + \sum_{B>A}^{N_A}\frac{Z_AZ_B}{|\boldsymbol{R}_A-\boldsymbol{R}_B|} - \sum_{i}^{N_e}\sum_{A}^{N_A}\frac{Z_A}{|\boldsymbol{r}_i-\boldsymbol{R}_A|}\end{aligned} \tag{I.1.1}$$

where $\hat{T}_{\mathrm{e}}(\boldsymbol{r})$, $\hat{U}_{\mathrm{ee}}(\boldsymbol{r})$, $\hat{T}_{\mathrm{N}}(\boldsymbol{R})$, $\hat{U}_{\mathrm{NN}}(\boldsymbol{R})$, and $\hat{U}_{\mathrm{e}\mathbf{N}}(\boldsymbol{r};\boldsymbol{R})$ are kinetic energy of electrons, electron-electron repulsion potential energy, kinetic energy of nucleus, nuclear-nuclear repulsion potential energy, and electron-nuclear potential energy, respectively. The parameters $\boldsymbol{r}_i$, $\boldsymbol{R}_A$, M_A, and Z_A represent the position of i'th electron and the position, mass, and charge of A'th nucleus, respectively, and ∇_i and ∇_A represent the position derivatives of i'th electron and A'th nucleus, respectively. We denote $\{\boldsymbol{r}_i\}$ and $\{\boldsymbol{R}_A\}$ as $\boldsymbol{r}$ and $\boldsymbol{R}$, respectively. The time-independent Schrödinger equation of wavefunction $\Psi(\boldsymbol{r},\boldsymbol{R})$ including electron and nuclear coordinates is given as eq. (I.1.2)

$$H\Psi(\boldsymbol{r},\boldsymbol{R}) = E\Psi(\boldsymbol{r},\boldsymbol{R}) \tag{I.1.2}$$

where E represents the eigenenergy of Schrödinger equation.

Let us consider that the wavefunction $\Psi(\boldsymbol{r},\boldsymbol{R})$ is written as the linear combination of electronic wavefunction of nth state $\Phi_n(\boldsymbol{r};\boldsymbol{R})$ as parameters of fixed nuclear coordinates $\boldsymbol{R}$ [2]

$$\Psi(\boldsymbol{r},\boldsymbol{R}) = \sum_{n}\Theta_n(\boldsymbol{R})\Phi_n(\boldsymbol{r};\boldsymbol{R}) \tag{I.1.3}$$

where $\Theta_n(\boldsymbol{R})$ is the expansion coefficients. This approximation is called *adiabatic approximation*. Substituting eqs. (I,1,1) and (I.1.3) to (I.1.2), we derive

$$\sum_{n}\left\{\Theta_n(\boldsymbol{R})\hat{H}_{el}(\boldsymbol{r};\boldsymbol{R})\Phi_n(\boldsymbol{r};\boldsymbol{R}) + \hat{T}_{\mathrm{N}}(\boldsymbol{R})\Theta_n(\boldsymbol{R})\Phi_n(\boldsymbol{r};\boldsymbol{R})\right\} = \sum_{n}E\Theta_n(\boldsymbol{R})\Phi_n(\boldsymbol{r};\boldsymbol{R}), \tag{I.1.4}$$

where

$$\hat{H}_{el}(\boldsymbol{r};\boldsymbol{R}) = \hat{T}_{\mathrm{e}}(\boldsymbol{r}) + \hat{U}_{\mathrm{e}\mathbf{N}}(\boldsymbol{r};\boldsymbol{R}) + \hat{U}_{\mathrm{ee}}(\boldsymbol{r}) + \hat{U}_{\mathrm{NN}}(\boldsymbol{R}) \tag{I.1.5}$$

is the electronic Hamiltonian with the fixed nuclei parameter including nuclear repulsion energy and $\hat{T}_{\mathrm{N}}(\boldsymbol{R})\Theta_n(\boldsymbol{R})\Phi_n(\boldsymbol{r};\boldsymbol{R})$ is written as

$$\hat{T}_{\mathrm{N}}(\boldsymbol{R})\Theta_n(\boldsymbol{R})\Phi_n(\boldsymbol{r};\boldsymbol{R}) = -\sum_A \frac{1}{2M_A}\left[\left(\nabla_A^2\Theta_n(\boldsymbol{R})\right) + 2\nabla_A\Theta_n(\boldsymbol{R})\cdot\nabla_A + \Theta_n(\boldsymbol{R})\nabla_A^2\right]\Phi_n(\boldsymbol{r};\boldsymbol{R}) \tag{I.1.6}$$

The first term is kinetic energy of nuclear motion, and the second and the third term in above equation is called the non-adiabatic coupling (NAC) terms.[3,4] By multiplying $\Phi_m(\boldsymbol{r};\boldsymbol{R})$ from the light-hand-side and by integrating by electron coordinate $\boldsymbol{r}$, (I.1.5) and (I.1.6) gives the Schrödinger equation of the wavefunction becomes:

$$H_{el,mn}\Theta_n(\boldsymbol{R}) \equiv \sum_n \left[\left\{\hat{T}_{\mathrm{N}}(\boldsymbol{R}) + E_{el,n}(\boldsymbol{R})\right\}\delta_{mn} + 2\tau_{mn}^{(1)}\cdot\nabla + \tau_{mn}^{(2)}\right]\Theta_n(\boldsymbol{R}) = E\Theta_m(\boldsymbol{R}), \tag{I.1.7}$$

where

$$\tau_{mn}^{(1)} = -\sum_A \frac{1}{2M_A}\langle\Phi_m(\boldsymbol{r};\boldsymbol{R})|\nabla_A|\Phi_n(\boldsymbol{r};\boldsymbol{R})\rangle \tag{I.1.8}$$

$$\tau_{mn}^{(2)} = -\sum_A \frac{1}{2M_A}\left\langle\Phi_m(\boldsymbol{r};\boldsymbol{R})\middle|\nabla_A^2\middle|\Phi_n(\boldsymbol{r};\boldsymbol{R})\right\rangle \tag{I.1.9}$$

are referred to as the first- and the second- order NAC elements, which are the matrix elements of the first and the second derivatives with nuclei coordinates under the representation with eigenstates of the $H_{el}(\boldsymbol{r};\boldsymbol{R})$.

The $E_{el,n}(R)$ is the eigenenergy for *n*th adiabatic electronic states of the electron Hamiltonian. In Born-Oppenheimer approximation, $\tau_{mn}^{(1)}$ and $\tau_{mn}^{(2)}$ are neglected because nuclei are much heavier and move much more slowly than electrons. Thus, the eigenproblem of total Hamiltonian is simplified by solving the Schrödinger equation of electronic wavefunction independently of the nuclear motion, which is formulated as

$$\hat{H}_{el}(\boldsymbol{r},\boldsymbol{R})\Phi_n(\boldsymbol{r};\boldsymbol{R}) = E_{el,n}(\boldsymbol{R})\Phi_n(\boldsymbol{r};\boldsymbol{R}) \tag{I.1.10}$$

with the nuclei treated as fixed. The nth eigenenergy $E_{\boldsymbol{el,n}}(\boldsymbol{R})$ is written as a function of nuclei position, which is called as adiabatic potential energy surface (PES). The time-independent Schrödinger equation for the nuclei motion on the *n*th adiabatic PES under the Born-Oppenheimer approximation is describes as

$$-\sum_{A=1}^{N_A} \frac{1}{2M_A}\nabla_A^2\Theta_n(\boldsymbol{R}) + E_{\mathrm{el,n}}(\boldsymbol{R})\Theta_n(\boldsymbol{R}) = E\Theta_n(\boldsymbol{R}). \tag{I.1.11}$$

In order to discuss the state-to-state transition dynamics, however, it is necessary to consider the NAC terms which perturb the electronic wavefunctions and cause the mixing of the adiabatic electronic states.

Calculating the NAC can be challenging due to the divergence problem around $\partial R \to 0$, which results in a singularity near the conical intersection between PESs. However, since adiabatic states, as well as eigenstates, represent the physically observable states during the excited state dynamics in the aggregate system. Thus, NAC is an important quantity not only for the implementation of the computational methodology for the non-adiabatic process such as trajectory surface hopping (TSH)[5,6] and multi-configurational time-dependent Hartree (MCTDH) method,[7,8] but also for the accurate description of such process. In SF research, Krylov and her coworkers have introduced an efficient computational approach to bypass explicit calculations by using the norm of one-particle transition density.[4] This method has been successfully applied to various SF molecular systems, such as oligoacenes, diphenyl-isobenzofuranes, and diphenyl-hexatrienes.

1.1.2 Diabatic representation

In the adiabatic representation, it is difficult to exactly calculate NAC. This problem can be bypassed by using the *diabatic representation* for the electron basis.[1,2] In this representation, the total wavefunction is expressed in the linear combination of the orthonormal electronic state basis $\Phi_I'(\boldsymbol{r};\boldsymbol{R})$, on the reference structure $\boldsymbol{R}_0$ which satisfies

$$\left\langle \Phi'_I(\boldsymbol{r},\boldsymbol{R_0}) \middle| \Phi'_J(\boldsymbol{r},\boldsymbol{R_0}) \right\rangle = \delta_{IJ} \tag{I.1.12}$$

where δ_{IJ} denote the Kronecker's delta and cancels the first order NAC term as follows:

$$\left\langle \Phi'_I(\boldsymbol{r},\boldsymbol{R_0}) \middle| \nabla_A \middle| \Phi'_J(\boldsymbol{r},\boldsymbol{R_0}) \right\rangle = 0 \text{ for } I \neq J. \tag{I.1.13}$$

The wavefunction is described as

$$\Psi(\boldsymbol{r},\boldsymbol{R}) = \sum_I \chi_I(\boldsymbol{R}) \Phi'_I(\boldsymbol{r},\boldsymbol{R}_0)\,. \tag{I.1.14}$$

In this representation, the time-independent Schrödinger equation (I.1.2) becomes

$$\sum_I \hat{H}_{el}(\boldsymbol{r};\boldsymbol{R}) \Phi'_I(\boldsymbol{r},\boldsymbol{R_0}) \chi_I(\boldsymbol{R}) + \sum_I \Phi_I'(\boldsymbol{r},\boldsymbol{R}_0) \hat{T}_N(\boldsymbol{R}) \chi_I(\boldsymbol{R}) = E \sum_I \Phi'_I(r,R_\mathbf{0}) \chi_I(R) \tag{I.1.15}$$

and by introducing the potential difference

$$\hat{V}(\boldsymbol{R}) = \hat{H}_{el}(\boldsymbol{r};\boldsymbol{R}) - \hat{H}_{el}(\boldsymbol{r};\boldsymbol{R}_0) = \hat{U}_{\mathrm{eN}}(\boldsymbol{r};\boldsymbol{R}) - \hat{U}_{\mathrm{eN}}(\boldsymbol{r};\boldsymbol{R}_0) + \hat{U}_{\mathrm{NN}}(\boldsymbol{R}) - \hat{U}_{\mathrm{NN}}(\boldsymbol{R}_0), \tag{I.1.16}$$

and by multiplying $\Phi'_J(\boldsymbol{r},\boldsymbol{R}_0)$ from the left-hand-side of eq. (I.1.15) and taking integrals over electron coordinate $\boldsymbol{r}$, eq. (I.1.15) is reformulated as

$$\sum_I \left\{ H_{el,JI}(\boldsymbol{R}_0) + V_{JI}(\boldsymbol{R}) \right\} \chi_I(\boldsymbol{R}) + \hat{T}_N(\boldsymbol{R}) \chi_J(\boldsymbol{R}) = E \chi_J(\boldsymbol{R}) \tag{I.1.17}$$

where $H_{el,JI}(\boldsymbol{R}_0) = \langle \Phi'_J(r,R_\mathbf{0}) | \hat{H}_{el}(\boldsymbol{r};\boldsymbol{R}) | \Phi'_{\boldsymbol{I}}(r,R_\mathbf{0}) \rangle$ is the diabatic representation of the electronic Hamiltonian, which is not necessarily diagonal formula ($H_{el,JI}(\boldsymbol{R}_0) \neq 0$ even for $J \neq I$). The $V_{JI}(\boldsymbol{R}) = \langle \Phi'_J(r,R_\mathbf{0}) | \hat{V}(\boldsymbol{R}) | \Phi'_I(r,R_\mathbf{0}) \rangle$ is called the vibronic coupling (VC) interpreted as the effect on the electronic states of the change of the nuclei coordinates from $\boldsymbol{R}_0$ to $\boldsymbol{R}$. In diabatic representation, the transition between PES (eigenenergy of $H_{el,JI}(\boldsymbol{R})$) is described by VC term. The eq. (I.1.17) is simpler than adiabatic representation of eq. (I.1.7).

Unfortunately, the diabatic wavefunction is not uniquely determined and is criticized due to its strong dependence on the construction method compared with the non-adiabatic coupling method. In order to solve a direct solution for the problem of arbitrariness of the diabatic basis, ones have to select the transformation matrix from adiabatic state to the diabatic basis so that the diabatic representation provides chemical and physical insights. In community of SF, several diabatization schemes have been reported based on the post-HF method such as complete active space (CAS) method such as Nakamura-Truhlar's four-fold way scheme.[9,10] In the following section, we present a model Hamiltonian approach based on the diabatic picture.

1.2 Electronic Coupling

Initial process generating TT states

In this section, we introduce the diabatic basis to construct the model Hamiltonian for SF. In this study, we need to construct the exciton states in multimer system consisted of over three molecules, and it is Smith and Michl have proposed the essential five types of exciton bases to describe the electronic state associated to the SF dynamics. These diabatic state basis are Frenkel exciton (FE) states (S_1S_0 and S_0S_1), charge-transfer states (cation-anion [CA] and anion-cation [AC] state), and correlated triplet (TT) state.[11,12] The excitation energies and the electronic coupling calculated in dimer subsystem correspond to the diagonal and off-diagonal value of the model Hamiltonian.

There are two advantages to introduce model Hamiltonian with electronic couplings comparing with adiabatic approach. First, diabatic treatment make it easy to expand Hamiltonian to the aggregate system consisting of over three molecules. The model Hamiltonian is parametrized by the diabatic state energies of S_1, CT, and TT states, and the electronic coupling between these diabatic states. These parameters are calculated in neighboring dimer structure, and do not require computation of excited electronic states in multimer structure, which leads to reduce the computational costs. Although how to obtain these coupling should be taken into account,[2] it is sufficient for discussion of qualitative trends of SF dynamics. The second advantage is that model Hamiltonian approach allows us to separate discussion of the complex relationship between "*structure and excited electronic states in aggregate level*" into a discussion of "*structure–electronic coupling correlation in neighboring dimer system*" and "*(parametrized) electronic coupling–Hamiltonian correlation in multimer*". This makes it possible to understand the general trends of the electronic structure in aggregate systems as a function of excitation energy, electronic coupling, and aggregation topology, which reflect the constituent molecules, their intermolecular relative configuration, and global aggregation structure, respectively.

In this method, the wavefunction of the diabatic wave function is represented as the Slater determinant composed of the HOMOs and the LUMOs of two molecules. In the dimer system consists of molecule X and Y, the exciton basis of FE, CT, and TT states are described as follows when the HOMO and the LUMO of these molecules denoted as h_{X}, h_{Y}, l_{X}, and l_{Y}, respectively[11,12]:

$$|\mathrm{S_1S_0}\rangle = \frac{1}{\sqrt{2}}\left(\left|h_{\mathrm{X}}\overline{l_{\mathrm{X}}}h_{\mathrm{Y}}\overline{h_{\mathrm{Y}}}\right| - \left|\overline{h_{\mathrm{X}}}l_{\mathrm{X}}h_{\mathrm{Y}}\overline{h_{\mathrm{Y}}}\right|\right) \tag{I.1.18}$$

$$|\mathrm{S_0S_1}\rangle = \frac{1}{\sqrt{2}}\left(\left|h_{\mathrm{X}}\overline{h_{\mathrm{X}}}h_{\mathrm{Y}}\overline{l_{\mathrm{Y}}}\right| - \left|h_{\mathrm{X}}\overline{h_{\mathrm{X}}}\overline{h_{\mathrm{Y}}}l_{\mathrm{Y}}\right|\right) \tag{I.1.19}$$

$$|\mathrm{CA}\rangle = \frac{1}{\sqrt{2}}\left(\left|h_{\mathrm{X}}\overline{l_{\mathrm{Y}}}h_{\mathrm{Y}}\overline{h_{\mathrm{Y}}}\right| - \left|\overline{h_{\mathrm{X}}}l_{\mathrm{Y}}h_{\mathrm{Y}}\overline{h_{\mathrm{Y}}}\right|\right) \tag{I.1.20}$$

$$|\mathrm{AC}\rangle = \frac{1}{\sqrt{2}}\left(\left|h_{\mathrm{X}}\overline{h_{\mathrm{X}}}l_{\mathrm{X}}\overline{h_{\mathrm{Y}}}\right| - \left|h_{\mathrm{X}}\overline{h_{\mathrm{X}}}\overline{l_{\mathrm{X}}}h_{\mathrm{Y}}\right|\right) \tag{I.1.21}$$

$$|\mathrm{TT}\rangle = \frac{1}{\sqrt{3}}\left(\left|h_{\mathrm{X}}l_{\mathrm{X}}\overline{h_{\mathrm{Y}}}\overline{l_{\mathrm{Y}}}\right| + \left|\overline{h_{\mathrm{X}}}\overline{l_{\mathrm{X}}}h_{\mathrm{Y}}l_{\mathrm{Y}}\right|\right)$$
$$-\frac{1}{2\sqrt{3}}\left(\left|h_{\mathrm{X}}\overline{l_{\mathrm{X}}}h_{\mathrm{Y}}\overline{l_{\mathrm{Y}}}\right| + \left|h_{\mathrm{X}}\overline{l_{\mathrm{X}}}\overline{h_{\mathrm{Y}}}l_{\mathrm{Y}}\right| + \left|\overline{h_{\mathrm{X}}}l_{\mathrm{X}}h_{\mathrm{Y}}\overline{l_{\mathrm{Y}}}\right| + \left|\overline{h_{\mathrm{X}}}l_{\mathrm{X}}\overline{h_{\mathrm{Y}}}l_{\mathrm{Y}}\right|\right). \tag{I.1.22}$$

The orbitals without overline denote the α-spin function and that with overline denote β-spin function. Using these diabatic state basis, the exciton Hamiltonian in dimer system is denoted as follows:

$$H_{\mathrm{el}} = \begin{pmatrix} \langle \mathrm{S_1S_0}|H_{\mathrm{el}}|\mathrm{S_1S_0}\rangle & \langle \mathrm{S_1S_0}|H_{\mathrm{el}}|\mathrm{S_0S_1}\rangle & \langle \mathrm{S_1S_0}|H_{\mathrm{el}}|\mathrm{CA}\rangle & \langle \mathrm{S_1S_0}|H_{\mathrm{el}}|\mathrm{AC}\rangle & \langle \mathrm{S_1S_0}|H_{\mathrm{el}}|\mathrm{TT}\rangle \\ \langle \mathrm{S_0S_1}|H_{\mathrm{el}}|\mathrm{S_1S_0}\rangle & \langle \mathrm{S_0S_1}|H_{\mathrm{el}}|\mathrm{S_0S_1}\rangle & \langle \mathrm{S_0S_1}|H_{\mathrm{el}}|\mathrm{CA}\rangle & \langle \mathrm{S_0S_1}|H_{\mathrm{el}}|\mathrm{AC}\rangle & \langle \mathrm{S_0S_1}|H_{\mathrm{el}}|\mathrm{TT}\rangle \\ \langle \mathrm{CA}|H_{\mathrm{el}}|\mathrm{S_1S_0}\rangle & \langle \mathrm{CA}|H_{\mathrm{el}}|\mathrm{S_0S_1}\rangle & \langle \mathrm{CA}|H_{\mathrm{el}}|\mathrm{CA}\rangle & \langle \mathrm{CA}|H_{\mathrm{el}}|\mathrm{AC}\rangle & \langle \mathrm{CA}|H_{\mathrm{el}}|\mathrm{TT}\rangle \\ \langle \mathrm{AC}|H_{\mathrm{el}}|\mathrm{S_1S_0}\rangle & \langle \mathrm{AC}|H_{\mathrm{el}}|\mathrm{S_0S_1}\rangle & \langle \mathrm{AC}|H_{\mathrm{el}}|\mathrm{CA}\rangle & \langle \mathrm{AC}|H_{\mathrm{el}}|\mathrm{AC}\rangle & \langle \mathrm{AC}|H_{\mathrm{el}}|\mathrm{TT}\rangle \\ \langle \mathrm{TT}|H_{\mathrm{el}}|\mathrm{S_1S_0}\rangle & \langle \mathrm{TT}|H_{\mathrm{el}}|\mathrm{S_0S_1}\rangle & \langle \mathrm{TT}|H_{\mathrm{el}}|\mathrm{CA}\rangle & \langle \mathrm{TT}|H_{\mathrm{el}}|\mathrm{AC}\rangle & \langle \mathrm{TT}|H_{\mathrm{el}}|\mathrm{TT}\rangle \end{pmatrix} \tag{I.1.23}$$

The diagonal elements of this exciton Hamiltonian are the energy of exciton basis of eqs. (I.1.18)-(I.1.22), and we denote them as $E(\mathrm{S_1S_0})$, $E(\mathrm{S_0S_1})$, $E(\mathrm{CA})$, $E(\mathrm{AC})$, and $E(\mathrm{TT})$, respectively. The off-diagonal matrix elements are denoted by the one-electron and two-electrons integrals calculated by the quantum chemical calculation when we ignore the orbital overlaps.

$$\langle \mathrm{S_1S_0}|H|\mathrm{S_0S_1}\rangle = 2\langle h_{\mathrm{A}}h_{\mathrm{B}}|l_{\mathrm{A}}l_{\mathrm{B}}\rangle - \langle l_{\mathrm{A}}h_{\mathrm{A}}|l_{\mathrm{B}}h_{\mathrm{B}}\rangle \equiv V_{\mathrm{ex}} \tag{I.1.24}$$

$$\langle \mathrm{S_1S_0}|H|\mathrm{CA}\rangle = \left\langle l_A\middle|\hat{F}\middle|l_{\mathrm{B}}\right\rangle + 2\langle h_{\mathrm{A}}h_{\mathrm{A}}|l_{\mathrm{A}}l_{\mathrm{B}}\rangle - \langle h_{\mathrm{A}}l_{\mathrm{A}}|h_{\mathrm{A}}l_{\mathrm{B}}\rangle \sim V_{\mathrm{LL}} \tag{I.1.25}$$

$$\langle \mathrm{S_1S_0}|H|\mathrm{AC}\rangle = -\left\langle h_{\mathrm{A}}\middle|\hat{F}\middle|h_{\mathrm{B}}\right\rangle + 2\langle h_{\mathrm{A}}h_{\mathrm{A}}|l_{\mathrm{A}}l_{\mathrm{B}}\rangle - \langle h_{\mathrm{A}}l_{\mathrm{A}}|h_{\mathrm{B}}l_{\mathrm{A}}\rangle \sim -V_{\mathrm{HH}} \tag{I.1.26}$$

$$\langle \mathrm{CA}|H|\mathrm{TT}\rangle = \sqrt{3/2}\left(\left\langle l_{\mathrm{A}}\middle|\hat{F}\middle|h_{\mathrm{B}}\right\rangle + \langle l_{\mathrm{A}}l_{\mathrm{B}}|h_{\mathrm{B}}l_{\mathrm{B}}\rangle - \langle l_{\mathrm{A}}h_{\mathrm{A}}|h_{\mathrm{A}}h_{\mathrm{B}}\rangle\right) \sim \sqrt{3/2}\,V_{\mathrm{LH}} \tag{I.1.27}$$

$$\langle \mathrm{AC}|H|\mathrm{TT}\rangle = \sqrt{3/2}\left(\langle h_A|F|l_B\rangle + \langle h_A l_A|l_B l_A\rangle - \langle h_A h_B|l_B h_B\rangle\right) \sim \sqrt{3/2}\,V_{\mathrm{HL}} \tag{I.1.28}$$

$$\langle \mathrm{CA}|H|\mathrm{AC}\rangle = 2\langle h_{\mathrm{A}}l_{\mathrm{A}}|l_{\mathrm{B}}h_{\mathrm{B}}\rangle - \langle h_{\mathrm{A}}l_{\mathrm{A}}|h_{\mathrm{B}}l_{\mathrm{B}}\rangle \sim 0 \tag{I.1.29}$$

$$\langle \mathrm{S_1S_0}|H|\mathrm{TT}\rangle = \sqrt{3/2}\left(\langle l_{\mathrm{A}}l_{\mathrm{A}}|h_{\mathrm{B}}l_{\mathrm{B}}\rangle - \langle h_{\mathrm{A}}h_{\mathrm{A}}|h_{\mathrm{B}}l_{\mathrm{B}}\rangle\right) \sim 0 \tag{I.1.30}$$

The operator $\hat{F}$ denotes the Fock operator in dimer electronic structure. The $\langle \phi_p\phi_q|\phi_r\phi_s\rangle$ is two-electron integrals described as the physicists' notation $\int \mathrm{d}v_1 \mathrm{d}v_2 \phi_p^*(\boldsymbol{r}_1)\phi_q^*(\boldsymbol{r}_2) r_{12}^{-1} \phi_r(\boldsymbol{r}_1)\phi_s(\boldsymbol{r}_2)$. Since integrand of the two-electrons integrals in eqs. (I.1.25)–(I.1.30) and in the second term of eq. (I.1.24) is written as the product of molecular orbitals on the different molecules. Thus, these terms are small and is frequently considered negligible. The two electron integrals $V_{\mathrm{ex}} \sim 2\langle h_{\mathrm{A}} h_{\mathrm{B}} | l_{\mathrm{A}} l_{\mathrm{B}} \rangle$ contributes to the Davydov splitting of the FE states, which leads to the delocalization of S₁ exciton and the energy splitting of the FE energy levels. By denoting the Fock matrix elements as $V_{ij} \approx \langle i_A | F | j_B \rangle$ with i_A and j_B being the orbitals localized to molecules A and B, respectively, the eq. (I.1.23) is approximately reformulated as follows:

$$H_{\mathrm{el}} = \begin{pmatrix} E(\mathrm{S_1S_0}) & V_{\mathrm{ex}} & V_{\mathrm{LL}} & -V_{\mathrm{HH}} & 0 \\ V_{\mathrm{ex}} & E(\mathrm{S_0S_1}) & -V_{\mathrm{HH}} & V_{\mathrm{LL}} & 0 \\ V_{\mathrm{LL}} & -V_{\mathrm{HH}} & E(\mathrm{CA}) & 0 & \sqrt{3/2}\,V_{\mathrm{LH}} \\ -V_{\mathrm{HH}} & V_{\mathrm{LL}} & 0 & E(\mathrm{AC}) & \sqrt{3/2}\,V_{\mathrm{HL}} \\ 0 & 0 & \sqrt{3/2}\,V_{\mathrm{LH}} & \sqrt{3/2}\,V_{\mathrm{HL}} & E(\mathrm{TT}) \end{pmatrix}. \qquad (\mathrm{I.1.31})$$

There are two advantages of the representation by eq. (I.1.31). The first is that the matrix elements of the exciton Hamiltonian are physically informative. The energy of FE states, CT states, and TT states are interpreted as the S₁ excitation of the molecules $E(\mathrm{S_1})$, the interaction energies of cation and anion of two molecules, and the sum of the T₁ excitation energy of the molecules $2E(\mathrm{T_1})$. The off-diagonal matrix elements, Fock matrix elements V_{ij} and FE coupling V_{ex} are interpreted as the one electron transfer and the exciton transfer process between molecules A and B. The second advantage is that the model Hamiltonian is easily expanded for the electronic structure in the multimer systems. The eigenstates of the exciton Hamiltonian represented as eqs. (I.1.23) or (I.1.31) are defined as *adiabatic states*, which correspond to the solution of the time-independent Schrödinger equation $H_{el}|\alpha\rangle = E_\alpha |\alpha\rangle$ (E_α is an eigenenergy of adiabatic state $|\alpha\rangle$). The adiabatic states are denoted as the linear combination of the diabatic exciton basis as follows.

$$|\alpha\rangle = \sum_{m}^{N_{state}} C_{m\alpha} |m\rangle \qquad (\mathrm{I.1.32})$$

where the $C_{m\alpha} = \langle m|\alpha\rangle$ is the expansion coefficients of $|m\rangle$ in $|\alpha\rangle$ and the number of states N_{state} is 5 in dimer system of SF chromophore.

As explained in the next section, we can understand the efficiency and the rate of SF using excitation energy and distribution of the frontier MOs.

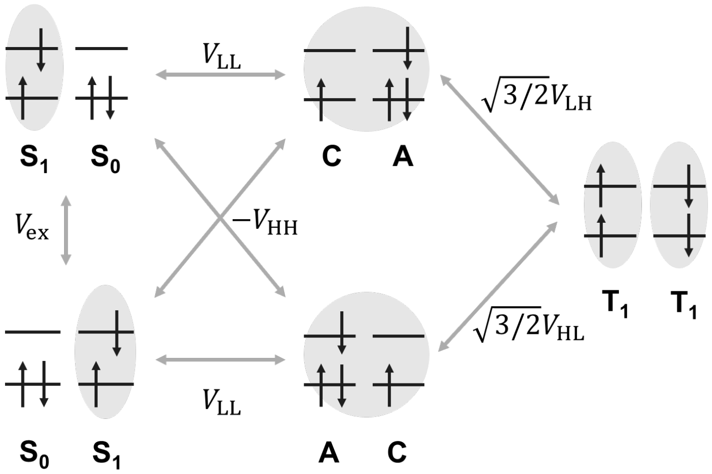

Figure. I.1.1. Diabatic state basis in SF.

Effective SF coupling

The rate of SF process is an important factor to evaluate the efficiency of SF materials. Since SF occurs in at least dimer systems, ones have to discuss the relationship between the neighboring dimer geometry and SF rate. In the simplest formula, the Fermi's golden rule gives the estimation of the SF rate from the electronic coupling between the initial (S_1S_0) and the final (TT) states. Including the effect of the structural reorganization of the nuclear coordinates, the SF rate $k_{\rm SF}$ is expressed by the following Marcus theory[13]:

$$k_{SF} = \frac{|V_{\rm SF}|^2}{\hbar}\sqrt{\frac{\pi}{\lambda k_B T}}\exp\left[-\frac{(\Delta E + \lambda)^2}{4\lambda k_B T}\right] \tag{I.1.33}$$

where $V_{\rm SF}$, ΔE, and λ are the SF coupling, the energy difference, and the reorganization energy between S_1S_0 and TT states, respectively. k_B and T is Boltzmann constant and temperature, respectively.

Because the direct coupling $\langle {\rm S_1S_0}|H|{\rm TT}\rangle$ is too weak (~ 0.1 meV) compared with the other couplings such as S_1S_0-CT or CT-TT couplings ranging from tens to hundreds of meV, the SF coupling $V_{\rm SF}$ is often approximated as the effective coupling including the CT-mediated transition paths obtained from perturbation theory (PT).[13,14] According to the quasi-degenerate perturbation theory up to the second order, the matrix element of the effective Hamiltonian ($\hat{H}_{\rm eff}$) between i and j is given by

$$\langle i|\hat{H}_{\rm eff}|j\rangle = \langle i|H_{el}|j\rangle + \frac{1}{2}\left[\langle i|H_{el}\hat{Q}_i H_{el}|j\rangle + \langle i|H_{el}\hat{Q}_j H_{el}|j\rangle\right], \tag{I.1.34}$$

with

$$\hat{Q}_i = \sum_{m \in Q} \frac{|m\rangle\langle m|}{E_i - E_m}, \tag{I.1.35}$$

where *i* and *j* are included in the reference space (*P*) of interest, while *m* is in its complement space (*Q*). By including S_1S_0 and TT states in *P* and CT states in *Q*, the effective S_1S_0-TT coupling is expressed as follows:

$$V_{\mathrm{SF}} = \langle \mathrm{S_1S_0}|H_{el}|\mathrm{TT}\rangle + \frac{1}{2}\sum_{m=\mathrm{AC,CA}} \langle \mathrm{S_1S_0}|H_{el}|m\rangle\langle m|H_{el}|\mathrm{TT}\rangle \left[\frac{1}{E(\mathrm{S_1S_0}) - E_m} + \frac{1}{E(\mathrm{TT}) - E_m}\right]$$
$$= \sqrt{\frac{3}{2}}\left[\frac{V_{\mathrm{LL}}V_{\mathrm{LH}}}{\Delta E_{\mathrm{CA}}} - \frac{V_{\mathrm{HH}}V_{\mathrm{HL}}}{\Delta E_{\mathrm{AC}}}\right] \tag{I.1.36}$$

where ΔE_{CA} and ΔE_{AC} are defined as

$$\frac{1}{\Delta E_{\mathrm{CA}}} = \frac{1}{2}\left[\frac{1}{E(\mathrm{S_1S_0}) - E(\mathrm{CA})} + \frac{1}{E(\mathrm{TT}) - E(\mathrm{CA})}\right], \tag{I.1.37a}$$

$$\frac{1}{\Delta E_{\mathrm{AC}}} = \frac{1}{2}\left[\frac{1}{E(\mathrm{S_1S_0}) - E(\mathrm{AC})} + \frac{1}{E(\mathrm{TT}) - E(\mathrm{AC})}\right]. \tag{I.1.37b}$$

From eq. (I.1.36), the SF rate is roughly estimated, and it is written as the summation of the terms which is inversely proportional to the S_1S_0-CT and CT-TT energy gaps, and is proportional to the one-electron transfer integrals V_{LL}, V_{HH}, V_{LH} and V_{HL}. Therefore, it is necessary to optimize packing structures in aggregates and crystals for efficient SF. Michl et al. have pointed out that the SF rate at face-to-face stacking dimer structure (**Figure I.1.2 (a)**) become for D_{2h} molecules such as pentacene, and the slip-stacked structure (**Figure I.1.2 (b)**) is preferable for the efficient SF, which is explained by the relationships between the trends of the one-electron transfer integrals on the intermolecular relative geometry. From **Figure I.1.2 (a)**, the out-of-phase relationships between frontier orbitals in the face-to-face pentacene stacking structure indicate that the V_{LL} and V_{HH} exhibit positively large values. By the larger displacement along the short axis of pentacene molecule, the overlap between π-plane become smaller, resulting in the smaller values of V_{LL} and V_{HH}. On the contrary, the contributions of the in-phase and out-of-phase parts of HOMO-LUMO overlap for the V_{LH} and V_{HL} cancel each other,[16] leading to these coupling become zero in face-to-face stacking geometry, while these coupling become non-zero value in slip-stacked geometry. The Marcus theory of eq. (I.1.36) is useful to capture this trend and frequently used for the rough estimation of SF at dimer level.

On the other hand, several problems of applying Marcus theory to the SF dynamics are pointed out. For example, since Marcus theory is based on the perturbative treatment of the electronic coupling, it breaks down and overestimates k_{SF} when the CT states are too close in energy to S_1S_0 or TT states (small ΔE_{CA} and ΔE_{AC} in eq. (I.1.36)) and when V_{mn} are too large.

Moreover, the Marcus theory does not consider the quantum nature of the eigenstates of excitonic Hamiltonian correctly, which includes the delocalization of S_1 states, the superposition or the state mixing of S_1, CT, and TT states, and the change in eigenenergy from the diabatic state energy due to the electronic coupling. Although the Marcus theory works well if the effect of the nuclear geometrical reorganization was sufficiently larger than that of the electronic coupling, more accurate description for the exciton dynamics and the relaxation by interstate migration process is needed in some cases.

Effective Triplet-Triplet Exciton Transfer Coupling

For the purpose of modeling the triplet-triplet spatial separation in addition to the initial TT generation process by SF, it is required to calculate the triplet-triplet exciton transfer (TTET) coupling between T_1S_0 and S_0T_1. In SF, the large TTET coupling value results in the Davydov splitting of the energy levels of adiabatic states including TT states due to the delocalization of triplet excitons. Several methods for theoretical estimation of TETT coupling have been proposed in the field of organic semiconductors, for example, Fleming et al. suggested that it can be estimated as half the energy difference between the first and the second triplet excited states calculated in a symmetric dimer model.[17] However, this method cannot be applied to the asymmetric dimer structure seen in the pentacene crystals and heterofission systems.

More practically, the direct TTET coupling is denoted as $\langle \mathrm{T_1S_0}|H_{el}|\mathrm{S_0T_1}\rangle$ in 4-electrons and 4-orbitals model shown in **Figure I.1.3**, called Dexter type coupling. The direct Dexter coupling mainly written as the two-electron integral $\langle h_X h_Y | l_X l_Y \rangle$ which is too small to reproduce the Davydov spitting in dimer systems suggested by Fleming et al., because the integrand includes the product of HOMO and LUMO on the different molecules. Alternatively, we introduce the effective triplet CT(^{3}CT)-mediate TTET coupling estimated by the quasi-degenerate perturbation theory.[18,19] By inserting T_1S_0 and S_0T_1 states to i and j and triplet CT states (denoted as CA_3 and AC_3), the effective TTET coupling t is formulated from previously described eq. (I.1.33) as follows:

$$t = \langle \mathrm{T_1S_0}|H_{el}|\mathrm{S_0T_1}\rangle + \frac{\langle \mathrm{T_1S_0}|H_{el}|\mathrm{CA_3}\rangle\langle \mathrm{CA_3}|H_{el}|\mathrm{S_0T_1}\rangle}{\Delta E_{\mathrm{CA}}} + \frac{\langle \mathrm{T_1S_0}|H_{el}|\mathrm{AC_3}\rangle\langle \mathrm{AC_3}|H_{el}|\mathrm{S_0T_1}\rangle}{\Delta E_{\mathrm{AC}}} \quad (\mathrm{I.1.38})$$

where

$$\frac{1}{\Delta E_{\mathrm{CA}}} = \frac{1}{2}\left(\frac{1}{E(\mathrm{T_1S_0}) - E(\mathrm{CA_3})} - \frac{1}{E(\mathrm{S_0T_1}) - E(\mathrm{CA_3})}\right), \quad (\mathrm{I.1.39})$$

$$\frac{1}{\Delta E_{\mathrm{AC}}} = \frac{1}{2}\left(\frac{1}{E(\mathrm{T_1S_0}) - E(\mathrm{AC_3})} - \frac{1}{E(\mathrm{S_0T_1}) - E(\mathrm{AC_3})}\right) \quad (\mathrm{I.1.40})$$

and $E(\mathrm{T_1S_0})$, $E(\mathrm{S_0T_1})$, $E(\mathrm{CA_3})$, and $E(\mathrm{AC_3})$ are the energy of the triplet exciton states and triplet

CT states, respectively. Because the $\langle \mathrm{T_1S_0}|H|\mathrm{CA_3}\rangle\langle \mathrm{CA_3}|H|\mathrm{S_0T_1}\rangle$ and $\langle \mathrm{T_1S_0}|H|\mathrm{AC_3}\rangle\langle \mathrm{AC_3}|H|\mathrm{S_0T_1}\rangle$ in eq. (I.1.38) correspond to the product of the HOMO-HOMO electron transfer and LUMO-LUMO electron transfer coupling, the TTET coupling t become large at the face-to-face stacking dimer structure. Although the direct TTET coupling term is at the order of 0.1~1 meV. the ^{3}CT-mediate TTET coupling becomes tens of meV, leading to the delocalization of the triplet excitons during the dissociation process of the TT states.

In the following chapter, we present the vibronic Hamiltonian theory based on the diabatic bases to obtain the parameter for describing the electron-phonon coupling during the quantum dynamics simulation.

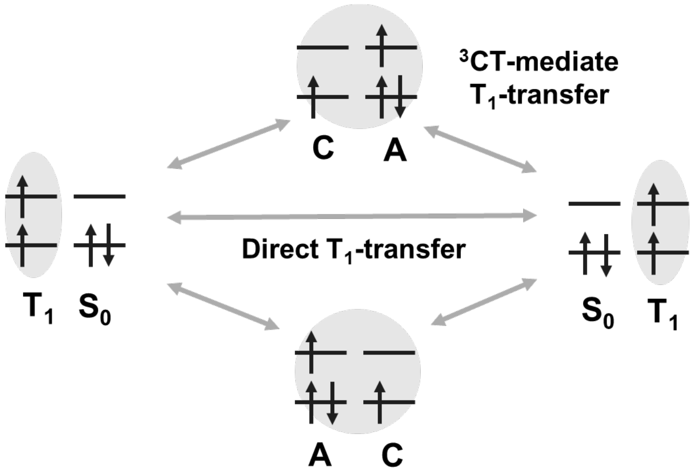

Figure. I.1.2. CT-mediate triplet exciton transfer.

1.3 Vibronic Coupling

As discussed in the previous section, it is important to consider the interaction between nuclear vibration and electronic state (vibronic coupling) for the simulation of the non-equilibrium dynamical process. In order to describe the vibronic coupling, we introduce the vibronic Hamiltonian approach.

Before introducing the vibronic Hamiltonian, we explain the coordinates to represent the nuclear vibration mathematically. In molecules with N_{A} atoms, the degree of the freedom of the nuclear motion is $3N_{\mathrm{A}}$, and it is reduced to the $3N_{\mathrm{A}}-6$ modes for non-linear molecules ($3N_{\mathrm{A}}-5$ modes for linear moelcules) by diagonalizing the hessian matrix excepting the translation and the rotation modes. These modes are called *normal modes*, which consists of the orthonormal basis to describe any transformation of molecules around the equilibrium structure. The hessian matrix $\boldsymbol{K}$ is represented by the *mass-weighted Cartesian coordinates* for *A*th atom $\boldsymbol{q}_A = \sqrt{M_A}\Delta\boldsymbol{R}_A$ ($\Delta\boldsymbol{R}_A$ are the displacement under the Cartesian coordinate on the equilibrium geometly and $A = 1,2,\ldots,N_{\mathrm{A}}$) as follows:

$$\boldsymbol{K} = \frac{\partial^2 E_{el}(\boldsymbol{R})}{\partial \boldsymbol{q}_A \partial \boldsymbol{q}_B} \tag{I.1.41}$$

By diagonalizing hessian $\boldsymbol{K}$, the diagonalization matrix $\boldsymbol{L}$ and normal mode frequency ω_k is obtained so that satisfy the following relations:

$$\boldsymbol{L}^{-1}\boldsymbol{K}\boldsymbol{L} = \boldsymbol{\Omega} \tag{I.1.42}$$

$$(\boldsymbol{\Omega})_{kl} = \omega_k \delta_{kl} \tag{I.1.43}$$

Where diagonal matrix $\boldsymbol{\Omega}$ have the normal mode frequency ω_k as the diagonal elements. The normal mode (*mass-weighted normal mode*) is then described as $\boldsymbol{Q}^{\mathrm{MW}} = \boldsymbol{L}^{-1}\boldsymbol{q}$, where the $\boldsymbol{q}$ is coordinate vector of the $3N_{\mathrm{A}}$ degree of the freedom. The standard quantum chemical calculation package gives the $\boldsymbol{Q}^{\mathrm{MW}}$. However, in the vibronic Hamiltonian, it is convenient to describe the Hamiltonian with the *mass-frequency weighted normal mode* or *dimensionless vibrational modes*, which is denoted as

$$\boldsymbol{Q}_k^{\mathrm{DL}} = \sqrt{\frac{\omega_k}{\hbar}}\boldsymbol{Q}_k^{\mathrm{MW}} = \sum_A \sqrt{\frac{\omega_k}{\hbar}}(\boldsymbol{L}^{-1})_{kA}\boldsymbol{q}_A = \sum_A \sqrt{\frac{\omega_k M_A}{\hbar}}(\boldsymbol{L}^{-1})_{kA}\Delta\boldsymbol{R}_A\,. \tag{I.1.44}$$

This is because the hessian matrix element is represented as

$$\frac{\partial^2 E_{el}(\boldsymbol{R})}{\partial \boldsymbol{Q}_k^{\mathrm{DL}} \partial \boldsymbol{Q}_l^{\mathrm{DL}}} = \hbar\omega_k\delta_{kl}, \tag{I.1.45}$$

which corresponds to the notation frequently used for the second quantization formalisms. The normal modes for the translation and the rotation shows $\omega_k = 0$, and often neglected because they do not cause the intrinsic change of the VC nature.

In this representation, the potential energy surface around the equilibrium is approximated as the harmonic oscillator potential with frequency ω_k and the displacement of the nucleus along the normal modes $\boldsymbol{Q}_k^{\mathrm{DL}}$. In the following part of this section, we denote $\boldsymbol{Q}_k^{\mathrm{DL}}$ as $\boldsymbol{Q}_k$ for simplicity. The matrix element of the vibronic coupling operator in eq. (I.1.16) is expanded by the Taylor series as follows:

$$\begin{aligned}\hat{V}(\boldsymbol{R}) &= \hat{H}_{el}(\boldsymbol{r};\boldsymbol{R}) - \hat{H}_{el}(\boldsymbol{r};\boldsymbol{R}_0)\\ &= \hat{U}_{\mathrm{eN}}(\boldsymbol{r};\boldsymbol{R}) - \hat{U}_{\mathrm{eN}}(\boldsymbol{r};\boldsymbol{R}_0) + \hat{U}_{\mathrm{NN}}(\boldsymbol{R}) - \hat{U}_{\mathrm{NN}}(\boldsymbol{R}_0)\\ &= \sum_k \hat{V}_k\boldsymbol{Q}_k + \frac{1}{2}\sum_{kl}\hat{V}_{kl}\boldsymbol{Q}_k\boldsymbol{Q}_l + \cdots\end{aligned} \tag{I.1.46}$$

The $\hat{V}_k$ and $\hat{V}_{kl}$ is describes as the first and the second derivatives of the potential term and denoted as:

$$\hat{V}_k = \left(\frac{\partial\hat{V}(\boldsymbol{R})}{\partial\boldsymbol{Q}_k}\right)_{R_0} = \left(\frac{\partial\hat{U}_{\mathrm{eN}}(\boldsymbol{r};\boldsymbol{R})}{\partial\boldsymbol{Q}_k}\right)_{R_0} + \left(\frac{\partial\hat{U}_{\mathrm{NN}}(\boldsymbol{R})}{\partial\boldsymbol{Q}_k}\right)_{R_0}, \tag{I.1.47}$$

$$\hat{V}_{kl} = \left(\frac{\partial^2\hat{V}(\boldsymbol{R})}{\partial\boldsymbol{Q}_k\partial\boldsymbol{Q}_l}\right)_{R_0} = \left(\frac{\partial^2\hat{U}_{\mathrm{eN}}(\boldsymbol{r};\boldsymbol{R})}{\partial\boldsymbol{Q}_k\partial\boldsymbol{Q}_l}\right)_{R_0} + \left(\frac{\partial^2\hat{U}_{\mathrm{NN}}(\boldsymbol{R})}{\partial\boldsymbol{Q}_k\partial\boldsymbol{Q}_l}\right)_{R_0}. \tag{I.1.48}$$

Under the diabatic representation, the matrix elements of $\hat{V}(\boldsymbol{R})$ is describes as follows:

$$\begin{aligned} V_{IJ}(\boldsymbol{R}) &= \langle \Phi'_I(\boldsymbol{r}, \boldsymbol{R_0}) | \hat{V}(\boldsymbol{R}) | \Phi'_J(\boldsymbol{r}, \boldsymbol{R_0}) \rangle \\ &= \sum_k V_{IJ,k} \boldsymbol{Q}_k + \frac{1}{2} \sum_{kl} V_{IJ,kl} \boldsymbol{Q}_k \boldsymbol{Q}_l + \cdots \end{aligned} \tag{I.1.49}$$

Then, the $V_{IJ,k}$ and $V_{IJ,kl}$ is interpreted as the effect of the displacement of the nuclear coordinates on the electron Hamiltonian $H_{el,IJ}(\boldsymbol{R}_0)$ at reference geometry $\boldsymbol{R}_0$ (frequently defined as the equilibrium geometry) in eq. (I.1.17). These matrix elements are called first- and second- order vibronic coupling constants (VCCs). In the research field of SF, the first order VCCs are mainly considered because they often contribute mainly to the SF process. The diagonal ($I = J$) and the off-diagonal ($I \neq J$) elements of the first-order VCCs represents the nuclear derivatives of the diabatic excited-state energy and electronic coupling, respectively, and are called as Holstein coupling and Peierls coupling, respectively.

The matrix element of the nuclear derivatives of potential $V_{IJ,k}$ is obtained as follows. We define the reference geometry $\boldsymbol{R}_0$ as the equilibrium geometry of ground state. For diagonal term (Holstein VCC), the note that the nuclear derivatives in ground state Φ'_G denoted as $V_{gg,k}$ becomes zero at equilibrium geometry, which is represented as:

$$V_{gg,k} = \left.\frac{\partial E_G}{\partial \boldsymbol{Q}_k}\right|_{\boldsymbol{R}_0} = \left(\frac{\partial \langle \Phi'_G | \hat{U}_{\mathrm{eN}}(\boldsymbol{r}; \boldsymbol{R}) | \Phi'_G \rangle}{\partial \boldsymbol{Q}_k}\right)_{\boldsymbol{R}_0} + \left(\frac{\partial \hat{U}_{\mathrm{NN}}(\boldsymbol{R})}{\partial \boldsymbol{Q}_k}\right)_{\boldsymbol{R}_0}. \tag{I.1.50}$$

By using eqs (I.1.47) and (I.1.50), the Holstein VCCs of the excitation energy is represented as

$$\begin{aligned} \left.\frac{\partial (E_I - E_G)}{\partial \boldsymbol{Q}_k}\right|_{\boldsymbol{R}_0} &= \left(\frac{\partial \langle \Phi'_I | \hat{U}_{\mathrm{eN}}(\boldsymbol{r}; \boldsymbol{R}) | \Phi'_I \rangle}{\partial \boldsymbol{Q}_k}\right)_{\boldsymbol{R}_0} - \left(\frac{\partial \langle \Phi'_G | \hat{U}_{\mathrm{eN}}(\boldsymbol{r}; \boldsymbol{R}) | \Phi'_G \rangle}{\partial \boldsymbol{Q}_k}\right)_{\boldsymbol{R}_0} \\ &= \int \mathrm{d}\boldsymbol{r} \Delta\rho_I(\boldsymbol{r}) v_k(\boldsymbol{r}) \end{aligned} \tag{I.1.51}$$

where $v(\boldsymbol{r})$ is differential of potential denoted as

$$v_k(\boldsymbol{r}) = \left(\sum_A \frac{\partial}{\partial \boldsymbol{Q}_k} \frac{-Z_A}{|\boldsymbol{r}_i - \boldsymbol{R}_A|}\right)_{\boldsymbol{R}_0} \tag{I.1.52}$$

and $\Delta\rho_I(\boldsymbol{r}) \equiv \rho_I(\boldsymbol{r}) - \rho_G(\boldsymbol{r})$ is the electron density difference between excited state *I* and ground state G, and $v(\boldsymbol{r})$ is the nuclear-electron potential energy. This equation indicated that the VCCs according to Holstein coupling is obtained by integrating the products of the density difference and the differential of potentials, which enable us to separately understand the contribution of these factors as functions of spatial coordinates. On the other hand, the off-diagonal ($I \neq J$) VC terms (Peierls coupling) in VCD formula is denoted as

$$V_{IJ,k} = \left.\frac{\partial \langle \Phi'_I | \hat{U}_{\mathrm{eN}}(\boldsymbol{r}; \boldsymbol{R}) | \Phi'_J \rangle}{\partial \boldsymbol{Q}_k}\right|_{\boldsymbol{R}_0}$$

$$= \int \mathrm{d}\boldsymbol{r}\rho_{IJ}(\boldsymbol{r})v_k(\boldsymbol{r}) \tag{I. 1.53}$$

where $\rho_{IJ}(\boldsymbol{r})$ denotes the transition density matrix between I'th and J'th diabatic states. This method to analyze the origin of microscopic structure is called vibronic coupling density (VCD) analysis.[20–22]

From the viewpoint of the potential energy surfaces (PESs) of the ground and the excited states, we obtain the relationships between the Holstein VCCs and the reorganization energies. **Figure 1.1.3** shows the PESs of the ground state G and the excited state I along the normal mode $\boldsymbol{Q}_k$. We approximate the PESs as the parabolic shape with respect to the mode k. As shown innthe **Figure 1.1.3**, the difference in the energy of Ith state at $\boldsymbol{R}_0$ and at the potential minimum is called reorganization energy λ_I^k of Holstein coupling, which is formulated as

$$\lambda_I^k = \frac{V_{II,k}^2}{2\hbar\omega_k}. \tag{I. 1.54}$$

The summation over all vibrational modes gives the total reorganization energy:

$$\lambda_I = \sum_k \lambda_I^k. \tag{I. 1.55}$$

By the analogy with this Holstein coupling, the reorganization energy λ_{IJ}^k and the total reorganization energy λ_{IJ} of the Peierls coupling are also denoted as

$$\lambda_{IJ}^k = \frac{V_{IJ,k}^2}{2\hbar\omega_k}. \tag{I. 1.56}$$

$$\lambda_{IJ} = \sum_k \lambda_{IJ}^k. \tag{I. 1.57}$$

These reorganization energy gives the strength of the VCCs, and it appears again in the next chapter as a parameter to determine the shape of spectral density.

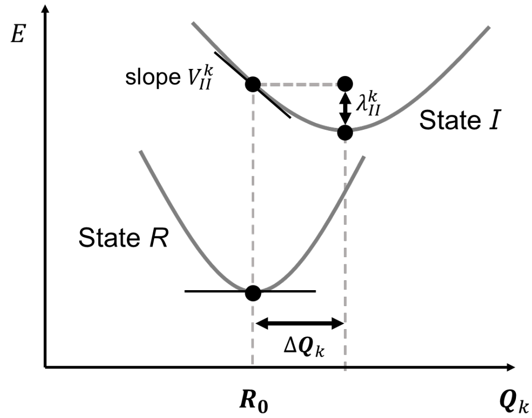

Figure. I.1.3. Schematic picture of vibronic coupling for the excited state energy. $V_{i,k}$ and $\lambda_{i,k}$ indicate the energy gradient of the excited state i and its reorganization energy with respect to the mode k.

References

(1) M. Baer, *Phys. Rep.*, **2002**, *358*, 75–142.

(2) D. Casanova, *Chem. Rev.*, **2018**, *118*, 7164–7207.

(3) S. Matsika, X. Feng, A. V. Luzanov and A. I. Krylov, *J. Phys. Chem. A*, **2014**, *118*, 11943–11955.

(4) X. Feng, A. B. Kolomeisky and A. I. Krylov, *J. Phys. Chem. C*, **2014**, *118*, 19608–19617.

(5) G. Tao, *J. Phys. Chem. C* **2014**, *118*, 17299−17305.

(6) G. Tao, G *J. Chem. Theory Comput.* **2015**, *11*, 28−36.

(7) J. Zheng, Y. Xie, S. Jiang, Z. Lan *J. Phys. Chem. C* **2016**, *120*, 1375−1389.

(8) S. R. Reddy, P. B. Coto, M. Thoss *J. Chem. Phys.* **2019**, *151*, 044307.

(9) H. Nakamura and D. G. Truhlar, *J. Chem. Phys.*, **2001**, *115*, 10353–10372.

(10) H. Nakamura and D. G. Truhlar, *J. Chem. Phys.*, **2002**, *117*, 5576–5593.

(11) M. B. Smith and J. Michl, *Chem. Rev.*, **2010**, *110*, 6891–6936.

(12) M. B. Smith and J. Michl, *Annu. Rev. Phys. Chem.*, **2013**, *64*, 361–386.

(13) R. A. Marcus and N. Sutin, *Biochim. Biophys. Acta*, **1985**, *811*, 265–322.

(14) H. Nakano, R. Uchiyama and K. Hirao, *J. Comput. Chem.*, **2002**, *23*, 1166–1175.

(15) I. Shavitt and L. T. Redmon, *J. Chem. Phys.*, **1980**, *73*, 5711–5717.

(16) I. Paci, J. C. Johnson, X. Chen, G. Rana, D. Popović, D. E. David, A. J. Nozik, M. A. Ratner, J. Michl, *J. Am. Chem. Soc.* **2006**, *128*, 16546-16553.

(17) G. D. Scholes, R. D. Harcourt, G. R. Fleming *J. Phys. Chem. B* **1997**, *101*, 7302-7312.

(18) R. D. Harcourt, G. D. Scholes, K. P. Ghiggino *J. Chem. Phys.* **1994**, *101*, 10521−10525.

(19) J. Wehner, B. Baumeier *J. Chem. Theory Comput.* **2017**, *13*, 1584−1594.

(20) T. Sato, K. Shizu, T. Kuga, K. Tanaka and H. Kaji, *Chem. Phys. Lett.*, **2008**, *458*, 152–156.

(21) T. Sato, R. Hayashi, N. Haruta and Y. J. Pu, *Sci. Rep.*, **2017**, *7*, 1–9.

(22) T. Nagami, T. Tonami, K. Okada, W. Yoshida, H. Miyamoto and M. Nakano, *J. Chem. Phys.*, **2020**, *153*, 134302.

Chapter 2

Quantum Master Equation for Singlet Fission Dynamics

In this chapter, we introduce the quantum master equation (QME) which describes the time-evolution of exciton states during the SF process. First, in Section 2.1, we introduce the density matrix and its time-evolution equation, the Liouville-von Neumann equation, to derive the general formulation of quantum dynamics. In the following Section 2.2, we introduce Hamiltonian and reduced density matrix (RDM) for the open quantum systems by tracing out the degree of freedom of phonon bath states. From the time evolution of RDM, ones can obtain the information about exciton (electronic) states such as the population (diagonal terms) and the coherence (off-diagonal terms) at each time. As described in Section 2.3, the effects of exciton–phonon coupling is represented as continuous spectral density functions of which line shape is obtained from vibronic coupling (VC) parameters such as reorganization energy λ and cut-off frequency Ω. Then, the relaxation rates are derived from the exciton wavefunction of adiabatic states and spectral density as a function of energy gap between initial and final states. In Section 2.4, we introduce the relative relaxation factor (RRF) analysis methods which is convenient to interpret the origin of dynamics as the kinetic models with state-to-state transition between adiabatic states.

2.1 General Formulation of Quantum Dynamics

2.1.1 Density Matrix and Liouville-von Neumann equation

Any states of quantum system are represented as state vector $|\Psi(t)\rangle$, which follows time-dependent Schrödinger equation under atomic unit ($\hbar = 1$)

$$i\frac{\partial}{\partial t}|\Psi(t)\rangle = H|\Psi(t)\rangle, \tag{I.2.1}$$

and

$$-i\frac{\partial}{\partial t}\langle\Psi(t)| = \langle\Psi(t)|H \tag{I.2.2}$$

where H represents the Hamiltonian of the quantum systems. Here, we consider time-independent Hamiltonian, and the formal solution is given as:

$$|\Psi(t)\rangle = e^{-iHt}|\Psi(0)\rangle \tag{I.2.3}$$

and its Hermitian conjugate is

$$\langle\Psi(t)| = \langle\Psi(0)|e^{iHt}, \tag{I.2.4}$$

Here, we introduce the density matrix which is another representation of the state of the system. First, we consider the density matrix of pure state $\Psi(t)$ in the closed system. The density operator $\rho(t)$ is written as the tensor product of bra- and ket- vector as follows:

$$\rho(t) = |\Psi(t)\rangle\langle\Psi(t)| \tag{I.2.5}$$

Let us consider the physical operator A, and its eigenvalue and eigenstates being written as a and $|a\rangle$. Because the set of $|a\rangle$ is nonorthogonal basis, $|\Psi(t)\rangle$ is written as the linear combination of them:

$$|\Psi(t)\rangle = \sum_a c_a(t)|a\rangle \tag{I.2.6}$$

where the expansion coefficient $c_a(t)$ is normalized as

$$\sum_a |c_a(t)|^2 = 1. \tag{I.2.7}$$

The matrix element $\rho_{ab}(t) = \langle a|\rho(t)|b\rangle$ is given as

$$\rho_{ab}(t) = c_a(t)c_b^*(t) \tag{I.2.8}$$

This indicates that the diagonal element of density matrix $\rho_{aa}(t) = |c_a(t)|^2$ corresponds to the probability of finding system in state $|a\rangle$ (or population) when observing the system with respect to the observable A. The off-diagonal element of density matrix $\rho_{ab}(t) = c_a(t)c_b^*(t)$ with $a \neq b$ represents the degree of quantum interference between state a and b, which is called coherence.

The expectation value $\langle A \rangle$ of observable A is given as

$$\langle A \rangle = \sum_{a} |c_a(t)|^2 a = \sum_{a,b} \rho_{ab}(t) a \delta_{ab} = \sum_{a,b} \rho_{ab} A_{ba} = \mathrm{tr}(\rho(t)A) \tag{I.2.9}$$

where $\mathrm{tr}(\cdots) = \sum_a \langle a| \cdots |a\rangle$ is called trace operator.

To discuss the equation of motion formulated by density matrix, we begin with eqs. (I.2.3) and (I.2.4). Using these equations, $\rho(t)$ is given as

$$\rho(t) = e^{-iHt} \rho(0) e^{iHt} \tag{I.2.10}$$

The time-evolution of the density matrix of pure state is derived can be derived by using eqs. (I.2.3) and (I.2.4):

$$\frac{\partial \rho(t)}{\partial t} = -i[H, \rho(t)] \equiv -i\hat{L}\rho(t) \tag{I.2.11}$$

where $\hat{L} \star \equiv i[H, \star]$ is called an Liouville super operator. This equation is referred to as Liouville-von Neumann equation. The formal solution of eq. (I.2.7) is given as

$$\rho(t) = e^{-i\hat{L}t} \rho(0) \tag{I.2.12}$$

By introducing density matrix, we can describe the time-dependent equations and probabilistic behavior of quantum systems in a consistent formalism, not only for pure states but also for mixed states. A mixed state represents a probabilistic mixture of several possible states. The state of the system is expressed by a density matrix rather than a single wave function, and the probabilities associated with each state in the mixture reflect the likelihood of the system being found in that state upon measurement. For example, we consider density matrix of mixed states as an ensemble average of several states denoted as $|\psi_n(t)\rangle$ with weight constant p_n:

$$\rho(t) = \sum_{n} p_n |\psi_n(t)\rangle\langle\psi_n(t)| \tag{I.2.13}$$

with normalization condition $\sum_n p_n = 1$. When state vectors are written by the linear combination of orthogonal basis such as $|\psi_n(t)\rangle = \sum_a c_{na}(t)|a\rangle$, the density matrix element represented is written as

$$\rho_{ab}(t) = \sum_{n} p_n c_{na}(t) c_{nb}^*(t) = \overline{c_a(t) c_b^*(t)} \tag{I.2.14}$$

where $\overline{c_a(t) c_b^*(t)}$ represents the ensemble average of the population with $a = b$, and the quantum interference between state a and b with $a \neq b$. The mixed state is more appropriate for representing the state of the system than wavefunction when we discuss the statistical behaviors of the system which is fluctuated by random external forces such as electron-phonon coupling. In this case, off-diagonal elements of density matrix often disappear when taking ensemble average, which is called decoherence. Starting from eq. (I.2.10), we can obtain the same equation about an expectation value of observables as eq. (I.2.9), and about the equation of motion as eq. (I.2.12), and following forms in this chapter can be applied to both pure and mixed states.

2.1.2 Liouville-von Neumann equation at Interaction Picture

In this section, we introduce the interaction picture (I.P.) to make simple for the derivation of the equation of motion. The total Hamiltonian is given as the unperturbed Hamiltonian H_0 and perturbed Hamiltonian H_1.

$$H = H_0 + H_1 \tag{I.2.15}$$

The unperturbed Hamiltonian is often selected so that we can obtain the solution of eigenproblem $H_0|n\rangle = \omega_n|n\rangle$. The perturbed Hamiltonian H_1 is often denoted as interaction Hamiltonian in sense that it induces interactions or transition between eigenstates of H_0. In interaction picture, we introduce time-dependent operators of observables given as

$$A(t) = e^{iH_0t}Ae^{-iH_0t} \tag{I.2.16}$$

From LvN equation, the time-evolution of density matrix in I.P. $\tilde{\rho}(t)$ is obtained as

$$\frac{\partial}{\partial t}\tilde{\rho}(t) = \frac{i}{\hbar}\left\{e^{iH_0t}H_0\rho(t)e^{-iH_0t} - e^{iH_0t}\rho(t)H_0e^{-iH_0t}\right\} + e^{iH_0t}\frac{\partial\rho(t)}{\partial t}e^{-iH_0t} \tag{I.2.17}$$

By applying $e^{iH_0t/\hbar}e^{-iH_0t/\hbar} = 1$ and eq. (I.2.11) to (I.2.17), we obtain

$$\frac{\partial}{\partial t}\tilde{\rho}(t) = -i[H_1(t), \tilde{\rho}(t)] \tag{I.2.18}$$

where the perturbed Hamiltonian in I.P. $H_1(t)$ is denoted as

$$H_1(t) = e^{iH_0t}H_1e^{-iH_0t} \tag{I.2.19}$$

The formal solution of equation (I.2.17) is given as

$$\tilde{\rho}(t) = \tilde{\rho}(0) - i\int_0^t ds[H_1(s), \tilde{\rho}(s)] \tag{I.2.20}$$

By substituting equation (I,2,20) in the $\tilde{\rho}(s)$ in itself, the $\tilde{\rho}(t)$ is written as

$$\tilde{\rho}(t) = \tilde{\rho}(0) - i\int_0^t ds[H_1(s), \tilde{\rho}(s)] - \int_0^t ds\int_0^s d\tau\big[H_1(s), [H_1(\tau), \tilde{\rho}(\tau)]\big] \tag{I.2.21}$$

This is called second-order perturbation solution of LvN equation. The time-derivative of equation (I.2.22) is written as the integrant form

$$\frac{\partial\tilde{\rho}(t)}{\partial t} = -i[H_1(t), \tilde{\rho}(t)] - \int_0^t d\tau\big[H_1(t), [H_1(\tau), \tilde{\rho}(\tau)]\big] \tag{I.2.22}$$

and this equation is the starting point of derivation of quantum master equation.

2.2 Quantum Dynamics in Open System

2.2.1 Hamiltonian of Open Quantum System

In the following section, we introduce *open quantum systems*, where a quantum system with one's particular interest (denoted as S) is coupled to another quantum system B, which is not interested in and called bath, reservoir, or environment (**Figure I.1.2**).[1] The Hilbert space of the composite system (S+B) is written by the tensor product of Hilbert spaces of its subsystems $\mathcal{H}_S$ and $\mathcal{H}_B$.

$$\mathcal{H}_{S+B} = \mathcal{H}_S \otimes \mathcal{H}_B \tag{I.2.23}$$

When state vectors of subsystems $\mathcal{H}_S$ and $\mathcal{H}_B$ are written as $|s\rangle_S$ and $|b\rangle_B$, respectively, we can construct the new vector of the composite system written as the tensor product state such as $|sb\rangle \equiv |s\rangle_S|b\rangle_B$, which is the basis in the Hilbert space $\mathcal{H}_{S+B}$. In case of weak coupling between S and B, an arbitral state vector in composite system $|\Psi\rangle$ is written as the direct product of state vectors in S (denoted as $|\psi\rangle_\mathrm{S}$) and B (denoted as $|\varphi\rangle_\mathrm{B}$), respectively, such as $|\Psi\rangle \approx |\psi\rangle_\mathrm{S} \otimes |\varphi\rangle_\mathrm{B}$.

The total Hamiltonian H including system S and bath B is written as

$$H = H_S + H_B + H_I \tag{I.2.24}$$

where H_S, H_B, and H_I is Hamiltonians of system, bath, and S-B interaction, respectively. The H_S and H_B only act on the Hilbert space $\mathcal{H}_S$ and $\mathcal{H}_B$, respectively, while interaction Hamiltonian acts on both the state vectors in $\mathcal{H}_S$ and $\mathcal{H}_B$. In the I.P., this Hamiltonian is divided into two parts as show in eq. (I.2.15), where $H_0 = H_S + H_B$ and $H_1 = H_I$, and time-evolution of the total density matrix follows (I,2,22).

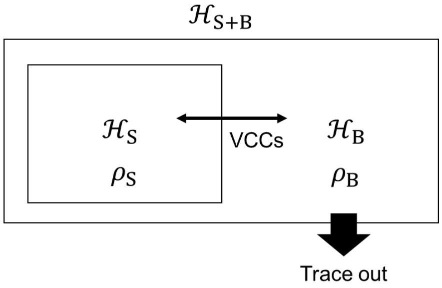

Figure I.2.1 Composite system of system (S) and bath (B), and reduced density matrix

2.2.2 Reduced Density Matrix (RDM)

Next, we introduce partial trace and reduced density matrix (RDM), where the trace is taken to ρ only for the degree of freedom B. Let us consider the expectation value of an operator A that works only for S as

$$\langle A\rangle = \mathrm{tr}(A\rho) = \sum_{s,b}\langle sb|A\rho|sb\rangle \tag{I.2.25}$$

Then, we use completeness of basis set $\sum_{s',b'}|s'b'\rangle\langle s'b'| = 1$

$$\langle A\rangle = \sum_{s,s'}\sum_{b,b'}\langle sb|A|s'b'\rangle\langle s'b'|\rho|sb\rangle \tag{I.2.26}$$

Since A is independent of B,

$$\langle sb|A|s'b'\rangle = \langle s|A|s'\rangle\langle b|b'\rangle = \langle s|A|s'\rangle\delta_{bb'} \tag{I.2.27}$$

and thus, eq. (I.2.26) becomes

$$\begin{aligned}\langle A\rangle &= \sum_{s,s'}\langle s|A|s'\rangle\sum_{b}\langle s'b|\rho|sb\rangle = \sum_{s,s'}\langle s|A|s'\rangle\left\langle s'\left|\sum_{b}\langle b|\rho|b\rangle\right|s\right\rangle \\ &= \sum_{s,s'}\langle s|A|s'\rangle\langle s'|tr_B(\rho)|s\rangle = \sum_{s,s'}\langle s|A|s'\rangle\langle s'|\rho_{\mathrm{S}}|s\rangle \end{aligned} \tag{I.2.28}$$

where $\mathrm{tr}_B(\cdots) \equiv \sum_b\langle b|\cdots|b\rangle$ is the partial trace of B, and operator form of RDM ρ_{S} is given as

$$\rho_{\mathrm{S}} = \mathrm{tr}_{\mathrm{B}}(\rho) \tag{I.2.29}$$

By the RDM and eq. (I.2.28), the expectation value of operator $\langle A\rangle$ is written as

$$\langle A\rangle = tr_{\mathrm{S}}(A\rho_{\mathrm{S}}). \tag{I.2.30}$$

By taking partial trace of B for the both sides of eq. (I.2.22), we can derive quantum master equation which represents the time-evolution of RDM for the system of interest.

2.2.3 Derivation of QME

In this section, we derive the quantum master equation in *time-convolutionless formula* and introduce two assumptions called Born approximation and Markov approximation in order to simplify the dynamics of open quantum systems.

The Born approximation assumes that the interaction between the system and its environment (or bath) is weak. This allows us to treat the system-bath coupling perturbatively, meaning that the influence of the system on the bath is negligible. As a result, the bath remains in a thermal equilibrium state or its initial state, unaffected by the system. This approximation simplifies the interaction term and allows us to write the master equation in a form where the system's evolution only depends on the system's state and some fixed properties of the bath. The density matrix under Bron approximation is written as

$$\rho(t) = \rho_{\mathrm{S}}(t)\otimes\rho_{\mathrm{B}}. \tag{I.2.31}$$

The Markov approximation assumes that the memory effects of the environment can be neglected, meaning that the system's future evolution only depends on its present state and not past state. This is valid when the bath correlation time is much shorter than the system's time scale of evolution. Under this approximation, the master equation becomes time-local, leading to a simpler, time-independent description of the system's dynamics.

By taking trace for B, eq. (I.2.22) becomes

$$\frac{\partial \tilde{\rho}_{\mathrm{S}}(t)}{\partial t} = -i\mathrm{tr}_{\mathrm{B}}\{[H_I(t), \tilde{\rho}(t)]\} - \int_0^t d\tau \mathrm{tr}_{\mathrm{B}}\{[H_I(t), [H_I(\tau), \tilde{\rho}_{\mathrm{S}}(\tau) \otimes \rho_{\mathrm{B}}]]\} \tag{I.2.32}$$

Because of the cyclicity of trace, $\mathrm{tr}_{\mathrm{B}}(AB) = \mathrm{tr}_{\mathrm{B}}(BA)$, the first term right hand side in eq. (I.2.32) is 0. Furthermore, by using substitution $\tau = t - s$ in second term, we derive

$$\frac{\partial \tilde{\rho}_{\mathrm{S}}(t)}{\partial t} = -\int_0^t ds \mathrm{tr}_{\mathrm{B}}\{[H_I(t), [H_I(t-s), \tilde{\rho}_{\mathrm{S}}(t-s) \otimes \rho_{\mathrm{B}}]]\} \tag{I.2.33}$$

which is called time-convolution quantum master equation up to second order. This is non-local equation in time where the time derivative of RDM depends on that at all past time. When the time-scale of the system relaxation τ_{R} is slower than that of the decay of bath correlation functions τ_{B}, the integrand $\tilde{\rho}_{\mathrm{S}}(t-s)$ is approximately replaced by $\tilde{\rho}_{\mathrm{S}}(t)$, resulting in

$$\frac{\partial \tilde{\rho}_{\mathrm{S}}(t)}{\partial t} = -\int_0^t \mathrm{d}s \mathrm{tr}_{\mathrm{B}}\{[H_I(t), [H_I(t-s), \tilde{\rho}_{\mathrm{S}}(t) \otimes \rho_{\mathrm{B}}]]\} \tag{I.2.34}$$

which is called as time-convolutionless quantum master equation (TCL QME) up to the second order.[1] This is local to the present time t and $\partial \tilde{\rho}_{\mathrm{S}}(t)/\partial t$ is not affected by its past information. In Markov approximation, the upper limit of t in the integral is replaced by infinity ($t \to \infty$).

2.2.4 QME for SF Dynamics

Let us derive the QME for SF relaxation dynamics. The total Hamiltonian in Schrödinger picture is written by the sum of the exciton Hamiltonian (H_{ex}), the phonon bath Hamiltonian for Holstein and Peierls coupling ($H_{\mathrm{ph}}^{\mathrm{H}}$, $H_{\mathrm{ph}}^{\mathrm{P}}$), and the exciton-phonon coupling Hamiltonian for Holstein and Peierls coupling ($H_{\mathrm{ex-ph}}^{\mathrm{H}}$, $H_{\mathrm{ex-ph}}^{\mathrm{P}}$).

$$H = H_{\mathrm{ex}} + H_{\mathrm{ph}}^{\mathrm{H}} + H_{\mathrm{ph}}^{\mathrm{P}} + H_{\mathrm{ex-ph}}^{\mathrm{H}} + H_{\mathrm{ex-ph}}^{\mathrm{P}} \tag{I.2.35}$$

Comparing with eq. (I.2.24), system Hamiltonian H_S, bath Hamiltonian H_B, and interaction Hamiltonian H_I satisfy

$$H_S = H_{\mathrm{ex}} \tag{I.2.36}$$

$$H_B = H_{\mathrm{ph}}^{\mathrm{H}} + H_{\mathrm{ph}}^{\mathrm{P}} \tag{I.2.37}$$

$$H_I = H_{\mathrm{ex-ph}}^{\mathrm{H}} + H_{\mathrm{ex-ph}}^{\mathrm{P}}, \tag{I.2.38}$$

respectively.

The exciton Hamiltonian H_{ex} which is denoted in diabatic representation as

$$H_{\mathrm{ex}} = \sum_{n}^{N_{state}} E_n |n\rangle\langle n| + \sum_{m\neq n}^{N_{state}} V_{mn} |m\rangle\langle n| \tag{I.2.39}$$

where E_n represents diabatic state energy of n'th state and V_{mn} represents the electronic coupling between m'th and n'th states, and N_{state} denotes the number of exciton states. For example, in dimeric SF system, there are 5 diabatic states (S_1S_0, S_0S_1, CA, AC, and TT) included in the model Hamiltonian as we mentioned in Chapter 3. The Hamiltonian matrix in diabatic representation is diagonalized by adiabatic states, denoted as $\{|\psi_i\rangle\}$, and satisfy following relations

$$H_{\mathrm{ex}}|\psi_i\rangle = E_i|\psi_i\rangle, \tag{I.2.40}$$

and $|\psi_i\rangle$ is written by the linear combination of diabatic state bases

$$|\psi_i\rangle = \sum_m |m\rangle\langle m|\psi_i\rangle = \sum_m C_{mi}|m\rangle. \tag{I.2.41}$$

The phonon bath Hamiltonian for Holstein and Peierls term (fluctuation of the diagonal and the off-diagonal elements of H_{ex}, respectively) are written in the second-quantized form as follows:

$$H_{\mathrm{ph}}^X = \sum_m \sum_p \omega_{mp}^X b_{mp}^{X\dagger} b_{mp}^X \tag{I.2.42}$$

where ω_{mp}^X is the frequency of harmonic oscillator and $b_{mp}^{X\dagger}$ and b_{mp}^X is the creation/annihilation operator of p'-th phonon bath mode, which satisfy the commutation relations:

$$\left[b_{mp}^X, b_{mp}^{X\dagger}\right] = 1 \tag{I.2.43}$$

and using number operator $N_{mp}^X \equiv b_{mp}^{X\dagger} b_{mp}^X$,

$$\left[N_{mp}^X, b_{mp}^X\right] = -b_{mp}^X \tag{I.2.44}$$

$$\left[N_{mp}^X, b_{mp}^{X\dagger}\right] = b_{mp}^{X\dagger}. \tag{I.2.45}$$

For Peierls coupling ($X = \mathrm{P}$), the index by m represents the off-diagonal elements of H_{ex} or the pair of diabatic state basis. Hereafter, the index m for Peierls coupling represents the pair of diabatic state basis, i.e., $m = (m', n') = (\mathrm{S_1S_0}, \mathrm{S_0S_1}), (\mathrm{S_1S_0}, \mathrm{CA}), (\mathrm{S_1S_0}, \mathrm{AC})$ and so on.

The interaction Hamiltonian $H_{\mathrm{ex-ph}}$ for Holstein and Peierls coupling are typically written in the form as follows[1]:

$$H_{\mathrm{ex-ph}}^X = \sum_m A_m^X \otimes B_m^X \tag{I.2.46}$$

where the sum over m is taken by the diabatic state bases for $X = \mathrm{H}$ and by pair of diabatic state bases (m', n') for $X = \mathrm{P}$. The operator A_m^X acting on $\mathcal{H}_S$ is written as

$$A_m^{\mathrm{H}} \equiv |m\rangle\langle m| \tag{I.2.47}$$

$$A_m^{\mathrm{P}} \equiv |m'\rangle\langle n'|, \tag{I.2.48}$$

where A_m^X is projection onto diabatic state m if $m = n$, or transition operator from n'th state to m'th state of $m \neq n$, which relate to the diagonal and off-diagonal elements of H_{ex}, respectively ($H_{\mathrm{ex}} \equiv \sum_{mn} H_{\mathrm{ex},mn} A_{mn}$). The operator B_m^X acting on $\mathcal{H}_B$ is written in the second-quantized form as:

$$B_m^X = \sum_p \hbar\omega_{pm}^X\left(g_{pm}^X b_{pm}^X + g_{pm}^{X*} b_{pm}^{X\dagger}\right) \tag{I.2.49}$$

where complex value g_{pm}^X represents the (dimensionless) exciton-phonon coupling constant.

For simpler derivation of QME in the following section, we here introduce the *eigenoperator technique*. Let us introduce the projection onto the eigenspace belonging to the eigenvalue ε by $\Pi(\varepsilon) \equiv |\varepsilon\rangle\langle\varepsilon|$, and operator $A_m^X(\omega)$ defined as following relation:

$$A_m^X(\omega) = \sum_{\varepsilon-\varepsilon'=\omega} \Pi(\varepsilon) A_m^X \Pi(\varepsilon') \tag{I.2.50}$$

The sum in eq. (I.2.38) is extended over all energy eigenvalues ε and ε' of H_{ex} with a fixed energy difference of $\omega \equiv \varepsilon - \varepsilon'$. The projection A_m is inversely obtained by summing $A_m^X(\omega)$ over energy difference ω:

$$\begin{aligned} A_m^{\mathrm{H}} &= |m\rangle\langle m| = \sum_{\alpha\beta} |\Psi_\alpha\rangle\langle\Psi_\alpha|m\rangle\langle m|\Psi_\beta\rangle\langle\Psi_\beta| \\ &= \sum_\omega \left(\sum_{\substack{\alpha,\beta \\ (E_\alpha - E_\beta = \omega)}} C_{m\alpha}^* C_{m\beta} |\Psi_\alpha\rangle\langle\Psi_\beta| \right) = \sum_\omega A_m^X(\omega) \end{aligned} \tag{I.2.51}$$

$$A_m^{\mathrm{P}} = \sum_\omega \left(\sum_{\substack{\alpha,\beta \\ (E_\alpha - E_\beta = \omega)}} C_{m'\alpha}^* C_{n'\beta} |\Psi_\alpha\rangle\langle\Psi_\beta| \right) = \sum_\omega A_m^X(\omega) \tag{I.2.52}$$

The operator $A_{mn}(\omega)$ satisfies the following commutation relations between H_{ex} as:

$$[H_{\mathrm{ex}}, A_m^X(\omega)] = -\omega A_m^X(\omega) \tag{I.2.53}$$

$$\left[H_{\mathrm{ex}}, A_m^{X\dagger}(\omega)\right] = +\omega A_m^{X\dagger}(\omega). \tag{I.2.54}$$

The operators $A_{mn}^\dagger(\omega)$ and $A_{mn}(\omega)$ are called *eigenoperators* or *quantum jump operator*. From eqs. (I.2.53) and (I.2.54), following relations are obtained

$$\begin{aligned} &H_S(A_m^X(\omega)|\Psi_i\rangle) = (A_m^X(\omega)H_S - \omega A_m^X(\omega))|\Psi_i\rangle \\ &= (E_i - \omega)(A_m^X(\omega)|\Psi_i\rangle) \end{aligned} \tag{I.2.55}$$

$$\begin{aligned} &H_S(A_m^{X\dagger}(\omega)|\Psi_i\rangle) = (A_m^{X\dagger}(\omega)H_S + \omega A_m^{X\dagger}(\omega))|\Psi_i\rangle \\ &= (E_i + \omega)(A_m^{X\dagger}(\omega)|\Psi_i\rangle). \end{aligned} \tag{I.2.56}$$

These equations indicate that $A_{mn}^\dagger(\omega)$ and $A_{mn}(\omega)$ is the operators that lowers/raises the energy of the system by ω. The eigenoperators also satisfy following relations:

$$\left[H_{\mathrm{ex}}, A_m^{X\dagger}(\omega) A_m^X(\omega)\right] = \left[H_{\mathrm{ex}}, A_m^X(\omega) A_m^{X\dagger}(\omega)\right] = 0. \tag{I.2.57}$$

By using eqs. (I.2.44) and (I.2.45), and inserting $X = H_{\mathrm{S}}$ and $Y = A_m^X(\omega)$ to the Baker-Campbell-Hausdorff's formula:

$$e^X Y e^{-X} = Y + [X, Y] + \frac{1}{2!}\left[X, [X, Y]\right] + + \frac{1}{3!}\left[X, \left[X, [X, Y]\right]\right] \cdots, \tag{I.2.58}$$

the corresponding I.P. operators of $A_m^X(\omega)$ and $A_m^{X\dagger}(\omega)$ take the form

$$e^{iH_{\mathrm{S}}t} A_m^X(\omega) e^{-iH_{\mathrm{S}}t} = e^{-i\omega t} A_m^X(\omega) \tag{I.2.59}$$

$$e^{iH_{\mathrm{S}}t} A_m^{X\dagger}(\omega) e^{-iH_{\mathrm{S}}t} = e^{i\omega t} A_m^{X\dagger}(\omega). \tag{I.2.60}$$

Furthermore, according to eqs. (I.2.55) and (I.2.56), we note that

$$A_m^{X\dagger}(\omega) = A_m^X(-\omega). \tag{I.2.61}$$

Thus, the sum over all energy differences of eq. (I.2.61) results in

$$\sum_{\omega} A_m^X(\omega) = \sum_{\omega} A_m^{X\dagger}(\omega) = A_m^X \tag{I.2.62}$$

From eqs. (I.2.51) and (I.2.52), the interaction Hamiltonian (eq.(I.2.46)) is reformulated as

$$H_{\mathrm{ex-ph}}^X = \sum_{\omega}\sum_{m} A_m^X(\omega) \otimes B_m^X = \sum_{\omega}\sum_{m} A_m^{X\dagger}(\omega) \otimes B_m^{X\dagger} \tag{I.2.63}$$

and I.P. interaction Hamiltonian decomposed by eigenoperator is

$$\begin{aligned} H_I(t) &= e^{iH_{\mathrm{S}}t} e^{iH_{\mathrm{B}}t} \left(\sum_{X=\mathrm{H,P}} H_{\mathrm{ex-ph}}^X\right) e^{-iH_{\mathrm{B}}t} e^{-iH_{\mathrm{S}}t} \\ &= \sum_{X=\mathrm{H,P}} \sum_{\omega} \sum_{m} \left(e^{iH_{\mathrm{S}}t} A_m^X(\omega) e^{-iH_{\mathrm{S}}t}\right) \otimes \left(e^{iH_{\mathrm{B}}t} B_m^X e^{-iH_{\mathrm{B}}t}\right) \\ &= \sum_{X=\mathrm{H,P}} \sum_{\omega} \sum_{m} e^{-i\omega t} A_m^X(\omega) \otimes B_m^X(t) = \sum_{X=\mathrm{H,P}} \sum_{\omega} \sum_{m} e^{i\omega t} A_m^{X\dagger}(\omega) \otimes B_m^{X\dagger}(t) \end{aligned} \tag{I.2.64}$$

where $B_m^X(t)$ is bath operator in the I.P. form, which is reformulated by using eqs. (I.2.42), (I.2.44), (I.2.45), (I.2.49), and (I.2.58)

$$B_m^X(t) = e^{iH_{\mathrm{B}}t} B_m^X e^{-iH_{\mathrm{B}}t} = \sum_{p} \hbar\omega_{pm}^X \left(g_{pm}^X e^{-i\omega_{pm}^X t} b_{pm}^X + g_{pm}^{X*} e^{i\omega_{pm}^X t} b_{pm}^{X\dagger}\right). \tag{I.2.65}$$

Inserting the form (I.2.64) into the TCL-QME (eq. (I.2.34)), we obtain

$$\begin{aligned} \frac{\partial \tilde{\rho}_{\mathrm{S}}(t)}{\partial t} = -\int_0^t ds \mathrm{tr}_{\mathrm{B}}\{ & H_{\mathrm{I}}(t) H_{\mathrm{I}}(t-s) \tilde{\rho}_{\mathrm{S}}(t) \otimes \rho_{\mathrm{B}} - H_{\mathrm{I}}(t) \tilde{\rho}_{\mathrm{S}}(t) \otimes \rho_{\mathrm{B}} H_{\mathrm{I}}(t-s) \\ & - H_{\mathrm{I}}(t-s) \tilde{\rho}_{\mathrm{S}}(t) \otimes \rho_{\mathrm{B}} H_{\mathrm{I}}(t) + \tilde{\rho}_{\mathrm{S}}(t) \otimes \rho_{\mathrm{B}} H_{\mathrm{I}}(t-s) H_{\mathrm{I}}(t)\} \end{aligned}$$

$$= \int_0^t ds \mathrm{tr}_{\mathrm{B}}\{H_{\mathrm{I}}(t-s)\tilde{\rho}_{\mathrm{S}}(t) \otimes \rho_{\mathrm{B}} H_{\mathrm{I}}(t) - H_{\mathrm{I}}(t) H_{\mathrm{I}}(t-s)\tilde{\rho}_{\mathrm{S}}(t) \otimes \rho_{\mathrm{B}}\} + h.c. \tag{I.2.66}$$

and

$$(1^{st}\ term) = \int_0^t \mathrm{dstr}_{\mathrm{B}}\{H_{\mathrm{I}}(t-s)\tilde{\rho}_{\mathrm{S}}(t) \otimes \rho_{\mathrm{B}} H_{\mathrm{I}}(t)\}$$

$$= \sum_X \sum_{\omega,\omega'} \sum_{m,n} \int_0^t \mathrm{d}s e^{-i\omega'(t-s)} A_n^X(\omega')\tilde{\rho}_{\mathrm{S}}(t) e^{i\omega t} A_m^{X\dagger}(\omega) \mathrm{tr}_{\mathrm{B}}\left\{B_n^X(t-s)\rho_{\mathrm{B}} B_m^{X\dagger}(t)\right\}$$

$$= \sum_X \sum_{\omega,\omega'} \sum_{m,n} e^{-i(\omega'-\omega)t} A_n^X(\omega')\tilde{\rho}_{\mathrm{S}}(t) A_m^{X\dagger}(\omega) \int_0^t \mathrm{d}s e^{i\omega' s} \mathrm{tr}_{\mathrm{B}}\left\{B_m^{X\dagger}(t) B_n^X(t-s)\rho_{\mathrm{B}}\right\}$$

$$= \sum_X \sum_{\omega,\omega'} \sum_{m,n} e^{-i(\omega'-\omega)t} \Gamma_{mn}^X(\omega',t) A_n^X(\omega')\tilde{\rho}_{\mathrm{S}}(t) A_m^{X\dagger}(\omega) \tag{I.2.67}$$

$$\left(2^{nd}\ term\right) = -\int_0^t \mathrm{dstr}_{\mathrm{B}}\{H_{\mathrm{I}}(t) H_{\mathrm{I}}(t-s)\tilde{\rho}_{\mathrm{S}}(t) \otimes \rho_{\mathrm{B}}\}$$

$$= -\sum_X \sum_{\omega,\omega'} \sum_{m,n} \int_0^t \mathrm{d}s e^{i\omega t} A_m^{X\dagger}(\omega) e^{-i\omega'(t-s)} A_n^X(\omega')\tilde{\rho}_{\mathrm{S}}(t) \mathrm{tr}_{\mathrm{B}}\left\{B_m^{X\dagger}(t) B_n^X(t-s)\rho_{\mathrm{B}}\right\}$$

$$= -\sum_X \sum_{\omega,\omega'} \sum_{m,n} e^{-i(\omega'-\omega)t} A_m^{X\dagger}(\omega) A_n^X(\omega')\tilde{\rho}_{\mathrm{S}}(t) \int_0^t \mathrm{d}s e^{i\omega' s} \mathrm{tr}_{\mathrm{B}}\left\{B_m^{X\dagger}(t) B_n^X(t-s)\rho_{\mathrm{B}}\right\}$$

$$= -\sum_X \sum_{\omega,\omega'} \sum_{m,n} e^{-i(\omega'-\omega)t} \Gamma_{mn}^X(\omega',t) A_m^{X\dagger}(\omega) A_n^X(\omega')\tilde{\rho}_{\mathrm{S}}(t) \tag{I.2.68}$$

with scalar functions $\Gamma_{mn}^X(\omega',t)$ being as follows

$$\Gamma_{mn}^X(\omega',t) = \int_0^t \mathrm{d}s e^{i\omega' s} \mathrm{tr}_{\mathrm{B}}\left\{B_m^{X\dagger}(t) B_n^X(t-s)\rho_{\mathrm{B}}\right\}. \tag{I.2.69}$$

The $\Gamma_{mn}^X(\omega',t)$ is one-sided Fourier transform of bath correlation functions. The bath correlation functions are defined as

$$C_{mn}(t_1 - t_2) \equiv \left\langle B_m^{X\dagger}(t_1) B_n^X(t_2)\right\rangle_{\mathrm{eq}} \equiv \mathrm{tr}_{\mathrm{B}}\left\{B_m^{X\dagger}(t_1) B_n^X(t_2)\rho_{\mathrm{B}}\right\}. \tag{I.2.70}$$

When we consider that ρ_{B} is a thermal distribution of the bath, that is $[H_B, \rho_B] = 0$. Thus, the bath correlation functions are then homogeneous in time:

$$C_{mn}(s) = \left\langle B_m^{X\dagger}(t) B_n^X(t-s) \right\rangle_{\mathrm{eq}} = \left\langle B_m^{X\dagger}(s) B_n^X(0) \right\rangle_{\mathrm{eq}}. \tag{I.2.71}$$

Then, the QME is simplified as following relation

$$\frac{\partial \tilde{\rho}_{\mathrm{S}}(t)}{\partial t} = \sum_X \sum_{\omega,\omega'} \sum_{m,n} e^{-i(\omega'-\omega)t} \Gamma_{mn}^X(\omega', t) \left\{ A_n^X(\omega') \tilde{\rho}_{\mathrm{S}}(t) A_m^{X\dagger}(\omega) - A_m^{X\dagger}(\omega) A_n^X(\omega') \tilde{\rho}_{\mathrm{S}}(t) \right\} + h.c. \tag{I.2.72}$$

Here, we perform the secular approximation, which is referred to as the omission of all the terms with $\omega' \neq \omega$. To explain this approximation, we denote by $\tau_{\mathrm{S}} = |\omega' - \omega|^{-1}$ the typical timescale of the intrinsic evolution of the system which make $\tilde{\rho}_{\mathrm{S}}(t)$ oscillating with a period of τ_{S} as denoted by $e^{-i(\omega'-\omega)t}$ in eq. (I.2.72). On the other hand, the time scale of the relaxation, τ_{R}, is decided by the exciton-phonon coupling. In secular approximation, we consider that the relaxation time τ_{R} is much slower than the oscillation associated withand non-secular term with $\omega' \neq \omega$ can be averaged out in eq. (I.2.72) oscillate very rapidly during the time τ_{R}. Thus, we have

$$\frac{\partial \tilde{\rho}_{\mathrm{S}}(t)}{\partial t} = \sum_X \sum_{\omega} \sum_{m,n} \Gamma_{mn}^X(\omega, t) \left\{ A_n^X(\omega) \tilde{\rho}_{\mathrm{S}}(t) A_m^{X\dagger}(\omega) - A_m^{X\dagger}(\omega) A_n^X(\omega) \tilde{\rho}_{\mathrm{S}}(t) \right\} + h.c. \tag{I.2.73}$$

It is convenient to decompose the Fourier transformed bath correlation functions $\Gamma_{mn}^X(\omega', t)$ by their real part and imaginary part as follows

$$\Gamma_{mn}^X(\omega, t) = \frac{1}{2} \gamma_{mn}(\omega) + i S_{mn}(\omega) \tag{I.2.74}$$

with

$$\gamma_{mn}(\omega) = 2\mathrm{Re}\left(\Gamma_{mn}^X(\omega, t)\right) = \Gamma_{mn}^X(\omega, t) + \Gamma_{mn}^{X*}(\omega, t) \tag{I.2.75}$$

and

$$S_{mn}(\omega) = \mathrm{Im}(\Gamma_{mn}^X(\omega, t)) = \frac{1}{2i}\{\Gamma_{mn}^X(\omega, t) - \Gamma_{mn}^{X*}(\omega, t)\}. \tag{I.2.76}$$

With these definitions, the obtain the following form

$$\begin{aligned} \frac{\partial \tilde{\rho}_{\mathrm{S}}(t)}{\partial t} &= \sum_X \sum_{\omega} \sum_{m,n} \left[\frac{1}{2}\gamma_{mn}(\omega) + i S_{mn}(\omega)\right] \left[A_n^X(\omega) \tilde{\rho}_{\mathrm{S}}(t) A_m^{X\dagger}(\omega) - A_m^{X\dagger}(\omega) A_n^X(\omega) \tilde{\rho}_{\mathrm{S}}(t)\right] \\ &\quad + \sum_X \sum_{\omega} \sum_{m,n} \left[\frac{1}{2}\gamma_{mn}(\omega) - i S_{mn}(\omega)\right] \left[A_m^X(\omega) \tilde{\rho}_{\mathrm{S}}(t) A_n^{X\dagger}(\omega) - \tilde{\rho}_{\mathrm{S}}(t) A_n^{X\dagger}(\omega) A_m^X(\omega)\right] \\ &= -i[H_{\mathrm{LS}}(t), \tilde{\rho}_{\mathrm{S}}(t)] + \sum_X \sum_{\omega} \sum_{m,n} \gamma_{mn}^X(\omega, t) \left[A_n^X(\omega) \tilde{\rho}_{\mathrm{S}}(t) A_m^{X\dagger}(\omega) - \frac{1}{2}\left\{A_m^{X\dagger}(\omega) A_n^X(\omega), \tilde{\rho}_{\mathrm{S}}(t)\right\}\right] \end{aligned} \tag{I.2.77}$$

where $H_{\mathrm{LS}}(t)$ is defined as

$$H_{\mathrm{LS}}(t) \equiv \sum_{X}\sum_{\omega}\sum_{m,n} S_{mn}(\omega) A_m^{X\dagger}(\omega) A_n^X(\omega) \tag{I.2.78}$$

which is known as the *Lamb-shift Hamiltonian* since it leads to a Lamb-type renormalization of the coherent oscillation frequencies induced by the system-bath coupling. This term is negligible because it does not bring intrinsic change to the relaxation dynamics. Furthermore, we assume that the diagonal relaxation function $\gamma_{mn}^X(\omega,t) = \delta_{mn}\gamma_m^X(\omega,t)$, which means that we consider only the aitocorrelation function for the bath and $A_n^X(\omega)$ interacts individually with its own set of the phonon bath. By transforming QME in interaction picture into Schrödinger picture, eq. (77) becomes

$$\begin{aligned}\frac{\partial \rho_S(t)}{\partial t} &= -i[H_S, \rho_S(t)] \\ &+ \sum_X \sum_\omega \sum_m \gamma_m^X(\omega,t)\left[A_m^X(\omega)\rho_{\mathrm{S}}(t)A_m^{X\dagger}(\omega) - \frac{1}{2}\left\{A_m^{X\dagger}(\omega)A_m^X(\omega), \rho_{\mathrm{S}}(t)\right\}\right].\end{aligned} \tag{I.2.79}$$

This is the working equation for solving time-evolution of RDM of exciton states. In the eq. (I.2.79), the first term is unitary time-evolution of system density matrix and the second term is called dissipation part in sense that the equation of motion becomes identical to the LvN equation if there were no system-bath coupling which provoke the system relaxation.

2.3. Spectral Density for Vibronic Coupling

2.3.1 *Spectral Density*

According to the eq. (I.2.75), the relaxation rate $\gamma_m^X(\omega,t)$ in eq. (I.2.79) is represented as the Fourier transformation of the self-time-correlation function of system-bath coupling, which is called bath correlation function. The bath correlation function is denoted as follows:

$$C_m(\tau) = \left\langle B_m^{X\dagger}(\tau) B_m^X(0)\right\rangle_{\mathrm{eq}} = \mathrm{tr}_{\mathrm{B}}\left\{B_m^{X\dagger}(\tau)B_m^X(0)\rho_{\mathrm{B}}\right\} \tag{I.2.80}$$

By inserting eq. (I.2.49) and eq. (I.2.65), the eq. (I.2.80) gives

$$C_m(\tau) = \mathrm{tr}_{\mathrm{B}}\left\{\sum_{p,q} \hbar^2 \omega_{pm}^X \omega_{qm}^X \left(g_{pm}^X e^{-i\omega_{pm}^X t} b_{pm}^X + g_{pm}^{X*} e^{i\omega_{pm}^X t} b_{pm}^{X\dagger}\right)\left(g_{qm}^X b_{qm}^X + g_{qm}^{X*} b_{qm}^{X\dagger}\right)\rho_{\mathrm{B}}\right\} \tag{I.2.81}$$

When we assume that the coupling constant is real,

$$C_m(\tau) = \mathrm{tr}_{\mathrm{B}} \left\{ \sum_{p,q} \hbar^2 \omega^X_{pm} \omega^X_{qm} g^X_{pm} g^X_{qm} \left(e^{-i\omega^X_{pm}t} b^X_{pm} + e^{i\omega^X_{pm}t} b^{X\dagger}_{pm} \right) \left(b^X_{qm} + b^{X\dagger}_{qm} \right) \rho_{\mathrm{B}} \right\}. \tag{I.2.82}$$

According to the Broch-de Dominicis theorem, the value of $\langle b^X_{pm} b^X_{pm} \rangle_{eq}$, $\langle b^{X\dagger}_{pm} b^{X\dagger}_{qm} \rangle_{eq}$, $\langle b^{X\dagger}_{pm} b^X_{qm} \rangle_{eq}$, and $\langle b^X_{pm} b^{X\dagger}_{qm} \rangle_{eq}$ are formulated as

$$\langle b^X_{pm} b^X_{pm} \rangle_{eq} = \langle b^{X\dagger}_{pm} b^{X\dagger}_{qm} \rangle_{eq} = 0 \tag{I.2.83}$$

$$\langle b^{X\dagger}_{pm} b^X_{qm} \rangle_{eq} = \delta_{pq} n_B(\omega^X_{pm}, T) \tag{I.2.84}$$

$$\langle b^X_{pm} b^{X\dagger}_{qm} \rangle_{eq} = \delta_{pq} \left(1 - n_B(\omega^X_{pm}, T)\right) \tag{I.2.85}$$

where $n_B(\omega, T) = \left(e^{\beta\hbar\omega} - 1\right)^{-1}$ is the Bose-Einstein distribution function $n_B(\omega, T) = \left(e^{\beta\hbar\omega} - 1\right)^{-1}$ at temperature T and inverse temperature $\beta = 1/k_B T$ with the Boltzmann constant k_B. Then, the bath correlation $C_m(\tau)$ becomes

$$C_m(\tau) = \sum_p \hbar^2 \left(\omega^X_{pm}\right)^2 \left(g^X_{pm}\right)^2 \left(e^{-i\omega^X_{pm}t} \left(1 - n_B(\omega^X_{pm}, T)\right) + e^{i\omega^X_{pm}t} n_B(\omega^X_{pm}, T) \right) \tag{I.2.86}$$

By using the definition of the Dirac delta function, eq. (I.2.86) is written as

$$C_m(\tau) = \int_0^\infty \mathrm{d}\omega' \sum_p \hbar^2 \left(\omega^X_{pm}\right)^2 \left(g^X_{pm}\right)^2 \delta\left(\omega' - \omega^X_{pm}\right) \left(e^{-i\omega' t} (1 - n_B(\omega', T)) + e^{i\omega' t} n_B(\omega', T) \right). \tag{I.2.87}$$

Let us introduce the spectral density function $J^X_m(\omega)$ defined as

$$J^X_m(\omega) = \sum_p \hbar^2 \left(\omega^X_{pm}\right)^2 \left(g^X_{pm}\right)^2 \delta\left(\omega' - \omega^X_{pm}\right). \tag{I.2.88}$$

The bath correlation function $C_m(\tau)$ becomes

$$C_m(\tau) = \int_0^\infty \mathrm{d}\omega' J^X_m(\omega) \left(e^{-i\omega' t} (1 - n_B(\omega', T)) + e^{i\omega' t} n_B(\omega', T) \right) \tag{I.2.89}$$

and relaxation rate $\gamma^X_m(\omega, t)$ is rewritten from eq. (I.2.75) as

$$\gamma^X_m(\omega) = 2\mathrm{Re} \left[\int_0^t \mathrm{d}\tau e^{i\omega\tau} \int_0^\infty \mathrm{d}\omega' J^X_m(\omega') \left(e^{-i\omega' t} \left(1 - n_B(\omega', T)\right) + e^{i\omega' t} n_B(\omega', T) \right) \right]$$

$$= \int_0^{\infty} \mathrm{d}\omega' J_m^X(\omega') \left(\frac{\sin(\omega - \omega')t}{\omega - \omega'} \left(1 - n_B(\omega', T)\right) + \frac{\sin(\omega + \omega')t}{\omega + \omega'} e^{i\omega' t} n_B(\omega', T) \right). \tag{I.2.90}$$

This equation indicates that the relaxation rate is obtained from the spectral density function. However, in order to describe the irreversible dynamics of the non-equilibrium open quantum system interacting with bath, the spectral density should be modeled as a continuous function rather than a discrete function such as eq. (I.2.88). Several other forms of spectral density have been proposed. For example, the Ohmic formula with Lorentz-Drude cutoff is frequently used[2], which is defined as

$$J_m^X(\omega, T) = \frac{1}{\hbar\pi} \frac{2\lambda_m^X \Omega_m^X \omega}{\omega^2 + (\Omega_m^X)^2}. \tag{I.2.91}$$

where λ_m and Ω_m are the phenomenological parameters called the total reorganization energy and the cut-off frequency, respectively. The total reorganization energy and the spectral density satisfy the following relation:

$$\lambda_m^X = \hbar \int_0^{\infty} \mathrm{d}\omega \frac{J_m^X(\omega, T)}{\omega}. \tag{I.2.92}$$

and eq. (I.2.91) indicates that the vibronic coupling has a peak value of λ_m^X/π at $\omega = \Omega_m$.

By applying the Markov approximation ($t \to \infty$), the relaxation rate $\gamma_m^X(\omega)$ becomes

$$\gamma_m^X(\omega) \xrightarrow[t\to\infty]{} 2\mathrm{Re}\left[\int_0^{\infty} \mathrm{d}\tau \int_0^{\infty} \mathrm{d}\omega' J_m^X(\omega') \left(e^{i(\omega-\omega')t}\left(1 - n_B(\omega', T)\right) + e^{i(\omega+\omega')t} n_B(\omega', T) \right) \right]. \tag{I.2.93}$$

Using the relation between the delta function, the Cauchy's principal value and the integral of exponential function as

$$\int_0^{\infty} d\tau e^{\pm i\Omega\tau} = \pi\delta(\Omega) \pm i\mathrm{P.v.}\left(\frac{1}{\Omega}\right), \tag{I.2.94}$$

the eq. (I.2.93) is calculated as

$$\begin{aligned} \gamma_m^X(\omega) \xrightarrow[t\to\infty]{} 2\pi\mathrm{Re}&\left[\int_0^{\infty} \mathrm{d}\omega' J_m^X(\omega') \left(\delta(\omega - \omega')\left(1 - n_B(\omega', T)\right) + \delta(\omega + \omega') n_B(\omega', T) \right) \right] \\ &= \begin{cases} 2\pi J_m^X(\omega)\left(1 - n_B(\omega, T)\right) & (\omega > 0) \\ 2\pi J_m^X(-\omega) n_B(-\omega, T) & (\omega > 0) \\ \lim\limits_{\omega' \to 0} \pi J_m^X(\omega')[2n_B(\omega', T) + 1] & (\omega = 0) \end{cases} \end{aligned} \tag{I.2.95}$$

When we consider the Ohmic spectral density with Lorentz-Drude cutoff (eq. (I.2.91)), the $\gamma_m^X(\omega)$ at $\omega = 0$ become

$$\gamma_m^X(0) = \frac{4\lambda_m^X k_B T}{\hbar^2 \Omega_m^X}. \tag{I.2.96}$$

By using eqs. (I.2.79) and (I.2. 96), we can derive the working equation of the quantum master equation described in the following section.

2.3.2 Practical Imprementation of VCCs

In practical simulation of SF dynamics, the VCC parameters, which are represented as reorganization energy λ_m and cut-off frequency Ω_m, are set as 50 and 180 meV for each mode, respectively, which is obtained from Girland et al. performed by semi-empirical calculation.[3] This also approximates state independent spectral density. Moreover, we only consider Holstein coupling because the magnitudes of Peierls coupling (VCCs on off-diagonal Hamiltonian) is only about one-tenth and negligible.[3,4] This approximation is suitable because our interest in this study is on the influence of electronic structure dependent on molecular aggregate structures on the SF dynamics, and the selection of VCC parameters is expected to have small effect on the general trends of structure–property correlations. However, in this section, we discuss the systematic differences in outcomes that arise from the choice of VCC parameters.

Nagami et al. have analyzed state dependent VCC parameters in crystalline pentacene and explained the trends of VCC peaks[5] by utilizing vibronic coupling density proposed by Sato et al. which is one of method to clarify the structural origin of VCC values.[6] They clarified that VCCs for Holstein coupling CT states and Peierls coupling was contributed by the low-frequency normal modes (under 250 cm^{-1}). This possibly enhance transition between adiabatic states with small energy gap. Especially, it is suggested to be important to consider Peierls coupling to explain SF in crystalline rubrene, where two molecules are arranged with face-to-face structure.[7] However, Peierls coupling is much smaller than Holstein coupling and electronic couplings, and the change of them is expected to have small impact on general trends of SF dynamics.

2.4. Relative Relaxation Factor

2.4.1 Adiabatic population dynamics of QME

In order to numerically solve eq. (I.2.79), the time-evolution of the matrix elements of RDM ρ_{pq} is obtained by acting adiabatic states (eigenvector of the system Hamiltonian) $\langle\psi_p|$ and $|\psi_q\rangle$ from the left-hand and right-hand side, respectively.

$$\begin{aligned}
\frac{\partial}{\partial t}\rho_{pq}(t) &= \frac{\partial}{\partial t}\langle\psi_p|\rho_S(t)|\psi_q\rangle \\
&= -i\langle\psi_p|[H_S,\rho_S(t)]|\psi_q\rangle \\
&+\sum_X\sum_\omega\sum_m \gamma_m^X(\omega,t)\left[\langle\psi_p|A_m^X(\omega)\rho_{\mathrm{S}}(t)A_m^{X\dagger}(\omega)|\psi_q\rangle-\frac{1}{2}\left\langle\psi_p\middle|A_m^{X\dagger}(\omega)A_m^X(\omega)\rho_{\mathrm{S}}(t)\middle|\psi_q\right\rangle\right. \\
&\left.-\frac{1}{2}\left\langle\psi_p\middle|\rho_{\mathrm{S}}(t)A_m^{X\dagger}(\omega)A_m^X(\omega)\middle|\psi_q\right\rangle\right]
\end{aligned}$$

(I.2.97)

The first term in eq. (I.2.80) is

$$\begin{aligned}-i\langle\psi_p|[H_S,\rho_S(t)]|\psi_q\rangle &= -i\langle\psi_p|H_S\rho_S(t)-\rho_S(t)H_S|\psi_q\rangle = -i\langle\psi_p|E_p\rho_S(t)-\rho_S(t)E_q|\psi_q\rangle \\ &= -i(E_p-E_q)\langle\psi_p|\rho_S(t)|\psi_q\rangle = -i\omega_{pq}\rho_{pq}(t)\end{aligned} \tag{I.2.98}$$

where $\omega_{pq} \equiv E_p - E_q$ is energy gap between p'th and q'th adiabatic states and used eq. (I.2.40). Because a set of eigenvectors consist of the complete basis set, the completeness relation $\sum_i |\psi_i\rangle\langle\psi_i| = 1$ holds. The matrix element of quantum jump operator $A_m^X(\omega)$ of Holstein coupling term becomes

$$\begin{aligned}\langle\psi_p|A_m^{\mathrm{H}}(\omega)|\psi_q\rangle &= \sum_{\substack{\alpha,\beta \\ (E_\alpha-E_\beta=\omega)}} C_{m\alpha}^*C_{m\beta}\langle\psi_p|\psi_\alpha\rangle\langle\psi_\beta|\psi_q\rangle \\ &= C_{mp}^*C_{mq}\delta(\omega-\omega_{pq}),\end{aligned} \tag{I.2.99}$$

$$\langle\psi_p|A_m^{\mathrm{H}\dagger}(\omega)|\psi_q\rangle = C_{mp}^*C_{mq}\delta(\omega-\omega_{qp}) \tag{I.2.100}$$

and that of Peierls coupling term become

$$\begin{aligned}\langle\psi_p|A_m^{\mathrm{P}}(\omega)|\psi_q\rangle &= \sum_{\substack{\alpha,\beta \\ (E_\alpha-E_\beta=\omega)}} C_{m'\alpha}^*C_{n'\beta}\langle\psi_p|\psi_\alpha\rangle\langle\psi_\beta|\psi_q\rangle \\ &= C_{m'p}^*C_{n'q}\delta(\omega-\omega_{pq}).\end{aligned} \tag{I.2.101}$$

$$\langle\psi_p|A_m^{\mathrm{P}\dagger}(\omega)|\psi_q\rangle = C_{m'p}^*C_{n'q}\delta(\omega-\omega_{qp}) \tag{I.2.102}$$

The $C_{m\alpha}$ is the expansion coefficients of m'th diabatic states in α'th adiabatic states. By applying these relations, the eq. (I.2.80) is rewritten by the coefficients of adiabatic states under diabatic representation, which is the working equation of the QME for obtaining the time-evolution of the RDM elements under adiabatic representation as follows:

$$\begin{aligned}\frac{\partial}{\partial t}\rho_{pq}(t) &= -i\omega_{pq}\rho_{pq}(t) \\ &+\sum_m\sum_\omega \gamma_m^{\mathrm{H}}(\omega,t)\left[\sum_{\substack{r,s \\ \omega_{pr}=\omega_{qs}=\omega}} C_{mp}^*C_{mr}C_{mq}C_{ms}^*\rho_{rs}(t)\right. \\ &\qquad\left. -\frac{1}{2}\left\{\sum_{\substack{r,s \\ \omega_{rp}=\omega_{rs}=\omega}} |C_{mr}|^2C_{ms}C_{mp}^*\rho_{sq}(t) + \sum_{\substack{r,s \\ \omega_{sr}=\omega_{sq}=\omega}} |C_{mr}|^2C_{mq}C_{ms}^*\rho_{ps}(t)\right\}\right]\end{aligned}$$

$$+\sum_{m=(m',n')}\sum_{\omega}\gamma_m^{\mathrm{P}}(\omega,t)\left[\sum_{\substack{r,s\\ \omega_{pr}=\omega_{qs}=\omega}} C_{m'p}^{*}C_{n'r}C_{m'q}C_{n's}^{*}\rho_{rs}(t)\right.$$

$$\left.-\frac{1}{2}\left\{\sum_{\substack{r,s\\ \omega_{rp}=\omega_{rs}=\omega}}|C_{m'r}|^2C_{n's}C_{n'p}^{*}\rho_{sq}(t)+\sum_{\substack{r,s\\ \omega_{sr}=\omega_{sq}=\omega}}|C_{m'r}|^2C_{n'q}C_{n's}^{*}\rho_{ps}(t)\right\}\right]. \tag{I.2.103}$$

Note here that the summation over *m* is taken as the pair of the index of the diabatic states (*m'*, *n'*). The first term of this equation indicates the origin of quantum beating oscillating with the frequency $\omega_{pq} = E_p - E_q$, which express the coherent dynamics between the states p and q. The second and the third terms express the relaxation and the decoherence part of the quantum system due to the Holstein and the Peierls coupling, respectively. Then, the time-evolution of the *p*'th adiabatic population $\rho_{pp}(t)$ is formulated as

$$\frac{\partial}{\partial t}\rho_{pp}(t) = -\sum_{q}\left[\delta_{pq}\sum_{m}\sum_{r}\left|C_{mp}\right|^2|C_{mr}|^2\gamma_m^{\mathrm{H}}(\omega_{pr},t) - \sum_{m}\left|C_{mp}\right|^2\left|C_{mq}\right|^2\gamma_m^{\mathrm{H}}(\omega_{pq},t)\right]\rho_{qq}(t)$$

$$-\sum_{q}\left[\delta_{pq}\sum_{m=(m',n')}\sum_{r}\left|C_{m'p}\right|^2|C_{n'r}|^2\gamma_m^{\mathrm{P}}(\omega_{pr},t) - \sum_{m=(m',n')}\left|C_{m'p}\right|^2\left|C_{n'q}\right|^2\gamma_m^{\mathrm{P}}(\omega_{pq},t)\right]\rho_{qq}(t) \tag{I.2.104}$$

This equation is interpreted as the kinetic rate equation of the adiabatic population. Then, when the rate constant of the transition from the state q to the state p is denoted by the $\Gamma_{pq}^{\mathrm{H}}(t)$ and $\Gamma_{pq}^{\mathrm{P}}(t)$, the QME takes the form:

$$\frac{\partial}{\partial t}\rho_{pp}(t) = -\sum_{q}\left[\Gamma_{pq}^{\mathrm{H}}(t) + \Gamma_{pq}^{\mathrm{P}}(t)\right]\rho_{qq}(t) \tag{I.2.105}$$

with

$$\Gamma_{pq}^{\mathrm{H}}(t) = \delta_{pq}\sum_{m}\sum_{r}\left|C_{mp}\right|^2|C_{mr}|^2\gamma_m^{\mathrm{H}}(\omega_{pr},t) - \sum_{m}\left|C_{mp}\right|^2\left|C_{mq}\right|^2\gamma_m^{\mathrm{H}}(\omega_{pq},t) \tag{I.2.106}$$

and

$$\Gamma_{pq}^{\mathrm{P}}(t) = \delta_{pq}\sum_{m=(m',n')}\sum_{r}\left|C_{m'p}\right|^2|C_{n'r}|^2\gamma_m^{\mathrm{P}}(\omega_{pr},t)$$

$$-\sum_{m=(m',n')}\left|C_{m'p}\right|^2\left|C_{n'q}\right|^2\gamma_m^{\mathrm{P}}(\omega_{pq},t) \tag{I.2.107}$$

<u>2.4.2 Relative relaxation factor analysis</u>

In general, the relaxation dynamics simulation of SF in molecular aggregate systems includes many excitonic states. It is convenient to compare the contribution of each state-to-state relaxation path, which is conducted by relative relaxation factor (RRF) analysis produced by Nakano and coworkers.[8,9] The population RRF between adiabatic states p and q is defined by the difference of relaxation factors between $p \rightarrow q$ and $q \rightarrow p$ relaxation paths as follows.

$$\Delta\Gamma_{pq} = \Delta\Gamma_{pq}^{\mathrm{H}} + \Delta\Gamma_{pq}^{\mathrm{P}} \tag{I. 2.108}$$

where the Holstein coupling term denoted as $\Delta\Gamma_{pq}^{\mathrm{H}}$ is

$$\Delta\Gamma_{pq}^{\mathrm{H}} = \sum_{m} |C_{m\alpha}|^2 \left|C_{m\beta}\right|^2 \left[\gamma_m^{\mathrm{H}}(\omega_{pq}, t) - \gamma_m^{\mathrm{H}}(\omega_{\beta\alpha}, t)\right] \tag{I. 2.109}$$

and the Peierls coupling term denoted as $\Delta\Gamma_{pq}^{\mathrm{P}}$ is

$$\Delta\Gamma_{pq}^{\mathrm{P}} = \sum_{m=(m',n')} |C_{m'\alpha}|^2 \left|C_{n'\beta}\right|^2 \left[\gamma_m^{\mathrm{P}}(\omega_{pq}, t) - \gamma_m^{\mathrm{P}}(\omega_{\beta\alpha}, t)\right]. \tag{I. 2.110}$$

Since RRF is defined by the difference between the pre-coefficients of $\rho_{pp}(t)$ and $\rho_{qq}(t)$, it corresponds to the net relaxation rate for the $p \rightarrow q$ transition when these states have the same population quantity. As seen from these equations, the total RRF consists of the product of the diabatic configurations in the adiabatic states ($|C_{m\alpha}|^2 \left|C_{m\beta}\right|^2$ and $|C_{m'\alpha}|^2 \left|C_{n'\beta}\right|^2$) and the vibronic coupling effects $\gamma_m^X(\omega_{pq}, t) - \gamma_m^X(\omega_{\beta\alpha}, t)$. Since $|C_{m\alpha}|^2 \left|C_{m\beta}\right|^2$ is referred as the exciton overlap terms, the RRF is related to the contribution of diabatic states in each adiabatic state for the Holstein coupling. In Markovian approximation, the relaxation rate $\gamma_m^X(\omega_{pq}, t)$ becomes independent of time. We show the distribution of $J_m^X(\omega, T)$, $\gamma_m^X(\omega_{pq}, t)$, and $[\gamma_m(\omega_{pq}) - \gamma_m(\omega_{qp})]$ in **Figure I.2.2** with reorganization energy $\lambda = 50$ meV, cut-off frequency $\Omega_c = 180$ meV, and temperature $T = 300$ K. In conclusion, RRF is a powerful tool to interpret the results from the quantum dynamics simulation by QME approach by individually discussing the contribution of the Holstein and Peierls terms, exciton (electron) wavefunction and exciton-phonon coupling factor.

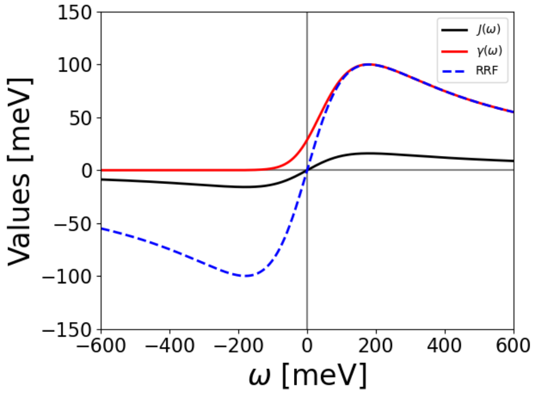

Figure I.2.2. Plots of $\boldsymbol{J_m^X(\omega, T)}$, $\boldsymbol{\gamma_m^X(\omega_{pq})}$, and RRF ($\boldsymbol{[\gamma_m(\omega_{pq}) - \gamma_m(\omega_{qp})]}$) with ($\boldsymbol{\lambda}$, $\boldsymbol{\Omega_c}$) = (50, 180) meV with temperature being 300 K.

References

(1) H. P. Breuer and F. Petruccione, *The Theory of Open Quantum Systems*, Oxford University Press, Oxford, U.K., **2002**.

(2) G. Tao *J. Phys. Chem. C* **2014**, *118*, 27258−27264.

(3) A. Girlando, L. Grisanti, M. Masino, A. Brillante, R. G. Della Valle, E. Venuti *J. Chem. Phys.* **2011**, *135*, 084701.

(4) T. C. Berkelbach, M. C. Hybertsen, D. R. Reichman *J. Chem. Phys.* **2013**, *138*, 114102.

(5) T. Nagami, T. Takayoshi, K. Okada, W. Yoshida, H. Miyamoto, M. Nakano *J. Chem. Phys.* **2020**, *153*, 134302.

(6) T. Sato, K. Shizu, T. Kuga, K. Tanaka and H. Kaji, *Chem. Phys. Lett.*, **2008**, *458*, 152–156.

(7) K. Miyata, Y. Kurashige, K. Watanabe, et al. *Nature Chem.* **2017**, *9*, 983−989.

(8) M. Nakano, S. Ito, T. Nagami, Y. Kitagawa, T. Kubo, *J. Phys. Chem. C.* **2016**, *120*, 22803-22816.

(9) M. Takahata, M. Nakano, H. Fujita, K. Yamaguchi, *Chem. Phys. Lett.* **2002**, *363*, 422-428.

PART II

Structure–SF Dynamics Relationships for Efficient TT generation in Ring-Shaped Pentacene Molecular Aggregate Systems

Chapter 1.

Theoretical Study on Singlet Fission Dynamics in Symmetric H- and J- Ring-Shaped Aggregate Models

Using the quantum master equation method, we investigate size and monomer configuration dependences of singlet fission (SF) in pentacene J- and H-type ring-shaped aggregate (*N*-mer) models. Interestingly, it is found that SF rates in the J-aggregate models monotonically decrease with increasing *N*, while those in the H-aggregate models show different variation behaviors depending on the parity of *N*, where the H-type pentamer model exhibits the maximum SF rate. It is also found that correlated triplet-pair yields in the J-aggregate models rapidly increase from ~45 % toward 100 %, while those in the H-aggregate gradually decrease from ~96 % toward 0 %. These features are explained by relative relaxation factor analysis between adiabatic states and by the point group symmetry of the ring-shaped aggregate models. The present results contribute to a deeper understanding of the correlation between the aggregate size, monomer configuration and SF dynamics, and thus to constructing new design guidelines for highly efficient SF ring-shaped aggregates.

1. Introduction

As mentioned in the General Introduction, intermolecular interactions and aggregation topology are predicted to have great impact on SF. Recently, the SF mechanism of linear and ring-shaped aggregate models has been investigated by Nakano et al.[1] They focused on how the number of consisting molecules N and periodical structure of molecular aggregates affect the SF rate and TT yield, and it has been found that there exists an optimal aggregate size yielding the maximum SF rate. However, the variation in intermolecular electronic coupling depending on the size of aggregates has not been examined, though it is predicted to vary with aggregate size due to the change of relative configuration between the neighboring molecules. Furthermore, there are two types of ring-shaped aggregates defined as J- and H-type rings, where the intermolecular relative configuration between neighboring molecules approaches to the J- and H-type linear aggregates, and there have been no remarks on the difference of SF dynamics between these structures.

In this study, therefore, we investigate the dependences of SF rate and TT yield on the aggregate size (N) in two types of pentacene ring-shaped aggregate models (J- and H-type aggregates) using the quantum master equation (QME) method[1-3] with explicitly considered electronic couplings. Although these ring-shaped aggregate models are just theoretical systems, investigation of SF dynamics in such systems is important for revealing a novel structure–SF correlation and is intriguing since in photosynthetic systems, porphyrin ring-shaped aggregate models are known to play an essential role in their efficient energy transfer by Frenkel excitons.[4–6] Also, recently, new types of acene based molecules with ring-shaped configurations, pentacene based nanotubes, have been synthesized and found to exhibit SF with high quantum yields.[7] These findings are expected to stimulate interest in the study on SF in ring-shaped systems. The mechanism of the SF dynamics in the present ring-shaped aggregates is analyzed based on relative relaxation factor (RRF) analysis, which can clarify the primary SF pathways between adiabatic exciton states together with the origin of the relaxation rates.[1,8–10] Furthermore, we reveal the fundamental correlations between geometrical structure and SF efficiency more generally by examining the electronic couplings based on point group symmetry structures in ring-shaped aggregate models in comparison with the linear aggregate models. These results are expected to contribute to constructing more general and fundamental SF design guidelines for aggregate systems with various geometrical structures and size.

2. Model and Methods

2.1. *Model Structure*

Figure II.1.1 (a) shows the structure of J- and H-ring-shaped pentacene aggregate models, whose configurations are defined as being equal to the linear J- and H-aggregate models at the limit of infinite aggregate size ($N \to \infty$ in **Figure II.1.1(b)**). In these ring-shaped aggregate models, note that completely delocalized Frenkel exciton states have no net transition moments from the ground state, while in linear J- and H-aggregate models, the absorption spectra are red- and blue-shifted, respectively, as compared to that of monomer. Geometry optimization of pentacene monomer is performed at RB3LYP/cc-pVDZ level of approximation. We calculate the intermolecular electronic coupling using the pentacene dimer unit as shown in **Figure II.1.1(b)** with R = 3.7 Å and θ = 180°/N (in the J-aggregate) or 90°–180°/N (in the H-aggregate), where R indicates the intermolecular distance between the neighboring carbon atoms in the zigzag edges, and θ indicates the angle between the pentacene monomer plane and the longitudinal axis in parallel to the R direction.[1,9]

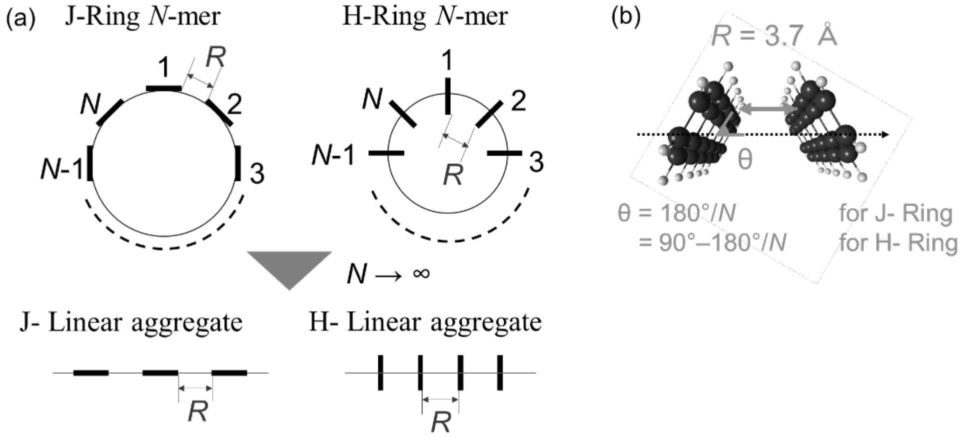

Figure II.1.1. (a) pentacene J- and H-type ring-shaped aggregate (N-mer) models. Infinite system with $N \to \infty$ corresponds to the J- and H-type linear aggregate systems. (b) substructure of dimer unit in ring-shaped aggregate model.

2.2. *Construction of Exciton Hamiltonian*

In order to perform SF dynamics simulation for molecular aggregates, we construct Hamiltonian in the diabatic representation. The total Hamiltonian is expressed as

$$H = H_{\mathrm{ex}} + H_{\mathrm{ph}} + H_{\mathrm{ex-ph}} \tag{II.1.1}$$

Here, H_{ex}, H_{ph}, and $H_{\mathrm{ex-ph}}$ are exciton, phonon bath, and exciton–phonon coupling Hamiltonian. Here, we consider only Holstein coupling and thus the latter two Hamiltonians are described as shown in eqs. (I.2.42) and (I.2.46) with X = H. In this section, we introduce the diabatic exciton basis representing FE, CT, and TT states as follows:

$$\{|m\rangle\} = \{|\mathrm{S_1S_0}\cdots\mathrm{S_0}\rangle \equiv |\mathrm{FE_1}\rangle, |\mathrm{S_0S_1}S_0\cdots\mathrm{S_0}\rangle \equiv |\mathrm{FE_2}\rangle, \cdots, |\mathrm{S_0S_0}\cdots\mathrm{S_1}\rangle \equiv |\mathrm{FE}_N\rangle,$$

$$|\mathrm{CAS_0}\cdots\mathrm{S_0}\rangle \equiv |\mathrm{CA_1}\rangle, |\mathrm{S_0CAS_0}\cdots\mathrm{S_0}\rangle \equiv |\mathrm{CA_2}\rangle, \cdots, |\mathrm{S_0}\cdots\mathrm{S_0CA}\rangle \equiv |\mathrm{CA}_{N-1}\rangle,\ |\mathrm{AS_0}\cdots\mathrm{S_0C}\rangle \equiv |\mathrm{CA}_N\rangle,$$

$$|\mathrm{ACS_0}\cdots\mathrm{S_0}\rangle \equiv |\mathrm{AC_1}\rangle, |\mathrm{S_0ACS_0}\cdots\mathrm{S_0}\rangle \equiv |\mathrm{AC_2}\rangle, \cdots, |\mathrm{S_0}\cdots\mathrm{S_0AC}\rangle \equiv |\mathrm{AC}_{N-1}\rangle,\ |\mathrm{CS_0}\cdots\mathrm{S_0A}\rangle \equiv |\mathrm{AC}_N\rangle,$$

$$|\mathrm{TTS_0}\cdots\mathrm{S_0}\rangle \equiv |\mathrm{TT_1}\rangle, |\mathrm{S_0TTS_0}\cdots\mathrm{S_0}\rangle \equiv |\mathrm{TT_2}\rangle, \cdots, |\mathrm{S_0}\cdots\mathrm{S_0TT}\rangle \equiv |\mathrm{TT}_{N-1}\rangle,\ |\mathrm{TS_0}\cdots\mathrm{S_0T}\rangle \equiv |\mathrm{TT}_N\rangle\}$$

$$\text{(II.1.2)}$$

Here, diabatic exciton bases $|\mathrm{AS_0}\cdots\mathrm{S_0C}\rangle$, $|\mathrm{CS_0}\cdots\mathrm{S_0A}\rangle$ and $|\mathrm{TS_0}\cdots\mathrm{S_0T}\rangle$ reflect the periodic structure of ring-shaped aggregate models. In this model, we employ only one (one pair) of excitations for singlets (triplets), according to the previous singlet fission studies.[1,9] Furthermore, all TT states are located on adjacent monomers, i.e., the migration of triplet excitons are ignored. The numbers of FE, CT and TT bases for the ring-shaped *N*-mer are *N*, 2*N*, and *N*, respectively, resulting in the total number of bases, 4*N*.

In exciton Hamiltonian H_{ex}, we consider only intermolecular coupling between nearest neighboring molecules. While it is theoretically possible to include the interactions between more distant molecules by expanding diabatic electronic state basis and by adding corresponding electronic couplings, such contributions are negligible compared to those involving nearest neighbors. The approximate exciton Hamiltonian is expressed as

$$H_{ex} = H_{\mathrm{FE}} + H_{\mathrm{CT}} + H_{\mathrm{TT}} + H_{\mathrm{int}} \tag{II.1.3}$$

where the FE, CT, and TT Hamiltonians is represented as

$$H_{\mathrm{FE}} = \sum_{i=1}^{N} E_{\mathrm{S}_1} F_i^\dagger F_i + V_{\mathrm{ex}} \left(\sum_{i=1}^{N-1} F_i^\dagger F_{i+1} + F_N^\dagger F_1 + h.c. \right) \tag{II.1.4}$$

$$H_{\mathrm{CT}} = \sum_{i=1}^{N-1} E_{\mathrm{AC}} C_{i,i+1}^\dagger C_{i,i+1} + \sum_{i=1}^{N-1} E_{\mathrm{CA}} C_{i+1,i}^\dagger C_{i+1,i} + E_{\mathrm{AC}} C_{N,1}^\dagger C_{N,1} + E_{\mathrm{CA}} C_{1,N}^\dagger C_{1,N} \tag{II.1.5}$$

$$H_{\mathrm{TT}} = \sum_{i=1}^{N-1} E_{\mathrm{TT}} T_{i,i+1}^\dagger T_{i,i+1} + E_{\mathrm{TT}} T_{N,1}^\dagger T_{N,1} \tag{II.1.6}$$

Here, $F_i^\dagger$ (F_i) represents the creation (annihilation) operator for an FE state at the *i*th monomer, $C_{i,j}^\dagger$ ($C_{i,j}$) represents the creation (annihilation) operator of an anion (A) and a cation (C) at the *i*th and *j*th monomers, respectively, and $T_{i,j}^\dagger$ ($T_{i,j}$) represents the creation (annihilation) operator of two triplets over the *i*th and *j*th monomers. The term *h.c.* indicates the Hermitian conjugate of the terms already included in each parenthesis.

Interaction Hamiltonian between different diabatic states are described as follows,

$$H_{\mathrm{int}} = H_{\mathrm{FE/CT}} + H_{\mathrm{CT/TT}} \tag{II.1.7}$$

where the FE-CT coupling and CT-TT coupling terms are described as

$$\begin{aligned} H_{\mathrm{FE/CT}} = {} & V^{S_1S_0/AC}\left(\sum_{i=1}^{N-1} F_i^{\dagger} C_{i,i+1} + F_N^{\dagger} C_{N,1} + h.c.\right) \\ & + V^{S_1S_0/CA}\left(\sum_{i=1}^{N-1} F_i^{\dagger} C_{i+1,i} + F_N^{\dagger} C_{1,N} + h.c.\right) \\ & + V^{S_0S_1/AC}\left(\sum_{i=1}^{N-1} F_{i+1}^{\dagger} C_{i,i+1} + F_1^{\dagger} C_{N,1} + h.c.\right) \\ & + V^{S_0S_1/CA}\left(\sum_{i=1}^{N-1} F_{i+1}^{\dagger} C_{i+1,i} + F_1^{\dagger} C_{1,N} + h.c.\right) \end{aligned} \tag{II.1.8}$$

$$\begin{aligned} H_{\mathrm{CT/TT}} = {} & V^{\mathrm{TT}/AC}\left(\sum_{i=1}^{N-1} T_{i,i+1}^{\dagger} C_{i,i+1} + T_{N,1}^{\dagger} C_{N,1} + h.c.\right) \\ & + V^{\mathrm{TT}/CA}\left(\sum_{i=1}^{N-1} T_{i,i+1}^{\dagger} C_{i+1,i} + T_{N,1}^{\dagger} C_{1,N} + h.c.\right). \end{aligned} \tag{II.1.9}$$

Because we here consider the symmetric ring-shaped aggregates composed of identical monomers with the same interactions, FE exciton energy ($E_{\mathrm{S_1S_0}}$) at all monomers, CT energies (E_{CA} and E_{AC}) at all neighboring monomers, and TT energies (E_{TT}) are equal, respectively, and are referred to as E_{FE}, E_{CT}, and E_{TT}, respectively. Furthermore, in the off-diagonal matrix elements, there are some relationships between electronic couplings derived from symmetry structure of ring-shaped aggregates. First, the FE coupling between $\mathrm{S_1S_0}$ and $\mathrm{S_0S_1}$ at the neighboring monomers, which are described as $V^{\mathrm{S_1S_0/S_0S_1}}$ and $V^{\mathrm{S_0S_1/S_1S_0}}$, are equal to each other and they are referred to as V_{ex}. Second, two types of the FE–CT couplings, $V^{\mathrm{S_1S_0/CA}} = V^{\mathrm{S_0S_1/AC}}$ and $V^{\mathrm{S_1S_0/AC}} = V^{\mathrm{S_0S_1/CA}}$, are considered. Third, there are also two types of the CT–TT couplings, $V^{\mathrm{TT/CA}}$ and $V^{\mathrm{TT/AC}}$. Note that the variation in intermolecular couplings depending on aggregate size is explicitly considered by calculating Hamiltonian matrix elements for all *N*, in contrast to the previous study.[1,9]

In this study, all the matrix elements of H_{ex} are calculated using the CAM-B3LYP /cc-pVDZ method, where the optimized geometry of pentacene monomer is obtained at RB3LYP level of approximation, which is known to well reproduce that obtained at higher level of approximation like spin-flip density functional theory (DFT).[11] The FE exciton energy E_{FE} and TT energy E_{TT} are approximated by $E(\mathrm{S}_1)$ and $2E(\mathrm{T}_1)$ (where $E(\mathrm{S}_1)$ and $E(\mathrm{T}_1)$ indicate the excitation energy of the singlet and the triplet excited state, respectively, at the monomer), and they are calculated using the time-dependent (TD) DFT and Tamm-Dancoff approximation (TDA) methods,[12] respectively. The CT exciton energy E_{CT} for the dimer model is estimated by

$$E_{\mathrm{CT}} = E_{\mathrm{C}} + E_{\mathrm{A}} - E_{\mathrm{N}} + E_{\mathrm{static}} \qquad \mathrm{(II.1.10)}$$

where E_{C}, E_{A} and E_{N} represent the self-consistent-field (SCF) energies of the C, A, and neutral (N) states, respectively. The electrostatic interaction between the C and A monomers in the dimer configuration is approximately calculated by

$$E_{static} \approx \sum_{m\in C}\sum_{n\in A} \frac{q_m q_n}{r_{mn}} \qquad \mathrm{(II.1.11)}$$

where q_m and q_n indicates the Mulliken atomic charges at the atom sites m (in C monomer) and n (in A monomer), respectively, and r_{mn} is the distance between sites m and n.

The off-diagonal matrix elements of H_{ex} are calculated by eqs. (I.1.24) – (I.1.30) in Chapter I.1.2 described as[13,14]

$$V^{S_1S_0/CA} \equiv \langle CA|H_{ex}|S_1S_0\rangle = \langle l_A|F|l_B\rangle + 2\langle h_A l_A|l_B h_A\rangle - \langle h_A l_A|h_A l_B\rangle \approx V_{\mathrm{LL}} \qquad \mathrm{(II.1.12)}$$

$$V^{S_1S_0/AC} \equiv \langle AC|H_{ex}|S_1S_0\rangle = -\langle h_A|F|h_B\rangle + 2\langle h_A l_A|l_A h_B\rangle - \langle h_A l_A|h_B l_A\rangle \approx -V_{\mathrm{HH}} \qquad \mathrm{(II.1.13)}$$

$$V^{TT/CA} \equiv \langle TT|H_{ex}|CA\rangle = \sqrt{\frac{3}{2}}[\langle l_A|F|h_B\rangle + \langle l_A l_B|h_B l_B\rangle - \langle l_A h_B|h_B h_A\rangle] \approx \sqrt{\frac{3}{2}}V_{\mathrm{LH}} \qquad \mathrm{(II.1.14)}$$

$$V^{TT/AC} \equiv \langle TT|H_{ex}|AC\rangle = \sqrt{\frac{3}{2}}[\langle h_A|F|l_B\rangle + \langle h_A l_A|l_B l_A\rangle - \langle h_A h_B|l_B h_B\rangle] \approx \sqrt{\frac{3}{2}}V_{\mathrm{HL}} \qquad \mathrm{(II.1.15)}$$

$$\begin{aligned} V_{ex} &\equiv \langle S_1S_0|H_{ex}|S_0S_1\rangle = 2\langle l_A h_B|h_A l_B\rangle - \langle l_A h_B|l_B h_A\rangle \\ &\approx 2\langle l_A h_B|h_A l_B\rangle \approx \sum_{m\in C}\sum_{n\in A}\frac{\rho_m\rho_n}{r_{mn}} \end{aligned} \qquad \mathrm{(II.1.16)}$$

where h_X and l_X represent the HOMO (the highest occupied molecular orbital) and the LUMO (the lowest unoccupied molecular orbital) of monomer X (X = A, B: different monomers in the dimer models). The V_{ij} ($\equiv \langle i|F|j\rangle$) is the Fock matrix, and $\langle ij|kl\rangle$ indicates a two-electron integral. In eqs (II.1.12)-(II.1.15), we approximately calculate these electronic couplings using the corresponding Fock matrix elements, because two-electron integrals are known to be much smaller than one-electron integrals.[15] In eq. (II.1.16), ρ_m and ρ_n are the Mulliken transition densities at atom sites m [in monomer A ($h_A \rightarrow l_A$)] and n [in monomer B ($h_B \rightarrow l_B$)], and r_{mn} is the distance between sites m and n. The quantum chemical calculations in this study were performed by Gaussian 09[16] and exciton dynamics simulation was done by a home-made program.[8] The atomic units ($m = c = \hbar = 1$ a.u.) are used for expressions of equations in this study.

2.3. *Quantum Master Equation*

To investigate the quantum dynamics of exciton relaxation (SF dynamics), we used the second-order time-convolutionless (TCL) QME method, which describes a time evolution of the reduced density matrix for the exciton system weakly coupled with the phonon bath. The second-order TCL QME under the Markov approximation is represented by[8,17,18]

$$\frac{d}{dt}\rho_{ex}(t) = -i[H_{ex}, \rho_{ex}(t)] \\ + \sum_{\omega,m} \gamma_m(\omega)\left(A_m(\omega)\rho_{ex}(t)A_m(\omega)^\dagger - \frac{1}{2}\{A_m(\omega)^\dagger A_m(\omega), \rho_{ex}(t)\}\right) \tag{II.1.17}$$

Here, $A_m(\omega) = \sum_{E_\beta - E_\alpha = \omega} |\alpha\rangle\langle\alpha|A_m|\beta\rangle\langle\beta|$, where $\{|\alpha\rangle\ (= \sum_m C_{m\alpha}|m\rangle)\}$ and E_α represent an eigenstate (adiabatic exciton state) and an eigenvalue of H_{ex}, i.e., $H_{ex}|\alpha\rangle = E_\alpha|\alpha\rangle$. The relaxation parameter $\gamma_m(\omega)$ under the Markov approximation is expressed as[8,18]

$$\gamma_m(\omega) = \begin{cases} 2\pi J_m^X(\omega)\left(1 - n_B(\omega, T)\right) & (\omega > 0) \\ 2\pi J_m^X(-\omega)n_B(-\omega, T) & (\omega > 0) \\ \dfrac{4\lambda_m^X k_B T}{\hbar^2 \Omega_m^X} & (\omega = 0) \end{cases} \tag{II.1.18}$$

where $n_B(\omega, T)$ is the Bose–Einstein distribution at temperature T, and $J_m(\omega)$ is the spectral density of the Holstein vibrational modes of the mth diabatic exciton state. The spectral density $J_m(\omega)$ is approximated by an Ohmic function with a Lorentz-Drude cutoff,[8,19]

$$J_m(\omega) = \frac{1}{\pi}\frac{2\lambda_m \Omega_m \omega}{\omega^2 + (\Omega_m)^2} \tag{II.1.19}$$

where λ_m and Ω_m indicate the reorganization energy and the cutoff frequency, respectively, in the mth diabatic exciton state. This spectral density indicates a distribution with a peak value of λ_m/π at Ω_m vibrational mode. In this study, we adopt the approximation that the spectral density is identical ($\lambda \equiv \lambda_m, \Omega \equiv \Omega_m$) for different diabatic exciton states, though the effects of the state-dependent spectral densities are discussed in previous paper.[1] Namely, we focus on how the variation of intermolecular electronic couplings, which depend on the size and the structure of aggregates, affects the SF dynamics.

In this Chapter, we numerically solve eqs (II.1.17) with Holstein vibronic coupling at $T = 300$ K using the eight-step and sixth-order Runge-Kutta method. We employ $(\lambda, \Omega) = (50, 180)$ meV in eq. (II.1.19) for all diabatic exciton states, the parameter of which is known to be typical for acenes and other conjugated organic molecules.[20] The time evolution of diabatic TT exciton populations $P_{\mathrm{TT}}(t)$ is fitted with a single exponential function $P_{\mathrm{TT}}(t) = a - b\exp(-kt)$ to evaluate the SF rate k (ps^{-1}) and TT yield (a), with the initial population of $|\mathrm{S}_1\mathrm{S}_0 \cdots \mathrm{S}_0\rangle$ is 100 %.

2.4. *Relative Relaxation Factor (RRF) Analysis*

In order to reveal the origin of the exciton dynamics in SF process, we employ RRF analysis, which can clarify the relaxation between the adiabatic exciton states $\{|\alpha\rangle\}$. In the case of Holstein coupling under the Markov approximation, RRF is defined by[8-10]

$$\mathit{\Delta\Gamma}(\alpha \to \beta) = \sum_m |C_{m\alpha}|^2 |C_{m\beta}|^2 \left[\gamma_m(\omega_{\alpha\beta}) - \gamma_m(\omega_{\beta\alpha})\right] \qquad \text{(II. 1.20)}$$

where $\omega_{\alpha\beta} = \omega_\alpha - \omega_\beta$ (ω_α: the eigenenergy of the adiabatic state $|\alpha\rangle$), and $\gamma_m(\omega_{\alpha\beta})$ and $\gamma_m(\omega_{\beta\alpha})$ on the right-hand side indicate the relaxation rate from state α to β and that from state β to α, respectively, due to the vibronic coupling. The positive and negative values of $\mathit{\Delta\Gamma}(\alpha \to \beta)$ indicates the exciton relaxation from α to β, and that from β to α, respectively. The amplitude of $\mathit{\Delta\Gamma}(\alpha \to \beta)$ indicates the magnitude of net relaxation rate between states α and β, which becomes large when both the adiabatic states α and β include common diabatic exciton configurations as seen from $|C_{m\alpha}|^2|C_{m\beta}|^2$ in eq.n (II.1.20).

2.5. *Point Group Approach to Analyze Symmetry Structure of Exciton States*

We investigate how structural symmetry in pentacene-based J- and H-type ring-shpaed aggregate models affects the mixing of adiabatic electronic wavefunctions using a point group theoretical approach. To clarify the origin of state mixture among the symmetry-adapted siabatic FE, CT, and TT exciton bases, we propose the following systematic, group-theory-based procedure.

1. **Assignment of the point group**
   Choose an appropriate point group G for the aggregate system.
2. **Definition of monomer orbitals**
   Define the HOMO and LUMO localized on each monomer X ($X = 1, \cdots, N$), labeled h_X and l_X, respectively. In the ring-shaped aggregate N-mer, h_X and l_X are obtained by rotating the first MOs h_1 and l_1 around the principal N-fold rotational axis of $D_{N\mathrm{h}}$ (or its subgroup $C_{N\mathrm{v}}$).
3. **Transformation under symmetry operations**
   Determine how the sets $\{h_X\}$ and $\{l_X\}$ transform under each symmetry operation in G. This analysis uniquely specifies how the symmetry operation acts on the diabatic exciton bases shown in eq. (II.1.2).
4. **Construction of reducible representations**
   Obtain the reducible representations $\mathit{\Gamma}^Y$ [Y = FE, CT (or CA, AC), TT] and their characters

$\chi^Y(R_i)$ [where R_i $(i = 1, \cdots, g)$ indicates the symmetry operations in point group G, and g is the number of symmetry elements] under the diabatic exciton basis $\{|\mathrm{FE}\rangle\}$, $\{|\mathrm{CT}\rangle\}$ (or $\{|\mathrm{CA}\rangle\}$ and $\{|\mathrm{AC}\rangle\}$) and $\{|\mathrm{TT}\rangle\}$ are obtained.

5. **Decomposition into irreducible representation**
   Resolve each reducible representation Γ^Y into its irreducible representation (Γ_α) of the point group G, and is expressed as

$$\Gamma_Y = \sum_\alpha c_\alpha \Gamma_\alpha \tag{II.1.21}$$

   where the c_α denote the number of energy levels, which belongs to the irreducible representation Γ_α among the energy levels of the diabatic exciton state Y. The c_α is calculated using

$$c_\alpha = \frac{1}{g}\sum_i \chi_\alpha(R_i)\chi^Y(R_i) \tag{II.1.22}$$

   Here, $\chi_i(R_i)$ is the character corresponding to the symmetry operation R_i in irreducible representation Γ_α, which is obtained from character table of the point group G.

6. **Obtain symmetry-adapted linear combination**
   Finally, the new exciton basis that diagonalizes each diabatic exciton block in the H_{ex} matrix is given by the symmetry-adapted linear combinations (SALC) of the diabatic exciton bases. Their irreducible representations are determined using the character table in conjunction with the transformations found in step (3). Notably, there are no electronic couplings between symmetry-adapted exciton bases belonging to different irreducible representations.

3. Results and Discussion

3.1. *Electronic Couplings*

In this study, we discuss the variation of intermolecular electronic couplings, which is dependent on the aggregate size (N: $3 \leq N \leq 15$). As a result of quantum chemical calculations, the Frenkel exciton energy E_{FE}, and the double triplets state energy E_{TT} are given as 2250 meV, and 2072 meV, respectively, which are approximated to be identical for all N. Thus, only the energy of CT state E_{CT}, and FE coupling V_{ex}, and electronic couplings are found to depend on N. **Figure II.1.2(a)** shows the variation in CT energies E_{CT} in J- and H-ring-shaped N-mers with increasing N, which indicates that E_{CT} in J-(H-)aggregates increases (decreases) with increasing N. **Figure II.1.2 (b)** and **(c)** show the N-dependences of intermolecular electronic coupling (V_{HH}, V_{LL}, V_{HL}, V_{LH}, and V_{ex}) in J- and H-aggregates, respectively. As seen from **Figure II.1.2 (b)**, the amplitudes of V_{HH}, V_{LL}, V_{HL}, V_{LL}, monotonically decrease with increasing N. On the contrary to J-aggregate, **Figure**

II.1.2 (c) indicates that the amplitudes of V_{HH}, and V_{LL} monotonically increases in H-aggregate, while those of V_{HL} and V_{LH} increase up to $N = 9$, and slightly decrease for larger N. **Figure II.1.2 (b)** and **(c)** indicate that the amplitudes of V_{ex} are almost constant between 40–60 meV for all N. This is because the angle θ in **Figure II.1.1 (b)** increase in H-ring on the contrary to the J-ring model. When angle θ increase, the π-orbital overlap between the adjacent monomers approaches to face-to-face stacking structure. The sign of electronic couplings is explained from the distribution of HOMO, LUMO, and transition dipole moments in dimer structure shown in **Figure II.1.3**. **Figure II.1.3 (a)** represents the phase of HOMO and LUMO, and transition density (~ HOMO × LUMO). The V_{HL} and V_{LL} shows negative value in J-ring model because of in-phase relationships in HOMO – LUMO and LUMO – HOMO pair (**Figure II.1.3 (b)**), while the other shows out-of-phase relationships (**Figure II.1.3 (b)** and **(c)**). As we described in General Introduction, FE coupling V_{ex} become negative in J-ring because of the negative integrand of eq. (II.1.16), on the contrary to the H-ring model.

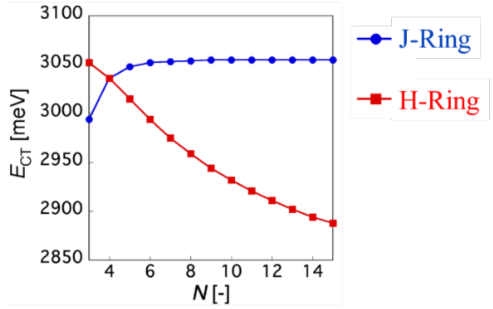
(a) *E*(CT)

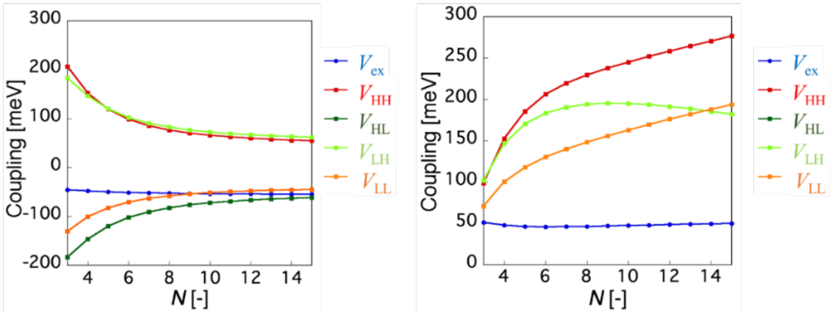
(b) Off-diagonal terms in J-ring

(c) Off-diagonal terms in H-ring

Figure II.1.2. Aggregate size (N) dependences of (a) the localized charge transfer (CT) state energies E_{CT} in J-(blue) and H-(red) aggregates, and of the off-diagonal matrix elements of exciton Hamiltonian: V_{ij} (i, j = H, L), and V_{ex} in (b) J- and (c) H-aggregates. Note here that $V_{\mathrm{HL}} = V_{\mathrm{LH}}$ in H-ring system.

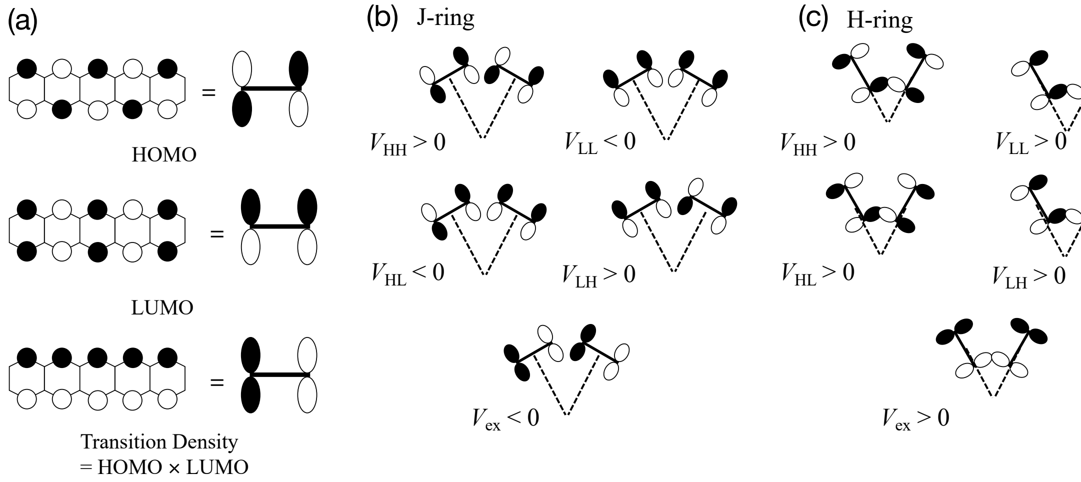

Figure II.1.3. (a) Spatial phase distributions of the HOMO, the LUMO, and the transition density of pentacene monomer, and phase distributions of the HOMO and the LUMO of the dimer unit in pentacene (b) J- and (c) H-ring-shaped aggregates at $N = 6$.

3.2. Size Dependency of SF rates and TT yields

We investigate the time-evolution of diabatic exciton {FE, CT, TT} population for J- and H-type ring-shaped aggregate N-mer models ($3 \leq N \leq 15$) by solving QME using the 6-order Runge-Kutta method with the initial population localized in $|\mathrm{S}_1\mathrm{S}_0 \cdots \mathrm{S}_0\rangle$. **Figure II.1.4** shows the time-evolution of diabatic exciton states {FE, CT, TT} populations for J- and H-aggregate models with $N = 3, 5, 8$. In J-aggregate model (**Figure II.1.4(a)-(c)**), it is found that SF rates k monotonically decrease [$k = 0.682\ \mathrm{ps}^{-1}$ (3-mer) → $0.0710\ \mathrm{ps}^{-1}$ (8-mer) in FE coupling case], while TT yields a monotonically increase [$a = 44.9$ % (3-mer) → 95.6 % (8-mer) in FE coupling case]. On the other hand, as seen from the results of the H-aggregate 3-mer and 5-mer models in FE coupling case (**Figure II.1.4(d)** and **(e)**, SF rate of 5-mer is enhanced as compared to that of 3-mer by a factor of ~24 [$k = 0.352\ \mathrm{ps}^{-1}$(3-mer) → $8.46\ \mathrm{ps}^{-1}$ (5-mer)], though the TT yield slightly decreases [$a = 95.6$ % (3-mer) → 78.0 % (5-mer)]. Since the population of the diabatic TT state in H-aggregate 8-mer shows a rapid increase at first, but then follows the gradual decay to a constant value (see **Figure II.1.4 (f)**), it is impossible to fit the time-evolution of the TT population with single-exponential function, and thus the SF rate in H-aggregate 8-mer is not determined.

To clarify the size dependences of SF dynamics in the J- and H-type ring-shaped aggregates in more details, we investigate the variation in TT yield a (**Figure II.1.5 (a)**) and SF rate k (**Figure II.1.5 (b)**) as a function of N ($3 \leq N \leq 15$) (**Figure II.1.5**). **Figure II.1.5 (a)** indicates that the TT yield in the J-type ring-shaped aggregate is found to monotonically increase with increasing N from $a = 44.9$ % toward about 100 %. Although SF rate in J-ring shows monotonical decrease with increasing N, that in the H-ring model show more complicated size dependences. Interestingly, the zigzag plot in **Figure II.1.5 (b)** indicates that the SF rate k is enhanced when N is odd number without significantly sacrificing the TT yields a, and there exist an optimal aggregate size at $N = 5$ yielding the maximum SF rate. In the following section, we focus on the origin of zig-zag behaviors of SF rate in H-ring model by using point group theory: examine the irreducible representation of SALC of diabatic basis by comparing H-even and odd rings.

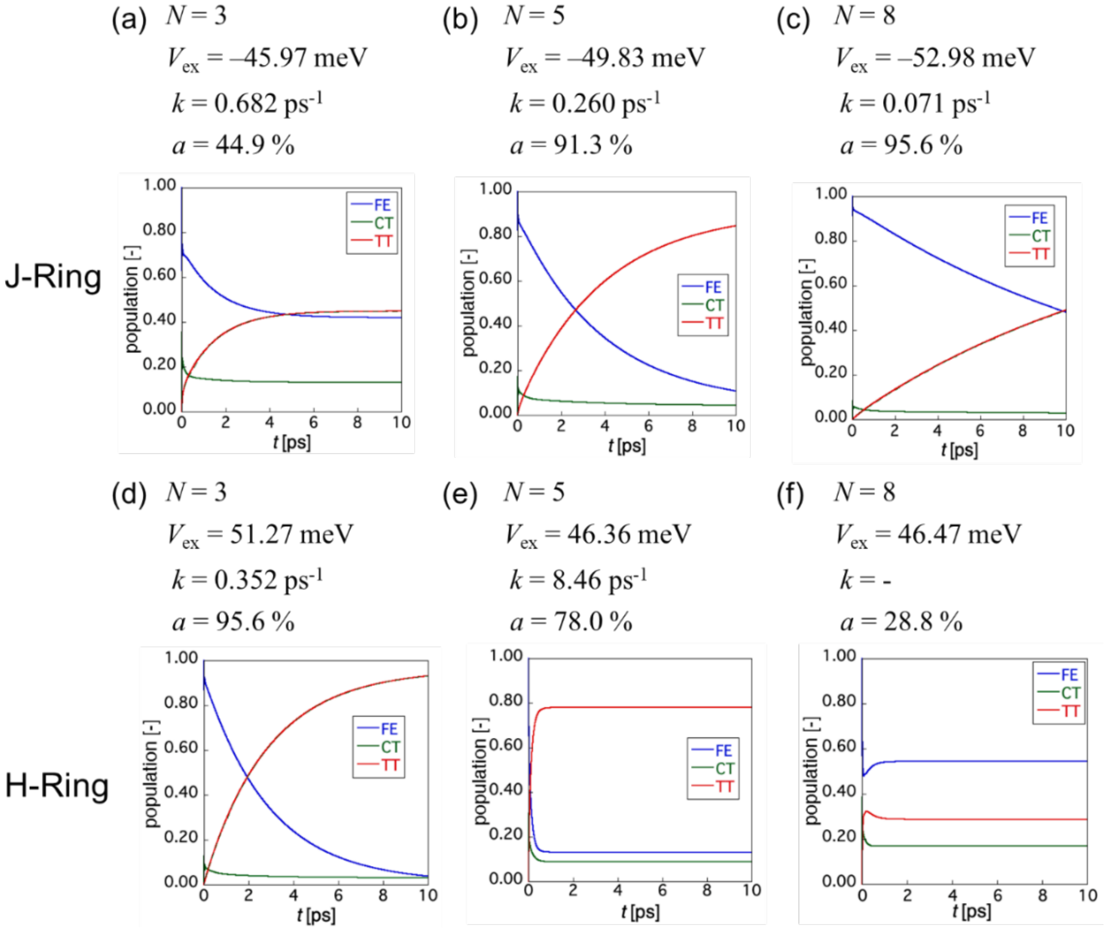

(a) $N = 3$, $V_{\mathrm{ex}} = -45.97$ meV, $k = 0.682$ ps^{-1}, $a = 44.9$ %

(b) $N = 5$, $V_{\mathrm{ex}} = -49.83$ meV, $k = 0.260$ ps^{-1}, $a = 91.3$ %

(c) $N = 8$, $V_{\mathrm{ex}} = -52.98$ meV, $k = 0.071$ ps^{-1}, $a = 95.6$ %

(d) $N = 3$, $V_{\mathrm{ex}} = 51.27$ meV, $k = 0.352$ ps^{-1}, $a = 95.6$ %

(e) $N = 5$, $V_{\mathrm{ex}} = 46.36$ meV, $k = 8.46$ ps^{-1}, $a = 78.0$ %

(f) $N = 8$, $V_{\mathrm{ex}} = 46.47$ meV, $k = -$, $a = 28.8$ %

Figure II.1.4. Time-evolution of diabatic exciton states {FE, CT, TT} populations in SF dynamics of pentacene ring-shaped J- [(a)-(c)] and H- [(d)-(f)] aggregates for $N = 3$ [(a),(d)], 5 [(b), (e)], and 8 [(c), (f)]. SF rate k [ps^{-1}] and TT yield a [%] are also shown.

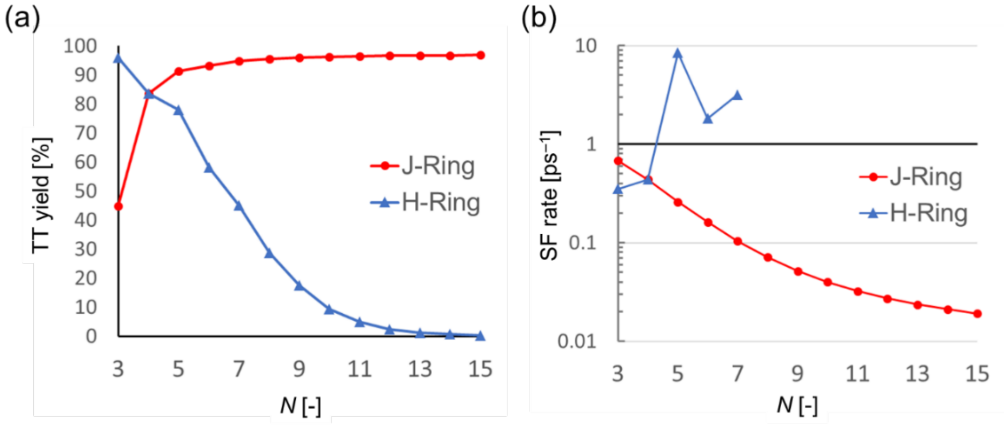

Figure II.1.5. *N*-dependences of (a) TT yield *a* [-] and (b) SF rate *k* [ps^{-1}] in pentacene J- and H-ring-shaped aggregate models.

3.3. Effects of Symmetry on the Adiabatic Electronic States

In this section, we discuss the effects of spatial symmetry structure in pentacene J- and H-ring-shaped aggregate 3-mer and 4-mer models on the electronic couplings between FE, CT, and TT diabatic exciton states using group symmetrical approach. Then, by extending the obtained results to any *N*-mers, we reveal the reason why SF rate *k* in only H-ring models depends on the parity of *N*. In Section II.2.5, we presented a systematic method to construct SALCs of diabatic FE, CT, and TT states, respectively. Using this method, we discuss the electronic couplings between the symmetry-adapted FE, CT, and TT diabatic exciton bases, which belong to common irreducible representations. In ring trimer systems, we consider a novel set of SALCs of diabatic exciton bases {FE(a)-(c), CT(g)-(l), TT(d)-(f)}, which are obtained by diagonalizing each diabatic exciton block of the H_{ex} matrix. The detail formalism of SALCs of diabatic FE, CT, and TT states and their irreducible representations are summarized in **Table A.1** for J-ring trimer (J3) and H-ring trimer (J4), and in **Table A.2** for J-ring tetramer (J4) and H-ring tetramer (H4). The graphical illustration of the coupling structure between SALC states are given in **Figure II.1.6** for trimer systems and **Figure A.1** for tetramer systems.

The order of adiabatic FE-like state (FE’) energy is explained by the superposition of diabatic states in FE’. In J-ring, since the sign of the V_{ex} is negative and FE(c) is strongly coupled with CT states as shown in **Figure II.1.6 (a)**, the lowest adiabatic FE’ state is composed of in-phase superposition of diabatic FE states with mainly contributed from FE(c) in J3 model. On the other hand, the lowest adiabatic FE’ state are composed of out-of-phase superposition of diabatic FE states which is mainly described as the superposition of SALC diabatic states FE(a) and FE(b). In the 3-mer model, the correspondences between symmetry adapted diabatic basis and its irreducible representations are {FE(a, b) [*E*], FE(c) [A_2/A_1], CT(g) [A_2/A_1], CT(h, i) [*E*], CT(j) [A_1/A_2], CT(k, l) [*E*], TT(d) [A_1], TT(e, f) [*E*]} in J-/H-rings, respectively, where the symbols in square brackets show the irreducible representation of the point group C_{3v} to which the SALC of diabatic base (bases) belongs. Because there is no symmetry adapted diabatic TT basis belonging to irreducible representation A_2 in both J- and H-ring-shaped aggregates, diabatic basis FE(c) in J-aggregate 3-mer has no electronic couplings with TT(d) basis via diabatic CT bases, while all symmetry adapted FE bases in H-aggregate have FE-CT-TT couplings. Thus, in J-aggregate, the lowest-FE' (FE'(c)) and TT'(d) states do not involve TT and FE configurations, respectively, so that an approach of FE'(c) to TT'(d) is not expected to accelerate the SF rate.[1] On the contrary, the lowest-FE' ((FE'(a,b))) and TT'(e-f) states in H-aggregate model involve TT and FE(a or b) configurations, respectively.

Second, we focus J- and H-ring-shaped 4-mer models. Like the 3-mer model, we consider a novel set of SALC diabatic exciton bases {FE(a)-(d), CT(i)-(p), TT(e)-(h)}. From the same reason for 3-mer models, FE'(d) and FE'(a), of which the configurations are composed of the all in-phase (out-of-phase) superpositions of diabatic FE states, becomes the lowest-FE' state in J4 and H4, respectively. From **Figure A.1**, the reason why the lowest adiabatic FE' states in both 4-mer does not involve TT states is explained by the irreducible representation: the lowest FE' states belong to the irreducible representations A_2 (B_1), and there are no symmetry-adapted diabatic TT bases belonging to such an irreducible representation, while the next lowest FE' states involve TT configurations because of the existence of the TT bases belonging to *E*. This feature – the lowest-FE' does not involve the TT configurations – is predicted to hold for all even-ring models, because it arises from the reflection symmetry σ_v and σ_d. Here, σ_v (σ_d) represents a vertical (dihedral) mirror plane including primary *N*-fold axis and either passes through the pentacene longitudinal axis (or lies between adjacent pentacene molecules) in ring-shaped aggregate models. Consequently, as in the J3 model, the approach of the lowest-FE' state to the TT'-manifold in J-(H-) aggregate even-ring model does not accelerate the SF dynamics, whereas the degenerate next-lowest-FE' states do promote SF due to their involvement of TT configurations.

In conclusion, it is found that the non-degenerate lowest-FE' state in J-aggregate models and H-even-ring models do not involve configurations of diabatic TT bases, while the degenerate lowest-FE' state in H-odd-ring models involve them. From the definition of RRF in eq. (II.1.20), exciton overlaps of adiabatic exciton states have an impact on the population relaxation dynamics from the lowest-FE' to TT'-manifold.

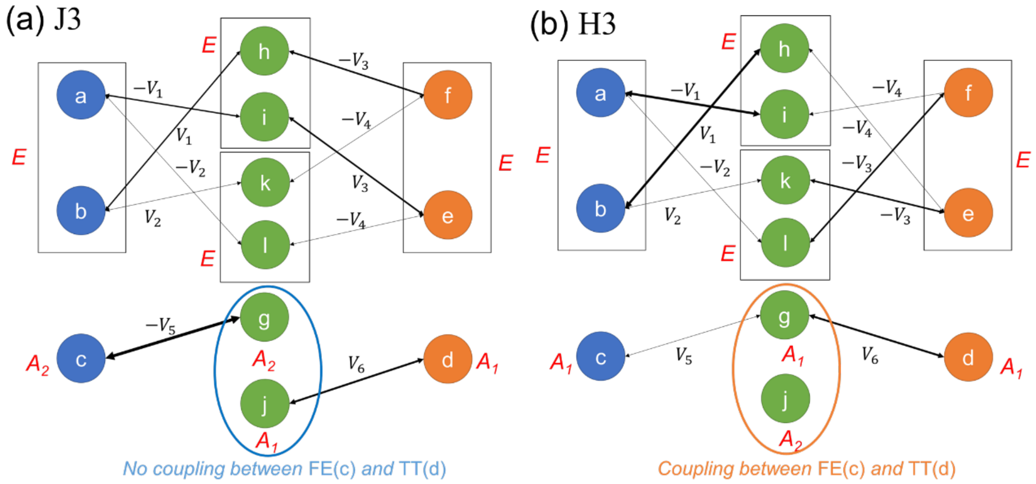

$$V_1 = \frac{1}{\sqrt{2}}(2|V_{\mathrm{HH}}|-|V_{\mathrm{LL}}|) = 199\ \mathrm{meV}$$

$$V_2 = \sqrt{\frac{3}{2}}|V_{\mathrm{LL}}| = 160\ \mathrm{meV}$$

$$V_3 = \frac{3}{4}(|V_{\mathrm{LH}}|+|V_{\mathrm{HL}}|) = 275\ \mathrm{meV}$$

$$V_4 = \frac{\sqrt{3}}{4}(|V_{\mathrm{LH}}|+|V_{\mathrm{HL}}|) = 159\ \mathrm{meV}$$

$$V_5 = \sqrt{2}(|V_{\mathrm{LL}}|+|V_{\mathrm{HH}}|) = 476\ \mathrm{meV}$$

$$V_6 = \frac{\sqrt{3}}{2}(|V_{\mathrm{LH}}|+|V_{\mathrm{HL}}|) = 318\ \mathrm{meV}$$

$$V_1 = \frac{1}{\sqrt{2}}(2|V_{\mathrm{HH}}|+|V_{\mathrm{LL}}|) = 190\ \mathrm{meV}$$

$$V_2 = \sqrt{\frac{3}{2}}|V_{\mathrm{LL}}| = 87\ \mathrm{meV}$$

$$V_3 = \frac{3}{4}(|V_{\mathrm{LH}}|+|V_{\mathrm{HL}}|) = 154\ \mathrm{meV}$$

$$V_4 = \frac{\sqrt{3}}{4}(|V_{\mathrm{LH}}|+|V_{\mathrm{HL}}|) = 89\ \mathrm{meV}$$

$$V_5 = \sqrt{2}(|V_{\mathrm{LL}}|-|V_{\mathrm{HH}}|) = 39\ \mathrm{meV}$$

$$V_6 = \frac{\sqrt{3}}{2}(|V_{\mathrm{LH}}|+|V_{\mathrm{HL}}|) = 177\ \mathrm{meV}$$

Figure II.1.6. Electronic couplings between symmetry adapted diabatic basis {FE(*x*) [*x* = a-d], CT(*x*) [*x* = i-p], TT(*x*) [*x* = e-h]}. The red characters indicate the irreducible representation of each basis for point group $C_{3\mathrm{v}}$. The two direction arrows with corresponding non-zero electronic couplings are also shown.

3.4. RRF Analysis

In order to clarify how the symmetry of exciton states affect the SF dynamics, we here conducted RRF analysis for J3 and H5 models. Note that the value of θ in J3 model is 60° which is close to that in H5 model with 54°. This means that the π-orbital overlap is smaller in H5 model than J3 model, however, more efficient SF occurs in H5 model rather than J3 model with 12 times and 1.7 times larger value of SF rate and TT yield as shown in **Figure II.1.4 (a)** and **(e)**. **Figure II.1.7** and **Figure II.1.8** shows the adiabatic exciton FE' and TT' states with RRFs for J3 and H5 models. The spatial distributions of diabatic exciton states {FE, CT, TT} at each monomer and coefficients $\{C_{m\alpha}\}$ for diabatic configurations *m* are also shown at several adiabatic states.

From RRF analysis, the SF process is found to occur in two steps: (i) fast relaxation from high-lying FE'(a) and FE'(b) to low-lying FE'(c) states, (ii) slow relaxation from the lowest

FE'(c) states to the TT' states until reaching the thermal equilibrium population. In J3 model, the slow relaxation from FE'(c) to TT' manifold is found to originate from only the exciton overlap of CT configurations between these states (CT-mediate path), because there are no common FE/TT exciton configurations in FE'(c) and TT'(d). The reason why FE/TT mixing do not arise is mentioned before: because the lowest FE'(c) and TT'(d) belong to different irreducible representation.

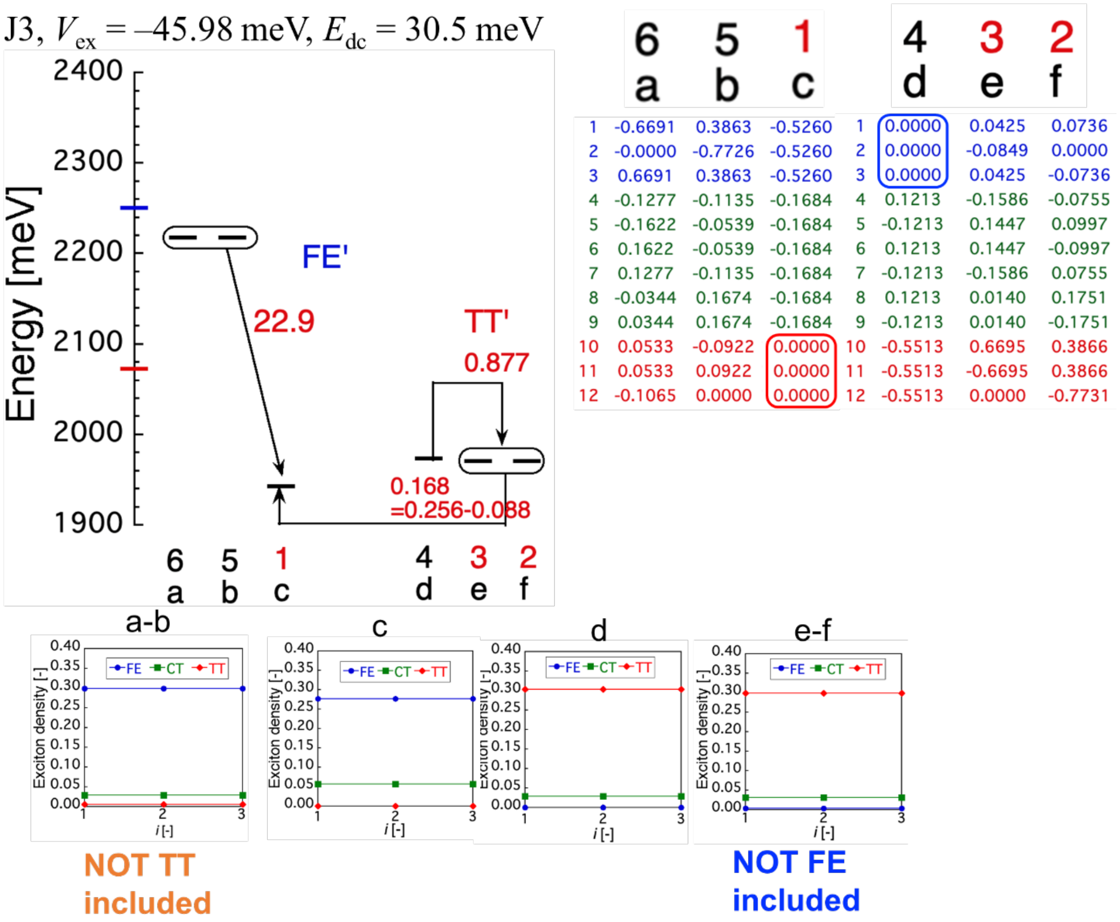

	6 a	5 b	1 c		4 d	3 e	2 f
1	-0.6691	0.3863	-0.5260	1	0.0000	0.0425	0.0736
2	-0.0000	-0.7726	-0.5260	2	0.0000	-0.0849	0.0000
3	0.6691	0.3863	-0.5260	3	0.0000	0.0425	-0.0736
4	-0.1277	-0.1135	-0.1684	4	0.1213	-0.1586	-0.0755
5	-0.1622	-0.0539	-0.1684	5	-0.1213	0.1447	0.0997
6	0.1622	-0.0539	-0.1684	6	0.1213	0.1447	-0.0997
7	0.1277	-0.1135	-0.1684	7	-0.1213	-0.1586	0.0755
8	-0.0344	0.1674	-0.1684	8	0.1213	0.0140	0.1751
9	0.0344	0.1674	-0.1684	9	-0.1213	0.0140	-0.1751
10	0.0533	-0.0922	0.0000	10	-0.5513	0.6695	0.3866
11	0.0533	0.0922	0.0000	11	-0.5513	-0.6695	0.3866
12	-0.1065	0.0000	0.0000	12	-0.5513	0.0000	-0.7731

Figure II.1.7. Adiabatic exciton states with RRFs in J3-ring. Since RRF is proportional to the exciton density $|C_{m\alpha}|^2$ (see eq. (II.1.20)), the coefficients $\{C_{m\alpha}\}$ for diabatic exciton basis m included in each adiabatic state α are also shown. The states enclosed in rectangles indicate degenerate states. The number under each adiabatic state indicates the energy ascending order, where the number in red indicates the lowest state(s) in each adiabatic manifold {FE'(a-c) and TT'(d-f)}. E_{ij} indicates the energy differences (meV) between adiabatic states, $E_{ij} = E_i - E_j$.

On the other hand, in H5 model, the degenerate FE'(a, b) states, which involve diabatic TT configurations, are close to near-degenerate TT' manifold with energy gap E_{aj} = 25.8 meV, resulting in the large exciton overlaps of FE/TT configurations between FE’(a, b) and TT’(i, j) (see the exciton density in FE’(a) and TT’(i) in **Figure II.1.8**). This feature is found to activate the SF process because novel relaxation pathways from higher-lying FE’ states (FE’(c, d)) to TT’(i, j) opens, and the pathways from the lowest-FE’ states FE’(a, b) to TT’ states are also enhanced.

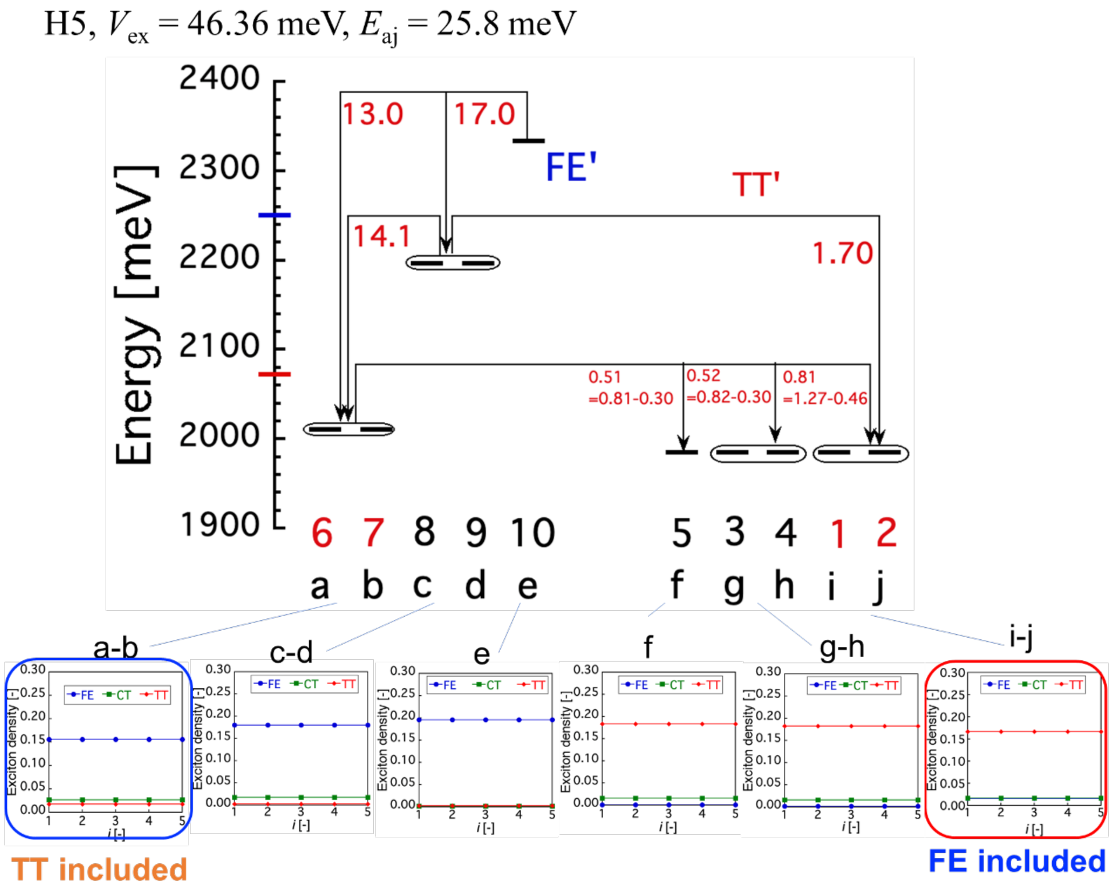

Figure II.1.8. Adiabatic exciton states with RRFs in pentacene H5 model in FE coupling case. See the legends of Figure 8 for further explanation.

3.5. Size Dependence of SF dynamics in Pentacene Ring-Shaped Aggregates

From the viewpoint of adiabatic energy matching conditions and SF acceleration mechanism, the general trends of TT yield and SF rate in J- and H-ring shaped aggregate systems are explained by investigating the *N*-dependences pf lower-edge of adiabatic state energies. **Figure II.1.9** shows the trends of energy of lowest FE’, the next lowest FE’ and TT’ states as functions of consisting molecules *N*. In J-ring systems, **Figure II.1.9 (a)** indicates that the energy of the lowest FE’ state rises with and moves away from TT’ manifold with increasing *N*. This is because the π-orbital overlaps between neighboring molecules decreases with increasing *N*, which leads to the reduction of the CT exciton configurations in the lowest FE' state. This feature of the relative intermolecular configuration in J-aggregate model results in the reduction of RRFs from the lowest FE' state to TT' states, which originates from only the common CT exciton overlaps between FE and TT, and of the SF rate *k* with increasing *N*. As a result, TT yield rises with increasing *N* because the energy gap between the lowest FE' states and TT' manifold increases.

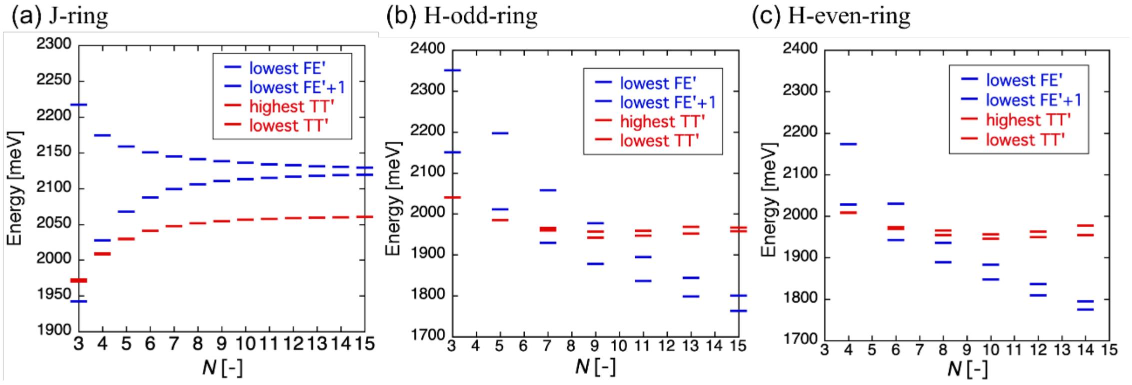
(a) J-ring (b) H-odd-ring (c) H-even-ring

Figure II.1.9. Size dependences of the energies of the adiabatic states, i.e., the lowest FE', the next lowest FE' (the lowest FE'+1) (blue), the lowest and the highest states in TT' manifold (red), as a function of *N* in (a) J-ring, b) H-type odd-ring and B) H-type even-ring.

On the other hand, the H-aggregate ring-shaped aggregate model exhibits more complicated size dependence of SF dynamics, and shows different tendencies from J-aggregate ring-shaped aggregate model in the following two points. Because the parity of *N* has a significant role on the SF rate in H-ring model, we separately plot the lowest and the next lowest FE' state energies and TT' energies for H-odd (**Figure II.1.9 (b)**) and H-even rings (**Figure II.1.9 (c)**). Since FE-CT-TT couplings in the lowest FE' states exist for odd *N*, but not for even *N*, the optimal *N* yielding the maximum SF rate is found to correspond to *N* at which the lowest FE' states are the closest to TT' manifold in odd-ring. This is because FE and TT states whose irreducible representation are equal to each other are strongly coupled, i.e., FE' and TT' states include a large amount of FE and TT configurations, and thus novel relaxation paths open from the high-lying FE' states to TT' manifold. As shown in **Figure II.1.9 (b)** the system satisfying this condition is predicted to be only the H5 model. In H6 model, the energy of the next lowest FE' state is too high to arise the FE/TT mixing. In H8 model, where the next lowest FE' state is degenerated with TT' states, the fast population relaxation occurs as shown in **Figure II.1.4 (f)**. However, the energy of the lowest FE' state is so lower than TT' states that TT yield becomes low and the backward process occur after TT state generation in few femtoseconds. Nevertheless, it is possible to design the aggregate systems which are not predicted to be optimal in this study by tuning the energy levels of monomer and coupling amplitudes (π-orbital overlaps) to meet these conditions.

4. Conclusion

In this study, we investigate the SF dynamics of pentacene J-type and H-type ring-shaped aggregate models to clarify the size (*N*) and the configuration dependences of SF rate and TT yield with electronic couplings explicitly depending on the aggregate size *N*. In the H-aggregate models, SF rate increases when *N* is odd number, where the H-type pentamer model exhibits the maximum SF rate ($k = 8.46$ ps^{-1}) in FE coupling case, while the SF rate in the J-aggregate models shows monotonical decrease from 0.682 ps^{-1} to 0 with increasing *N*. It is also found that TT yields monotonically increase from ~45 % toward 100 % (decrease from ~96 % toward 0 %) in J-(H-)aggregate models.

These relationships between SF dynamics and the geometry of pentacene J- and H-ring-shaped aggregate models are explained using symmetry structure and RRF analysis. The feature of SF rate depending on the parity of *N* is found to originate from whether or not the lowest adiabatic FE' state include the diabatic TT exciton configurations, which depends on the symmetry of the aggregate system. This feature affects the relaxation process from the lowest FE' state to TT' states. When the lowest adiabatic FE' states is allowed to include TT configuration, the relaxation from the FE' manifold to the TT' manifold is accelerated due to FE/TT mixing when the lowest FE' state is close in energy to TT' manifold. On the other hand, when the lowest FE' is prohibited to mix with TT states, this enhancement of relaxation process occurs when the next lowest FE' states approach TT' states. In such cases, however, the population backflow occurs from the TT' manifolds to the low-lying FE' states if the energy of FE' state is sufficiently lower than TT' states, like H-ring 8-mer in this study.

From the present results, it is predicted that the efficient SF materials can be obtained by the following procedures: (i) investigating the irreducible representation of the symmetry adapted diabatic exciton basis to clarify the condition to increase the SF rate due to the large mixing of FE/TT states, and (ii) investigating which FE state can give the lowest FE' state and whether this state is coupled with TT states, and (iii) tuning the energy levels of monomer levels (relative energy levels of FE, CT, and TT) of monomer and the intermolecular configurations to satisfy obtained conditions by using RRF analysis. Furthermore, we have clarified the importance of investigation of SF dynamics in the new types of ring-shaped aggregate models such as broken spatial symmetry systems as described in the next Chapter II.2 as well as of examining the effects of Peierls coupling on SF dynamics. The present results contribute to the comprehensive understanding of the correlation between the size and the structure of ring-shaped aggregate systems and SF dynamics as well as to the construction of new design guidelines for highly efficient SF ring-shaped aggregates.

Appendix

A.1. Symmetry Adapted Linear Combinations of Diabatic State Basis

Table A.1. Symmetry adapted diabatic exciton basis and its irreducible representations of point group C_{3v} in pentacene J- and H- aggregate trimer (J3 and H3, respectively).

Symmetry adapted diabatic basis	Irreducible representation in J3	Irreducible representation in H3
$\lvert \mathrm{FE(a)}\rangle = \frac{1}{\sqrt{2}}\{-\lvert \mathrm{S_1S_0S_0}\rangle + \lvert \mathrm{S_0S_0S_1}\rangle)$	E	E
$\lvert \mathrm{FE(b)}\rangle = \frac{1}{\sqrt{6}}\{-\lvert \mathrm{S_1S_0S_0}\rangle + 2\lvert \mathrm{S_0S_1S_0}\rangle - \lvert \mathrm{S_0S_0S_1}\rangle)$	E	E
$\lvert \mathrm{FE(c)}\rangle = \frac{1}{\sqrt{3}}\{\lvert \mathrm{S_1S_0S_0}\rangle + \lvert \mathrm{S_0S_1S_0}\rangle + \lvert \mathrm{S_0S_0S_1}\rangle\}$	A_2	A_1
$\lvert \mathrm{CT(g)}\rangle = \frac{1}{\sqrt{6}}\{\lvert \mathrm{CAS_0}\rangle + \lvert \mathrm{ACS_0}\rangle + \lvert \mathrm{S_0CA}\rangle + \lvert \mathrm{S_0AC}\rangle + \lvert \mathrm{AS_0C}\rangle +$	A_2	A_1
$\lvert \mathrm{CT(h)}\rangle = \frac{1}{\sqrt{12}}\{-2\lvert \mathrm{CAS_0}\rangle + \lvert \mathrm{ACS_0}\rangle + \lvert \mathrm{S_0CA}\rangle - 2\lvert \mathrm{S_0AC}\rangle + \lvert \mathrm{AS_0C}\rangle + \lvert \mathrm{CS_0A}\rangle\}$	E	E
$\lvert \mathrm{CT(i)}\rangle = \frac{1}{2}\{-\lvert \mathrm{ACS_0}\rangle + \lvert \mathrm{S_0CA}\rangle - \lvert \mathrm{AS_0C}\rangle + \lvert \mathrm{CS_0A}\rangle\}$	E	E
$\lvert \mathrm{CT(j)}\rangle = \frac{1}{\sqrt{6}}\{\lvert \mathrm{CAS_0}\rangle - \lvert \mathrm{ACS_0}\rangle + \lvert \mathrm{S_0CA}\rangle - \lvert \mathrm{S_0AC}\rangle + \lvert \mathrm{AS_0C}\rangle - \lvert \mathrm{CS_0A}\rangle\}$	A_1	A_2
$\lvert \mathrm{CT(k)}\rangle = \frac{1}{2}\{-\lvert \mathrm{ACS_0}\rangle - \lvert \mathrm{S_0CA}\rangle + \lvert \mathrm{AS_0C}\rangle + \lvert \mathrm{CS_0A}\rangle\}$	E	E
$\lvert \mathrm{CT(l)}\rangle = \frac{1}{\sqrt{12}}\{-2\lvert \mathrm{CAS_0}\rangle - \lvert \mathrm{ACS_0}\rangle + \lvert \mathrm{S_0CA}\rangle + 2\lvert \mathrm{S_0AC}\rangle + \lvert \mathrm{AS_0C}\rangle - \lvert \mathrm{CS_0A}\rangle\}$	E	E
$\lvert \mathrm{TT(d)}\rangle = \frac{1}{\sqrt{3}}\{\lvert \mathrm{TTS_0}\rangle + \lvert \mathrm{S_0TT}\rangle + \lvert \mathrm{TS_0T}\rangle\}$	A_1	A_1
$\lvert \mathrm{TT(e)}\rangle = \frac{1}{\sqrt{6}}\{-\lvert \mathrm{TTS_0}\rangle + 2\lvert \mathrm{S_0TT}\rangle - \lvert \mathrm{TS_0T}\rangle\}$	E	E
$\lvert \mathrm{TT(f)}\rangle = \frac{1}{\sqrt{2}}\{-\lvert \mathrm{TTS_0}\rangle + \lvert \mathrm{TS_0T}\rangle\}$	E	E

Table A.2. Symmetry adapted diabatic exciton basis and their irreducible representations of point group C_{4v} in pentacene J- and H- aggregate trimer (J4 and H4, respectively).

Symmetry adapted diabatic basis	Irreducible representation in J4	Irreducible representation in H4

$\lvert\mathrm{FE(a)}\rangle = \frac{1}{2}(-\lvert\mathrm{S_1S_0S_0S_0}\rangle + \lvert\mathrm{S_0S_1S_0S_0}\rangle - \lvert\mathrm{S_0S_0S_1S_0}\rangle + \lvert\mathrm{S_0S_0S_0S_1}\rangle)$	B_2	B_1
$\lvert\mathrm{FE(b)}\rangle = \frac{1}{2}(\lvert\mathrm{S_1S_0S_0S_0}\rangle - \lvert\mathrm{S_0S_1S_0S_0}\rangle - \lvert\mathrm{S_0S_0S_1S_0}\rangle + \lvert\mathrm{S_0S_0S_0S_1}\rangle)$	E	E
$\lvert\mathrm{FE(c)}\rangle = \frac{1}{2}(-\lvert\mathrm{S_1S_0S_0S_0}\rangle - \lvert\mathrm{S_0S_1S_0S_0}\rangle + \lvert\mathrm{S_0S_0S_1S_0}\rangle + \lvert\mathrm{S_0S_0S_0S_1}\rangle)$	E	E
$\lvert\mathrm{FE(d)}\rangle = \frac{1}{2}(\lvert\mathrm{S_1S_0S_0S_0}\rangle + \lvert\mathrm{S_0S_1S_0S_0}\rangle + \lvert\mathrm{S_0S_0S_1S_0}\rangle + \lvert\mathrm{S_0S_0S_0S_1}\rangle)$	A_2	A_1
$\lvert\mathrm{CT(i)}\rangle = \frac{1}{\sqrt{8}}(\lvert\mathrm{CAS_0S_0}\rangle + \lvert\mathrm{ACS_0S_0}\rangle + \lvert\mathrm{S_0CAS_0}\rangle + \lvert\mathrm{S_0ACS_0}\rangle + \lvert\mathrm{S_0S_0CA}\rangle + \lvert\mathrm{S_0S_0AC}\rangle + \lvert\mathrm{AS_0S_0C}\rangle + \lvert\mathrm{CS_0S_0A}\rangle)$	A_2	A_1
$\lvert\mathrm{CT(j)}\rangle = \frac{1}{2}(\lvert\mathrm{S_0CAS_0}\rangle + \lvert\mathrm{S_0ACS_0}\rangle - \lvert\mathrm{AS_0S_0C}\rangle - \lvert\mathrm{CS_0S_0A}\rangle)$	E	E
$\lvert\mathrm{CT(k)}\rangle = \frac{1}{2}(\lvert\mathrm{CAS_0S_0}\rangle + \lvert\mathrm{ACS_0S_0}\rangle - \lvert\mathrm{S_0S_0CA}\rangle - \lvert\mathrm{S_0S_0AC}\rangle)$	E	E
$\lvert\mathrm{CT(l)}\rangle = \frac{1}{\sqrt{8}}(\lvert\mathrm{CAS_0S_0}\rangle - \lvert\mathrm{ACS_0S_0}\rangle - \lvert\mathrm{S_0CAS_0}\rangle + \lvert\mathrm{S_0ACS_0}\rangle + \lvert\mathrm{S_0S_0CA}\rangle - \lvert\mathrm{S_0S_0AC}\rangle - \lvert\mathrm{AS_0S_0C}\rangle + \lvert\mathrm{CS_0S_0A}\rangle)$	B_2	B_1
$\lvert\mathrm{CT(m)}\rangle = \frac{1}{\sqrt{8}}(\lvert\mathrm{CAS_0S_0}\rangle - \lvert\mathrm{ACS_0S_0}\rangle + \lvert\mathrm{S_0CAS_0}\rangle - \lvert\mathrm{S_0ACS_0}\rangle + \lvert\mathrm{S_0S_0CA}\rangle - \lvert\mathrm{S_0S_0AC}\rangle + \lvert\mathrm{AS_0S_0C}\rangle - \lvert\mathrm{CS_0S_0A}\rangle)$	A_1	A_2
$\lvert\mathrm{CT(n)}\rangle = \frac{1}{2}(\lvert\mathrm{S_0CAS_0}\rangle - \lvert\mathrm{S_0ACS_0}\rangle - \lvert\mathrm{AS_0S_0C}\rangle + \lvert\mathrm{CS_0S_0A}\rangle)$	E	E
$\lvert\mathrm{CT(o)}\rangle = \frac{1}{2}(-\lvert\mathrm{CAS_0S_0}\rangle + \lvert\mathrm{ACS_0S_0}\rangle + \lvert\mathrm{S_0S_0CA}\rangle - \lvert\mathrm{S_0S_0AC}\rangle)$	E	E
$\lvert\mathrm{CT(p)}\rangle = \frac{1}{\sqrt{8}}(\lvert\mathrm{CAS_0S_0}\rangle + \lvert\mathrm{ACS_0S_0}\rangle - \lvert\mathrm{S_0CAS_0}\rangle - \lvert\mathrm{S_0ACS_0}\rangle + \lvert\mathrm{S_0S_0CA}\rangle + \lvert\mathrm{S_0S_0AC}\rangle - \lvert\mathrm{AS_0S_0C}\rangle - \lvert\mathrm{CS_0S_0A}\rangle)$	B_1	B_2
$\lvert\mathrm{TT(e)}\rangle = \frac{1}{2}(\lvert\mathrm{TTS_0S_0}\rangle + \lvert\mathrm{S_0TTS_0}\rangle + \lvert\mathrm{S_0S_0TT}\rangle + \lvert\mathrm{TS_0S_0T}\rangle)$	A_1	A_1
$\lvert\mathrm{TT(f)}\rangle = \frac{1}{\sqrt{2}}(-\lvert\mathrm{TTS_0S_0}\rangle + \lvert\mathrm{S_0S_0TT}\rangle)$	E	E

$\|\mathrm{TT(g)}\rangle = \frac{1}{\sqrt{2}}(\|\mathrm{S_0TTS_0}\rangle - \|\mathrm{TS_0S_0T}\rangle)$	E	E
$\|\mathrm{TT(h)}\rangle = \frac{1}{2}(-\|\mathrm{TTS_0S_0}\rangle + \|\mathrm{S_0TTS_0}\rangle - \|\mathrm{S_0S_0TT}\rangle + \|\mathrm{TS_0S_0T}\rangle)$	B_2	B_2

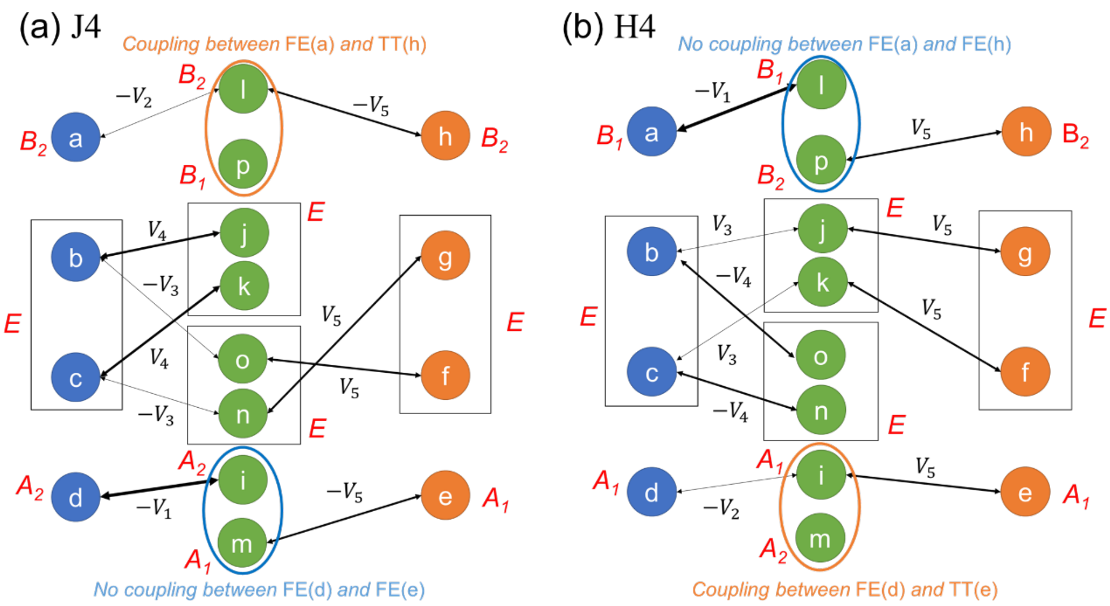

$$V_1 = \sqrt{2}(|V_{\mathrm{HH}}| + |V_{\mathrm{LL}}|) = 357\ \mathrm{meV}$$

$$V_2 = \sqrt{2}(|V_{\mathrm{HH}}| - |V_{\mathrm{LL}}|) = 74\ \mathrm{meV}$$

$$V_3 = |V_{\mathrm{HH}}| - |V_{\mathrm{LL}}| = 52\ \mathrm{meV}$$

$$V_4 = |V_{\mathrm{HH}}| + |V_{\mathrm{LL}}| = 253\ \mathrm{meV}$$

$$V_5 = \sqrt{3}|V_{\mathrm{LH}}| = 254\ \mathrm{meV}$$

Figure A.1. Electronic couplings between symmetry adapted diabatic basis {FE(x) [x = a-d], CT(x) [x = i-p], TT(x) [x = e-h]}. The red characters indicate the irreducible representation of each basis for point group C_{4v}. The two direction arrows with corresponding non-zero electronic couplings are also shown.

References

(1) M. Nakano, *J. Chem. Phys*. **2019**, *150*, 234305.
(2) T. C. Berkelbach, M. S. Hybertsen, D. R. Reichman, *J. Chem. Phys.* **2013**, *138*, 114102.
(3) T. C. Berkelbach, M. S. Hybertsen, D. R. Reichman, *J. Chem. Phys.* **2013**, *138*, 114103.
(4) R. van Grondelle, J. P. Dekker, T. Gillbro, V. Sundström, *Biochim. Biophys. Acta.* **1994**, *1187*, 1-65.

(5) G. McDermott, S. M. Prince, A. A. Freer, A. M. Hawthornthwaite-Lawless, M. Z. Papiz, R. J. Cogdell, N. W. Isaacs, *Nature*. **1995**, *374*, 517-521.

(6) T. Pullerits, V. Sundström, *Acc. Chem. Res.* **1996**, *29*, 381-389.

(7) K. Kuroda, K. Yazaki, Y. Tanaka, M. Akita, H. Sakai, T. Hasobe, N. V. Tkachenko, M. Yoshizawa, *Angew. Chem. Int. Ed.* **2019**, *58*, 1115-1119.

(8) M. Nakano, S. Ito, T. Nagami, Y. Kitagawa, T. Kubo, *J. Phys. Chem. C.* **2016**, *120*, 22803-22816.

(9) M. Nakano, T. Nagami, T. Tonami, K. Okada, S. Ito, R. Kishi, Y. Kitagawa, T. Kubo, *J. Comput. Chem.* **2019**, *40*, 89-104.

(10) M. Takahata, M. Nakano, H. Fujita, K. Yamaguchi, *Chem. Phys. Lett.* **2002**, *363*, 422-428.

(11) S. Ito, M. Nakano, *J. Phys. Chem. C* **2015**, *119*, 148−157.

(12) S. Hirata, M. Head-Gordon, *Chem. Phys. Lett.*, **1999**, *314*, 291-299.

(13) M. B. Smith, J. Michl *Chem. Rev*. **2010**, *110*, 6891-6936.

(14) M. B. Smith, J. Michl *Annu. Rev. Phys. Chem.* **2013**, *64*, 361-386.

(15) L. Wang, Y. Olivier, O. V. Prezhdo, D. Beljonne, *J. Phys. Chem. Lett.* **2014**, *5*, 3345-3353.

(16) M. J. Frisch, G. W. Trucks, H. B. Schlegel, G. E. Scuseria, M. A. Robb, J. R. Cheeseman, G. Scalmani, V. Barone, B. Mennucci, G. A. Petersson et al. GAUSSIAN 09, Revision B.01, Gaussian, Inc., Wallingford, CT, 2010.

(17) T. C. Berkelbach, M. S. Hybertsen, D. R. Reichman, *J. Chem. Phys.* **2013**, *138*, 114102.

(18) H.-P. Breuer and F. Petruccione, The Theory of Open Quantum Systems (Oxford University Press, 2002).

(19) G. Tao *J. Phys. Chem. C* **2014**, *118*, 27258−27264.

(20) A. Girlando, L. Grisanti, M. Masino, A. Brillante, R. G. Della Valle, E. Venuti *J. Chem. Phys.* **2011**, *135*, 084701.

Chapter 2.

Theoretical Study on Singlet Fission Dynamics in Asymmetric Ring-Shaped Aggregate Systems

We investigate the singlet fission (SF) dynamics of asymmetric pentacene ring-shaped aggregate model constructed by rotating each pentacene unit around its longitudinal axis in H-aggregate ring. Using quantum master equation method, we explored how the aggregate size (*N*) and rotation angle (α) influence the SF rates and double-triplet (TT) yields. It is found that, for each *N*, there exist optimal ranges of α yielding efficient SF with both high SF rates and TT yields.

For example, in 8-mer model, SF rates at α = 23˚ and 43º are 18.9 and 38.6 times as high as that at α = 30º, respectively, and the TT yields are as high as 87.1 %, 98.8 %, and 88.2 % at α = 23˚, 30˚ and 43º, respectively. Analysis of the relative relaxation factors (RRFs) reveals the novel acceleration mechanism of SF by opening many-to-many relaxation paths from adiabatic Frenkel exciton (FE)-like states to TT-like states at optimal α and *N* ranging from 30–40º in *N* > 7.

This mechanism is interpreted via second-order perturbation theory for electronic couplings. Specifically, the energy inequalities of the charge-transfer (CT) states (the CA and AC states) and the changes in amplitude and sign of the couplings between the FE, CT, and TT states give rise to a FE/TT mixing. This breakdown of quantum interference effect contributes to the high TT yield and SF rate. The present results advance our understanding of SF dynamics in ring-shaped aggregates and provide new design guidelines for future SF materials development.

1. Introduction

In previous Chapter II.1, we have investigated the size and configuration dependences of SF dynamics in symmetric J- and H- ring-shaped aggregate models.[1] It has been revealed by the group theoretical approach that the structural symmetry of the lowest adiabatic FE-like exciton states for the ring-flipping operations affect the SF dynamics, which negatively influences the SF efficiency in J-ring and H-even ring models. In other words, there probably exist optimal structures between the J- and H- aggregate systems, and understanding the SF dynamics in such broken symmetry systems with respect to the ring-flipping operations may provide more comprehensive guidelines for SF material design. This inspired us to investigate SF dynamics in asymmetric ring-shaped systems shown in **Figure II.2.1**, which possess asymmetric structures between J- and H-aggregates. The structure of this model can be constructed asymmetrically to the ring-flipping operations by rotating each pentacene by α degrees around its longitudinal axis in H-aggregate systems. The present study is important to clarify in more detail and quantitatively the effects of the structural asymmetry, which depends on the rotation angle and the number of monomers, on the SF rate and TT yield, for constructing practical design guidelines for ring-shaped molecular aggregates for efficient SF.

We here examine the size (*N*) and α dependences of SF dynamics in the asymmetric ring-shaped aggregate systems using the quantum master equation (QME) method.[2–6] The SF dynamics is analyzed based on relative relaxation factor (RRF) analysis, which is useful to reveal the primary SF paths between adiabatic exciton states (eigenstates of exciton Hamiltonian) and the contribution of exciton overlap in each relaxation path. In addition, we examined the perturbative approach to discuss the origin of FE/TT mixing at lowest FE' states from the viewpoint of the quantum interference effect. These results are expected to contribute to the development of more general and fundamental SF design guidelines for ring-shaped aggregate systems with various monomer configurations and sizes.

2. Model and Methods

2.1. Model Structure

In this study, we investigated SF dynamics in pentacene asymmetric ring-shaped aggregate models (**Figure II.2.1**). The structural optimization of pentacene monomer was performed using the RB3LYP/cc-pVDZ method by Gaussian09.[7] The asymmetric aggregate structure was defined by the aggregate size *N* and rotation angle *α*. The $\alpha = 0^{\circ}$ structure was defined as an H-ring *N*-mer with $d = 4.0$ Å, where *d* indicates the intermolecular distance between the middle carbon atoms at the inner zigzag edges. Asymmetric ring N-mer was defined by rotating the monomers counterclockwise by α around their longitudinal axes in the H-ring N-mer with fixed ring radius R (distance from the center of the ring to the center of mass of the monomer) as $l + 4.0/2\cos(\pi/N)$ Å, where l represents half C–C distance along pentacene short axis. Each monomer was given a clockwise number.

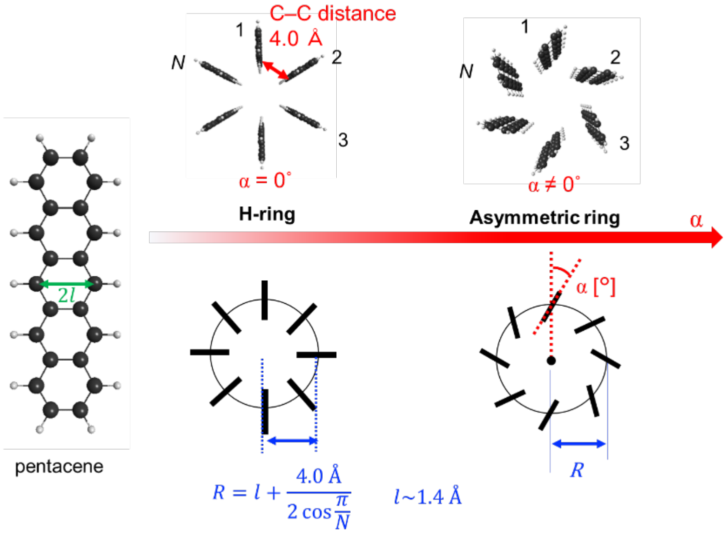

Figure II.2.1 Pentacene H-(left) ring-shaped aggregate structure and asymmetric ring-shaped aggregate models with all units of the H-ring rotated by α around the longitudinal axis of pentacene monomers.

2.2. Exciton Hamiltonian

The diabatic exciton basis and exciton Hamiltonian were introduced in the same formula as previous Chapter II.1. For pentacene ring-shaped aggregate structure, the diabatic exciton state basis was described in eq. (II.1.2), and the exciton Hamiltonian is described as eqs. (II.1.3) – (II.1.9). In asymmetric structure with α ≠ 0°, the energy of neighboring two CT states, E_{CA} and E_{AC}, is not identical. Furthermore, the amplitudes of V_{HL} and V_{LH} become different in asymmetric dimer structure.

2.3. Computational Detail of Electronic Coupling

The geometrical optimization of pentacene molecule was performed at the level of RB3LYP/cc-pVDZ. We here employed the diabatization method using complete active space configuration interaction (CASCI) method, which has been proposed by Ma et al.[8] First, the reference molecular orbital (MO) set of each monomer A and B were obtained from CAM-B3LYP/cc-pVDZ. Then, the localized orthonormal orbital set of the dimer $\{\varphi^{\mathrm{LO}}\}$ was constructed by symmetrical orthogonalization from the MOs $\{\phi\}$ in dimer AB in the active and core orbital spaces, and the overlap matrix $\boldsymbol{S}$ was obtained for the neighboring dimer structures. The localized orthonormal orbitals φ^{LO} were obtained by

$$\varphi^{\mathrm{LO}} = \boldsymbol{S}^{-\frac{1}{2}}\phi \tag{II.2.1}$$

Note here that included only core and active space orbitals in the orthonormalization, and φ^{LO} shows localization close to the distributions of the highest occupied molecular orbitals (HOMO) and the lowest unoccupied molecular orbitals (LUMO) of each monomer A and B. The wave functions of 5 diabatic exciton states $|\Psi_i\rangle$ corresponding to S_1S_0, S_0S_1, CA, AC, and TT in dimer models are written in eqs. (I.1.18) – (I.1.22) in General Introduction. Since results of CASCI(4e,4o) calculations gives wavefunctions of 20 eigenstates $|\Phi_a\rangle$ as a linear combination of configuration state functions (CSFs) including$|\Psi_i\rangle$:

$$|\Psi_i\rangle = \sum_a |\Phi_a\rangle\langle\Phi_a|\Psi_i\rangle = \sum_a C_{ia}\,|\Phi_a\rangle \tag{II.2.2}$$

where $C_{ia} = \langle\Phi_a|\Psi_i\rangle$ is the expansion coefficients of diabatic state $|\Psi_i\rangle$ in adiabatic states $|\Phi_a\rangle$. Then, the energy of diabatic state ε_i and electronic couplings V_{ij} between diabatic states i and j are calculated from the expansion coefficients C_{ia} and adiabatic state energy E_a as

$$\varepsilon_i = \langle\Psi_i|H_{\mathrm{ex}}|\Psi_i\rangle = \sum_a |C_{ia}|^2 E_a \tag{II.2.3}$$

$$V_{ij} = \langle\Psi_i|H_{\mathrm{ex}}|\Psi_j\rangle = \sum_a C_{ia}^* C_{ja} E_a \tag{II.2.4}$$

Then, the energies of diabatic states are shifted so that the TT state energy was shifted to twice the lowest triplet excited state at the level of Tamm-Dancoff approximation (TDA) method using CAM-B3LYP/cc-pDZ level, that is, $E(\mathrm{TT}) \sim 2E(\mathrm{T}_1) = 2072$ meV. Furthermore, the energies of diabatic FE states are defined as the average of diabatic state energies $E(\mathrm{S}_1\mathrm{S}_0)$ and $E(\mathrm{S}_0\mathrm{S}_1)$ obtained from the CI calculation in the dimer model, because the $E(\mathrm{S}_1\mathrm{S}_0)$ and $E(\mathrm{S}_0\mathrm{S}_1)$ are almost the same values and the identical energy of FE state is required in the ring-shaped model as mentioned before.

Comparing with the method in previous Chapter II.1, which performed separate approximations for different coupling parameters, the method used here is preferable in that it treats all couplings at the same level of approximation. These two approaches produce quantitatively different results. For example, it is found that the CASCI based method produce larger amplitude of V_{ex} comparing with the method used in previous chapter. However, these two methods lead to the same conclusions regarding the qualitative properties discussed in this chapter.

The diabatic state energy and the electronic couplings are compared with those obtained by the method used in Chapter II.1, where the V_{ex} and CT state energies are evaluated using the Mulliken transition density and charge density, respectively, and the Fock matrices are calculated using the non-orthogonal HOMO and LUMO between the monomers.

2.4. Quantum Master Equation

For the SF dynamics simulation, we performed the eight-step and sixth-order Runge-Kutta method to solve the second-order time-convolutionless QME under Markov approximation mentioned in previous Chapter II.1. We consider only Holstein coupling, which causes the fluctuation in the excitation energy and is known to be primarily related to the C-C bond stretching modes of pentacene.[3] The vibronic coupling parameters for Ohmic spectral density with Lorentz–Drude cutoff frequency is represented as reorganization energies λ and cut-off frequency Ω_c and they are set to 50 and 180 meV, respectively, for all diabatic exciton states.[2,3] The temperature T is set to 300 K. We also evaluated the SF rate k and TT yield a, which are obtained by fitting the time evolution of TT exciton populations $P_{\mathrm{TT}}(t)$ with a single exponential function $P_{\mathrm{TT}}(t) = a - b\exp(-kt)$ with an initial population of $|\mathrm{S}_1\mathrm{S}_0 \cdots \mathrm{S}_0\rangle$ is 100 %. The time range for fitting $P_{\mathrm{TT}}(t)$ is taken so that the fitting of the TT population by the single exponential function gives a reliable value of the TT yield. As in the previous Chapter, in order to clarify the origin of the exciton dynamics in SF, we perform RRF analysis[1,4–6] to reveal the relaxation between the adiabatic exciton states.

3. Results and Discussion

3.1. α-Dependence of Electronic Coupling in 8-mer Model

We here show α dependences of the FE and CT state energies and electronic couplings for 8-mer models in **Figure II.2.2 (a)** and **(b)**, respectively. As mentioned before, the TT state energy is shifted to 2072 meV, and the FE state energy is shown to be almost stationary around 2297±3 meV. Note here that at $\alpha = 0^\circ$, the energies of CA and AC are equal to each other, while at $\alpha \neq 0^\circ$, the energy of AC is lower than the energy of CA. The FE coupling V_{ex} shows larger values than 100 meV at small α (< 23°), which decreases monotonically to 0 meV until α ~ 41°, and turns to negative at α > 42°. Furthermore, all the electronic couplings V_{ij} are found to be positive in sign at α < 30° because of their H-ring-like structures, the V_{HH} and V_{HL} turn to negative in sign at α > 30° on the contrary to the V_{LL} and V_{LH}. Although the values of these diabatic state energies and coupling parameters depend on how the structure of the aggregate model is defined (for example, increasing the distance d between the neighboring monomers or the radius R of the ring is expected to result in weaker couplings and higher energies of the CT states), their general N- and α-dependences are expected to show qualitatively the same trend.

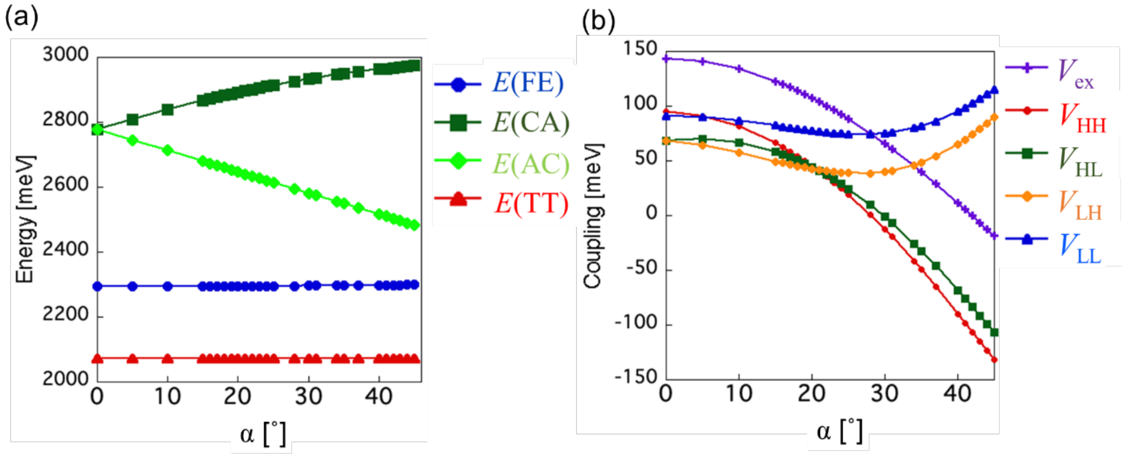

Figure II.2.2. α Dependences of CA and AC energies (a), and V_{ij} ($i, j = h$ or l) and $V_{\rm ex}$ (b) for the 8-mer models (see Figure II.2.1).

3.2. α-Dependence of SF Rate and TT Yields in 8-Mer Model

We first discuss the variation of SF rate k and TT yield a with respect to α in the ring-shaped aggregate 8-mer model. The result in 8-mer is found to be in good agreement with those in the intermediate N-mer (N = 6–12) models. **Figures II.2.3 (a)–(f)** show the time evolutions of populations of diabatic FE, CT, and TT exciton states at α = 0º, 15˚, 16º, 23º, 30˚ and 43º, respectively. It is found at α = 0º–15º, the diabatic TT population does not show a single exponential time evolution thus the SF rate k cannot be defined. In these systems, TT yields are too low around a = 2.98 – 34.2 % (**Figure II.2.3 (a)** and **(b)**). In contrast, it is shown that the TT population increases single-exponentially and is able to define k when α > 16º (**Figure II.2.3 (c)**). At intermediate α = 23º (**Figure II.2.3 (d)**), 30º (**Figure II.2.3** (e)), and 43˚ (**Figure II.2.3 (f)**), higher TT yields (a = 87.1 %, 98.8 %, and 88.2 %, respectively) are observed than at α = 16º (a = 40.3 %). It is notably found that SF rates at α = 23º and 43˚ (k = 6.56 and 13.4 ps^{-1}) are 18.9 and 38.6 times as high as that at α = 30˚ (k = 0.347 ps^{-1}), whereas the TT yields at α = 23º and 43˚ are slightly less than that at α = 30º. Both SF rate and TT yield at α = 43º are shown to be higher than those at α = 23º, which indicates that more efficient SF occurs at α = 43º than at α = 23º.

(a) $\alpha = 0°$ $a = 2.98\ \%$, $k =$ -

(b) $\alpha = 15°$ $a = 34.2\ \%$, $k =$ -

(c) $\alpha = 16°$ $a = 40.3\ \%$, $k = 4.24\ \text{ps}^{-1}$

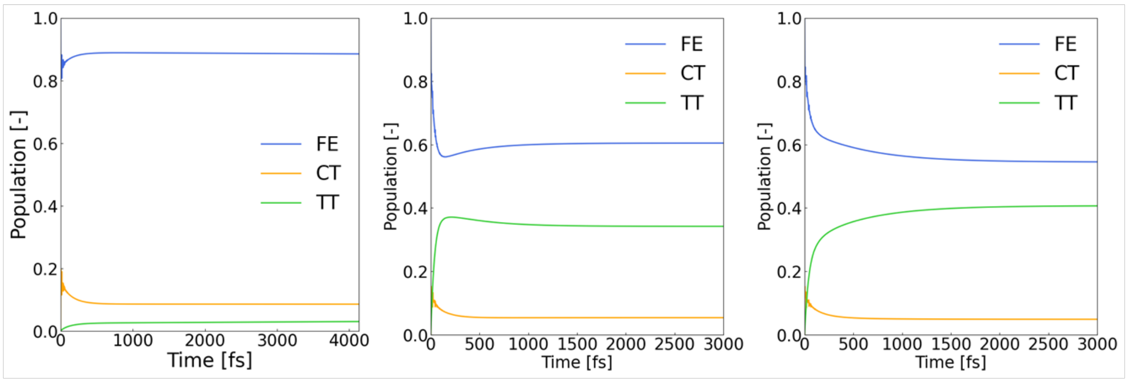

(d) $\alpha = 23°$ $a = 87.1\ \%$, $k = 6.56\ \text{ps}^{-1}$

(e) $\alpha = 30°$ $a = 98.8\ \%$, $k = 0.347\ \text{ps}^{-1}$

(f) $\alpha = 43°$ $a = 88.2\ \%$, $k = 13.4\ \text{ps}^{-1}$

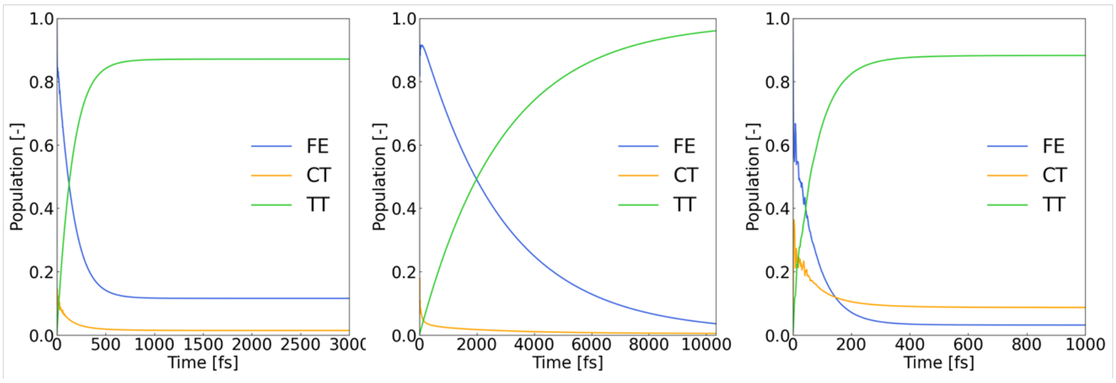

Figure II.2.3. Time evolution of diabatic FE (blue line), CT (yellow line), and TT (green line) exciton states in the pentacene symmetric or asymmetric 8-mer models at α = 0° (a), 15° (b), 16° (c), 23°(d), 30° (e), and 43°(f).

To capture the general trends of *k* and *a* for α, we examine their plots as a function of α in the 8- models (see **Figure II.2.4**). It is found that the TT yield increases at $15° \leq \alpha \leq 30°$ and the peak of the SF rate appears in this range of α $[(k_{\text{peak}}, \alpha_{\text{peak}}) = (6.56\ \text{ps}^{-1}, 23°)]$. This trend is interpreted as the acceleration process derived from the near-degeneration of the lower-lying adiabatic FE' states and TT' manifold, which is discussed again in section 3.3. It is also found that the high TT yield and the low SF rate are shown from the α_{peak} to 37° (for the 8-mer). After that, the SF rate is shown to dramatically increase with increasing α with a gradual decrease of TT yield. It is found that if α is too large, the TT yield is expected to significantly decrease, resulting in poor SF efficiency. This suggests the existence of an optimal region of α for highly efficient SF in the present ring-shaped aggregates. The reason for such behavior of *k* and *a* is discussed in section 3.3 using the RRF analysis. It is also predicted that *k* can be defined within a narrower range of α as N increases, which implies that the range of α yielding efficient SF also becomes narrower. The size dependence of this range of α is discussed in section 3.3.

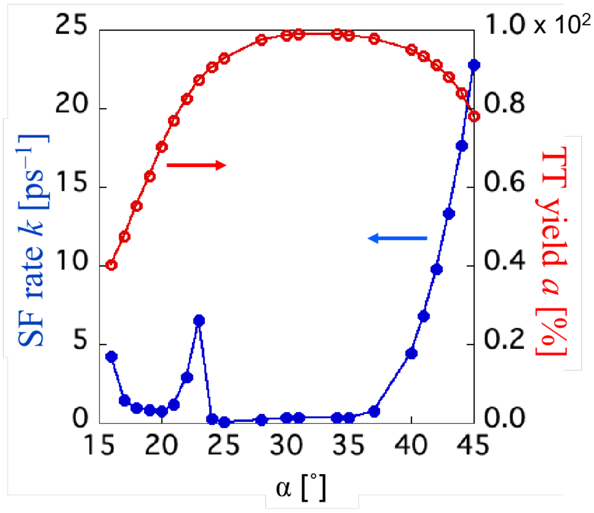

Figure II.2.4. Variations of SF rate k [ps^{-1}] (blue line) and TT yields a (red line) of ring-shaped 8-mer (16˚≤ α ≤ 45˚) model

3.3. Mechanisms for Acceleration of SF Dynamics

In order to clarify the origin of (1) the peak of SF rate at α = 23˚, (2) the decrease of SF rate at α = 30˚, and (3) dramatical increase of SF rate with gradual decrease of TT yield at α > 37˚, RRF analysis is applied to the 8-mer models with plural α, and the acceleration mechanisms at and 43˚. As well as in Chapter II.1, we define three types of bases, that is, diabatic exciton basis, adiabatic exciton basis, and symmetry-adapted linear combination (SALC) of diabatic exciton basis. The SALC bases are obtained so that they diagonalize each diabatic exciton block of the H_{ex} matrix in the diabatic representation, and are labeled $\{|X^{*}\rangle\}$ (X = FE, CA, AC, TT). They are also the symmetry-adapted linear combinations of the diabatic exciton bases for C_{Nh}-symmetry. According to the Hückel method for ring annulenes, these SALC diabatic bases are described as

$$|X_l^{*}\rangle = \frac{1}{\sqrt{N}}\sum_{m=1}^{N}\exp\left(i\frac{2\pi ml}{N}\right)|X_m\rangle \qquad (l = 1,2,\dots,N) \qquad (\mathrm{II}.2.5)$$

where the energies of SALC exciton bases {FE*, CA*, AC*, TT*} are given by $E_{\mathrm{FE}} + 2V_{\mathrm{ex}}\cos(2\pi l/N)$, E_{CA}, E_{AC}, and E_{TT}, respectively. The phase distribution, energy in $V_{\mathrm{ex}} > 0$, and number of nodes for $l = 1,2,\dots,N$ is summerized in **Figure II.2.5**. The l'th and (N – l)'th adiabatic exciton states denoted as $|X_l'\rangle$ and $|X_{N-l}'\rangle$ with $l \neq N$ (and $l \neq N/2$ for even-rings) whose principal components are $|X_l^{*}\rangle$ and $|X_{N-l}^{*}\rangle$, respectively, are degenerated due to the rotational symmetric structure. Thus, in the ring-shaped 8-mer models, the adiabatic FE’ and TT’ exciton states are labeled {FE’(a–e), TT’(f–j)}, where label a–j corresponds to l (or a pair of l and $N - l$) in eq (II.2.5). We describe FE’(a)–(e) in the order of decreasing number of nodes. For example, the SA diabatic FE* states for $l = N/2$ (= 4 in the 8-mer) and for $l = N$ (= 8 in the 8-mer) correspond to FE’(a) and FE’(e), respectively, in the sense that these adiabatic FE’(a) and FE’(e) include $\left|\mathrm{FE}^*_{N/2}\right\rangle = \frac{1}{\sqrt{N}}\sum_{m=1}^{N}(-1)^m\left|\mathrm{FE}_m\right\rangle$ and $\left|\mathrm{FE}^*_{N}\right\rangle = \frac{1}{\sqrt{N}}\sum_{m=1}^{N}\left|\mathrm{FE}_m\right\rangle$. We defined the TT’ states TT’(f)–TT’(j) correspond to SA TT* basis in the order of increasing number of nodes, following the notation of our previous study on symmetric H- and J- aggregate models in Chapter II.1, and the TT’(f) and TT’(j) correspond to $\left|\mathrm{TT}^*_{N}\right\rangle$ and $\left|\mathrm{TT}^*_{N/2}\right\rangle$, respectively.

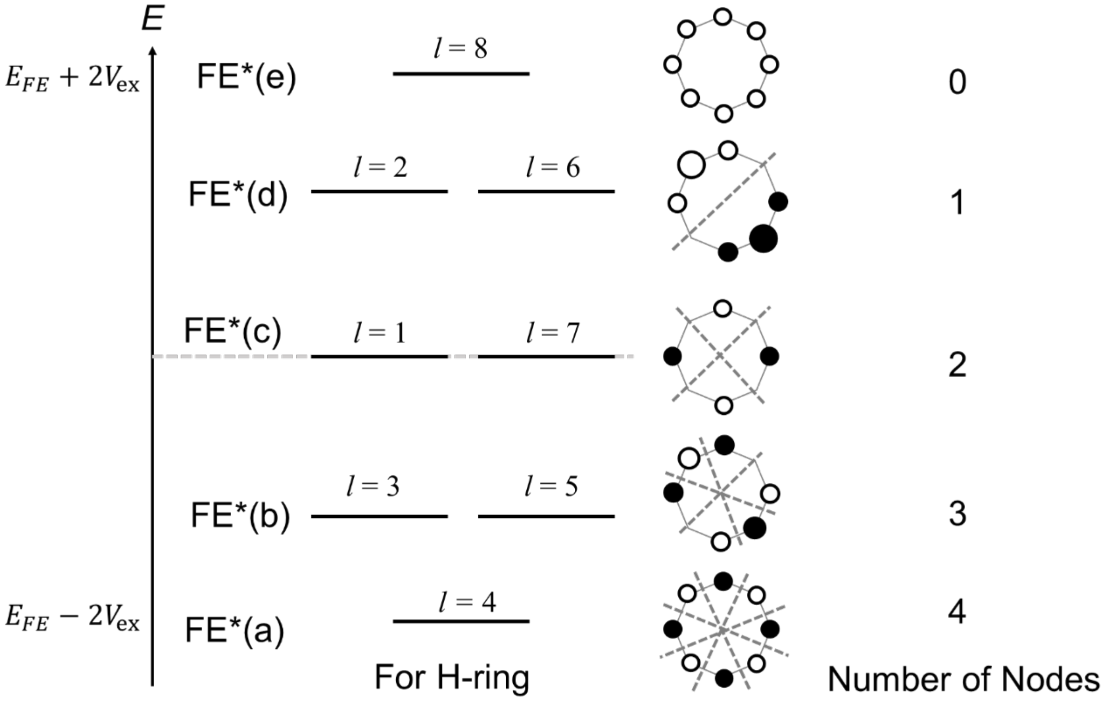

Figure II.2.5. Davydov splitting structure, phase distribution, and number of nodes in H-type ring.

Figure II.2.6 shows the energy diagram with the primary RRFs between the adiabatic states [FE’ manifold (a–e) and TT’ manifold (f–j)] in the 8-mer ring-shaped aggregate model at α = 23°, which shows a significant peak of SF rate (k = 6.56 ps^{-1}) and high TT yield (a = 87.1 %). The spatial distributions of diabatic excitons {FE, CT, TT} in each monomer are shown for adiabatic states FE’(a), (b) and TT’(i), (j). It is shown that the FE’ manifold (a-e) exhibits a wide energy band, while the TT’ manifold (f-j) is almost degenerate, and the lowest FE’(a) states are close to the TT’ manifold (E_{aj} = 3.9 meV). As a result, the FE/TT mixing increases, that is, the adiabatic FE’(a) and TT’(j) states involve SA diabatic TT*(j) and FE*(a) configurations, respectively (see the plot of the exciton density distributions for FE’(a) and TT’(j)). It is found that this FE/TT mixing increases the exciton overlaps between TT’(j) and other adiabatic FE’ states. As a result, the RRFs from higher-lying FE’ states to TT’(j) are found to become large, which leads to the acceleration of SF process.

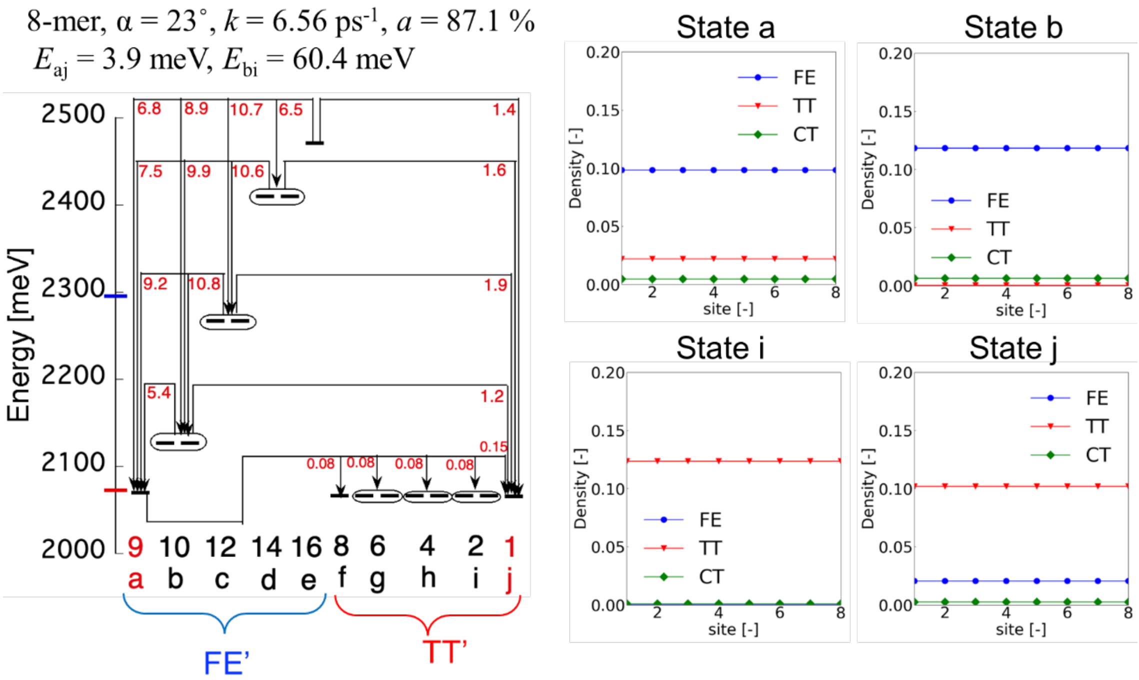

Figure II.2.6 Adiabatic exciton state diagram for the pentacene ring-shaped 8-mer model at α = 23º, where arrows with primary RRFs [meV] indicate the direction of relaxation of the exciton population. The circled states indicate degenerate states. The numbers below each adiabatic state indicate the ascending order of energy, where the red numbers indicate the lowest state(s) in each adiabatic manifold {FE’(a-e) and TT’(d-f)}. $\boldsymbol{E_{pq}}$ [meV] indicates the energy difference between adiabatic states, $\boldsymbol{E_{pq} = E_p - E_q}$. The spatial distributions of adiabatic exciton states FE’(a), FE’(b), TT’(i), and TT’(j) are also shown. Here we show the large RRFs for $m \rightarrow n$ ($n = 1, \ldots, m - 1$), note that we omit the RRFs with less than 10% of the maximum amplitudes. RRFs in the TT’ manifold are omitted since they are rapidly delocalized in the TT’ manifold.

We show the energy diagram with RRFs in the 8-mer ring at α = 30º in **Figure II.2.7**. On the contrary to at α = 23º, it is found that the lowest FE’(a) states are far from the TT’ manifold (E_{aj} = 81.4 meV). In this case, fast relaxation from higher-lying adiabatic FE’ states to lower-lying FE’(a) occurs first, followed by the CT-mediated relaxation from the adiabatic FE’(a) state to TT’ states, which contributes to the SF. This is the reason why the SF rate is significantly smaller and the TT yield is higher (k = 0.347 ps^{-1} and a = 98.7 %) at α = 30°. Actually, the SF acceleration mechanism due to the near degeneracy of the lower-lying adiabatic FE' and TT' states has already been investigated in previous studies and in Chapter II.1.[1,4] Hereafter, we refer this acceleration mechanism originating from the degeneration of the lowest-FE' and TT' states as "type I mechanism".

According to our previous study on symmetric ring-shaped aggregate models, the lowest FE' state in H-aggregate models in even N-mer,[1] which correspond to FE'(a) at α = 0° in this model, is found to have no overlap with the diabatic TT states. This is because FE*(a) and TT*(j) belong to different irreducible representation (B_1 and B_2, respectively) in point group C_{Nv}, and behave differently for the ring-flipping symmetry operations (σ_v and σ_d). However, by breaking the ring-flipping symmetry, the mixing between FE*(a) and TT*(j) is found to become non-zero, which results in the existence of the optimal α for realizing the type I acceleration mechanism due to the near degeneracy of FE'(a) and TT'(j).

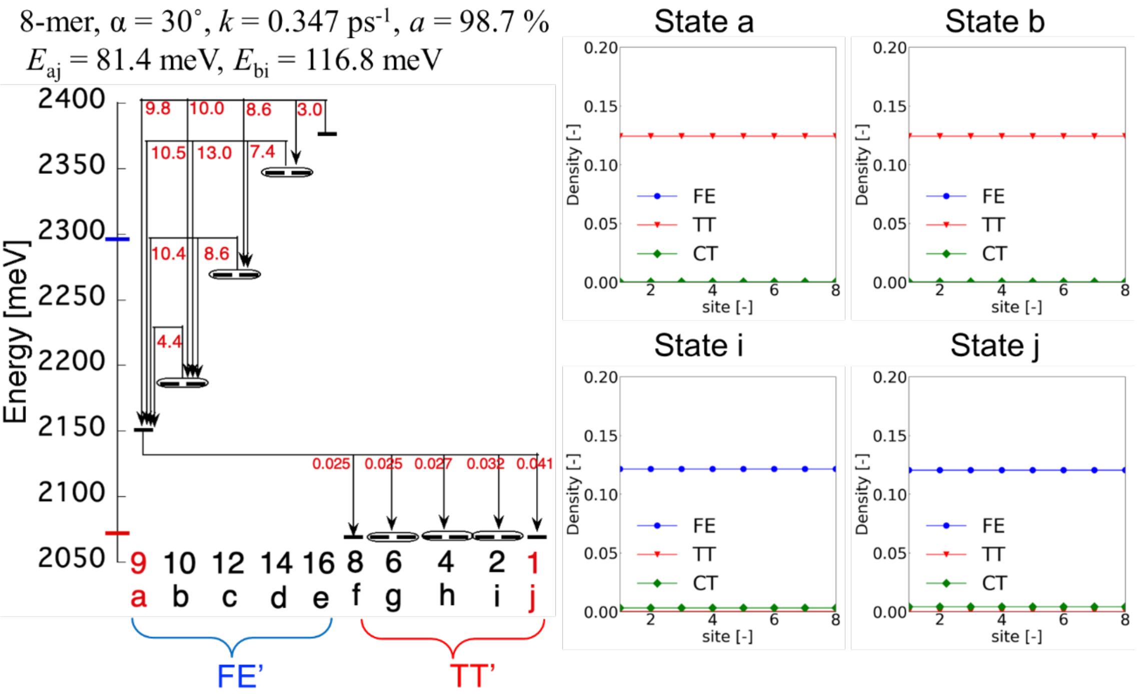

Figure II.2.7. Adiabatic exciton state diagram {FE'(a-e), TT'(f-j)} for the pentacene ring-shaped 8-mer model at α = 30°, where arrows with primary RRFs [meV] indicate the direction of relaxation of the exciton population. The spatial distribution of the exciton density in each adiabatic state is also shown. See the legend of Figure 6 for further explanation.

Next, RRF analysis of the 8-mer at α = 43° is performed to clarify the mechanism of the increase of SF rate in α ≥ 37°, that is, the reason for the relatively high TT yield (a = 88.2 %) and the fast SF (k = 13.4 ps^{-1}) process (Figure 7). The comparison of the 8-mers at α = 23° and 43° shows that the energy gap between the lowest FE' state and the TT' manifold is much larger at α = 43° (E_{ef} = 91.1) than at α = 23° (E_{aj} = 3.9 meV), which is the main reason for the relatively high TT yields at α = 43°. Interestingly, it turns out that more paths from FE' to TT' manifold contribute to the SF process at α = 43° (many-to-many relaxation), while the only paths from the FE' manifold to the TT'(j) state (many-to-one relaxation) contribute primarily to the acceleration of the SF process at α = 23°. This many-to-many relaxation at α = 43° is found to be caused by FE/TT mixing not only between the lower-lying FE' states and TT' states, but also between the higher-lying FE' states and the TT' manifold as shown in **Figure II.2.8 (b)**. This novel acceleration mechanism for SF induced by the enhancement of many-to-many relaxation paths from FE' to TT' is referred to as "type II mechanism".

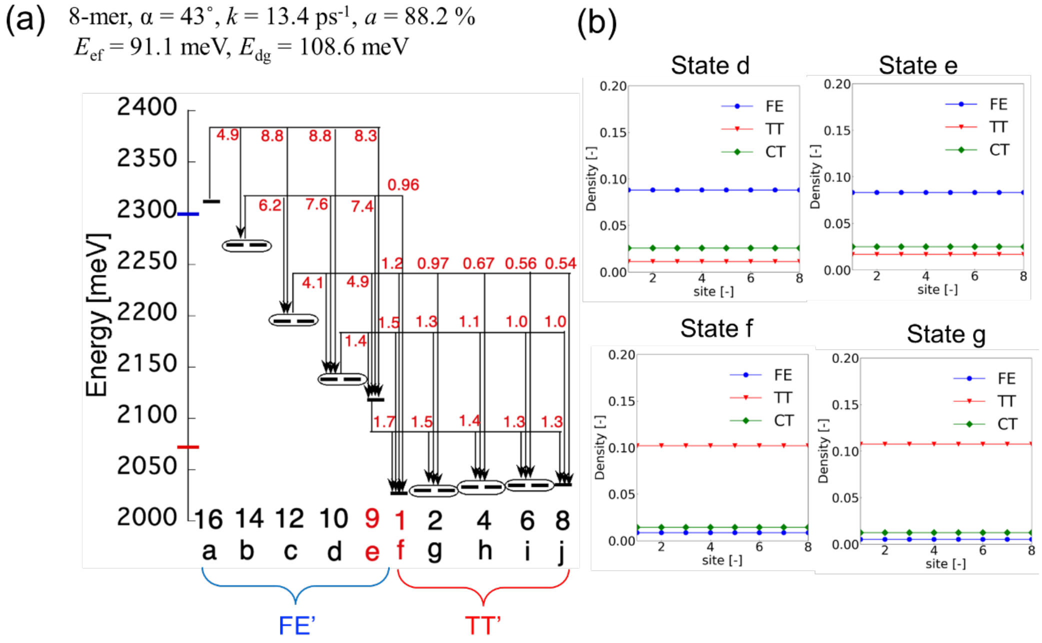

Figure II.2.8. Adiabatic exciton state diagram {FE'(a-e), TT'(f-j)} of the pentacene ring-shaped 8-mer model at α = 43°, where arrows with primary RRFs [meV] indicate the direction of relaxation of the exciton population. The spatial distribution of the exciton density in each adiabatic state is also shown in (b). See the legend of **Figure II.2.6** for further explanation.

3.4. α-Dependence of Adiabatic Energies and Wavefunctions in 8-mer Model

In order to more clarify the relationships between α, adiabatic state nature, and SF dynamics, we investigate the α dependences of the energies and the total configurations of diabats (the proportion of diabatic state X (= FE, CA, AC, TT) included in the adiabatic state p, or $\sum_{m\in X}|C_{mp}|^2$) in each adiabatic (FE', CA', AC', and TT') exciton state. The α dependences of adiabatic energy levels for $N = 8$ is shown in **Figure II.2.9**. Each bar representing an adiabatic exciton state is color-coded according to the contribution of the diabatic basis constituents.

It is found that from α = 0˚ to the α_{peak} = 23˚, the lowest FE' state energy is too low compared to the TT' states, resulting in low TT yield in this region. This is mainly because the absolute value of the FE coupling V_{ex} is too large (> 100 meV), resulting in a wide bandwidth of the FE' manifold. Indeed, efficient SF is found to occur due to smaller values of $|V_{\text{ex}}|$ at intermediate α larger than α_{peak}. It is found that α_{peak} = 23˚ correspond exactly to the α where the lowest FE' state is nearly degenerate with the TT' manifold. This indicates that the acceleration of SF for these α is caused by the type I mechanism. As increasing from α_{peak}=23˚ to α* = 37˚, the energy of the lowest FE' state (FE'$_{N/2}$) is shown to be larger than that of the TT' manifold and to increase with increasing α, which results in the increase of TT yield and the decrease of SF rate.

At α ≥ α*, where the SF rate starts to dramatically increase as shown in **Figure II.2.4**, it is found that the energy of the lowest FE' state (FE'$_N$) decreases with increasing α, and FE/TT mixing occurs between the lower-lying FE' states and the TT' manifold. Notably, this FE/TT mixing is found to occur without near-degeneration of FE' and TT' states (type II acceleration mechanism). It is found that because the diabatic AC (CA) state energy decreases with increasing N (see **Figure II.2.2**), adiabatic AC' (CA') states decrease and include more (less) diabatic FE and TT states as shown in **Figure II.2.9**. Thus, the indirect electronic coupling between FE and TT states via AC states is expected to contribute to FE/TT mixing more than that via CA states. Thus, we thought that the FE/TT mixing due to energy stabilization for one of CA or AC might be required for the type II SF acceleration.

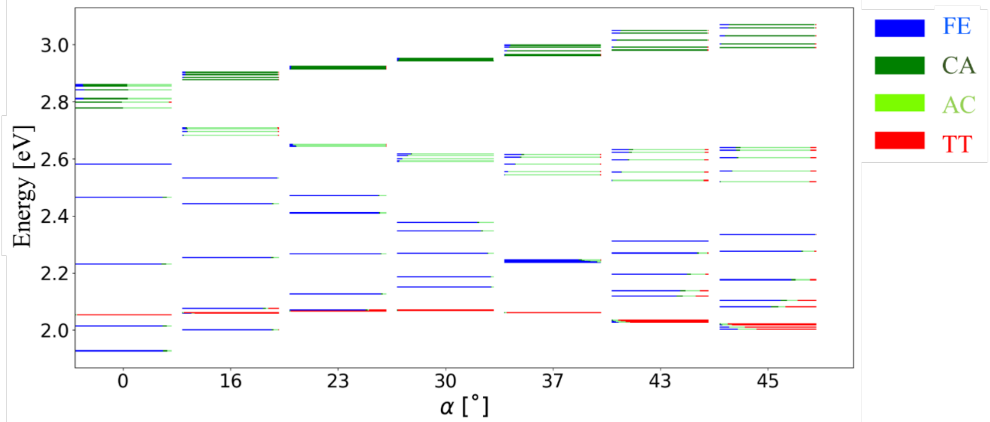

Figure II.2.9. α Dependence of adiabatic energy levels and their diabatic state contributions for $N = 8$. Each bar representing an adiabatic state is color-coded according to the contribution of diabatic FE (blue), CA (green), AC (light green), and TT (red) states.

The type II mechanism caused by symmetry breaking of the aggregate structure is explained using the second-order perturbation theory with intermediate normalized representation in 8-mer model. Let us focus on the off-diagonal matrix elements of the exciton Hamiltonian H_{ex} in the representation of the SALC exciton basis, and the large exciton overlaps between the higher-lying FE' and TT' manifolds derived not from CT-mediated, but from FE/TT mixing. We estimate the TT configuration of the adiabatic FE' using the second-order perturbation theory with the SALC diabatic basis as the zeroth-order approximation, which provides the approximate formulae for the results obtained from diagonalization of H_{ex}. The adiabatic FE' states corresponding to $\left|\mathrm{FE}_{N/2}^{*}\right\rangle$ and $\left|\mathrm{FE}_{N}^{*}\right\rangle$ approximated by the second-order perturbation theory before normalization are described as (see Appendix II.2 for derivation and discussion of the validity of the approximation)

$$\begin{aligned}\left|\mathrm{FE'}_{N/2}\right\rangle &= \left|\mathrm{FE}_{N/2}^{*}\right\rangle + \left|\mathrm{CA}_{N/2}^{*}\right\rangle \frac{V_{\mathrm{LL}}+V_{\mathrm{HH}}}{E_{\mathrm{FE}}-2V_{\mathrm{ex}}-E_{\mathrm{CA}}} - \left|\mathrm{AC}_{N/2}^{*}\right\rangle \frac{V_{\mathrm{LL}}+V_{\mathrm{HH}}}{E_{\mathrm{FE}}-2V_{\mathrm{ex}}-E_{\mathrm{AC}}} \\ &+\left|\mathrm{TT}_{N/2}^{*}\right\rangle \sqrt{\frac{3}{2}} \frac{V_{\mathrm{LL}}+V_{\mathrm{HH}}}{E_{\mathrm{FE}}-2V_{\mathrm{ex}}-E_{\mathrm{TT}}} \left(\frac{V_{\mathrm{LH}}}{E_{\mathrm{FE}}-2V_{\mathrm{ex}}-E_{\mathrm{CA}}} - \frac{V_{\mathrm{HL}}}{E_{\mathrm{FE}}-2V_{\mathrm{ex}}-E_{\mathrm{AC}}}\right) \qquad (\mathrm{II.2.6})\end{aligned}$$

$$\begin{aligned}\left|\mathrm{FE'}_{N}\right\rangle &= \left|\mathrm{FE}_{N}^{*}\right\rangle + \left|\mathrm{CA}_{N}^{*}\right\rangle \frac{V_{\mathrm{LL}}-V_{\mathrm{HH}}}{E_{\mathrm{FE}}+2V_{\mathrm{ex}}-E_{\mathrm{CA}}} + \left|\mathrm{AC}_{N}^{*}\right\rangle \frac{V_{\mathrm{LL}}-V_{\mathrm{HH}}}{E_{\mathrm{FE}}+2V_{\mathrm{ex}}-E_{\mathrm{AC}}} \\ &+\left|\mathrm{TT}_{N}^{*}\right\rangle \sqrt{\frac{3}{2}} \frac{V_{\mathrm{LL}}-V_{\mathrm{HH}}}{E_{\mathrm{FE}}+2V_{\mathrm{ex}}-E_{\mathrm{TT}}} \left(\frac{V_{\mathrm{LH}}}{E_{\mathrm{FE}}+2V_{\mathrm{ex}}-E_{\mathrm{CA}}} + \frac{V_{\mathrm{HL}}}{E_{\mathrm{FE}}+2V_{\mathrm{ex}}-E_{\mathrm{AC}}}\right) \qquad (\mathrm{II.2.7})\end{aligned}$$

This implies that in symmetric H- (J-) even-rings, the expansion coefficient of $\left|\mathrm{TT}_{N/2}^{*}\right\rangle$ ($\left|\mathrm{TT}_{N}^{*}\right\rangle$) in the lowest FE' state denoted as $\mathrm{FE'}_{N/2}$ ($\mathrm{FE'}_{N}$) become zero due to the cancellation between the first and the second terms in parentheses in eqs (II.2.6) and (II.2.7), where $V_{\mathrm{LH}} = V_{\mathrm{HL}}$ ($V_{\mathrm{LH}} = -V_{\mathrm{HL}}$) and $E_{\mathrm{CA}} = E_{\mathrm{AC}}$. Hereafter, this cancelation between transition probability amplitudes via CA*- and AC*-mediate path is called "*quantum interference effects*". When $\alpha \neq 0^{\circ}$, however, this quantum interference effect is broken because $|V_{\mathrm{LH}}| \neq |V_{\mathrm{HL}}|$ and $E_{\mathrm{CA}} \neq E_{\mathrm{AC}}$. In this sense, the FE/TT mixing is originated from the asymmetric structure of neighboring dimers. This interpretation is useful for qualitative discussion on whether the sign of couplings contributes to the enhancement of FE/TT mixing or not.

Figure II.2.10 shows the α-dependences of the approximate contribution of TT* states (TT* coefficients in normalized $\left|\mathrm{FE'}_{N/2}\right\rangle$ or $\left|\mathrm{FE'}_{N}\right\rangle$ represented by eqs (II.2.6) and (II.2.7), respectively) in the lowest FE' state in the 8-mer model. The perturbed adiabatic state energy is also shown by diabatic state energy and couplings as

$$E_{\mathrm{FE'}(l=N/2)} = E_{\mathrm{FE}} - 2V_{\mathrm{ex}} + |V_{\mathrm{LL}}+V_{\mathrm{HH}}|^{2}\left(\frac{1}{E_{\mathrm{FE}}-2V_{\mathrm{ex}}-E_{\mathrm{CA}}} + \frac{1}{E_{\mathrm{FE}}-2V_{\mathrm{ex}}-E_{\mathrm{AC}}}\right) \qquad (\mathrm{II.2.8})$$

$$E_{\mathrm{FE}'(l=N)} = E_{\mathrm{FE}} + 2V_{\mathrm{ex}} + |V_{\mathrm{LL}} - V_{\mathrm{HH}}|^2 \left(\frac{1}{E_{\mathrm{FE}} + 2V_{\mathrm{ex}} - E_{\mathrm{CA}}} + \frac{1}{E_{\mathrm{FE}} + 2V_{\mathrm{ex}} - E_{\mathrm{AC}}}\right) \quad (\mathrm{II.2.9})$$

$$E_{\mathrm{TT}'} = E_{\mathrm{TT}} + \frac{3}{2}\left(\frac{|V_{\mathrm{LH}}|^2}{E_{\mathrm{TT}} - E_{\mathrm{CA}}} + \frac{|V_{\mathrm{HL}}|^2}{E_{\mathrm{TT}} - E_{\mathrm{AC}}}\right) \quad (\mathrm{II.2.10})$$

As seen from these formulae, the positive sign of V_{ex} and the opposite signs between V_{LL} and V_{HH} contribute to lowering the energy of FE’$_{N/2}$ than FE’$_{N}$, while the negative sign of V_{ex} and the same sign between V_{LL} and V_{HH} contributes to lowering the energy of FE’$_{N}$ than FE’$_{N/2}$. Note that the perturbative approach breakdown when the lowest FE’ state is nearly degenerate with the TT’ manifold, and thus only for the 0° and 25°–43° cases are shown. The contributions of the first and second terms in parentheses in eqs (II.2.6) and (II.2.7) are also shown, which are interpreted as CT-mediate transition probability amplitudes through CA* (blue bars) and AC* (orange bars) bases, respectively. As seen from **Figure II.2.10**, the TT configuration of the lowest FE’ state is almost zero at small α < 25°, negative at α = 28°–34°, and positive at α = 37°–43°. The contributions of CA*- and AC*-mediate paths are found to exhibit mutually opposite signs except at α = 30° and 34°. **Figure II.2.10** demonstrates that the approximate TT configurations have non-zero values at α ≥ 28°. It turns out that the amplitudes of CA*- and AC*-mediate paths contribution is almost the same at α ≤ 30°, while the latter surpasses the former at α ≥ 37°, which is the main reason why the lowest FE’ state includes TT configuration. For example, since the amplitude of V_{HL} and V_{LH} are found to be almost equal to each other at α = 43° (V_{hl} = –91.32 meV and V_{lh} = 78.92 meV), the energy inequalities between CA and AC states (E_{CA} = 2970 meV and E_{AC} = 2497 meV) are the main cause of the significant TT contribution in the adiabatic FE$'_{N}$.

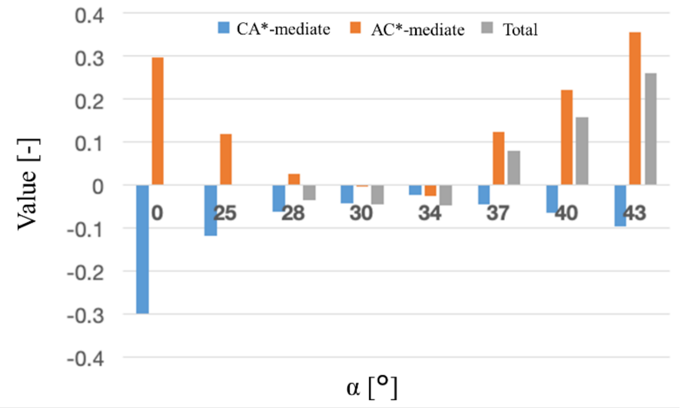

Figure II.2.10 α Dependences of TT configurations [gray bar] in the lowest adiabatic FE’ of the 8-mer model approximated by the second-order perturbation theory and the CA and AC contributions to them (FE-CA-TT [blue bar] and FE-AC-TT [orange bar] contributions, respectively), where the symmetry-adapted diabatic exciton states for $l = N/2$ or $l = N$ in eqs 26 and 27 are used as the zeroth-order approximation.

3.4. Size Dependences of SF Rates and TT Yields

In this section, we discuss the size (N) dependence of the SF dynamics in the pentacene ring-shaped aggregate models. In the present model, the adjacent pentacene molecular planes are found to approach parallel to each other as increasing N, where the amplitude of electronic coupling is predicted to increase as the interaction between the π-orbitals of the adjacent pentacene molecular planes approaches a σ-like interaction. It is also predicted that the energies of FE’ states tend to decrease with increasing N due to the increase in FE–CT coupling, making the SF rate k more sensitive to changes in α and narrowing the region of α in which the SF rate can be defined.

The plots of SF rate k and TT yield a as a function of the aggregate size with constant α ($\alpha = 20^\circ$, 30°, and 40°) are shown in **Figure II.2.11**. The points for N are omitted from **Figure II.11** when the SF rate (such as the 3- and 4-mers at $\alpha = 30^\circ$ and 40°) or the TT yield is so small that TT population is not able to fit with single exponential function. The SF rate exhibits complicated variations at $\alpha = 20^\circ$, a gradual increase with N with a peak at $N = 6$ and 10. On the other hand, SF rate at $\alpha = 30^\circ$and 40° shows monotonous and sharp increases with N. As discussed in Chapter II.1, it is supposed that Davydov splitting structure originating from the positive and large amplitudes of FE couplings at $\alpha = 20^\circ$ like H-ring models are found to cause the zig-zag behavior of the TT yield and SF rate. On the contrary, such a complex behavior of SF dynamics is not shown at $\alpha \geq 30^\circ$. Instead, the SF rate is shown to increase up to about 25 ps^{-1} at both 30° (for $N = 20$) and 40° (for $N = 11$) with relatively high TT yield $a \sim 70$ %, which implies that extraordinarily fast SF occurs as compared with the 6-mer model at $\alpha = 20^\circ$. This result indicates that the ring-shaped aggregate structures have the potential to induce efficient SF by tuning the intermolecular configuration and the size of the aggregates.

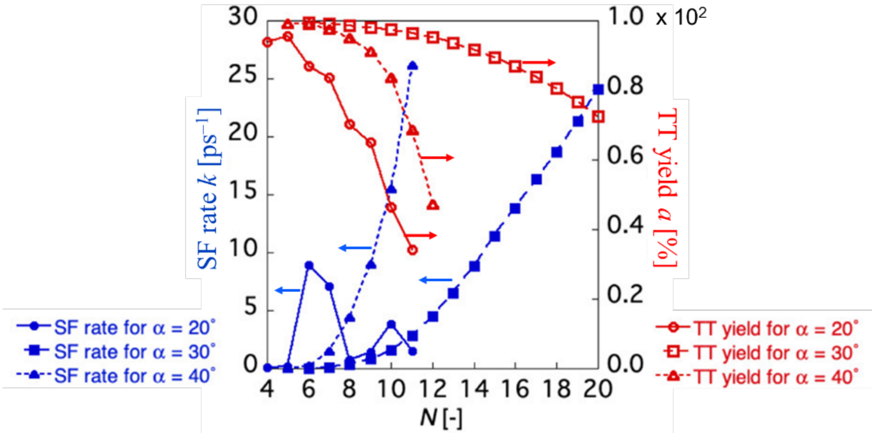

Figure II.2.11. Size (N) dependences of SF rate k [ps^{-1}] and TT yield a [%] at $\alpha = 20^\circ, 30^\circ, 40^\circ$.

In order to clarify the relationships between *N*, *k*, and *a*, we investigate the size (*N*) dependences of the energies and the total configurations of diabats in adiabatic FE' and TT' states at α = 20°, 30° and 40°, as shown in **Figure II.2.12 (a)–(c)**, respectively. The quantum interference between CA*- and AC*-mediate paths to the FE/TT mixing is also shown in **Figure II.2.13** for α = 30° and 40°. It is found from **Figure II.2.12 (a)** that the energy bandwidth of the FE' manifold increases with increasing *N*, and the lowest FE' states approach TT' manifold for *N* = 6, 7, and 10, respectively. The first and the second peaks of the SF rates at α = 20° for *N* = 6 and 10, respectively, (see **Figure II.2.12**), where the lowest FE' states and the next lowest FE' states are nearly degenerate with the TT' manifolds, and the fact that the TT configurations of these lower-lying FE' states are shown to be large indicates that the type I mechanism occurs for these *N* at α = 20°.

On the contrary, as seen at α = 30° (**Figure II.2.12 (b)**) and at large value of *N*, FE/TT mixing occurs not only in lower-lying FE' but also in higher-lying FE' states although the energy gap between these states is significantly large, resulting in type II SF acceleration mechanism. Although the small TT contributions to the lowest FE' in the 8-mer model, FE/TT mixing become large with increasing *N*. As shown in **Figure II.2.13 (a)**, it is found that CA*- and AC*-mediate path derived from eq. (II.2.7) have the same signs and amplitude of total TT contribution is strengthened in 12- and 16-mers. In present model, the orbital overlaps between neighboring molecules increase with *N*, which is the main reason of type II acceleration for $N \geq 14$ at α = 30° with SF rate exceeding 10 ps^{-1}.

Although the variations of SF rate and TT yield as a function of *N* at α = 40° are qualitatively similar to those at α = 30° as shown in **Figure II.2.11**, the reasons for the type II mechanism to occur are different. **Figure II.2.13 (b)** shows the size dependences of the first and second terms in parenthesis in eq (II.2.7) in the lowest FE' state for *N* = 8–12 at α = 40°. This indicates that at α = 40° the amplitude of AC*-mediate path contribution (positive in sign) is much larger than that of CA*-mediate path contribution (negative in sign) to the FE/TT mixing, leading to the non-zero total contribution of TT states to the FE' manifold (see also section 3.3). With increasing *N*, however, the energy of the lowest FE' state is found to be lower than that of the TT' manifold for *N* = 12 at α = 40°, which results in a low TT yield *a* = 47.2 %. In summary, it is expected that for medium-size aggregates ($10 \leq N \leq 16$ at α = 30° and $7 \leq N \leq 10$ at α = 40°), the type II mechanism achieves relatively fast SF (> 1 ps^{-1}) while keeping high TT yields (> 80 %), although for larger-size aggregates, the increases in electronic couplings cause an excess mixing of diabatic FE states into the lower-lying adiabatic TT' states, resulting in a significant reduction of the TT yields.

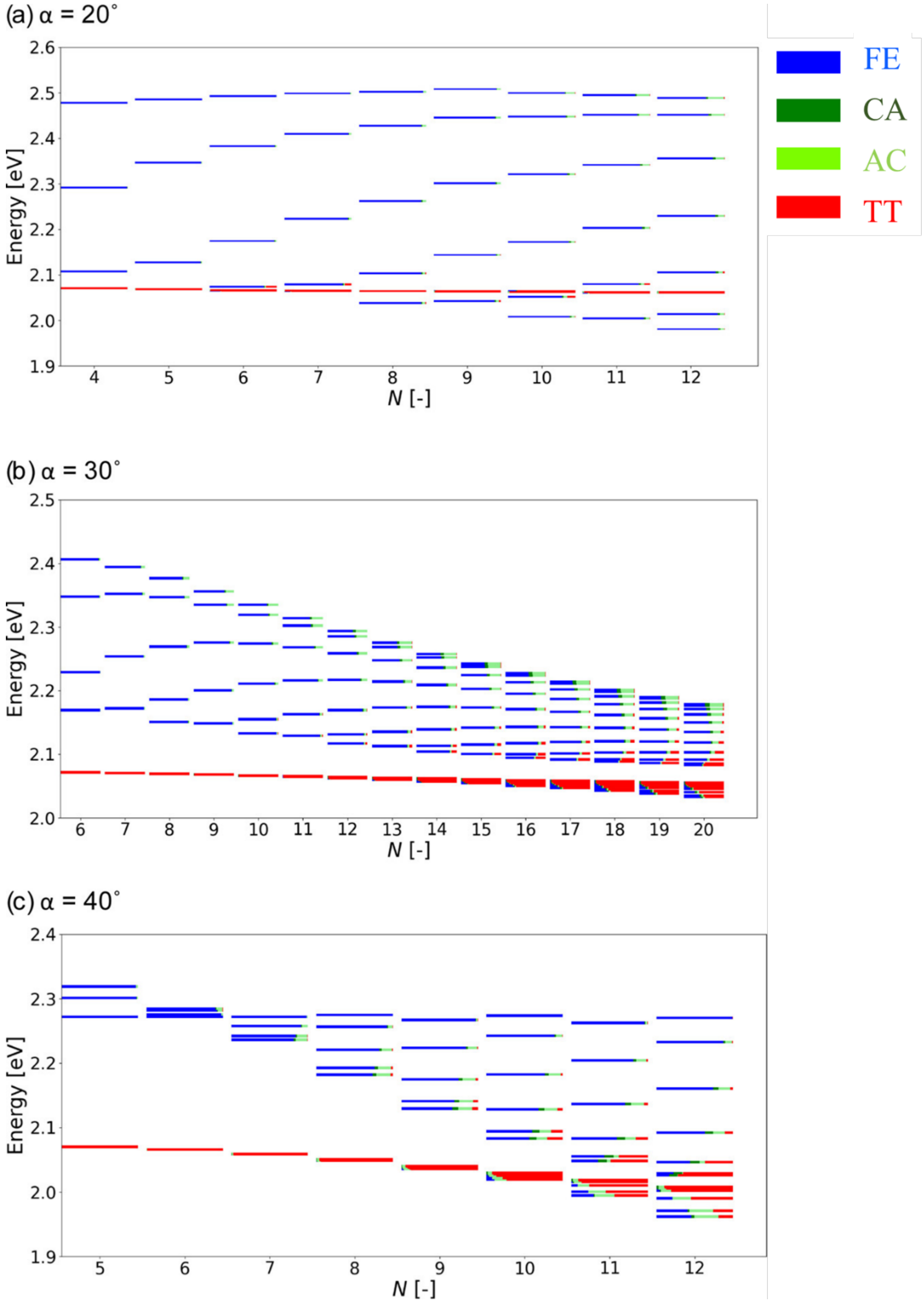

Figure II.2.12. Energy level diagrams for each N at α = 20˚, 30˚, and 40˚. Each bar representing an adiabatic state is color-coded according to the contribution of diabatic FE (blue), CA (green), AC (light green), and TT (red) states.

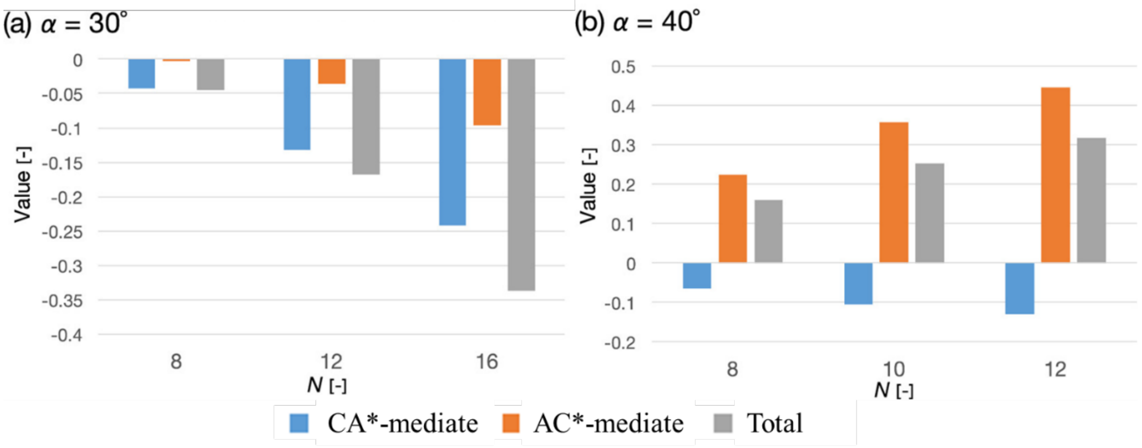

Figure II.2.13. Size dependences of TT configurations [gray bar], and CA* [blue bar] and AC* [orange bar]-mediate contributions to them in the lowest adiabatic FE' of the 8-, 12-, and 16-mer models at α = 30° (a) and the 8-, 10-, and 12-mer models at α = 40° (b) approximated by the second-order perturbation theory. See the legend of **Figure II.2.10** for further explanation.

4. Conclusion

In this study, we have investigated the effects of the intermolecular configuration, represented by the rotation angle α and the aggregate size (N), on the SF dynamics in pentacene structures ring-shaped aggregate structure asymmetric for ring-flipping operations. Because the amplitude of V_{ex} is larger than 100 meV at α ≤ 15°, the energy of the lowest FE' state is found to be too low compared with those of TT' manifold, resulting in low TT yields $a < 50$ %. However, SF is found to occur with high TT yield, when V_{ex} is sufficiently small at intermediate α. The numerical simulation based on QME in the 8-mer model exhibits a peak of SF rate at α = 23° and a sharp increase of SF rate at α > 37°, which indicates that there exists an optimal range of α giving high TT yields and SF rates. The RRF analysis of the 8-mer ring at α = 43° shows that this behavior is understood as many-to-many relaxation paths due to the large exciton overlaps between the lower-lying adiabatic FE' states and adiabatic TT' states. The FE/TT mixing in both TT' and FE' states, respectively, is found to contribute to the fast SF. Furthermore, the α and the size dependences of adiabatic energy states have revealed that the sharp increase in the SF rate at α = 30° and 40° with increasing size are also attributed to an increase in the FE (TT) configuration of the adiabatic TT' (FE') states with causing many-to-many relaxation paths from FE' to TT' manifold.

The second-order perturbation theory for exciton states enables us to describe the approximate contribution of TT states in FE' manifold as the sum (or cancellation) of the contributions of CA*- and AC*-mediate transition paths (see eqs (II.2.6) and (II.2.7)). The present method is convenient to consider these transition paths separately, and revealed that there are two conditions to cause this SF by type II mechanism. The first condition is that the CA*- and AC*-mediate contributions to lower-lying FE’ states are strengthened each other, which is satisfied in large $N \geq 12$ at $\alpha = 30^\circ$ (section 3.4). The second condition is that the quantum interference is broken, in other words, CA*- and AC*-mediate transition paths are incompletely cancelled each other due to the asymmetric CT structure, which is satisfied in intermediate N around 8-mer at large $\alpha > 40^\circ$ (see section 3.3 and 3.4). The type II mechanism is expected to provide higher TT yield than the type I mechanism discussed in Chapter II.1,[1] because the former does not require lowering the lowest FE’ energy so that the lowest-lying FE’ states are close in energy with the TT’ states.

The explanation for the type II mechanism using the second-order perturbation theory for the ring-shaped aggregate model is expected to be applicable not only to pentacene rings but also to a wide range of asymmetric monomers, such as bent-shaped molecules and acenes with donor/acceptor substituents, as long as the aggregate systems satisfy the rotational symmetry. The present results demonstrate the effectiveness of SF material design based on the asymmetry of the aggregate structures and contribute to a comprehensive understanding of the correlations between aggregate structure, size and SF efficiency for more general SF design guidelines.

Appendix

A.2. Derivation of Perturbative Approach for Estimation of Quantum Interference

In this section, eqs (II.2.6) and (II.2.7) in the main text, and the equations for adiabatic approximate exciton energies are derived by using the second-order perturbation theory with the symmetry adapted linear combination (SALC) diabatic basis as the zeroth-order approximation. For simplicity, we discuss only SALC diabatic basis $\left|X^*_{N/2}\right\rangle = \frac{1}{\sqrt{N}}\sum_{m=1}^{N}(-1)^m \left|X_m\right\rangle$ and $\left|X^*_N\right\rangle = \frac{1}{\sqrt{N}}\sum_{m=1}^{N}\left|X_m\right\rangle$ (X = FE, CA, AC, and TT) in even-ring aggregates in order to clarify the mechanism of increasing TT configuration in lower- and higher-lying FE’ states due to breaking the ring-flipping symmetry. Because the irreducible representations of all kinds of SA diabatic basis $\left|X^*_{N/2}\right\rangle$ ($\left|X^*_N\right\rangle$) are B (A), and the others belong to E-representation in C_N-symmetry, $\left|\mathrm{FE}^*_{N/2}\right\rangle$ ($\left|\mathrm{FE}^*_N\right\rangle$) couples with $\left|\mathrm{CA}^*_{N/2}\right\rangle$, $\left|\mathrm{AC}^*_{N/2}\right\rangle$, and $\left|\mathrm{TT}^*_{N/2}\right\rangle$ ($\left|\mathrm{CA}^*_N\right\rangle$, $\left|\mathrm{AC}^*_N\right\rangle$, and $\left|\mathrm{TT}^*_N\right\rangle$). Thus, the Hamiltonians represented by such SA diabatic exciton bases $\left|X^*_l\right\rangle$ ($l = N/2$ and N) are described, respectively, as

$$H_{\mathrm{ex}}^{*}=\begin{pmatrix} E_{\mathrm{FE}}-2V_{\mathrm{ex}} & V_{\mathrm{LL}}+V_{\mathrm{HH}} & -V_{\mathrm{LL}}-V_{\mathrm{HH}} & 0 \\ V_{\mathrm{LL}}+V_{\mathrm{HH}} & E_{\mathrm{CA}} & 0 & \sqrt{3/2}\,V_{\mathrm{LH}} \\ -V_{\mathrm{LL}}-V_{\mathrm{HH}} & 0 & E_{\mathrm{AC}} & \sqrt{3/2}\,V_{\mathrm{HL}} \\ 0 & \sqrt{3/2}\,V_{\mathrm{LH}} & \sqrt{3/2}\,V_{\mathrm{HL}} & E_{\mathrm{TT}} \end{pmatrix}\quad \text{for } l=\frac{N}{2} \tag{A1}$$

$$H_{\mathrm{ex}}^{*}=\begin{pmatrix} E_{\mathrm{FE}}+2V_{\mathrm{ex}} & V_{\mathrm{LL}}-V_{\mathrm{HH}} & V_{\mathrm{LL}}-V_{\mathrm{HH}} & 0 \\ V_{\mathrm{LL}}-V_{\mathrm{HH}} & E_{\mathrm{CA}} & 0 & \sqrt{3/2}\,V_{\mathrm{LH}} \\ V_{\mathrm{LL}}-V_{\mathrm{HH}} & 0 & E_{\mathrm{AC}} & \sqrt{3/2}\,V_{\mathrm{HL}} \\ 0 & \sqrt{3/2}\,V_{\mathrm{LH}} & \sqrt{3/2}\,V_{\mathrm{HL}} & E_{\mathrm{TT}} \end{pmatrix}\quad \text{for } l=\ N \tag{A2}$$

The configuration in an approximate adiabatic exciton state $|n'\rangle$ (n represents the index of SA diabatic state n^{*} mainly involved in n') by Rayleigh-Schrödinger second-order time independent perturbation theory without degeneration is described as

$$|n'\rangle=|n^{*}\rangle+\sum_{k\neq n}|k^{*}\rangle\frac{\langle k^{*}|H_{\mathrm{ex}}^{*}|n^{*}\rangle}{E_{n}^{*}-E_{k}^{*}}+\sum_{k\neq n}\sum_{l\neq n}|k^{*}\rangle\frac{\langle k^{*}|H_{\mathrm{ex}}^{*}|l^{*}\rangle\langle l^{*}|H_{\mathrm{ex}}^{*}|n^{*}\rangle}{(E_{n}^{*}-E_{k}^{*})(E_{n}^{*}-E_{l}^{*})} \tag{A3}$$

and the approximate energy is

$$E_{n'}=E_{n}^{*}+\sum_{k\neq n}\frac{|\langle k^{*}|H_{\mathrm{ex}}^{*}|n^{*}\rangle|^{2}}{E_{n}^{*}-E_{k}^{*}} \tag{A4}$$

where $E_{n'}$ and E_{n}^{*} indicate the energies of adiabatic state n' and SA state n^{*}, respectively. Here, all the perturbations to the diagonal matrix elements of H_{ex}^{*} are 0, and terms in eqs s3 and s4 including them are omitted from the general formulation of the Rayleigh-Schrödinger second-order perturbation equation.

Substituting the coupling and energy parameters of the Hamiltonians (eqs (A1) and (A2)) into eqs (A3) and (A4), the adiabatic FE'$_{N/2}$ and FE'$_{N}$ are described as

$$\begin{aligned}|\mathrm{FE'}_{\mathrm{N/2}}\rangle=&\;|\mathrm{FE}_{\mathrm{N/2}}^{*}\rangle+|\mathrm{CA}_{\mathrm{N/2}}^{*}\rangle\frac{V_{\mathrm{LL}}+V_{\mathrm{HH}}}{E_{\mathrm{FE}}-2V_{\mathrm{ex}}-E_{\mathrm{CA}}}-|\mathrm{AC}_{\mathrm{N/2}}^{*}\rangle\frac{V_{\mathrm{LL}}+V_{\mathrm{HH}}}{E_{\mathrm{FE}}-2V_{\mathrm{ex}}-E_{\mathrm{AC}}}\\ &+|\mathrm{TT}_{N/2}^{*}\rangle\sqrt{\frac{3}{2}}\frac{V_{\mathrm{LL}}+V_{\mathrm{HH}}}{E_{\mathrm{FE}}-2V_{\mathrm{ex}}-E_{\mathrm{TT}}}\left(\frac{V_{\mathrm{LH}}}{E_{\mathrm{FE}}-2V_{\mathrm{ex}}-E_{\mathrm{CA}}}-\frac{V_{\mathrm{HL}}}{E_{\mathrm{FE}}-2V_{\mathrm{ex}}-E_{\mathrm{AC}}}\right)\end{aligned} \tag{A5}$$

$$\begin{aligned}|\mathrm{FE'}_{N}\rangle=&\;|\mathrm{FE}_{N}^{*}\rangle+|\mathrm{CA}_{N}^{*}\rangle\frac{V_{\mathrm{LL}}-V_{\mathrm{HH}}}{E_{\mathrm{FE}}+2V_{\mathrm{ex}}-E_{\mathrm{CA}}}+|\mathrm{AC}_{N}^{*}\rangle\frac{V_{\mathrm{LL}}-V_{\mathrm{HH}}}{E_{\mathrm{FE}}+2V_{\mathrm{ex}}-E_{\mathrm{AC}}}\\ &+|\mathrm{TT}_{N}^{*}\rangle\sqrt{\frac{3}{2}}\frac{V_{\mathrm{LL}}-V_{\mathrm{HH}}}{E_{\mathrm{FE}}+2V_{\mathrm{ex}}-E_{\mathrm{TT}}}\left(\frac{V_{\mathrm{LH}}}{E_{\mathrm{FE}}+2V_{\mathrm{ex}}-E_{\mathrm{CA}}}+\frac{V_{\mathrm{HL}}}{E_{\mathrm{FE}}+2V_{\mathrm{ex}}-E_{\mathrm{AC}}}\right)\end{aligned} \tag{A6}$$

Approximate adiabatic $\mathrm{FE'}_{N/2}$, $\mathrm{FE'}_{N}$, and TT' state energies (the energies of $\mathrm{TT'}_{N/2}$ and $\mathrm{TT'}_{N}$ are found to be equal to each other in this approximation) are described as

$$E_{\mathrm{FE'}(l=\,N/2)}=E_{\mathrm{FE}}-2V_{\mathrm{ex}}+|V_{\mathrm{LL}}+V_{\mathrm{HH}}|^{2}\left(\frac{1}{E_{\mathrm{FE}}-2V_{\mathrm{ex}}-E_{\mathrm{CA}}}+\frac{1}{E_{\mathrm{FE}}-2V_{\mathrm{ex}}-E_{\mathrm{AC}}}\right) \tag{A7}$$

$$E_{\mathrm{FE}'(l=N)} = E_{\mathrm{FE}} + 2V_{\mathrm{ex}} + |V_{\mathrm{LL}} - V_{\mathrm{HH}}|^2 \left(\frac{1}{E_{\mathrm{FE}} + 2V_{\mathrm{ex}} - E_{\mathrm{CA}}} + \frac{1}{E_{\mathrm{FE}} + 2V_{\mathrm{ex}} - E_{\mathrm{AC}}}\right) \quad \text{(A8)}$$

$$E_{\mathrm{TT}'} = E_{\mathrm{TT}} + \frac{3}{2}\left(\frac{|V_{\mathrm{LH}}|^2}{E_{\mathrm{TT}} - E_{\mathrm{CA}}} + \frac{|V_{\mathrm{HL}}|^2}{E_{\mathrm{TT}} - E_{\mathrm{AC}}}\right) \quad \text{(A9)}$$

We apply this approximation to interpret the effects of simultaneous change of electronic coupling and CT state energy to configuration in adiabatic FE' states by obtaining the analytical formulation of the approximate results of diagonalization of exciton Hamiltonian. Note here that this approximation is expected to be quantitatively appropriate when the amplitudes of the off-diagonal elements of H_{ex}^* in eqs (A1) and (A2) are small enough comparing with energy gap between SALC diabatic FE and CT states. This condition is relatively satisfied when (i) the aggregate size is small ($N \leq 6$), and (ii) α is around 25°–30° in intermediate aggregate size ($7 \leq N \leq 12$) in our model. The first condition comes from absolute values of FE–CT and CT–TT couplings become low because of small overlap between π-orbitals in neighboring dimer systems, and FE–CT energy gap is large (~ 500 meV) in this range of N. The second condition comes from that $|V_{\mathrm{HH}}|$ and $|V_{\mathrm{HL}}|$ approaches 0 while $|V_{\mathrm{LL}}|$ and $|V_{\mathrm{LH}}|$ remain non-zero values (around 100–200 meV), respectively, where the type II acceleration mechanism is expected to occur. Thus, this approximation and the interpretation of the type II mechanism by perturbation theory are expected to be reasonable at this range of α and N. In case that the off-diagonal elements of H_{ex}^* cannot be considered as perturbation (for example, at α = 45° in 8-mer as shown in Figure II.2.11) this approximation of exciton states is expected not to quantitatively reproduce the results of diagonalization of H_{ex}. However, the discussion in section 3.2 and 3.3 in the main text based on perturbation theory is qualitatively valid for the purpose to explain the SF at α = 40° in 8-mer (section 3.2) and at α = 30° in large N (section 3.3), which states that the large FE–TT mixing in FE' and TT'-manifold results from the inequality of CA and AC states.

References

(1) H. Miyamoto, M. Nakano *ChemPhotoChem* **2020**, *4*, 5249−5263.

(2) T. C. Berkelbach, M. S. Hybertsen, D. R. Reichman, *J. Chem. Phys.* **2013**, *138*, 114102.

(3) T. C. Berkelbach, M. S. Hybertsen, D. R. Reichman, J. Chem. Phys. **2013**, *138*, 114103.

(4) M. Nakano, *J. Chem. Phys*. **2019**, *150*, 234305.

(5) M. Nakano, S. Ito, T. Nagami, Y. Kitagawa, T. Kubo, *J. Phys. Chem. C.* **2016**, *120*, 22803-22816.

(6) M. Nakano, T. Nagami, T. Tonami, K. Okada, S. Ito, R. Kishi, Y. Kitagawa, T. Kubo, *J. Comput. Chem.* **2019**, *40*, 89-104.

(7) M. J. Frisch, G. W. Trucks, H. B. Schlegel, G. E. Scuseria, M. A. Robb, J. R. Cheeseman, G. Scalmani, V. Barone, B. Mennucci, G. A. Petersson, et al. *GAUSSIAN 09, Revision B.01*; Gaussian, Inc.: Wallingford, CT, **2010**.

(8) X. Xie, A. Santana-Bonilla, W. Fang, C. Liu, A. Troisi, H. Ma *J. Chem. Theory Comput.* **2019**, *15*, 3721−3729.

PART III

Molecular Aggregate Structure – SF Dynamics Relationships for Directional TT migration

Chapter 1.

Theoretical Study on Singlet Fission Dynamics in Symmetric Heterotrimer model

In this chapter, we investigated SF dynamics in symmetric linear heterotrimer systems consisting of different unsubstituted or 6,13-substituted pentacene derivatives denoted as ***X*/*Y*** (***X*, *Y***: terminal and center monomer species) to develop design guidelines for engineering directional triplet exciton migration. Time-dependent density functional theory (TDDFT) calculations revealed that the substituent-induced electronic effects, represented as the Hammett's para-substitution coefficients σ_p, correlate with the excitation energies of S_1 and T_1 states, as well as the energies of the highest occupied and lowest unoccupied molecular orbitals (HOMO and LUMO). Electronic coupling calculations and SF dynamics simulations demonstrated that heterotrimers achieved over 70 % selectivity for spatially separated TT states, outperforming homotrimers. An optimal region of the difference in σ_p between the substituents of ***X*** and ***Y*** was identified for increasing the SF rate. This enhancement in SF rate is attributed to quantum interference effects: the reduction in structural symmetry introduces new interaction pathways, enabling the S_1-TT mixing and accelerating hetero-fission between the terminal and center molecules.

1. Introduction

As mentioned in the General Introduction, the triplet dissociation process in SF has attracted significant attention due to its potential in quantum spin information technologies, such as sensing and quantum computing.[1,2] The intermediate spin-entangled TT states with several spin multiplicities (^{1}TT, ^{3}TT, and ^{5}TT)[3,4] serves as key elements for these applications. However, the use of SF in quantum spin technologies remains limited by technical challenges, particularly in tracking the spatial distribution and manipulating the spin states of individual triplet excitons. A combination of the electron-spin-resonance (ESR) and the scanning tunneling microscopy (STM) technologies is a promising approach to observe and manipulate local spins at the atomic and molecular levels.[5] Despite its potential, further advancements of experimental techniques are required. Especially, the individual operation of the two triplet spins is particularly challenging when the positions of two triplets are close because the operation on one molecule affects another. Moreover, in a crystal or an aggregate system consisting of identical molecules, it is generally impossible to determine the migration pathways of triplet excitons. In this regard, tuning the molecular and aggregate structures offers an alternative strategy for separating two triplet excitons while maintaining the correlation between them and controlling the spatial distributions of TT excitons suitable for quantum spin operations.

In this study, we investigated SF dynamics in linear heterotrimer systems composed of different pentacene derivatives, denoted as ***X*/*Y***, where ***X*** and ***Y*** represent the terminal and center monomer species, respectively (see **Figure III.1(a)**). We propose design strategies for controlling the spatiotemporal distribution of TT states, based on quantum chemical calculations and dynamics simulation. The heterotrimer model allows us to explore following two key effects: (i) how the energy gradient of triplet excitation between ***X*** and ***Y*** influences the efficiency of directional triplet–triplet exciton transfer (TTET) from ***Y*** to ***X***, and (ii) how the exciton relaxation mechanism in heterotrimers differs from that in homotrimers. Previous studies on pentacene crystal structures[6-10] and ring-shaped aggregate structures (Chapter II.1 and II.2)[11,12] have shown that the SF rate decreased in highly symmetric systems. This is because the interference effects tend to cancel the interaction paths between S_1 and TT states mediated by various charge transfer (CT) states. This cancellation occurs when the excitons delocalize across entire aggregate and the energies of the two CT states (the cation-anion state [CA] and the anion-cation state [AC]) are identical, which is applied to the $\boldsymbol{X} = \boldsymbol{Y}$ case (homotrimer). In contrast, for $\boldsymbol{X} \neq \boldsymbol{Y}$ (heterotrimer), the exciton fission occurs between two different molecular species, referred to as hetero-fission, and the energies of CA and AC states are non-identical, which can mitigate the cancellation of interaction paths. These effects may resolve the cancellation of interaction paths and enhance the SF rate and TT yield.

This paper aims to clarify: (i) the optimal condition for ***X*** and ***Y*** to maximize both TT yield and the selectivity of separated TT pair states on ***X*** molecules, and (ii) the roles of asymmetric CT states in enabling an efficient hetero-fission process. We focused on a slip-stack configuration, as shown in **Figure III.1 (b)**, characterized by the stacking distance *d*. Although monomers are not directly connected by covalent linkers, we anticipate that the design strategies proposed here can also be applied to several covalently linked trimers like those synthesized by Nakamura et al..[13] This study is expected to provide physical insights into the mechanism of SF and propose design guidelines of efficient SF materials that are useful for realizing the quantum spin manipulations for molecular materials,[14-16] although further discussions on the dynamics involving the high-spin TT pair states is necessary to establish comprehensive guidelines for efficient the quantum spin manipulations.

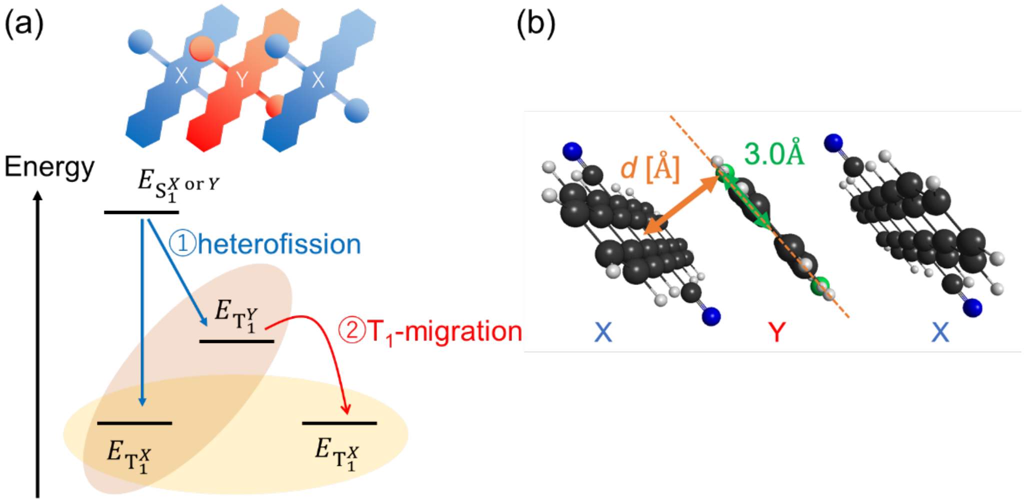

Figure III.1. The concept of a heterotrimer model consisting of molecules ***X*** and ***Y*** (denoted as ***X***/***Y***) and the example of the structure of the slip-stacked trimer models of **CN2PEN/Cl2PEN** (N and Cl atoms are shown as blue and green, respectively) with the stacking distance *d* [Å] and fixed displacement along the short molecular axis by 3.0 Å.

2. Methodology

2.1. Effective Energy-Matching Conditions for Heterotrimers

For the monomers ***X*** and ***Y***, we employed unsubstituted and 6,13-disubstituted pentacenes (**PEN** and **R2PEN**, where R represents the substituent group shown in **Figure III.2**). First, we conducted time-dependent density functional theory (TDDFT) calculation for the monomers only used in the pre-screening scheme for candidate systems. The geometrical optimization, TDDFT for vertical S_1 excitation energy, and TDDFT with Tamm-Dancoff approximation (TDA)[17] for vertical T_1 excitation energy of a single molecule were performed at the CAM-B3LYP/cc-pVDZ level[18] using Gaussian 16 package[19]. The monomer species explored in this study have been synthesized[20–26]. This pre-screening based on the TDDFT saves us the effort of calculating the electronic couplings of the dimer structure at the XMC-QDPT2/CASSCF(4,4) level for each ***X/Y*** pair.

Then, we evaluated effective energy-matching conditions for the heterotrimer in terms of S_1 ($E_{S_1^X}, E_{S_1^Y}$) and T_1 ($E_{T_1^X}, E_{T_1^Y}$) energies of ***X*** and ***Y***, as follows:

$$\Delta E_{\mathrm{SF}} = \min\left(E_{S_1^X}, E_{S_1^Y}\right) - 2E_{T_1^X} \geq 0 \qquad \text{(III.1)}$$

$$\Delta E_{\mathrm{TTET}} = E_{T_1^X} - E_{T_1^Y} < 0 \qquad \text{(III.2)}$$

The first condition is the isothermal/exothermal condition for hetero-fission, indicating that the energy of the final TT state should be lower than either the S_1 energy of ***X*** or ***Y***. The second condition describes the exothermal condition for TTET from ***Y*** to ***X***.

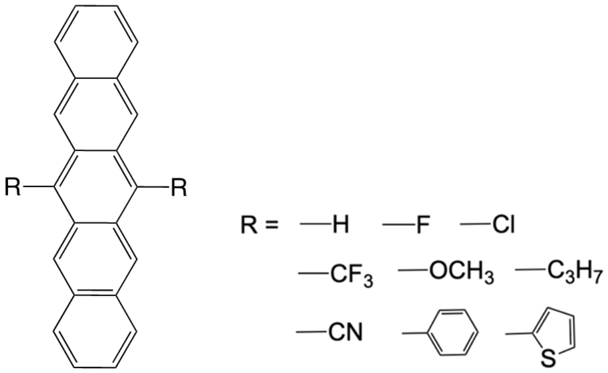

Figure III.2. Molecular structures of unsubstituted pentacene **PEN** (R = H) and 6,13-disubstituted pentacene derivatives **R2PEN**.

2.2. Construction of Exciton Hamiltonian

:

We conducted SF dynamics simulations for systems with appropriately satisfied the energy-matching conditions. To construct the exciton Hamiltonian (H_{ex}) required for the SF dynamics simulations, we employed diabatic state approximation. This approach includes three S_1 bases ($S_1S_0S_0$, $S_0S_1S_0$, and $S_0S_0S_1$), four CT bases (CAS_0, ACS_0, S_0CA, S_0AC, where C and A denote the cation and anion, respectively), and three TT bases (TTS_0, S_0TT, and TS_0T) as described in General Theory. The following 10 × 10 matrix expresses the exciton Hamiltonian in diabatic representation:

$$H_{\mathrm{ex}} = \begin{pmatrix} E_{\mathrm{S}_1^X} & V_{\mathrm{ex}} & 0 & V_{\mathrm{S}_1^X-\mathrm{C}^X\mathrm{A}^Y} & V_{\mathrm{S}_1^X-\mathrm{C}^Y\mathrm{A}^X} & 0 & 0 & V_{\mathrm{S}_1^X-\mathrm{T}^X\mathrm{T}^Y} & 0 & 0 \\ & E_{\mathrm{S}_1^Y} & V_{\mathrm{ex}} & V_{\mathrm{S}_1^Y-\mathrm{C}^X\mathrm{A}^Y} & V_{\mathrm{S}_1^Y-\mathrm{C}^Y\mathrm{A}^X} & V_{\mathrm{S}_1^Y-\mathrm{C}^Y\mathrm{A}^X} & V_{\mathrm{S}_1^Y-\mathrm{C}^X\mathrm{A}^Y} & V_{\mathrm{S}_1^Y-\mathrm{T}^X\mathrm{T}^Y} & V_{\mathrm{S}_1^Y-\mathrm{T}^X\mathrm{T}^Y} & 0 \\ & & E_{\mathrm{S}_1^X} & 0 & 0 & V_{\mathrm{S}_1^X-\mathrm{C}^Y\mathrm{A}^X} & V_{\mathrm{S}_1^X-\mathrm{C}^X\mathrm{A}^Y} & 0 & V_{\mathrm{S}_1^X-\mathrm{T}^X\mathrm{T}^Y} & 0 \\ & & & E_{\mathrm{C}^X\mathrm{A}^Y} & 0 & 0 & 0 & V_{\mathrm{TT}-\mathrm{C}^X\mathrm{A}^Y} & 0 & 0 \\ & & & & E_{\mathrm{C}^Y\mathrm{A}^X} & 0 & 0 & V_{\mathrm{TT}-\mathrm{C}^Y\mathrm{A}^X} & 0 & 0 \\ & & & & & E_{\mathrm{C}^Y\mathrm{A}^X} & 0 & 0 & V_{\mathrm{TT}-\mathrm{C}^Y\mathrm{A}^X} & 0 \\ & & & & & & E_{\mathrm{C}^X\mathrm{A}^Y} & 0 & V_{\mathrm{TT}-\mathrm{C}^X\mathrm{A}^Y} & 0 \\ & & & & & & & E_{\mathrm{T}^X\mathrm{T}^Y} & 0 & t \\ & & & & & & & & E_{\mathrm{T}^X\mathrm{T}^Y} & t \\ & & & & & & & & & E_{\mathrm{T}^X\mathrm{T}^X} \end{pmatrix} \tag{III.3}$$

The parameters $E_{\mathrm{S}_1^X}$, $E_{\mathrm{S}_1^Y}$ are the S$_1$ excitation energies. The $E_{\mathrm{C}^X\mathrm{A}^Y}$ is defined as the energy of CT states for CAS$_0$ and S$_0$AC (cation is on one or another ***X*** and anion is on ***Y***), and $E_{\mathrm{C}^Y\mathrm{A}^X}$ is the opposite one indicating ACS$_0$ and S$_0$CA (cation is on ***Y*** and anion is on one or another ***X***). The $E_{\mathrm{T}^X\mathrm{T}^Y}$, and $E_{\mathrm{T}^X\mathrm{T}^X}$ are the TT state energies where the former indicates that (one of) ***X*** and ***Y*** are in their T$_1$, the latter indicates that both ***X*** are in the T$_1$. Therefore, if $X = Y$, $E_{\mathrm{C}^X\mathrm{A}^Y} = E_{\mathrm{A}^X\mathrm{C}^Y}$ and $E_{\mathrm{T}^X\mathrm{T}^Y} = E_{\mathrm{T}^X\mathrm{T}^X}$. The calculation of TTET coupling *t* is approximated as the effective transfer coupling shown as eq. (I.1.38) – (I.1.40) in General Introduction.[27,28]

Each coupling parameter was obtained at the XMC-QDPT2/CASSCF(4e,4o)/6-31G(d) [29] level with the Nakamura–Truhlar 4-fold way diabatization scheme.[30] The diabatization and XMC-QDPT2 calculation were performed by GAMESS.[31] The eigenvalues of excited states, expressed as the linear combination of configuration state functions (CSFs) based on diabatic molecular orbitals (DMOs), were used to derive diabatic state energies and couplings through the unitary transformation of the diagonal Hamiltonian into the CSFs representation, which is proposed by Ma et al.[32] and described in previous Chapter II.2. The multi-excitonic and doubly excited states in the dimer structure are explicitly incorporated in this model through the CSFs for CAS(4e,4o) space. Further detail descriptions of these couplings is given in section 1.2 in General Introduction.

2.3. Quantum Master Equation

As well as the previous Chapter II.1 and Chapter II.2, the exciton relaxation dynamics simulation including state-to-state transition driven by the vibronic coupling (VC)[33] was performed by the time-convolutionless second-order quantum master equation (TCL-QME) within the Markov approximation with only considering Holstein coupling[34]. The TCL-QME is numerically solved by the eight-step and sixth-order Runge-Kutta method to derive the time revolution of reduced density matrix (RDM) ρ_{ex} projected on the exciton states denoted as.[35] The vibronic coupling parameters for Ohmic spectral density with Lorentz–Drude cutoff frequency is represented as reorganization energies λ and cut-off frequency Ω_c and they are set to 50 and 180 meV, respectively, for different diabatic exciton states and different molecular species. The temperature T is set to 300 K. Note that these VC parameters generally depend on the molecular species; however, we focused only on the qualitative changes in the exciton Hamiltonian for simplicity. The Peierls coupling, representing the VC on the off-diagonal terms of exciton Hamiltonian, was omitted in this study although Peierls coupling is expected to peak at low vibrational frequency modes. This is because the reorganization energy of Peierls coupling is typically much smaller than that of Holstein coupling, as reported in the previous study of SF in acene crystals.[36] The initial population was set to 100% for the S_1 state on the center molecule $\boldsymbol{Y}$, denoted as $|S_0S_1S_0\rangle$.

3. Results

3.1. Pre-screening of candidate systems

First, we conducted TDDFT calculations for monomer species to evaluate the energy matching conditions, eqs. (III.1) and (III.2), for pairs of $\boldsymbol{X}$ and $\boldsymbol{Y}$ shown in **Figure III.2**. **Figure III.3** represents the plots of ΔE_{SF} (horizontal axis) vs. ΔE_{TTET} (vertical axis). Data points in the lower-right region indicate conditions where both the yield of the TT state and the selectivity of the separated TT state (TS_0T) are expected to be high. In **Figure III.4**, markers of the the same type represent pairs ***X/Y*** with the same ***X***. The results show that $E_{\mathrm{T}_1^X} - E_{\mathrm{T}_1^Y}$ becomes significantly negative in the **CN2PEN/**$\boldsymbol{Y}$ system (green rhombus), where **CN2PEN** represents 6,13-dicyanopentacene.

Figures III.4 (a) and **4 (b)** illustrate the correlations between the absolute value of Hammett's *para*-substitution constant, $|\sigma_p|$,[37] and various properties of pentacene derivatives: the S_1 and T_1 excitation energies, the S_1-$2T_1$ and HOMO-LUMO energy gaps, respectively. The σ_p value of each molecule is summarized in **Appendix** in this Chapter. These results indicate that the SF process in homodimers of the pentacene derivatives tends to become exothermic as the $|\sigma_p|$ increases. Moreover, the findings also suggest that the inductive effects of substituents play a crucial role in tuning the excitation energies of heterotrimers. For example, ΔE_{SF} of **CN2PEN/F2PEN** system (**F2PEN**: 6,13-difluoropentacene) was significantly positive (0.063 eV), because both **CN2PEN** and **F2PEN** have large S_1-$2T_1$ gap, whereas that of **CN2PEN/PEN** (**PEN**: unsubstituted pentacene) was nearly zero (0.006 eV). In contrast, the difference in triplet energies between $\boldsymbol{X}$ and $\boldsymbol{Y}$, ΔE_{TTET}, was smaller in **CN2PEN/F2PEN** than **CN2PEN/PEN** due to the smaller difference in $|\sigma_p|$ in the former. Additionally, **Figure III.4 (c)** show that the HOMO and LUMO energies negatively correlates with σ_p, where the vertical axis shows the difference from that of pentacene: $E_{\mathrm{PEN}} - E$. These relative HOMO and LUMO energies difference between molecules influence the charge transfer character between them.

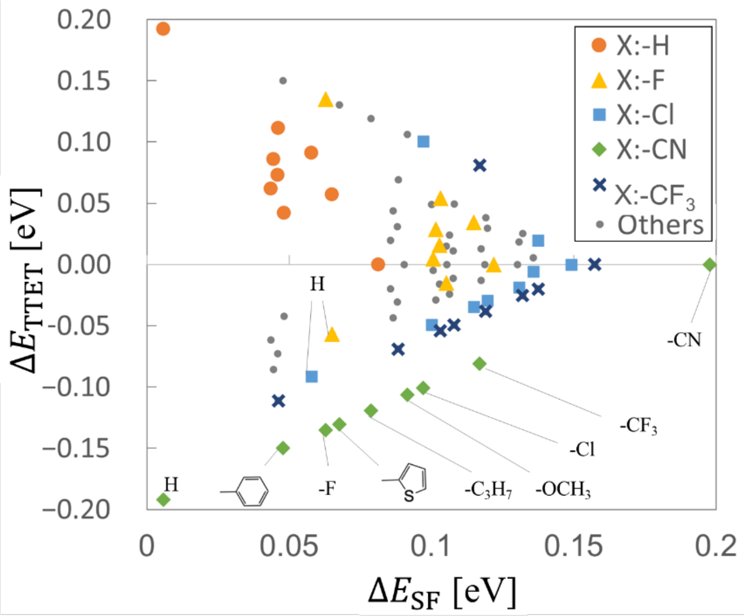

Figure III.3. The SF exothermal condition ($\Delta E_{\mathrm{SF}} = \min\left(E_{\mathrm{S}_1^X}, E_{\mathrm{S}_1^Y}\right) - 2E_{\mathrm{T}_1^X}$) on the horizontal axis and the exothermic condition for triplet-triplet exciton transfer (TTET) from ***Y*** to ***X*** ($\Delta E_{\mathrm{TTET}} = E_{\mathrm{T}_1^X} - E_{\mathrm{T}_1^Y}$) on the vertical axis in the pair of pentacene derivatives. The colored dots represent the data of fixed X = **R2PEN** for R = H (orange), F (yellow), Cl (light blue), CN (green), and CF$_3$ (dark blue). The small gray dots denote the data including X = **OCH$_3$2PEN**: R = CH$_3$O, **Pr2PEN**: R = C$_3$H$_7$, **Ar2PEN**: R = C$_6$H$_5$, **Thi2PEN**: R = C$_4$H$_3$S.

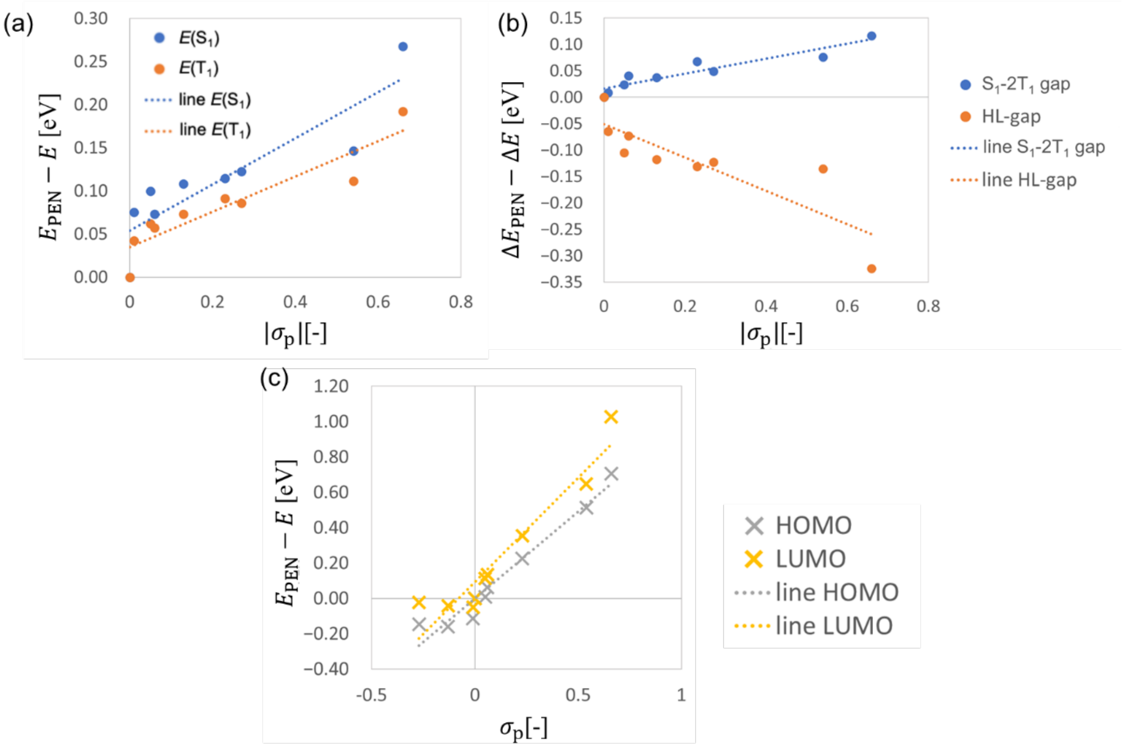

Figure III.4. The correlations between (a) $|\sigma_p|$ and the excitation energies of the S_1 and T_1 states, (b) $|\sigma_p|$ and S_1-$2T_1$ energy gap and HOMO-LUMO gap, and (c) σ_p and HOMO and LUMO energies. We took the corresponding energies or energy gaps of **PEN** (E_{PEN} or ΔE_{PEN}) as the standards, and we plotted $E_{\mathrm{PEN}} - E$ in (a) and (c) whereas $\Delta E - \Delta E_{\mathrm{PEN}}$ in (b) for clarity. The dotted approximate line shows the general trends of σ_p and several energies.

3.2. Electronic Coupling

Next, we examined the diabatic energies and electronic couplings. The coupling parameters for the slip-stacked structure were evaluated, as shown in **Figure III.1(b)**. The stacking distance d [Å] was varied from 3.6 to 5.0 Å with an increment of 0.2 Å, and the displacement along the short molecular axis was fixed at 3.0 Å. **Figure III.1(b)** illustrates an example of **CN2PEN/Cl2PEN** (**Cl2PEN**: 6,13-dichloropentacene). **Figure III.5** presents the coupling $V_{\mathrm{C}^X\mathrm{A}^Y-\mathrm{TT}}$, corresponding to one of off-diagonal elements of exciton Hamiltonian, as a function of d for **PEN/PEN**, **F2PEN/PEN**, and **CN2PEN/Cl2PEN**. These systems showed similar d-dependences of $V_{\mathrm{C}^X\mathrm{A}^Y-\mathrm{TT}}$. Moreover, the other off-diagonal electronic couplings also did not show apparent dependence on the molecular species of ***X*** and ***Y***. In contrast, the diabatic state energies, particularly the CT energies, strongly depend on molecular species ***X*** and ***Y***. **Figure III.6 (a)** shows diabatic state energies for S_1^X, S_1^Y, C^XA^Y, C^YA^X, T^XT^Y, and T^XT^X states for ***X/Y*** = **PEN/PEN**, **F2PEN/PEN**, **Cl2PEN/PEN**, **CN2PEN/PEN**, **CN2PEN/F2PEN**, and **CN2PEN/Cl2PEN**.

Notably, the diabatic state energies of S_1^X and T^XT^X were independent of the ***Y*** and that of S_1^Y was independent of ***X***. As shown in **Figure III.4 (c)**, systems with strong electron-withdrawing groups (EWGs) exhibited lower HOMO and LUMO energies. Thus, when the σ_p of ***X*** is larger than ***Y***, the energy of the C^YA^X state tends to be stable. For example, the C^YA^X state (light green) is lower in energy than S_1^X or T^XT^X states when ***X*** = **CN2PEN**, ***Y*** = **PEN** and **F2PEN** for $d \leq 3.8$ Å, which potentially lead to lower TT yields. In contrast, the energy of C^XA^Y state (green) remains energetically high. **Figure III.6 (b)** provides the *d*-dependence of diabatic state energies for **CN2PEN/Cl2PEN**. As the *d* increases, both C^YA^X and C^XA^Y state energies became higher, whereas S_1 and TT diabatic state energies remain unchanged. For $d > 3.8$ Å, the C^YA^X diabatic state energy surpasses the S_1 and TT diabatic states, mitigating the overstabilization of the C^YA^X and improving TT yields.

In summary, the CT energies are controllable by choosing appropriate ***X*** and ***Y*** molecular species and the stacking distance *d*. The stabilization energies of CT states depend on the difference in the substituents-inductive effect between ***X*** and ***Y***.

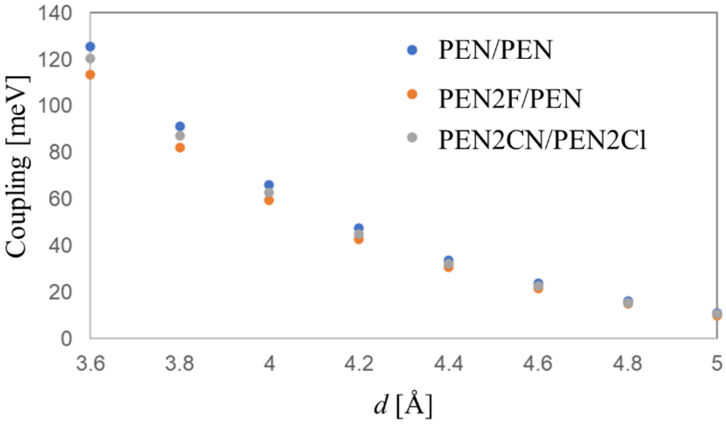

Figure III.5. Calculation results of $V_{C^YA^X-TT}$ as a function of stacking distance *d* [Å].

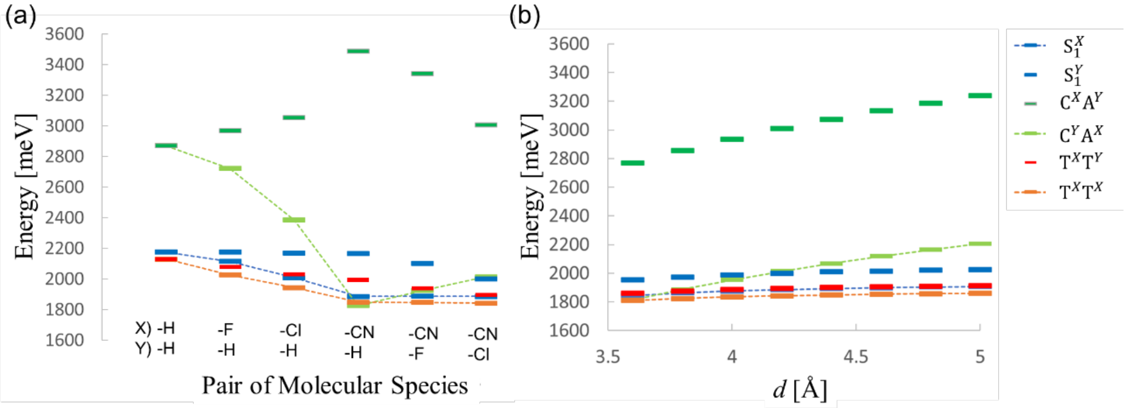

Figure III.6. Calculation results of diabatic state energies (a) of different combinations ***X/Y*** and (b) of **CN2PEN/Cl2PEN** with different *d* [Å].

3.2. SF Dynamics simulations

Finally, SF dynamics simulations were performed by numerically solving the TCL-QME for the constructed exciton Hamiltonian. SF dynamics simulations were conducted for the following systems: **PEN/PEN**, **F2PEN/PEN**, **Cl2PEN/PEN**, **CN2PEN/PEN**, **CN2PEN/F2PEN**, and **CN2PEN/Cl2PEN**. **Figures III.7 (a)** and **7(b)** present the results of total TT yield (*y*) and selectivity (*s*) of the separated TT pair state ($T_1S_0T_1$) as a function of stacking distance *d* [Å] at *t* = 1 ns. Note that, in general, the spin-decoherence of the TT state is about ns to μs order according to the many time-resolved EPR studies. The data at *t* = 10 ps were presented in the Appendix III.2. For small *d*, the TT populations usually converged to a specific value ~10^1 ps. However, for larger *d* (> 4.8 Å), the TT population converged at the timescale of 1 ns, which is comparable to the timescale of the spin-decoherence process.[4] Thus, we should consider the spin-decoherence process to fully understand the SF dynamics of the systems with large *d*.

As shown in **Figure III.7(a)**, the total TT yield at *d* = 3.6 Å was low (< 20%) for all systems, primally due to the strong interaction between S_1-CT states. With the exception of **CN2PEN/Cl2PEN**, whose total TT yield continued to increase in the range up to *d* ≤ 5.0 Å, the TT yields of the other systems initially increased and then decreased as *d* increased. The range of *d* where the total TT yield increased depends on the system: The total TT yield surpassed 70 % at *d* = 4.2-4.8 Å in **PEN/PEN**, at *d* = 4.0-4.8 Å in **F2PEN/PEN**, at *d* = 4.2-4.8 Å in **Cl2PEN/PEN**, at *d* = 4.8 Å in **CN2PEN/F2PEN**, and at *d* = 4.6-4.8 Å in **CN2PEN/PEN**. The TT yield of **CN2PEN/PEN** was low and took a local maximum (45 %) at *d* = 4.6 Å. The reduction of TT yield at larger *d* (> 4.8 Å) is attributed to the small π-orbital overlap between the neighboring molecules, leading to the slow SF rate with a time constant of > 1 ns.

As shown in **Figure III.7 (b)**, the selectivity for **PEN/PEN** (homotrimer) showed slight *d*-dependence and low values (20-35 %). In contrast, the selectivity increased gradually as the *d* increased from 3.6 Å to 4.8 Å for **F2PEN/PEN** and **Cl2PEN/PEN**. Furthermore, drastic enhancement of the selectivity was obtained for **CN2PEN/Y** (**Y=PEN**, **F2PEN**, **Cl2PEN**) in range of *d* = 3.8-4.4 Å. It was improved to >70 % at *d* = 4.0-4.8 Å in **F2PEN/PEN**, at *d* = 3.8-5.0 Å in **Cl2PEN/PEN**, at *d* = 4.4-5.0 Å in **CN2PEN/PEN**, at *d* = 4.2-4.8 Å in **CN2PEN/F2PEN**, and at *d* = 4.4-5.0 Å in **CN2PEN/Cl2PEN**. The optimal condition for balancing high *y* and high *s* is supposed to be at *d* = 4.8 Å in **Cl2PEN/PEN** (*y* = 86.1 %, *s* = 93.8 %, and *y* × *s* = 80.8 %) at long timescale *t* = 1 ns, or *d* = 4.2 Å (*y* = 79.6 %, *s* = 91.9 %, and *y* × *s* = 73.2 %) at short timescale *t* = 10 ps. These cases exhibited higher selectivity of separated TT states than **PEN/PEN** because of the lower T_1 energy of ***X*** than ***Y***.

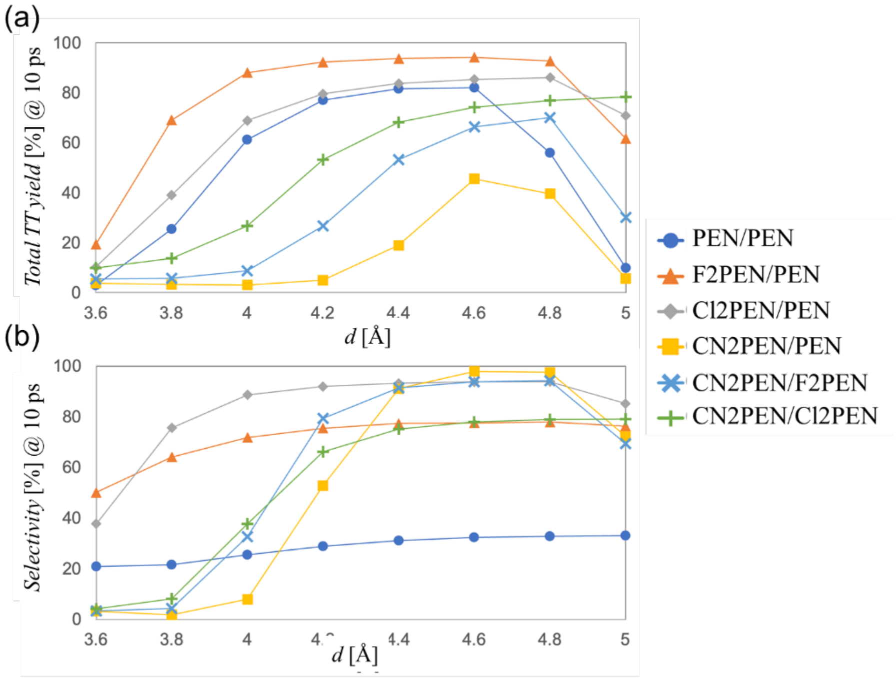

Figure III.7. (a) the total TT yield and (b) the selectivity of the separated TT state at $t = 1$ ns.

Figure III.8 shows the time-evolutions of the diabatic state populations for (a) **PEN/PEN** (y = 77.0 % and s = 22.3 %), (b) **Cl2PEN/PEN** (y = 79.6 % and s = 91.9 %), (c) **CN2PEN/PEN** (y = 5.0 % and s = 52.8 %), and (d) **CN2PEN/Cl2PEN** (y = 53.2 % and s = 66.2 %) at d = 4.2 Å. The horizontal axis is given on a log scale to see the slow increase of the TT population at large. d. From **Figure III.8 (a)**, the total TT population of **PEN/PEN** increased at $\sim 10^1$ ps, which consisted of both the neighboring and distant TT contributions. The selectivity of distant TT state was lower than that of neighboring TT in this homotrimer model. For **Cl2PEN/PEN** [**Figure III.8 (b)**], the total TT population increased at $\sim 10^0$ ps, about one-order faster than **PEN/PEN**. In this system, the distant TT population was more significant than the neighboring TT population in range of 10^0-10^1 ps. For **CN2PEN/PEN** [**Figure III.8 (c)**], the TT population remained low whereas the CT population became high in the time scale of 10^{-2}-10^{-1} ps. This is because the C^YA^X state is lower than S_1 and TT states as mentioned in **Figure III.7 (a)**. For **CN2PEN/Cl2PEN** [**Figure III.8 (d)**], the TT generation occured at $\sim 10^{-2}$ ps, which is about 10^3 times faster than that in **PEN/PEN**. Although the converged value of total TT population was ~50%, high selectivity of the distant TT was achieved. Next, we discuss the origin of faster SF in heterotrimers **Cl2PEN/PEN** and **CN2PEN/Cl2PEN** than homotrimer **PEN/PEN** in view of the quantum interference.

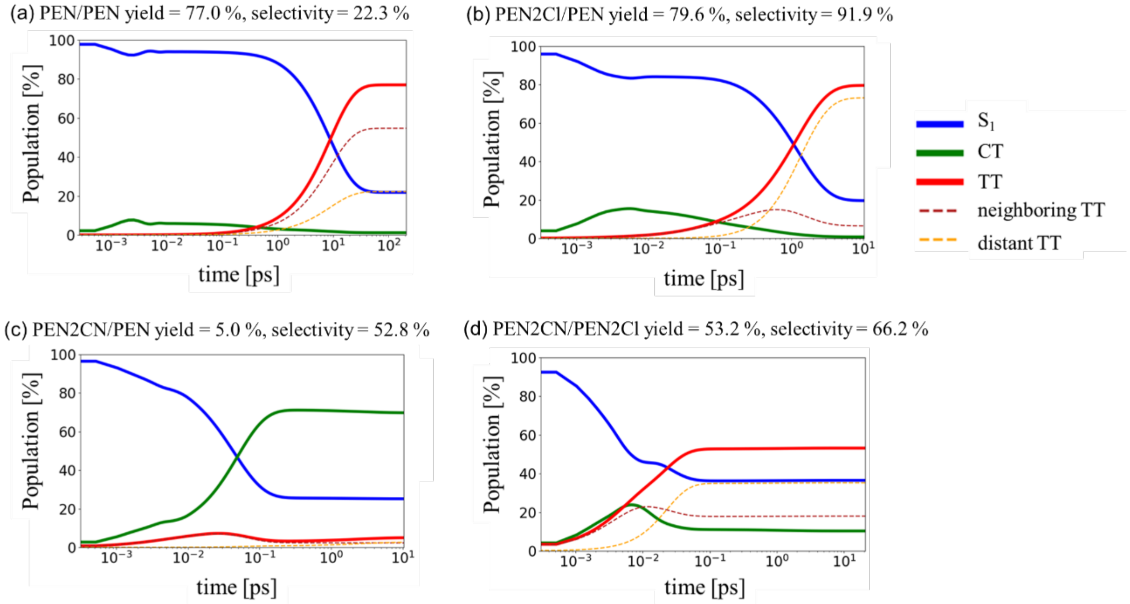

Figure III.8. Time-evolution of the diabatic population of S_1, CT, and TT states for **PEN/PEN**, **Cl2PEN/PEN**, **CN2PEN/PEN**, and **CN2PEN/Cl2PEN** systems with intermolecular distance $d = 4.2$ Å.

4. Discussion

The origin of the faster SF in heterotrimers is attributed to quantum interference effects driven by the stabilization of CT states. As described in Chapter II.2, we demonstrated that stabilization of one CT configuration (CA or AC) by local structural symmetry breaking resolves the quantum interference between the interaction paths via the CA and AC states which caused the cancellation in S_1-TT mixing in pentacene ring-shaped aggregate models. The study showed that the SF tends to occur more rapidly when the adiabatic S_1-like state includes the TT wavefunction component or the adiabatic TT-like state includes the S_1-wavefunction component. However, in some highly symmetric aggregate structures, such as slip-stack dimers or ring-shaped aggregates, the S_1-TT mixing vanishes. As illustrated in **Figure III.9**, this cancellation occurs because two effective interaction paths between delocalized S_1 state (denoted as S_1* state) and TT state mediated by C^XA^Y and C^YA^X state cancel each other. For simplicity, let us consider a hetero-dimer system consisting of $\boldsymbol{X}$ and $\boldsymbol{Y}$. By applying the second-order perturbation theory, the correlation between the delocalized S_1* and TT states is estimated by the following equation:

$$V' = \sqrt{\frac{3}{2}}\left(\frac{V_{\mathrm{LH}}}{E_{\mathrm{S}_1^*} - E_{\mathrm{TT}}}\frac{c_X V_{\mathrm{LL}} - c_Y V_{\mathrm{HH}}}{E_{\mathrm{S}_1^*} - E_{\mathrm{C^XA^Y}}} + \frac{V_{\mathrm{HL}}}{E_{\mathrm{S}_1^*} - E_{\mathrm{TT}}}\frac{c_Y V_{\mathrm{LL}} - c_X V_{\mathrm{HH}}}{E_{\mathrm{S}_1^*} - E_{\mathrm{C^YA^X}}}\right) \qquad \text{(III.4)}$$

Here, the S_1* is expressed as the linear combination of the S_1^X and S_1^Y, with expansion coefficients

c_X and c_Y, respectively. The first and the second terms in the right-hand-side of eq. (III.4) correspond to the upper and the lower CT-mediated interaction paths between S_1* and TT states provided in **Figure III.9**, respectively. For pentacene homodimer (***X*** = ***Y***) with H-aggregate type structure, inserting the relations $c_X = -c_Y = 1/\sqrt{2}$, $V_{\mathrm{LH}} = V_{\mathrm{HL}}$, and $E_{\mathrm{C}^X A^{\mathrm{Y}}} = E_{\mathrm{C}^Y A^X}$, the right-hand-side of eq. (III.4) becomes zero. The same situation can be obtained for the symmetric J-aggregate type structure where $c_X = c_Y = 1/\sqrt{2}$, $V_{\mathrm{LH}} = -V_{\mathrm{HL}}$, and $E_{\mathrm{C}^X A^{\mathrm{Y}}} = E_{\mathrm{C}^Y A^X}$. However, in hetero dimer cases (***X*** ≠ ***Y***), the energy of $\mathrm{C^YA^X}$ is more stabilized than that of $\mathrm{C^XA^Y}$. Consequently, the second term in the right-hand-side of eq. (III.4) becomes larger than the first term, leading to enhanced S_1-TT mixing. The correlation between S_1 and TT states becomes large when the energy gap between S_1, TT, and $\mathrm{C^YA^X}$ states (the denominators of the right-hand-side of eq. (III.4)) is small. However, if CT state energy becomes too low, as shown in the SF dynamics results of **CN2PEN/PEN**, the population of the CT state increases, reducing overall TT yield.

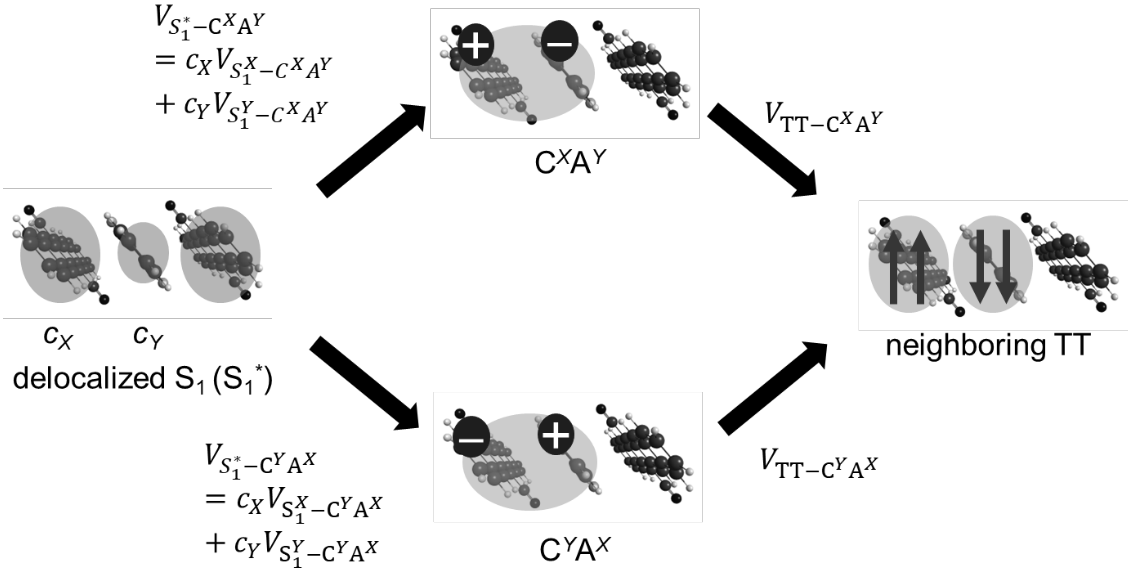

Figure III.9. Schematic illustration of the cancellation mechanism of the effective S_1-TT mixing between $\mathrm{C^XA^Y}$-mediate and $\mathrm{C^YA^X}$-mediate interaction paths.

Figure III.10(a) shows the calculation results of adiabatic state energies and percentages of the diabatic states in **CN2PEN/Cl2PEN** at d = 4.2 Å. To see how the quantum interference affects the energies and percentages of the diabatic states, we also evaluated these quantities by replacing the CT state energies in the exciton Hamiltonian with the average of $\mathrm{C}^Y\mathrm{A}^X$ and $\mathrm{C}^X\mathrm{A}^Y$ state energies (**Figure III.10(b)**) and with the $\mathrm{C}^Y\mathrm{A}^X$ state energy (**Figure III.10(c)**), while other electronic coupling parameters kept unchanged. For pristine **CN2PEN/Cl2PEN**, considerable S_1-TT hybridization occurs in the S_1-like adiabatic states with an energy of ~1.85 eV and in the TT-like adiabatic states with an energy of ~1.9 eV. However, the S_1-TT mixing was small for the latter cases with symmetrized coupling parameters. These results demonstrated how the stabilization of one CT state promoted the S_1-TT mixing and enhanced the rate of SF.

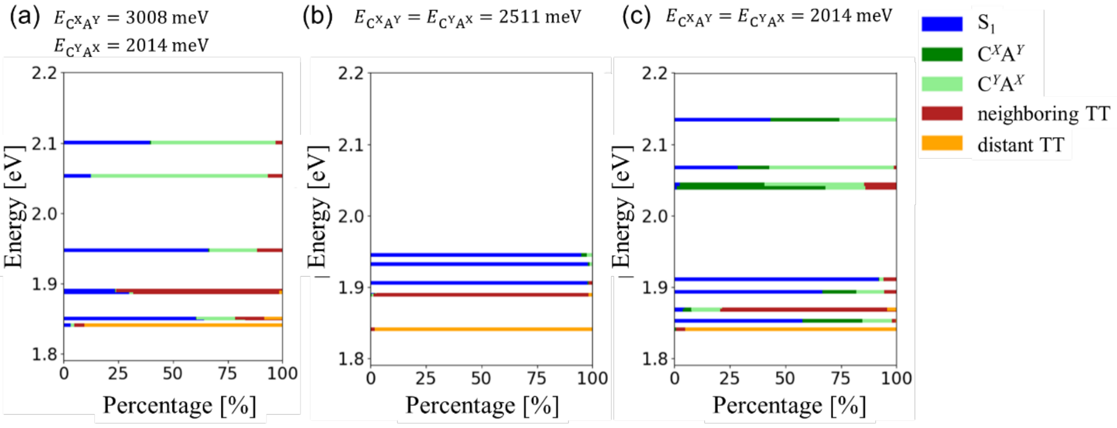

Figure III.10. (a) Calculation results of adiabatic state energies and percentages of the diabatic states in **CN2PEN/Cl2PEN** at $d = 4.2$ Å, and results when the CT state energies are parametrically set to (b) the average of C^YA^X and C^XA^Y state energies, and (c) the C^YA^X state energy. The C^XA^Y-like adiabatic state energies are too high in case (b) to be presented within the energy range of 1.8-2.2 eV. The adiabatic states pointed by the black arrows in (a) indicate the S_1-TT mixed states.

5. Conclusion

This study presents an efficient strategy for controlling the spatiotemporal evolution of TT pairs generated by the SF in heterotrimers, ***X/Y***. Using TDDFT calculations for pre-screening based on effective energy matching conditions and SF dynamics simulations based on the TCL-QME approach combined with the exciton Hamiltonian construction at the XMC-QDPT2 level, we identified optimal conditions for balancing high TT yield and high selectivity of the separated TT states. Considering the quantum interference, we clarified the roles of asymmetric CT states in enabling efficient heterofission. Two key advantages of heterofission systems were identified.

First, directional TT migration from the center to the terminal molecules was achieved with a probability exceeding 70 %. These efficiencies correlate with the absolute value of the Hammett's para-substitution constant ($|\sigma_p|$) of the substituents. Introducing halogen atoms or CN groups with large $|\sigma_p|$ into pentacene lowers the S_1 and T_1 excitation energies. By choosing the appropriate species of ***X*** and ***Y***, the T_1 energy difference can be tuned, leading to the higher selectivity of spatially separated TT states.

Second, the asymmetric energy levels of the CT states potentially enhance TT generation. When the σ_p of the substituents is larger in ***X*** than ***Y***, the C^YA^X state is energetically more stable than the C^XA^Y state. Such a reduction of symmetry breaks the destructive quantum interference between the S_1-TT mixing paths mediated by C^YA^X and C^XA^Y states. The stabilization energy of C^YA^X states is determined by the intermolecular distance and the electron-withdrawing ability of substituents, while the off-diagonal exciton Hamiltonian elements remain constant. An optimal difference in σ_p for substituents in ***X*** and ***Y*** is necessary to enhance SF efficiency.

We expect that the results and conclusions derived from the present model can be extended to the cases of 2D and 3D organic frameworks consisting of different molecular species as well as intramolecular SF for systems of covalently linked multimers in realistic situations. Notably, the optimal region of intermolecular distance for efficient TT separation was found to be relatively large (> 4 Å) compared with the typical distances between the neighboring π-planes in actual molecular crystals. In realistic conditions, additional factors such as the polar environment (e.g., the crystal or solvation field), as they often significantly influence CT energy stabilization.[8,9] Furthermore, it is necessary to consider the populations of high-spin states in the TT dissociation process to establish valuable quantum spin technology strategies.[2, 14-16] Despite these challenges, the present study provides a promising pathway for enhancing SF by utilizing the heterofission process. The insights gained here are expected to contribute to the development of advanced materials for such as quantum spin applications.

Appendix

A.1. Properties of 6,13-substituted Pentacene Derivatives

Table A1. S_1 and T_1 excitation energies, ST gaps, HOMO and LUMO energies, and HL gaps evaluated by the (TD)DFT calculations, and *para*-substitution coefficients for pentacene derivatives, σ_p. Energies are given in eV.

Molecule	$E(S_1)$	$E(T_1)$	ST-gap	HOMO	LUMO	HL-gap	σ_p *[1]
PEN	2.335	1.127	1.2079	-5.89	-1.56	4.33	0
F2PEN	2.261	1.070	1.1916	-5.95	-1.69	4.26	0.06
Cl2PEN	2.220	1.035	1.1845	-6.11	-1.91	4.20	0.23
CN2PEN	2.067	0.935	1.1324	-6.59	-2.59	4.01	0.66
$CF_3$2PEN	2.188	1.015	1.1728	-6.40	-2.20	4.20	0.54
Pr2PEN[*2]	2.226	1.054	1.1725	-5.73	-1.51	4.21	-0.13
$OCH_3$2PEN	2.212	1.041	1.1711	-5.74	-1.53	4.21	-0.27
Ar2PEN[*2]	2.259	1.085	1.1749	-5.77	-1.51	4.27	-0.01
Thi2PEN[*2]	2.235	1.065	1.1702	-5.90	-1.67	4.23	0.05

[1] The data is obtained from ref. [37]. [2] **Pr2PEN**: R = C_3H_7, **Ar2PEN**: R = C_6H_5, **Thi2PEN**: R = C_4H_3S.

A.2. TT Yield and Selectivity of Separated TT Pair at 10 ps

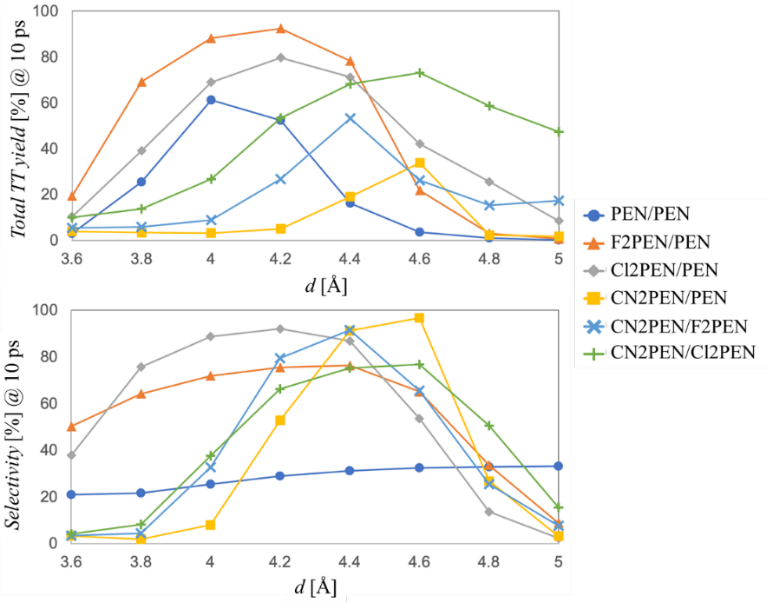

Figure A1. TT population and distant TT selectivity at time 10 ps.

References

(1) Y. Kawashima, T. Hamachi, A. Yamauchi, *et al. Nat. Commun.* **2023**, *14*, 1056.

(2) K. E. Smyser, J. D. Eaves *Sci. Rep.* **2020**, *10*, 18480.

(3) K. Miyata, F. S. Conrad-Burton, F. L. Geyer, X.-Y. Zhu *Chem. Rev.* **2019**, *119*, 4261-4292.

(4) S. Matsuda, S. Oyama, Y. Kobori *Chem. Sci.* **2020**, *11,* 2934.

(5) Y. Wang, M. Haze, H.T. Bui, *et al. npj Quantum Inf.* **2023**, *9*, 48.

(6) T. Zeng, R. Hoffman, N. Ananth *J. Am. Chem. Soc.* **2014**, *136*, 5755-5764.

(7) P. Petelenz, M. Snamina, G. Mazur *J. Phys. Chem. C* **2015**, *119*, 14338-14342.

(8) P. Petelenz M. Snamina *J. Phys. Chem. Lett.* **2016**, *7*, 1913-1916.

(9) T. Nagami, H. Miyamoto, R. Sakai, M. Nakano *J. Phys. Chem. C* **2021**, *125*, 2264–2275.

(10) T. Tonami, R Sugimori, R. Sakai, K. Tokuyama, H. Miyamoto *Phys. Chem. Chem. Phys.*, **2021**, *23*, 11624-11634.

(11) H. Miyamoto, M. Nakano *ChemPhotoChem* **2020**, *4*, 5249-5263.

(12) H. Miyamoto, K. Okada, R. Tokuyama, M. Nakano *J. Phys. Chem. A* **2021**, *125*, 5585–5600.

(13) S. Nakamura, H. Sakai, M. Fuki, R. Ooie, F. Ishiwari, A. Saeki, N. V. Tkachenko *Angew. Chem.* **2023**, *135*, e202217704.

(14) R. D. Dill, K. E. Smyser, B.K. Rugg, N. H. Damrauer, J. D. Eaves *Nat Commun* **2023**, *14*, 1180.

(15) S. L. Bayliss, L. R. Weiss, F. Kraffert, D. B. Granger, J. E. Anthony, J. Behrends, R. Bittl *Phys. Rev. X* **2020**, *10*, 021070.

(16) A. Mena S. K. Mann, A. Cowley-Semple, E. Bryan, S. Heutz, D. R. McCamey, M. Attwood, S. L. Bayliss *Phys. Rev. Lett.* **2024**, *133*, 120801.

(17) S. Hirata, M. Head-Gordon *Chem. Phys. Lett.* **1999**, *314*, 291–299.

(18) T. Yanai, D. P. Tew, N. C. Handy, *Chem. Phys. Lett.* **2004**, *393*, 51-57.

(19) Gaussian 16, Revision C.01, M. J. Frisch, G. W. Trucks, H. B. Schlegel, G. E. Scuseria, M. A. Robb, J. R. Cheeseman, G. Scalmani, V. Barone, G. A. Petersson, H. Nakatsuji, X. Li, M. Caricato, A. V. Marenich, J. Bloino, B. G. Janesko, R. Gomperts, B. Mennucci, H. P. Hratchian, J. V. Ortiz, A. F. Izmaylov, J. L. Sonnenberg, D. Williams-Young, F. Ding, F. Lipparini, F. Egidi, J. Goings, B. Peng, A. Petrone, T. Henderson, D. Ranasinghe, V. G. Zakrzewski, J. Gao, N. Rega, G. Zheng, W. Liang, M. Hada, M. Ehara, K. Toyota, R. Fukuda, J. Hasegawa, M. Ishida, T. Nakajima, Y. Honda, O. Kitao, H. Nakai, T. Vreven, K. Throssell, J. A. Montgomery, Jr., J. E. Peralta, F. Ogliaro, M. J. Bearpark, J. J. Heyd, E. N. Brothers, K. N. Kudin, V. N. Staroverov, T. A. Keith, R. Kobayashi, J. Normand, K. Raghavachari, A. P. Rendell, J. C. Burant, S. S. Iyengar, J. Tomasi, M. Cossi, J. M. Millam, M. Klene, C. Adamo, R. Cammi, J. W. Ochterski, R. L. Martin, K. Morokuma, O. Farkas, J. B. Foresman, and D. J. Fox, Gaussian, Inc., Wallingford CT, **2016**.

(20) M. W. Tripp, U. Koert *J. Org. Chem*. **2020**, *16*, 2136–2140.

(21) J. Li, M. Wang, S. Ren, X. Gao, W. Hong, H. Li, D Zhu *J. Mater. Chem.*, **2012**, *22*, 10496.

(22) J. Schwaben, N. Münster, T. Breuer, M. Klues, K. Harms, G. Witte, U. Koert *Eur. J. Org. Chem*. **2013**, 1639–1643.

(23) J. Schwaben, N. Münster, M. Klues, T. Breuer, P. Hoffmann, K. Harms, G. Witte, U. Koert *Chem.-Eur. J.* **2015**, *21*, 13758-13771.

(24) T. Takahashi, K. Kashima, S. Li, K. Nakajima, K. Kanno *J. Am. Chem. Soc.* **2007**, *129*, 15752–15753.

(25) Q. Miao, X. Chi, S. Xiao R. Zeis, M. Lefenfeld, T. Siegrist, M. L. Steigerwald, C. Nuckolls, *J. Am. Chem. Soc.* **2006**, *128*, 4, 1340–1345.

(26) K. Sakamoto, K. Hamachi, T. Miyokawa, K. Tateishi, T. Uesaka, Y. Kurashige, N. Yanai *Proc. Natl. Acad. Sci. U.S.A.* **2023**, *120*, e2307926120.

(27) R. D. Harcourt, G. D. Scholes, K. P. Ghiggino *J. Chem. Phys.* **1994**, *101*, 10521–25. J. Wehner, B. Baumeier *J. Chem. Theor. Comp.* **2017**, *13*, 1584-94.

(28) A. A. Granovsky *J. Chem. Phys.* **2011**, *134*, 214113.

(29) H. Nakamura, D. G. Truhlar *J. Chem. Phys.* **2002**, *117*, 5576.

(30) G. M. J. Barca, C. Bertoni, L. Carrington, D. Datta, N. De Silva, J. E. Deustua, D. G. Fedorov, J. R. Gour, A. O. Gunina, E. Guidez, T. Harville, S. Irle, J. Ivanic, K. Kowalski, S. S. Leang, H. Li, W. Li, J. J. Lutz, I. Magoulas, J. Mato, V. Mironov, H. Nakata, B. Q. Pham, P. Piecuch, D. Poole, S. R. Pruitt, A. P. Rendell, L. B. Roskop, K. Ruedenberg, T. Sattasathuchana, M. W. Schmidt, J. Shen, L. Slipchenko, M. Sosonkina, V. Sundriyal, A. Tiwari, J. L. G. Vallejo, B. Westheimer, M. Włoch, P. Xu, F. Zahariev, M. S. Gordon *J. Chem. Phys.* **2020**, *152*, 154102.

(31) X. Xie, A. Santana-Bonilla, W. Fang, C. Liu, A. Troisi, H. Ma *J. Chem. Theor. Comp.* **2019**, *15*, 3721-29.

(32) M. Nakano, T. Nagami, T. Tonami, K. Okada, S. Ito, R. Kishi, Y. Kitagawa, T. Kubo *J. Comput. Chem.* **2018**, *40*, 89−104.

(33) N. Renaud, F. C. Grozema *J. Phys. Chem. Lett.* **2015**, *6*, 360−65.

(34) H.-P. Breuer, F. Petruccione *The Theory of Open Quantum Systems*; Oxford University Press: Oxford, U.K. **2002**.

(35) S. R. Reddy, P. B. Coto, M. Thoss *J. Chem. Phys.* **2019**, *151*, 044307.

(36) T. Nagami, T. Takayoshi, K. Okada, W. Yoshida, H. Miyamoto, M. Nakano *J. Chem. Phys.* **2020**, *153*, 134302.

(37) C. Hansch, A. Leo, R. W. Taft *Chem. Rev.* **1991**, *91*, 165-95.

GENERAL CONCLUSION

This dissertation theoretically investigated the molecular aggregate structure–SF dynamics correlations and design guidelines for SF ranging from TT generation to spatial migration process. PART II proposed symmetry-based design guidelines by introducing pentacene ring-shaped aggregate systems for enhancing the SF rate without reducing the yield of TT generation. PART III investigated heterotrimer systems consisting of different pentacene derivatives to control the spatio-temporal distribution of triplet excitons after SF. Throughout the dissertation work, several key factors have been identified for enhancing SF and directional TT migration by examining the molecular species, intermolecular interaction, and aggregation topology in molecular aggregate structures.

PART II: Structure–SF Dynamics Relationships for Efficient TT generation in Ring-Shaped Pentacene Molecular Aggregate Systems

PART II elucidated the relationships between molecular aggregate structure and SF dynamics in the pentacene ring-shaped aggregate model and clarified a new perspective for optimizing the aggregate structures to achieve both high TT yield and SF rate.

Chapter 1 constructed J- and H-type ring-shaped molecular aggregate systems where the transition dipole moments of individual molecules align tangentially and perpendicularly to the ring, respectively. The SF dynamics simulation was conducted to investigate how the intermolecular configuration and aggregate size (*N*) affect the TT yield and SF rate. Quantum master equation (QME) simulation revealed distinct behaviors for the two ring types. In the J-type rings, the SF rate monotonically decreased while the TT yield increased with *N*. On the other hand, the H-type rings showed a zig-zag pattern in the SF rate for *N* with larger values for odd-*N* rings and exhibited a peak at $N = 5$. These relationships between the SF dynamics and the intermolecular configuration in the ring-shaped models were explained from the symmetry of exciton states and based on the RRF analysis. The parity-dependent feature of the SF rate arises from whether the lowest adiabatic FE-like state includes the diabatic TT exciton configurations, which are determined by the symmetry of the aggregate system.

Chapter 2 further investigated the effects of intermolecular configuration, represented by the rotation angle (α) of each monomer and the aggregate size (*N*), on the SF dynamics in pentacene ring-shaped aggregate models asymmetric for the ring-flipping operations. It is clarified that the equivalence of two types of CT states was crucial: CA and AC states were equivalent in the symmetric ring-shaped models, such as the J- and H-type rings, while one of the CT states was stabilized in lower symmetric structures. These two CT states are involved in the virtual quantum transition process of SF from the initial S_1 to the final TT. According to the second-order perturbation theory, the two transition pathways via the virtual CA and AC states in the high-symmetry structures canceled each other due to the quantum interference effects. However, reducing the structural symmetry broke this cancellation, enhancing the SF rate without compromising the TT yield.

The acceleration mechanism presented in these studies is expected to apply to pentacene rings and a wide range of aggregate systems. The present results highlight the effectiveness of symmetry-based design guidelines of molecular aggregate structures for enhancing SF rate without reducing the TT yield. They also contribute to a deeper understanding of the SF mechanisms and the construction of novel SF materials on a mesoscopic scale.

PART III: Molecular Aggregate Structure – SF Dynamics Relationships for Directional TT Migration

PART III established design guidelines balancing the efficient SF and directional triplet migrations. The author focused on the SF dynamics in symmetric heterotrimer models consisting of unsubstituted and 6,13-substituted molecules and considered several combinations of molecular species and different intermolecular relative configurations. Placing suitable triplet acceptors at the terminals, the excitons migrated efficiently to the terminals after the heterofission. The triplet excitation energy of pentacene derivatives correlated with the *para*-substituent constant of the substituent groups, and pentacenes with strong inductive substituents showed lower triplet energies. However, a combination of pentacenes with strong and weak electron-withdrawing groups resulted in a larger energy gap between the frontier orbitals. As a result, a lower TT yield was obtained due to the overstabilization of the CT energy during the heterofission. Consequently, an optimal range exists for the inductive effects of substituents for the combination of the central and terminal pentacenes. By optimizing the substituent species and the intermolecular distance, it was demonstrated that both the high TT yield and directional TT migrations from the center to the terminal were achieved, with their probabilities exceeding 80 and 70 %, respectively. Moreover, as described in Chapter II.2, asymmetric energy levels of CT states also contributed to enhancing the TT generation due to the breakdown of quantum interference between the S_1-TT interaction paths via the CA and AC states. The insights gained in Chapter III are expected to contribute to developing design guidelines and functionalities utilizing heterofission for controlling the spatial distribution of TT pairs.

In summary, this dissertation theoretically identified several key factors determining the SF dynamics, from the generation to the migration processes of TT, and established design strategies based on the molecular aggregate structures as novel descriptors for efficient SF. This dissertation work will significantly contribute to further development in the wide-ranging application study of SF, such as organic solar cells and quantum spin information technologies.

FUTURE PROSPECTS

This dissertation has explored many molecular aggregate systems to elucidate the mechanism of efficient SF and establish directional control strategies for triplet exciton pair migrations. While this dissertation has successfully clarified part of the mechanisms and proposed novel design strategies, unexplored aspects remain, and a frontier for advancing theoretical SF design remains. These topics are outlined below as prospects.

Design of SF Materials Involving Spin Decoherence Process

We have discussed the SF dynamics and design guidelines considering the spatial separation of the TT pair. However, for the application targeting the quantum spin information technologies, such as the sensing techniques based on dynamic nuclear polarization (DNP), it is essential to address not only the total singlet TT state ^{1}(TT) but also the high spin states like ^{3}(TT) and ^{5}(TT). Thus developing design principles for molecules and molecular aggregates that can enhance the spin entanglement decoherence timescale.

Several kinds of research on the spin decoherence mechanism after SF have been pursued in recent years, including simulations of the intramolecular SF dimer[1] or ring-shaped aggregate models.[2] However, the relaxation rates employed in these studies are phenomenological parameters, and the structure-property relationships from a molecular-level perspective remain unresolved. For practical implementation of the spin decoherence process for obtaining microscopic physical insights, the spin-spin and spin-phonon interactions must be modelled, and the dynamics simulation must be examined under the consideration of both the spatial TT migration and spin relaxation processes. The spin relaxation process occurs with a timescale ranging from few nanoseconds to microseconds because it involves transitions between the states with different spin multiplicities. However, in realistic systems, various conformational fluctuations and inter-state transitions occur on similar timescales, such as molecular rotation,[3] potentially influence the spin relaxation dynamics. Development of the methodologies in theoretical chemistry that can address the spin-phonon vibronic coupling accurately will pave the way for the novel SF material designs for applications in quantum spin information science, sensing, and other advanced functionalities.

SF dynamics and Triplet Migration in Larger Aggregate Structure

In PART III, we considered the SF dynamics and TT dissociation process in trimer systems. However, in more realistic systems, the dynamics in larger two- or three-dimensional crystals arouse our curiosity from the viewpoint of application to organic solar cells. However, it is challenging to execute the quantum master equation simulation for such high-dimensional systems due to the high computational costs. To understand such quantum dynamical behaviors at the mesoscopic scale, the Monte Carlo wavefunction approach[4] offers a feasible method to simulate the SF dynamics in larger clusters at an affordable computational cost. For macroscale dynamics, the continuum approximation or drift-diffusion approximation can be useful to model the exciton distribution in macroscopic device structures. Connecting the microscopic structure of molecular aggregate systems to these meso- and macroscopic perspectives will help establish comprehensive design guidelines for organic solar cells and quantum devices.

References

(1) R. K. Kathir, Pedro B. Coto, M. Thoss *J. Phys. Chem. Lett.* **2024** *15*, 46, 11517.

(2) F. Campaioli, A. Pagano, D. Jaschke, S. Montangero *PRX Energy*, **2024**, *3*, 043003.

(3) T. Hasobe, S. Nakamura, N. V. Tkachenko, Y. Kobori *ACS Energy Letters* **2022** *7*, 1, 390.

(4) M. Nakano, K. Okada, T. Nagami, T. Tonami, R. Kishi, Y. Kitagawa *Molecules* **2019**, *24*, 3, 541.

LIST OF PUBLICATIONS

Main Papers

[A1] H. Miyamoto, M. Nakano, "Theoretical study on singlet fission dynamics in pentacene ring-shaped aggregate models with different configurations", *ChemPhotoChem*, **2020**, *4*, 5249-5263.

[A2] H. Miyamoto, K. Okada, K. Tokuyama, M. Nakano, "Theoretical study on singlet fission dynamics in slip-stack-like pentacene ring-shaped aggregate models", *J. Phys. Chem. A*, **2021**, *125*, 5585-5600.

[A3] H. Miyamoto, K. Okada, K. Tada, R. Kishi, Y, Kitagawa, "Theoretical study on singlet fission dynamics and triplet migration process in symmetric heterotrimer models", *Molecules*, **2024**, *29*, 5449 (15 pages).

Related Papers

(1) T. Nagami, H. Miyamoto, W. Yoshida, K. Okada, T. Tonami, M. Nakano, "Theoretical molecular design of phenathenes for singlet fission by diazabora-substitution", *J. Phys. Chem. A*, **2020**, *124*, 6778-6789.

(2) T. Nagami, H. Miyamoto, R. Sakai, M. Nakano, "Stabilization of charge-transfer states in pentacene crystals and its role in singlet fission", *J. Phys. Chem. C*, **2021**, *125*, 2264-2275.

(3) T. Nagami, K. Okada, H. Miyamoto, W. Yoshida, T. Tonami, M. Nakano, "Molecular design principle for efficient singlet fission based on diradical characters and exchange integrals: Multiple heteroatom substitution effect on anthracenes", *J. Phys. Chem. C*, **2020**, *124*, 11800-11809.

(4) W. Yoshida, K. Okada, H. Miyamoto, T. Tonami, T. Nagami, M. Nakano "Theoretical study of non-Markov effects on singlet fission dynamics of model pentacene dimers using the second-order time-convolutionless quantum master equation method", *J. Phys. Chem. C*, **2020**, *124*, 12220-12229.

(5) K. Okada, M. Nakano, H. Miyamoto, H. Nakazawa, Y. Uetake, H. Sakurai, "Theoretical study on singlet fission dynamics in sumanene-fused acene dimers", *J. Phys. Chem. C*, **2020**, *124*, 19499-19507.

(6) W. Yoshida, H. Matsui, H. Miyamoto, T. Tonami, R. Sugimori, K. Yoneda, R. Kishi, M. Nakano, "Theoretical study on third-order nonlinear optical properties for one-hole-doped diradicaloids", *ACS Omega*, **2021**, *6*, 3046-3059.

(7) T. Tonami, T. Nagami, K. Okada, W. Yoshida, H. Miyamoto, M. Nakano, "Quantum design for singlet-fission-induced nonlinear optical systems: Effects of π-conjugation length and molecular packing of butterfly-shaped acenes", *J. Chem. Phys.*, **2020**, *153*, 084304.

(8) T. Nagami, T. Tonami, K. Okada, W. Yoshida, H. Miyamoto, M. Nakano, "Vibronic coupling density analysis and quantum dynamics simulation for singlet fission in pentacene and its halogenated derivatives", *J. Chem. Phys.*, **2020**, *153*, 134302.

(9) T. Tonami, R. Sugimori, R. Sakai, K. Tokuyama, H. Miyamoto, M. Nakano, “Theoretical study on the effect of applying an external static electric field on the singlet fission dynamics of pentacene dimer models”, *Phys. Chem. Chem. Phys.*, **2021**, *23*, 11624.
(10) T. Tonami, H. Miyamoto, M. Nakano, R. Kishi, Y. Kitagawa, “Theoretical study on thermal structural fluctuation effects of intermolecular configurations on singlet fission in pentacene crystal models”, *J. Phys. Chem. A*, **2023**, *127*, 1883-1893.
(11) W. Yoshida, Y. Shigeta, H. Matsui, H. Miyamoto, R. Kishi, Y. Kitagawa, “Theoretical study on molecular charge populations on 1D π-stacked multimers in neutral and electron oxidation states”, *Bull. Chem. Soc. Jan.*, **2024**, *97*, uoae009.
(12) W. Yoshida, H. Miyamoto, J. Shoda, H. Matsui, R. Sugimori, R. Kishi, Y. Kitagawa, “Theoretical study on open-shell electronic structures of through-bond/through-space hybrid conjugated ladder graphs”, *Chem. Phys. Lett.*, **2024**, *842*, 141196.

International Conferences

[1] H. Miyamoto, K. Okada, K. Tokuyama, M. Nakano, “Theoretical study on singlet fission dynamics in pentacene asymmetric multiple-ring aggregate models”, Pacifichem2021, Designed π-Electronic Systems: Synthesis, Properties, Theory and Function (#359), December 16-21, 2022, Honolulu, Hawaii, USA. (**Poster**)

[2] H. Miyamoto, K. Okada, R. Kishi, Y. Kitagawa, “Theoretical study on singlet fission dynamics in one-dimensional molecular aggregates: Effects of local changes of intermolecular interactions”, The 5th conference of Theory and Applications of Computational Chemistry (TACC2023), September 4-9, 2023, Sapporo, Japan. (**Poster**)

[3] H. Miyamoto, K. Okada, R. Kishi, Y. Kitagawa, “Theoretical study on singlet fission process in one-dimensional aggregate systems considering position-dependent intermolecular electronic couplings”, The 8th Japan-Czech-Slovakia (JCS) International Symposium on Theoretical Chemistry (JCS8), June 17-21, 2024, Sapporo, Japan. (**Poster**)

[4] H. Miyamoto, K. Okada, K. Tada, R. Kishi, Y. Kitagawa, “Theoretical study on singlet fission dynamics in finite-size molecular aggregates with various intermolecular interaction strengths and structures”, 11th Triennial Congress of the International Society for Theoretical Chemical Physics (ISTCP), October 13-18, 2024, Qingdao, China. (**Poster**)

ACKNOWLEDGEMENT

This dissertation study was carried out under the supervision of late Prof. Dr. Masayoshi Nakano and Prof. Dr. Yasutaka Kitagawa at Division of Chemical Engineering, Department of Materials Engineering Science, Graduate School of Engineering Science, Osaka University. Prof. Dr. Masayoshi has given me numerous insightful and helpful advice on my study and encouraged me to study with shaping my own philosophy through the research activity during 2019 – 2021. He gave many opportunities to participate in domestic and international conferences wishing my fruitful experiences. Prof. Dr. Yasutaka Kitagawa have also taken care of me during 2019 – 2025. I would like to express deepest gratitude to them.

I am deeply grateful to Prof. Dr. Nobuyuki Matubayasi, Dr. Tetsuro Kusamoto, and Dr. Ryohei Kishi (Graduate School of Engineering Science, Osaka University) for kindly accepting the referee of this dissertation.

I would like to express gratitude to Dr. Yasutaka Kitagawa and Dr. Ryohei Kishi (Graduate School of Engineering Science, Osaka University) for their insightful comments on my study and for the instructions of quantum chemistry.

I would like to thank all the members I have met in Quantum Chemical Engineering laboratory (former Nakano lab. or current Kitagawa lab.) for sharing the wonderful days during 2020–2025. I was happy to witness their achievements and to discuss a lot of things day and night. DC. Kenji Okada, Dr. Wataru Yoshida, Dr. Takayoshi Tonami, and Dr. Takanori Nagami have inspired me a lot because of their outstanding abilities and deep insights on study etc. This dissertation has never been accomplished without the help of them and gave me a lot of insightful comments on my study.

This dissertation study was financially supported by the Japan Society for the Promotion of Science (JSPS) Research Fellowship for Young Scientists (No. JP22KJ2221). Theoretical calculations were performed using Research Center for Computational Science, Okazaki, Japan.

Finally, I would like to thank my family, Shirou, Azusa, and Yuri for their kind supports and encouragements.

Hajime MIYAMOTO
March 2025